REPORT R-37[illegible] MAY, 1968

COORDINATED SCIENCE LABORATORY

A PROPOSED TEST OF THE EINSTEIN THEORY OF GRAVITATION BY MEANS OF AN UNSHIELDED ORBITING GYRO USING PASSIVE TELEMETRY

D.H. COOPER
G.R. KARR
J.L. MYERS
D. SKAPERDAS

UNIVERSITY OF ILLINOIS - URBANA, ILLINOIS

This work was supported in part by the Joint Services Electronics Program (U.S. Army, U.S. Navy, and U.S. Air Force) under contract DAAB07-67-C-0199; and in part by the National Aeronautics and Space Administration under Research Grant NsG-443.

This is the final report of a feasibility study of an experiment to measure the first-order precession, predicted by Einstein's General Theory of Relativity, of an earth-orbiting, free gyroscope. The results of this study show that a relatively inexpensive experiment, using an unshielded gyro and a passive data-readout and telemetry system, is now feasible for measuring this precession to an accuracy of about 1%. This study has been supported by the National Aeronautics and Space Administration under Research Grant NsG-443.

A report of this size, covering many disciplines, required the cooperation and results of investigations of many researchers who are no longer with the Coordinated Science Laboratory. We are indebted to Dr. Daniel Alpert, Dean of the U. of I. Graduate College, who as the previous director of the Coordinated Science Laboratory, was instrumental in proposing and initiating this project and who helped guide it in its early years. We were fortunate to have frequent consultations with Dr. Arnold Nordsieck, inventor of the electric vacuum gyro. The original impetus for this study had its origin in the successful development of this gyro while Dr. Nordsieck was a member of the Coordinated Science Laboratory. Dr. R. D. Palamera, whose doctoral dissertation entitled, "Syntheses of a General Relativity Experiment," introduced us to many of the problems associated with this study, participated in some of the analyses during a summer spent with the Laboratory. Dr. John Ray, a theoretical physicist specializing in relativity theory, guided the group through

the intricacies of that part of the theory (first developed by L. I. Schiff) that is the basis for this experiment.

Among the members of the Laboratory, we are especially indebted to Professor Howard W. Knoebel, leader of the Aerospace Group, for his many original ideas, helpful discussion and guidance, and to Professor Duane H. Cooper for devising the present overall plan of the experiment.

Professor Cooper also had the major responsibility for preparing Chapters 2, 3 and 9. Computations associated with Chapter 9 were programmed for the CDC 1604 computer by Jack Bouknight. Bill Kirkwood performed the associated experiments measuring photographic film noise for the type of film used in the Baker-Nunn cameras of the Smithsonian Astrophysical Observatory and recording images simulating ones which would be obtained by those cameras. Chapters 4 and 8 were prepared by James L. Myers. This material forms part of a doctoral thesis which will soon be submitted to the Department of Aeronautical and Astronautical Engineering of the University of Illinois. The section on micrometeoric cratering was analyzed by Professor Harold Barthel of the Aeronautical and Astronautical Engineering Department, who spent the summer with the Laboratory. Gerald R. Karr, a doctoral candidate in the Aeronautical and Astronautical Engineering Department, prepared Chapters 5 and 6. Some of this material was written in partial fulfillment for a Master's degree under Professor S. M. Yen of CSL and the Aeronautical

and Astronautical Department. Dominic Skaperdas had the major responsibility for preparing Chapters 7 and 10. Donald A. Lee prepared Appendix A of Chapter 7. Chapter 10 was taken from CSL Report R-330 by T. C. Chen, J. Hsu and D. Skaperdas. The material for Chapter 11 was taken from experiments performed by Clark W. Bullard.

Further acknowledgment must be made to the assistance of L. Schusterman, N. Mehta, C. Sutton, H. Morrison, K. Hasz, L. Hickok, and E. Marzullo, and to the helpful interest of the staff of the Laboratory. Acknowledgment is particularly owed to the encouragement and guidance of the Laboratory's present Director, Professor W. Dale Compton.

TABLE OF CONTENTS

1. INTRODUCTION

Two general relativity effects, which theoretically predict a precession of the spin axis of an ideal orbiting gyroscope, have been postulated by L. S. Schiff.[1,2,3] These effects, (1) the geodetic precession arising from motion through the earth's gravitational field, and (2) the Lense-Thirring precession, representing the difference between the gravitational field of a rotating and non-rotating earth, have magnitudes of, respectively, 6 and 0.1 seconds of arc per year for an earth satellite at 300 miles altitude. The prospect of developing a gyro of sufficient accuracy to measure the first effect appeared feasible when the results of CSL's experience with the electric vacuum gyro[4,5] were extrapolated to the orbital conditions of low acceleration (less than 10^{-6} g). Gravity-induced torques were by far the most disturbing effects in the electric vacuum gyro. Theoretical studies undertaken by CSL and other groups[6,7,8] have resulted in the unanimity of opinion that there is no known fundamental limitation to the feasibility of a satellite gyro experiment to measure the precession predicted by general relativity.

In the chapters that follow, the Coordinated Science Laboratory presents in detail the results of theoretical studies which have led to a proposed satellite gyroscope experiment for measuring the first-order general relativity effect. The significance of this effect, and accuracy considerations for measuring it, are described more fully in chapter 2.

The proposed experiment would consist of a passive, unshielded, spin-stabilized gyro with an appropriate device for imparting a spin to the gyro about a preferred axis and a thrust to separate the gyro from the pay-load satellite.

The gyro would be in the form of a polyhedron of solid, poorly conductive material with a built-in preferred moment-of-inertia axis. Read-out of the gyro spin-axis would be accomplished by terrestrial observations of solar reflections from optical mirrors placed on the gyro polyhedral facets. The main advantage of the proposed experiment is to transfer the system complexity from the satellite to terrestrial stations. The experiment is described more specifically in chapter 3.

The simplification of the gyro satellite to a completely passive, unshielded device imposes tighter tolerances on other parameters. The most severe problem is the spin-axis drift due to gravity-gradient. An optimization of gyro parameters for reducing gravity-gradient effects, including those due to micrometeoroid erosion, is described in chapter 4. All other known spurious torques are analyzed and their effects evaluated in succeeding chapters. Thus, the effects of atmospheric drag on the unshielded satellite gyro are shown in chapter 5 to be negligible with respect to the first order relativity effect at altitudes greater than 600 miles. An important experiment for measuring density, thermal and momentum accomodation coefficients using the proposed system, is also described in this chapter.

The effects of solar radiation pressure and heating are described in chapter 6. Tolerances on gyro electrical conductivity are specified as a result of studies of electric, magnetic and electromagnetic torques described in chapter 7. Read-out of the gyro spin-axis precession is discussed in chapters 8 and 9. Chapter 8 presents possible solar-reflection angle distributions for the satellite gyro for various orbital inclinations. Chapter 9 describes the optical method and accuracy with which the gyro spin-axis can be determined. The burden on the optical read-out method can be considerably reduced if any gyro spin-axis wobble due to inaccurate initial spin-up or micrometeoroid collision can be damped out in sufficient time. Damping requirements impose an additional constraint on possible gyro materials, as described in chapter 10. An analysis of possible initial spin-up devices and their requirements is described in chapter 11.

2. SIGNIFICANCE OF AN ORBITING-GYRO TEST OF GENERAL RELATIVITY

Measurement of the spin-axis precession of a torque-free orbiting gyroscope is of great interest to the scientific community, for it offers the possibility of testing a fundamental theory of physics in new ways. The Einstein Theory of General Relativity predicts a precession related to its description of the gravitational field by means of a space curvature. Three aspects of the theory could, however, be tested in new ways: (a) the applicability of the theory to describing the motion of bodies other than simple point masses, (b) the possible necessity for including certain corrections to the space-curvature theory, and (c) the description of fields in the neighborhood of rotating gravitational bodies. Of these, (a) and (c) have never been hitherto subjected to test. The latter would be marginally tested with the precision that is contemplated for the experiment here proposed, so that items (a) and (b) remain as the ones of principal interest.

Item (b) has been tested principally through observing the motion of the perihelion of the orbit of Mercury. The test has long been regarded as confirming the Einstein theory with an accuracy of one percent. Recently, however, Dicke has shown[1] that there is an observable oblateness in the figure of the sun sufficient to account, on purely classical grounds, for some 8% of the relativistic component of the orbital precession. He argues that this descrepancy may require the addition of a scalar term to the characteristically tensor field equations of Einstein. Whatever theoretical accommodations

the discrepancy, if real, may demand, it is clear that such an accommodation would have significant implications for all aspects of astrophysics related to unusually massive systems and the large-scale aspects of the cosmos. Included in such aspects would be the interpretations of mainly extra-galactic observations, whether by optical astronomy or by radio astronomy, and whether of other galaxies, novae, or the more-exotic pulsars. Thus, it is particularly important to find an independent check of this 8% discrepancy. The orbiting-gyro experiment could provide such a check, since the scalar-tensor theory predicts[2] a discrepancy also of about 8% in the relativistic spin-axis precession.

In the absence of a scalar contribution, the Schwarzschild metric in polar coordinates,

$$ds^2 = c^2dt^2(1-2V/c^2)-dr^2/(1-2V/c^2)-(d\theta^2+\sin^2\theta\, d\varphi^2)r^2, \qquad (1)$$

is the solution of the Einstein field equations in the spherically-symmetric case. The departures from the flat-space metric appear in both the time-like part, in the coefficient of c^2dt^2, and in the space-like part, in the coefficient of dr^2. In both these parts, the flat-space metric would obtain if the coefficients were unity, that is, if the term proportional to the gravitational potential V did not appear. This term is

$$V/c^2 = GM/rc^2, \qquad (2)$$

apart from the factor 2, in which G is the gravitational constant and M is the mass of the gravitating body for which the potential obtains at a radial distance r. As always, c is the speed of light, and division of V by c^2 results in a dimensionless quantity.

The appearance of the term shown in (1) for the time-like part is identified with the gravitational red shift. This has been quantitatively checked to an accuracy of 1% in experiments[3] using the Mossbauer effect. The necessity for a similar appearance in the space-like part has been checked to an accuracy of about 10% in measuring the deflection of starlight near the sun, as may be observed during a solar eclipse. As Schiff points out,[4] however, these are null-geodesic tests (the equation for the path of a light ray is $ds^2 = 0$.) and do not challenge the validity of the theory in its deeper aspects, those relating to nonlinearities or involving the motion of massive test particles (geodesics that are not null). In any case, the gravitational deflection of light would, in its limited accuracy, be deemed to test the space-like part. Similarly, the Mercury precession and the gyro spin precession would be deemed to test the space-like part to enhanced precession, and to test the scalar theory, since the latter does not affect the red shift. Moreover, they would confirm, apart from testing the latter discrepancy, the correctness of the handling of the geodesic for a massive test particle and of nonlinear terms in the theory.

TEST OF GENERAL RELATIVITY

The precession of the spin axis of the orbiting gyro involves these same deeper aspects of the theory, together with one that is new, item (a), the applicability of the theory to describe the motion of bodies other than simple point masses. The covariant representation of spin for a point mass was invented by Papapetrou as a combination of first-order moment integrals spanning the space-like volume of a vanishingly small tube, within which the particle is represented by a nonvanishing energy-momentum tensor, which tube is to enclose the time-like world line traced by the representative point for the particle. Schiff[4] used this representation to calculate the motion of the spin angular-momentum vector. To obtain unique solutions, however, certain supplementary conditions must be employed, each of which leads to a different description of the motion. The relationships among these were explored by Schiff showing that these varying descriptions may be understood as specifying, in the end, the same motion. The analysis given by Tonnelat[5] follows that of Schiff and uses the same representations.

The Russian theorists, Pustovoit and Bautin,[6] object to the complexity of the method using Papapetrou's representation, especially in its need to invoke supplementary conditions. They prefer to base their calculation on a Lagrangian function for each mass element in the spinning body, from which, using an approximate superposition principle, the Lagrangian for the whole body is obtained by integration.

From this, the motion of the spin angular-momentum vector follows directly. Their result agrees with that of Schiff, but the method is used by them to show that competing linear theories of gravitation will produce precessions in disagreement with that of general relativity.

Rastall[7] prefers to isolate the purely geometrical aspects of the problem from those of dynamics, for which the spinning test particle of Papapetrou is conceptually different from a physical gyroscope. He points out, for example, that the spin of the test particle perturbs its own orbit, though to a negligible degree for vanishingly small spin. This is, of course, also mentioned by Schiff. This is related to the objection of Synge[8] that a rigorous treatment of the contribution of the spinning body's stress tensor to its energy-momentum tensor is not obviously consistent with Papapetrou's representation. Fastall's calculation of the precession is essentially geometric, involving the transport of a vector along a geodesic in a space whose curvature tensor is given in terms of the gravitational potential. His result is for general gravitational potentials, but reduces to that of Schiff in the spherically-symmetric case.

All of these calculations agree that the result of the transport of the spin angular-momentum vector along the geodesic (orbit) for a massive particle in the space represented by Eq. (1) results in precession of the spin at the angular rate

$$\Omega = (3V/2c^2)\omega_o, \tag{3}$$

as seen by a co-moving observer. It is seen that the angular rate of precession Ω is proportional to the orbital angular rate ω_o, the proportionality constant being in terms of the gravitational potential V at the orbit. Also, Eq. (3) is a vector equation in which the axis of precession is in the same direction as the axis of the orbital revolution. This means that the greatest angular displacement of the spin vector will be observed when that vector lies in the plane of the orbit, and that it will be observed to turn in the same direction as the turning of the radius vector for the orbit.

While all these calculations lead to the same result, Eq. (3), they differ in their conception of the appropriate relativistic representation of the physical gyroscope. Each calculation also invokes an approximation that the spin angular momentum shall be small, a well-justified approximation but one which is invoked in a different way in each case. Since they agree on the result, it will not be possible to distinguish among these representations in an experiment. The experiment would, however, be the first test of any of these approaches to the representation of spin in a relativistic manner, and the correctness of what these approaches share in common, despite the logical distinctions that may be drawn, would be tested.

All of these calculations also address themselves to item (c), the possibility that the precession would reflect the rotation of the gravitating body (earth). These calculations use the off-diagonal

elements of the metric tensor calculated by Lense and Thirring to show that the additional precession would have an axis parallel to that of the earth though the rotational motion would be opposite to that of the earth, with magnitude $(2V/5c^2)(R/r)^2\omega_e$, in which R and ω_e are the radius and angular rotation rate, respectively, of the earth, and V is the potential at the orbital radius r. (Schiff also calculated the Thomas precession, one which would be numerically significant if a nongravitational force were applied to force the gyro to follow a non-geodesic, i.e., non-free-fall, orbit, as in an earth-bound laboratory. For the satellite gyro this precession would be many orders of magnitude smaller than the geodesic precession.) For R = 6380 mk and r = 7380 km the value of ω_o is about 14 times that of ω_e, so that the Lense-Thirring precession is only about 1.4% of the geodesic precession. It would be nearly undetected in an experiment that measured the geodesic precession to a precision of 1 to 2 percent. Its detectability would be enhanced if two equatorial-orbital experiments were done with opposing orbital directions, because it would augment the geodesic part in one and oppose it in the other. In this way, a deferrable "second shot" would provide an indication of an effect of deep theoretical interest, also for the first time.

REFERENCES

1. Dicke, R. H., Solar Oblateness and General Relativity, Phys. Rev. Letters 18, 313 (Feb. 27, 1967).
2. Dicke, R. H., private communication.
3. Pound, R. V. and Snider, R. L. Effect of Gravity on Gamma Radiation, Phys. Rev. 140, B788 (1965).
4. Schiff, L. I., Motion of a Gyroscope According to Einstein's Theory of Gravitation, Proc. Natl. Acad. Sci. U.S. 46, 871 (1960).
5. Tonnelat, M. A., Les Verifications Experimentals de la Relativite Generale, Masson * Cie, Paris 1964; pp. 81-97.
6. Pustovoit, V. I. and Bautin, A. V., The Motion of a Gyroscope in Gravitation Theories, Russ. Phys. Quart. 1, 96 (1964) [Trans. from Zh. Eksperim. i Teor. Fiz. 46, 1386 (1964)].
7. Rastall, P., Relativistic Precession of a Spinning Satellite, Can. J. Phys. 44, 3109 (1966).
8. Synge, J. L., Relativity: The General Theory, North-Holland Publishing Co., Amsterdam, 1964, pp. 246-252.

3.1. Introduction

The material of this chapter is intended to provide a survey of the design of the proposed orbiting-gyro experiment to test those features of the general theory of relativity and gravitation discussed in the preceding chapter. For detailed analyses of the various aspects of design, the reader is referred to the chapters following the present one. The demonstration of feasibility for conducting an experiment to measure the relativistic precession to an accuracy of 1% to 2% of its value rests upon these detailed considerations. In the present chapter, it will be possible only to indicate the nature of the more-important considerations and the manner of their interaction.

With the hope of providing an integrated view of the experiment, the topics of the design of the satellite body, data readout, readout accuracy, error propagation, environmental disturbances, choice of orbit, and choice of material are treated in an order differing from that of the succeeding chapters, and with differing emphasis. For example, launch procedures are not discussed in this chapter. Also, the historical development of the design is not discussed in any detail, it being thought sufficient to sketch some of the earlier background in the immediately-following section.

3.2. Preliminary Considerations

Because of the experience of this Laboratory in developing the electrostatically supported gyro,[1] it was initially proposed that

the feasibility of an orbiting-gyro experiment based on similar gyro designs be studied. In the essentially free-fall conditions of an orbital experiment, the principal concerns would shift from those of providing low-torque-inducing support to those of providing readout accuracy of a much higher order than had been needed (for navigational purposes) in the earlier gyro development. The reason is that the angular position of the spin axis would change by very small amounts during the course of the experiment, as may be calculated from Eq. (3) of the preceding chapter, and it is this change which is to be measured.

To make a sample calculation from Eq. (3) of the preceding chapter, let the orbital altitude be 1000 km. Then, the angular velocity in a circular orbit may be calculated to be

$$\omega_o = 1.00 \times 10^{-3} \text{ rad/sec.} \qquad (1)$$

(In practical units this would be 0.057 deg/sec, corresponding to an apparent orbital velocity for an observer at a slant range of 1000 km of 0.37 deg/sec, and corresponding also to an orbital frequency of 13.8 per day. The corresponding linear velocity is 7.38 km/sec.) The gravitational potential V/c^2 may be calculated first at the surface of the earth, using the surface value of the acceleration due to gravity, g, as being $V/c^2 = GM/Rc^2 = gR/c^2 = 7.0 \times 10^{-10}$, in which the value of R is 6380 km. Then, at orbital altitude, a value of

6.0×10^{-10} is obtained. With allowance for the factor 3/2 the precession rate $\Omega = 9.0\times10^{-13}$ rad/sec is obtained, which in practical units is

$$\Omega = 5.9 \text{ arcsec/year.} \tag{2}$$

For two angular-position observations of the spin axis, each made with an error ϵ and spaced a year apart, Ω would be determined with an error of $\epsilon\sqrt{2}$. Thus, if Ω were to be determined to an error of 1.0%, the value ϵ = 42 milliarcsec would be required. A greater number of observations or a more extended interval between them would soften this requirement for the individual observations.

The concept was that of a small, spherical gyro encased in an instrumentation system which would include a facility for readout of the gyro spin axis to an accuracy two to three orders of magnitude beyond that hitherto achieved. There would also be facilities for keeping the gyro centered within the instrumentation system to maintain readout accuracy and, of course, to avoid physical contact with the gyro. It was clear that, for the low relative accelerations involved, either the electrostatic support or the thrusting of the satellite to follow the gyro as a proof mass in true free fall[2] would very likely prove feasible. The concept would further include facilities for high-precision telescopic star tracking so that the spin-axis readout could be referenced to

celestial coordinates prior to telemetry.

The obviously high cost of such an experiment, of the order of that of the OAO (orbiting astronomical observatory) project at minimum, the developmental effort required to ensure sufficient precision and reliability, then somewhat beyond the state of the art, seemed necessitated by the demands for unusual precision. It seemed clear that no physical principles would ultimately forbid the successful design of such an experiment. Indeed, the group at Stanford University was already pursuing feasibility studies along these lines, and their work since that time has brought the engineering design of such an experiment to an advanced stage of development.[3] Though their studies are continuing, it seems reasonable to believe that a precision of 0.1% would be ultimately attainable.

Many of the problems of complexity and reliability for this concept seemed traceable to the fact that the gyro was to be shielded from its environment, and that the instrumentation system, then, had to be mounted on the shield to provide a means by which the orientation information could pierce this shield and be telemetered to earth for analysis. At CSL, interest developed around the question as to whether the shield might be eliminated with the hope that a significant part of the elaborate instrumentation system might not have to accompany the gyro into orbit. The second hope was that the orbital environment would offer so few torque-inducing

influences that the elimination of the shield would not seriously compromise the accuracy of a well-designed experiment. Low cost and high reliability were the factors that would make such an alternative appealing, then, if reasonable accuracy requirements could be met.

For an unshielded orbiting gyro, the principal environmental torque-inducing influence would be the magnetic field of the earth unless the gyro could be made to have a very low overall conductivity such as would be characteristic of dielectrics. Thus, if the whole of the satellite were to function as the gyro, conventional electronic telemetry could not be considered as available, once the satellite were finally separated from its parent vehicle. Attention focused on devising a completely passive spinning body whose interactions with its environment would suffice to provide information about its spin orientation, but not be so severe as to disturb the spin significantly. The only interaction that seemed to meet these requirements appeared to be optical. Two arrangements of promise were proposed, both requiring mirrors to be placed on the spinning satellite for terrestrial observation.

In the earliest of these mirrored-satellite proposals, the mirror borne by the satellite would be placed with its normal aligned with the spin axis of the satellite. A terrestrial observatory, suitably located, would observe sunlight reflected from this spin axis mirror, and, in effect, measure the position of the sun as seen through such a mirror. From knowledge of the true position of the

sun, the orientation of the mirror normal, and hence the spin axis, would be determined. In another mirrored-satellite proposal, mirrors with normals placed at angles from the spin axis would be employed, and terrestrial light sources (possibly using lasers) would be directed at the satellite for reflection to terrestrial observatories. The measurement would be that of incident-and-reflected-ray orientations in order to measure an instantaneous orientation of a mirror normal and thus sample a ray on the cone swept out by such a mirror normal. From three such measurements, the cone angle and cone axis (coincident with the spin axis) would be determined.*

Each of the proposals offered the promise of accurate determinations of the spin-axis orientation on the basis of very few observations. Each, however, was faced with severe initial data-acquisition problems in the absence of accurate a priori knowledge

---

*It was subsequently learned that a similar proposal had been considered by R. H. Dicke at Princeton University, except that roof mirrors rather than plane mirrors would be used to reflect the rays from terrestrial sources. The law of reflection from roof mirrors is the same as that for plane mirrors, except that the plane containing incident and reflected rays also contains the dihedral axis of the roof mirror, instead of containing the mirror normal. Similarly, the dihedral axis replaces the mirror normal as a reference against which the equal angles of incidence and reflection are defined. Thus, replacement of a plane mirror by a roof mirror introduces no new elements to the design of the experiment.

of the satellite orbit and spin-axis orientation, since they each required observing stations to be very accurately located with respect to such a priori information. For the earlier proposal, it was pointed out that chance naked-eye observations of the solar flash from the spin-axis mirror, as might be reported from the population at large or from interested amateurs, would provide for determining a suitable location for placing a mobile observing station, provided the observer would be able to report his position, the time, and the general direction in which he had seen the flash all to within easily-met tolerances. For the second proposal, a multiplicity of mirrors (perhaps 32) were proposed to provide a reasonable probability of initial data acquisition for arbitrarily-located observing stations.

A determined effort to solve these acquisition problems was never undertaken because it was soon realized that the multiple-mirror approach, using sunlight exclusively (instead of terrestrial sources), would offer no acquisition problems, and could, at the expense of requiring relatively numerous observations, all easily attainable at existing satellite-observing stations, provide a high order of accuracy. The reliability implied by using a satellite design making for 100% observability was so appealing as to capture the exclusive interest of the CSL group. It is this experimental design, then, towards which the feasibility study to be described here was directed.

An original goal of the feasibility study was to show that the passive-satellite scheme would provide for a measurement of the relativistic precession to within 10% of its value. The results of the study indicate that the inherent precision of the method is much better than that. Indeed, unusual weight, fabrication problems, or demands upon orbital precision are not encountered even for a design intended to fulfill an accuracy of 2%. The exact precision limits of the passive scheme are unknown, and may well extent to smaller errors than 2%. It is submitted, however, that 2% is certainly a very interesting accuracy figure, being comparable to the precision figure for the orbital-precession observation of Mercury, and being sufficient, therefore, to check the claimed discrepancy in that precession.

3.3. Proposed Design of the Passive Satellite

In the passive-satellite scheme, the satellite would be a solid body, fabricated of a "zero-temperature-coefficient" material, Owens-Illinois CerVit, about 0.6 m (approximately 2 feet) in diameter. It would be a polished specularly-reflecting sphere, employing a thin metallic coating to enhance its optical reflectivity. A low-density plastic coating could be added for protection against substantial disturbances in the figure of inertia caused by micrometeorite

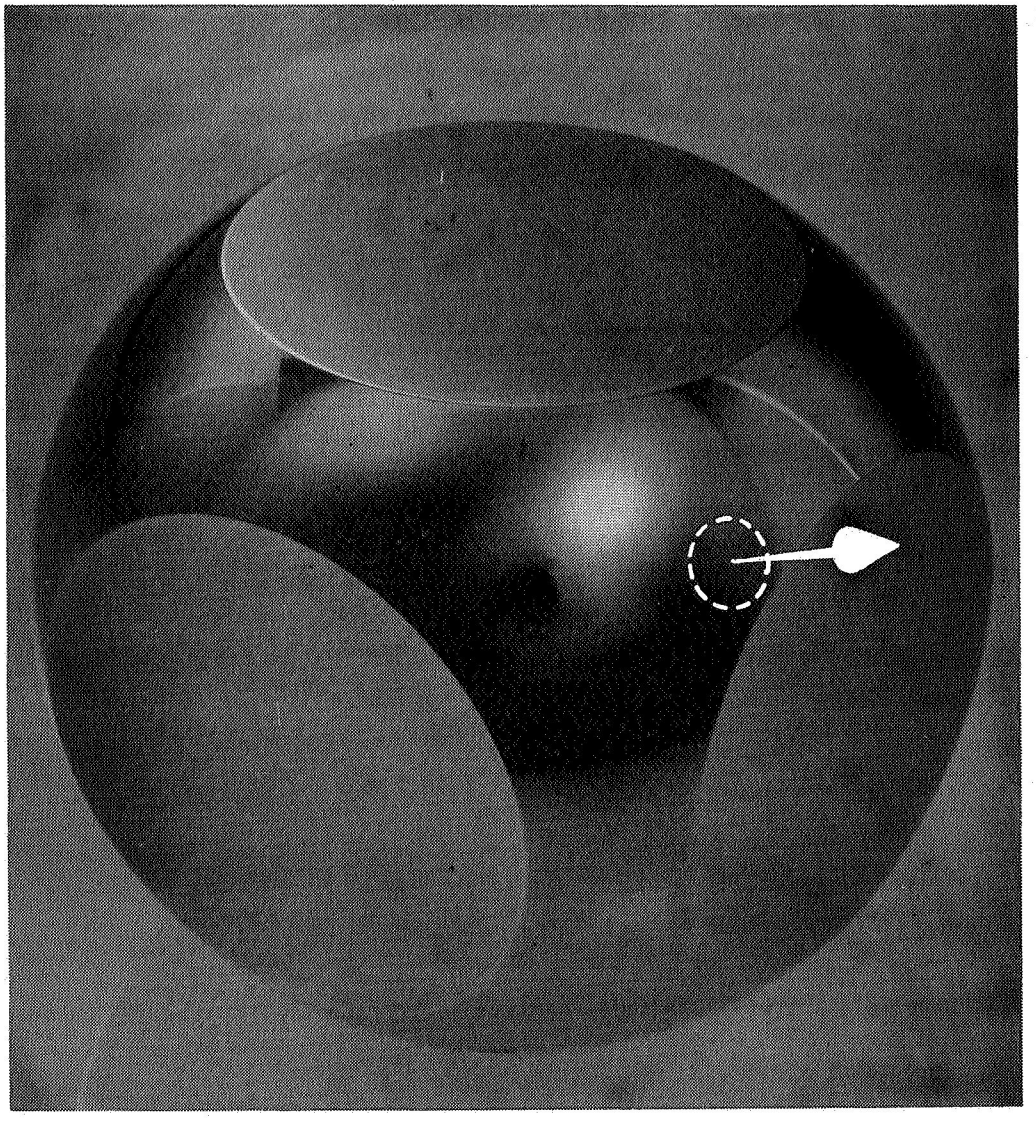

Figure 3.1. Model of the 60-cm relativity satellite. The large circular flats have an area of approximately 1000 cm^2 each. There are 6 of these, oriented as the faces of a cube and leaving about half the original spherical surface area undisturbed. In addition, there are to be two small polar facets, one indicated by the dashed circle, to establish a salient moment of inertia about the axis indicated by the arrow. Otherwise, the figure of inertia would be spherical. With the axis location approximately as shown, the large flats would be at the colatitude angles 42^o, 54^o, and 72^o, for the hemisphere visible here, together with a corresponding set of angles for the diametrically located flats. All surfaces are to be of optical quality and reflectively coated.

erosion. The spherical surface would provide a facility for tracking the orbit of the satellite by means of reflected sunlight on all occasions in which the illuminated satellite would be photographable against the night sky. Such photography would require the cameras, such as the existing Baker-Nunn cameras[4] used at the satellite-observing stations of the Smithsonian Astrophysical Observatory, to track the motion of the satellite to a precision of a few percent.

The spin axis of the satellite would be established in alignment with its salient moment of inertia, salient by about 1% and provided by removing material to locate a pair of diametrically opposed optical flats, "spin facets," each about 6 cm in diameter. The spin axis would then pass through the center of these spin facets. The alignment of the spin axis with the axis of the salient moment would be approximated during spin-up procedures before releasing the satellite from its parent vehicle. Thereafter, any residual misalignment would be damped out by the energy-loss mechanisms inherent in the elastic hysteresis characteristic of the dielectric material chosen. A damping time of a few hours has been selected.

Six other facets in a cubical array would also be established on the surface, each with an area of about 1000 cm^2, so that about half the spherical surface would be devoted to such facets, called "glitter facets." See Fig. 3.1. Relative to one spin facet, these facets would be located at 42, 54, and 72 degrees, with a second set similarly located relative to the other spin facet. The provision of

these glitter facets does not disturb the relative magnitudes of the moments of inertia. The glitter facets serve as the primary instrumentation facility for measuring and tracking the spin axis orientation.

3.4. Data Readout

Flashes of sunlight reflected from the glitter facets are photographically observable at the satellite-observing stations in late twilight or early dawn, provided that the satellite's orbit lies a useful distance above the horizon for the station in question and that the local cloud cover is not excessive. The frequency of such occurrences has been determined by digital computer simulation. For an equatorial orbit at an altitude of 1000 km, for example, the station at Curacao would average more than two sighting opportunities daily, because on some passes flashes from more than one glitter facet would satisfy, at different positions in the pass, the necessary angular conditions.

To photograph the flashes, orbital data are needed to orient the camera, but only low-precision data are needed because of the very wide field of view provided by the Baker-Nunn cameras. More precise data are needed to time the opening and closing of the shutter, although an error of a few seconds is tolerable, especially at first, while the temporal-ephemeris-data are few. These data may be augmented by photographing the reflection from the spherical surface,

with the camera motion tracking the orbital motion. To photograph the glitter flashes, however, the camera motion will be sidereal, in which case the reflection from the spherical surface will be well below the photographic threshold. The further datum needed to time the shutter opening is a knowledge of the spin-axis orientation so that a prediction of the time at which the angular conditions are fulfilled may be made. This orientation will be established during the final spin-up to coincide with the equinoxes to sufficient precision to allow the early data to be obtained. Later, more precise timing will allow the shutter to remain open for a minimal time to avoid overexposure to the essentially night-sky background, the more precise timing becoming a direct consequence of the accrual of data.

It is the photography of the glitter flashes against the stellar background that provides the precise measurement of the spin-axis orientation with minimal disturbance from atmospheric distortions. As the satellite is moving into position, the first glitter flash allows a sighting through the glitter-facet mirror of the limb of the solar disc. As the satellite moves further, successive flashes correspond to traversals of the reflected line of sight across the solar disc at greater and greater depths from the limb until the traversals finally reach the nether limb, after which the facet in question would produce no further flashes until a later orbital pass were made. Thus the flashes will be photographed as a pattern of flashes at points along the orbit. With an orbital speed

of 7.4 km/sec at a slant range of 2500 km, about 1.7 seconds would elapse between the first and last flash while the line of sight, following the orbital motion, turned through the half-degree width of the solar disc. At a sufficient spin rate, the individual flashes would fail to be resolved, and the photographed pattern would resemble the simulated image shown in Fig. 3.2.

The center of such an image as shown in Fig. 3.2 corresponds to a sighting through the glitter-facet mirror of the center of the solar disc. This measurement, together with knowledge of sun's true location, both with reference to the stellar background, fix the orientations of both the incident and reflected rays and thus determine the corresponding orientation of the facet normal. The facet normal, however, is constrained to lie on a cone whose axis is the spin axis. Thus, three such sightings serve to determine both the cone angle and the spin-axis orientation.

3.5. Readout Accuracy

The problem of predicting the accuracy with which the center of such an image as in Fig. 3.2 may be found is a statistical one, in essence. The random grain pattern of the photographic film causes density fluctuations which can produce small random fluctuations in the estimated center. Generally, the estimation procedure that one would plan to use would employ an averaging of the density fluctuations

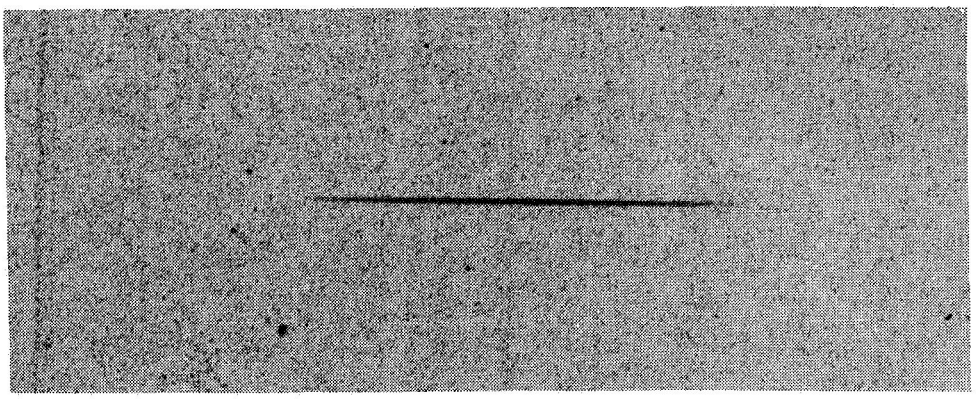

Figure 3.2. Enlarged photograph of a film image as it would be recorded by the Baker-Nunn camera. The image, simulated by photography of the sun using an anamorphic camera, represents the sequence of mirror flashes generated by a mirror on the spinning satellite as it reflects sunlight while in orbital motion, at such a slant range that the B-N camera is unable to resolve the individual flashes. The image is to scale relative to the graininess of the film, and its long axis represents the half-degree width of the solar disc scanned by the mirror.

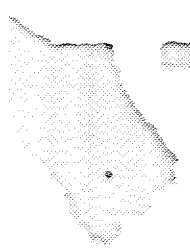

to find, for example, a center of gravity. The center-of-gravity weight is a linear weighting and not necessarily an optimum one, though it would be an easy one to implement using density wedges to weight the measuring aperture of a projection densitometer.

The density fluctuations that may be observed in the red-extended Royal-X pan film that is used in the Baker-Nunn cameras have been measured and subjected to statistical analysis. The analysis included correlation and probability distribution studies, showing that the fluctuations at one point are essentially independent of those at another point, if these be spaced a distance apart which is a fraction of the resolution distance of the camera, and that the probability functions are susceptible to mathematical modeling. Models were developed primarily to represent the probability distribution for opacity as depending upon an empirical relation between mean opacity and the standard deviation in opacity. This relation was determined from measurements covering an opacity range of nearly 100 to 1, a density range of 2, since density is the common logarithm of opacity.

The CDC-1604 computer was programmed, using these models, for a Monte-Carlo simulation of the opacity fluctuations to be expected along such an image as shown in Fig. 3.2, generating data points spaced either a resolution interval apart, or a flash interval apart, whichever would be the larger. In one run, many statistically independent images could be generated so that an rms error measurement

could be made expressing the accuracy of the estimation procedure based on particular weighting curves. A number of weighting curves were tried. For "faint" images (central density increment of 0.3 above night sky) it was found that assigning zero weight to the central 50% of the image with the weight growing parabolically towards the edges of the image, positive weight towards one edge, negative weight towards the other, with zero weight outside the image, gave results very close to an optimally-small rms error. For denser images, wider central zones of zero weight were more nearly optimum, until, for a density increment of 1.0 above night sky, the prescription was that essentially all of the weight should be on the outermost 3 or 4 resolution intervals. This prescription was found to be consistent with that of the maximum-likelihood estimator, which uses a simultaneous weighting of opacity and density for the statistical models used.

For this density increment of 1.0, the rms error was found to be smaller than the known standard error for locating hard-edged images on Baker-Nunn camera films, namely 1.1 arcsec.[5] Such hard-edged images are so located with respect to stellar images by cursor-aided visual methods on standard measuring machines. The form of the optimal weighting curves for the simulated images at a central density increment of 1.0 shows them also to be essentially hard-edged images and well-adapted to the same visual methods. Consequently, it was concluded that the more elaborate weighting methods need not be used

in practice, provided this density increment, or better, could be obtained, and that the standard accuracy of 1.1 arcsec should be taken as characterizing these images.

This density increment of 1.0 is obtained for a flash exposure that is greater than a certain threshold value by the factor 5. This threshold is defined as that producing a density increment of 0.35 ± 0.05 above night sky and is equal to 0.8×10^{-10} lumen-sec/m^2 at the input aperture of the camera.[6] An aperture of 1000 cm^2 at a slant range of 2500 km, opened for 14 μsec to transmit solar radiation, for example, will produce the exposure corresponding to this requisite density increment. These exposure requirements are met by the satellite design for the counted observing opportunities mentioned in the preceding section.

3.6. Error Propagation in the Experiment

If the center of the flash-pattern image may be located with an accuracy of 1.1 arcsec, then the mirror-normal orientation may be located to an accuracy of half that. For this, it must be assumed that the sun's position as seen from the satellite may be known to better than 1 arcsec. This is reasonable to expect in view of the smallness of the geocentric solar parallax, 8.8 arcsec, and of the small rate of the sun's apparent motion, less than 1 arcsec in 24 seconds of time, with reference to the stellar background. The use of

three such observations to determine the cone swept out by the mirror normal, results, for a reasonably uniform angular spacing, in a factor 2 in combining the errors, so that a suitable triad of observations determines the spin-axis orientation to within 1.1 arcsec.

In a week's time, the count of suitable observing opportunities for the Smithsonian net is predicted to be in excess of 30, and possibly as many as 60, depending upon the inclination of the orbit, the lower number corresponding to the lower inclination (essentially equatorial), and making no allowance for weather. The more conservative figure provides for 10 data triads per week, serving to locate the spin axis to within 0.35 arcsec for that week, during which time the expected relativistic motion would be 0.11 arcsec. For the purposes of making a schematic study of error propagation, then, it will be convenient to regard a week as being an essentially stationary data interval, during which it is expected that the spin-axis position may be determined with an rms error ϵ_θ which is 6% of the annual relativistic motion ω = 5.9 arcsec/yr.*

The assortment of data into weekly groups provides for a

---

*In a previous section, the capital letter Ω was used to denote this angular rate, in conformance with the theoretical literature. In later chapters, this capital letter will be used to denote a right-ascension angle in defining the orbit orientation. No attempt has been made to establish a rigidly consistent scheme of notation throughout this report, although consistencies within chapters have been generally observed.

model of data reduction that is useful for conceptual purposes without necessarily implying that the actual data reduction would proceed in such a manner. For example, two "good" weeks of data spaced one year apart would suffice to determine the spin-axis rate with an accuracy of 1.4X0.35 arcsec/year, amounting to a determination within 8.3%. Many more "good" weeks than that may be expected, however, and the fraction of "good" weeks may be characterized by a probability p which may be regarded as summarizing the expected experience with respect to cloud cover or other causes of missed observing opportunities. The model to be considered, then, is that of an experiment running for T years in which the expected number of "good" weeks of data would be 52pT, uniformly spaced in the interval T.

The precession rate would be determined by a least-squares fitting procedure in this model, for which it is easy to calculate the joint effect of error contributions. If the expected precession rate is ω seconds of arc per year with error ϵ_ω then ϵ_ω/ω represents the percentage accuracy of the experiment. The error in one week's data is denoted by ϵ_θ and is related to the expected yearly displacement by the ratio ϵ_θ/ω, a quantity estimated above to be 6%. Applying error analysis to the reduction model, one can determine the manner in which $(\epsilon_\omega/\omega)/(\epsilon_\theta/\omega)$ varies with T and p. For p = 100%, for example, it turns out that the ratio is unity, i.e., $(\epsilon_\omega/\omega) = (\epsilon_\theta/\omega)$ for T = 0.61 year, corresponding to a solid run of about 32 weeks, while at p = 25% the same condition is reached after 0.95 year or about

50 weeks. The general relationship may be seen plotted in Fig. 3.3. Interest particularly attaches to the condition in which the value of ϵ_θ/ω is reduced by the factor 6 to provide an ϵ_ω/ω value of 1%. This is seen to come at T = 2.0 years for p = 100% and at about T = 2.5 years for p = 50%.

Because of the steepness of the curves of Fig. 3.3, the necessary running time of the experiment is not particularly sensitive to losses of data represented by p values less than 100%. Thus it would appear that the proposed data-readout scheme is capable of providing a 1% measurement of the precession. The ultimate accuracy of the method will depend upon the number of years the experiment may be allowed to run. This would depend, apart from cost considerations, upon the useful life the satellite may be expected to exhibit, a factor which in an ultimate sense is unknown, but may be expected to exceed three years. If such is the case, it is more likely that the overall error would not be set by readout errors, but would be controlled by errors arising from disturbances traceable to the environment.

3.7. Environmental Disturbances

Among the possible environmental effects making for an experiment that is not entirely torque free, there are some that have been shown to be entirely negligible. One of these, torques arising

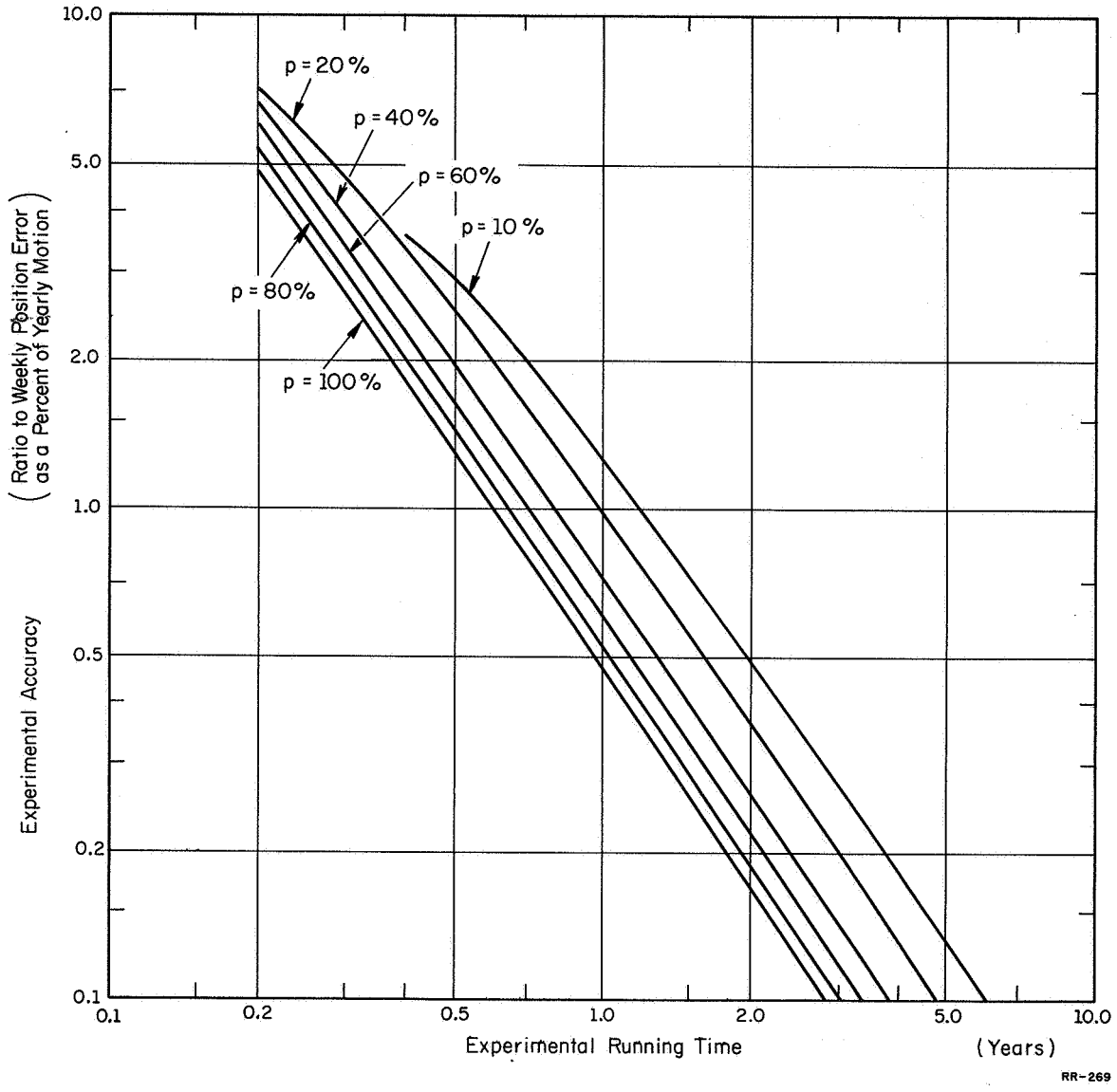

Figure 3.3. Percent error in the experimental value of the relativistic precession as a function of the running time in years and of the probability p that a week's position data would attain a given standard of accuracy. The percent error in the precession is given as the ratio to the standard of accuracy for the week's positional data, the latter also expressed as a percent of the yearly motion. Logarithmic scales are used.

from the generation of eddy currents in the satellite body because of the Earth's magnetic field, has been forced to be zero by choosing the material to have a sufficiently small conductivity. Even the reflective surface may be made sufficiently thin, without spoiling its optical properties, to provide for negligible eddy-current torques. A minimum conductivity is also required in order that non-uniform charge distributions be not established to produce significant torques arising from electric fields or plasma interactions that may be encountered. These upper and lower bounds on conductivity are quite widely spaced and are met by the material chosen, Owens-Illinois CerVit. Another negligible-by-design disturbance is aerodynamic torque; calculations show that the choice of an orbital altitude of 1000 km obviates such torques.* Finally, the momentum transfer caused by the impingement of micrometeors has been found to be of

*These aerodynamic studies have led to the showing that, at a lower orbital altitude, an experiment of similar design using a more asymmetric body may be used to measure orbital drag, spin run down, and aerodynamic precession, each of which is an independent function of atmospheric density and the two accommodation coefficients, allowing each of the three to be separately measured. The latter two have never been measured for low-altitude, orbital-drag situations, so that the deduction of density from previous drag experiments has been of doubtful validity, especially for the precise prediction of drag on objects hitherto untried. A proposal for such an upper-atmospheric aerodynamic experiment is in preparation. It could provide a preliminary test of the present instrumentation scheme.

negligible consequence for the quantities expected, because of the very large amount of stored angular momentum in the satellite.

Micrometeoric impingement is not negligible in regard to the energy transfer, however, since this energy would be expended in evaporating micro-craters in the surface of the satellite, causing disturbances in its figure of inertia. For example, if the satellite had a perfectly spherical figure of inertia (moments of inertia about the three principal axes all equal to one another), and a crater, however small, were formed at a certain point, then there would be created a salient moment of inertia, and the axis for that moment would thereafter have to pass through the center of gravity of that crater. This will cause a nutating motion, if the axis for the salient moment be not aligned with the angular-momentum vector, for then the angular-velocity vector would also not be aligned with the angular-momentum vector, and it is the angular-momentum vector which maintains a fixed orientation in locally-flat space. In this nutating motion, the angular-velocity vector and the salient-inertia axis execute rapid rotations about the angular-momentum vector. The nutation cannot be maintained in the presence of an energy dissipation mechanism, however, such as elastic hysteresis. As energy is lost from the nutation, the angular-velocity vector and the salient-moment axis both spiral in upon the angular-momentum vector and are eventually brought into alignment with it. For this reason, the axis of the salient moment of inertia is often called the "preferred spin axis."

The nutation is potentially very troublesome for the data read-out system, during the time taken for nutation to damp. The nutation rate, which could be essentially equal to the spin rate, is much faster than the rate at which observations may be made. In consequence, a mirror normal, instead of being constrained to lie on the surface of a cone coaxial with the spin axis, is constrained only to lie within the volume bounded by two coaxial cones having different angles of opening. If these angles differ by very much, the observations obtained during the nutation would be essentially worthless. After the nutation had been damped, however, the data would be valuable again, because the angular-momentum vector would not have changed orientation, even though the mirror normals would then lie at new angles with respect to that vector, and these angles are simultaneously measurable along with the measurement of the orientation of the spin axis, which is again in alignment with the angular momentum.

Alleviation of the micrometeoric-induced nutation troubles is to be obtained through rapid damping and through providing that the mirror-normal cones shall be "fattened" to essentially negligible extent during the nutation for all but the rarest of micrometeoric-impingement events. The damping of the nutation arises because the centrifugal stress field, which is symmetric about the angular-velocity vector, sweeps through the body as that vector nutates about the preferred spin axis, subjecting the material to cyclic straining

at this nutation rate. If there be any elastic hysteresis, this cyclic straining will progressively convert the nutational energy to thermal energy. A similar mechanism accounts for the damping of elastic vibrations in bodies sufficiently well isolated from their environment, and is expressed by means of a Q factor, which may be measured for a variety of materials (and vibrational modes). For the material selected for the satellite, Owens-Illinois CerVit, an e-fold damping time of an hour or two is expected.

It is not possible as a practical matter to fashion a body having a perfectly spherical figure of inertia, even though, of course, a sphere and all regular polyhedra, including, for example, the cube, would, if perfectly made, possess such a figure, as also would the proposed composite of cube and sphere. Apart from fabrication imperfections there would, at the very least, be established a salient moment of inertia in a spinning body because of centrifugal deformation. This centrifugal saliency is not useful in identifying a preferred spin axis, however, because the centrifugal stress field is coupled only to the angular-velocity vector and is free to sweep through the material of the body. If a preferred spin axis is to be established, the saliency must be an intrinsic property of the body. For the present satellite this intrinsic saliency will be established by grinding a pair of small polar flats on the spherical surface in addition to the 6 cubic-oriented flats. In this way, the set of mirror-normal angles relative to the preferred spin axis will be established.

Besides establishing definite mirror-normal angles, rather than leaving them to be determined by chance fabrication errors, the deliberate establishing of an intrinsic saliency provides for the magnitude of it, the ratio by which the salient moment exceeds the others, to be chosen as a design parameter. One could, for example, establish a 1% saliency with great confidence. With a saliency of this order of magnitude, one could guarantee that only very rare micrometeoric-impingement events, such as would occur only once per year, for example, would disturb the preferred spin axis by as much as 1 arcsec. For substantially smaller disturbances, the "fattening" of the cone surface would be of negligible consequence, and, even for the rarer larger disturbances, the data would be of very high quality again after a few hours.

Gravity-gradient torques, unfortunately, are present to non-negligible extent for any body which has a significantly salient moment of inertia, whether centrifugal or intrinsic in nature. For understanding this, the present axially-symmetric body may be regarded as a composite consisting of a sphere together with an equatorial belt of mass. If the spin axis be not directed along a radial line from the center of the Earth, one part of the belt will be nearer the Earth than the opposite part, and it will be attracted more strongly than the opposite part, producing a torque, because of the gradient of the inverse-square law of the gravitational field.

In general, this torque will consist of two parts, a periodic part matched to the period of revolution about the earth, or some submultiple, for harmonic terms, and a steady part. These give rise to both periodic and secular precessions. That part of the secular precession that would lie in the same direction as the relativistic precession would constitute a systematic error, while all other parts would be harmless.

There exists a choise of orbit and, more importantly, spin direction which would make the systematic error vanish, but, since these choices may be fulfilled only to a certain precision, it is necessary to make design choices to also minimize the scale of the gravity-gradient precession. Upon specifying the maximum rate for micrometeoric events producing a given magnitude of disturbance, it turns out that, taking all factors into account, there is an optimum diameter for the satellite to achieve a minimum gravity-gradient precession. The optimum is rather broad covering a range from 0.3 meter up to 1-to-3 meters depending upon the exact model for the micrometeoric flux. The scale of the resulting minimal precession then provides a satisfactorily small systematic error, if the spin axis may be located to specification within a tolerance of a few tenths of a degree, together with very broad tolerances, of several degrees, for the orbit inclination.

The third, and last, nonnegligible environmental disturbance is the torque arising from the radiation pressure of the solar

radiant flux coupling to any optical asymmetry, because of variations in reflectivity over the surface of the satellite. In this, only asymmetries with reference to the satellite's equator are important. Calculations based on reasonable assumptions regarding these asymmetries indicate that the precession could be an appreciable fraction of the relativistic precession. Also, the precession rate may possibly change with time as micrometeoric impingement may darken the optical surfaces in a way to augment or diminish those asymmetries initially appearing as fabrication and launch artifacts.

The radiation-pressure precession is, however, apart from a secular change of scale, periodic with a period equal to the sidereal year, and of a form which depends upon the orientation of the spin axis relative to the ecliptic plane. When the spin axis is normal to the ecliptic plane, the precession carries the tip of the spin vector about a small circle centered on the ecliptic pole, but when the spin axis lies in the ecliptic plane the vector merely nods up and down out of the plane through a small arc. In between, small ellipses of varying eccentricities are traced. In the nodding case, it is feasible to establish a substantial known angle between the direction of the nod and the direction of the relativistic motion so that the radiation-pressure precession, if significant, can be separately measured, and the component along the relativistic direction may be known.

These studies have shown, then, that, of the possible environmental disturbances that may not be guaranteed to be negligible *a priori*, means of control exist whereby their effects may be adjusted through choice of spin direction and detailed design of dynamical parameters to become either negligible or else measureable to sufficient precision so that their effects may be discounted.

3.8. Choice of Orbit

The relativistic precession causes the spin axis to turn about an axis normal to the plane of the orbit. This fact requires the spin axis to lie within moderately small angles from the orbital plane since the observable effect is greatest if the spin axis lies in the orbital plane, otherwise diminishing as the cosine of the out-of-plane angle, so that an out-of-plane angle of 30^{o} would leave 87% of the effect as observable. It is possible, in principle, to maintain the spin axis exactly in the orbital plane in only two cases, one in which the orbit does not precess, and one in which the orbit precesses about the normal to its own plane. These are polar and equatorial orbits respectively. In the polar orbit, unfortunately, the radiation-pressure precession would always show a large component in the same direction as the relativistic precession, regardless of how the spin axis were positioned in the orbital plane. For this reason, primarily, the polar orbit is to be excluded.

In any of these orbits, the gravity-gradient precession vanishes in its secular part if the spin-axis lies in the orbital plane, but if the orbital plane also precesses about the Earth's polar axis, as in the case of the near-equatorial orbits, then what had been regarded as the "secular" part becomes periodic with the orbital-precession period, and the true secular part that remains vanishes only if the spin axis lies in the equatorial plane. Thus, it appears that a near-equatorial orbit should be selected for which the spin-axis should be chosen to lie simultaneously in the equatorial plane and in the ecliptic plane.

These planes intersect in the equinoctal line, so that it would suffice, if the spin-direction were to be established at a time when the sun is at an equinox, to point the spin axis toward the sun with the help of a solar sensor on the parent spin-up vehicle. If the secular precession is to be less than 0.1 arcsec for the optimally designed 60 cm satellite, the pointing accuracy must be 0.1 degree, relative to the equatorial plane. This equatorial plane does turn (general precession), but not by more than 1 arcmin per year, so that the general precession does not compromise the accuracy with which this pointing may be maintained, for an experiment-running less than 6 years.

It should be noted that with a near-equatorial precessing orbit, a part of the relativistic precession becomes "averaged out," so that only that part of the relativistic precession along the

equatorial plane may be observed, since all of the out-of-plane motions are periodic, in one way or another, and will be larger than the periodic out-of-plane component of the relativistic motion.

Of the periodic, out-of-plane motions, none having a period shorter than twice the interval between observations may be measured, according to the sampling theorem for fixed sampling intervals. This interval is actually somewhat variable, but cannot be appreciably less than the time required to obtain three reasonably-spaced (in angle) observations of flash patterns from one mirror. Thus, periodic motions with periods less than about a day should be regarded as unobservable with the present instrumentation scheme, and, as a practical matter, periods as short as a week may be quite difficult to deal with. This automatically places periodic motions having a period related to the orbital revolution period in the unobservable category, with their rms values entering the observations only as random noise, whether in the equatorial plane or out of the equatorial plane. Fortunately, these rms values are fully negligible.

The most important periodic motion, periodic, that is, except for a possible secular change in scale, to be measured is the radiation-pressure precession, since it will have a component in the equatorial plane which must be determined from its out-of-plane component. This is sufficient, since the direction of the combined motion is known as being normal to the ecliptic plane. Fortunately,

the period for this motion is the sidereal year, so that there are no sampling-rate problems.

If the design doctrine that the gravity-gradient precession be minimized, subject only to the constraint that the one-arcsec micrometeoric disturbances have a mean time of occurrence of one year, be adhered to, then the 2% experiment is feasible if the initial spin-axis orientation may be set along the equinoctal line to a precision of 0.1 degree, and no periodic motions other than of the radiation-pressure precession need be measured. The appropriate orbit, then, would be within a dozen degrees, or so, of the equator. An alternative design doctrine has recently been discovered that, although not yet completely studied, promises to offer a means of relaxing the initial-pointing precision, allow the use of a greater orbital inclination, and provide even more immunity from micrometeoric impingement. This alternative doctrine requires that motions periodic with the orbital-plane-precession period also be measured. Such measurement would not present a challenge to the data rate, since periods of the order of a few months would be involved.

Since the form of all the motions, periodic and secular, in-plane and out-of-plane, may be determined a priori, the experiment may be regarded as one in which the observed motion is to be subjected to a least-squares fit to the predicted motion so as to determine the unknown parameters in that predicted motion. One of these parameters would be the relativisitc rate, and the others would

describe the gravity-gradient precession and the radiation-pressure precession. Under these circumstances, a much larger scale of gravity-gradient precession would be tolerable so that the saliency of the preferred spin-axis moment could be made large enough to exclude significant micrometeoric-impingement effects, while at the same time the initial pointing tolerance could be relaxed.

The larger orbital inclinations, which complicate the pattern of gravity-gradient precession by admitting significant in-plane periodic effects, would also be more easily tolerable, because the fitting to the combined in-plane and out-of-plane periodic motions actually determines the secular motion. These larger inclinations also serve to augment the data rate by exploiting those observing stations that lie farther from the equator. It is possible that a 30° inclination will prove acceptable. Such an inclination would be attractive from a cost point of view, especially if it made the launch compatible with the simultaneous orbiting of packages for other missions.

It may be concluded that suitable orbits exist for which the experiment would be feasible.

3.9. Choice of Material

The chosen material, Owens-Illinois CerVit, satisfies, as mentioned, the requirement that its electrical conductivity fall in

the appropriate broad range of values. It also exhibits an appropriate Q value for the damping of elastic vibrations, so that the nutational damping time shall have a reasonable value. Not hitherto mentioned, however, is its strength; it is stronger than ordinary glass.

The material must be strong enough to withstand the required spin rate without risk of rupture. Glass has been studied in this connection experimentally. The theory provides for a precise calculation of the centrifugal stress in a solid rotating sphere. In particular, the value may be shown to be greatest at the center of the sphere. This may be contrasted with the everyday experience with the breakage of glass in which the failure occurs because the stress exceeds the strength of the material at a point near the surface of the body so that the surface condition (microcracks) plays a strong role in the breakage phenomenon. For the satellite, surface flaws would play essentially no role. A slightly different, though similar in overall pattern, stress field may be calculated for a spinning disc, with which experiments may be more easily done. From the observed rupture speed for the disc, those for the sphere may be calculated. For the spin rate planned, 3000 rmp for the 60-cm sphere, glass would provide a very generous safety factor; yet CerVit is known to be stronger, and therefore it also provides a very generous safety factor.

The decisive factor for CerVit, however, is its well-known, remarkably-small, thermal expansivity. The satellite will be subjected to alternate heating and cooling as it passes in and out of

the Earth's shadow in its near-equatorial orbit. This will establish periodic thermal gradients within the body, which gradients, if the expansivity (or alternatively the thermal resistivity) be not very low, could distort the shape in a periodic fashion so as to periodically alter the mirror-normal angles to an extent sufficient to cause significant errors. Such errors may be minimized by sorting the observations into groups, an emerging-from-the-shadow group and an entering-the-shadow group, but it is wise also to minimize the thermal distortion, and CerVit will provide a minimum probably obtainable in no other way.

An exact determination of the temperature fluctuation depends on a balancing of the energy absorption rate for the incident solar radiation against the emissivity of the satellite for a much colder grey-body radiation spectrum. This determination presumably would be made as a part of a thorough design of the experiment, but it hardly seems necessary for the demonstration of feasibility. The general experience with reflectively-coated bodies of this sort is that temperature fluctuations of only a few dozen degrees, for bodies of lower heat capacity, may be expected. Thus only a dozen or so degrees of temperature difference within the body would be expected, at most. Under such circumstances, it certainly appears that a CerVit body would maintain an adequately constant shape, especially if data sorting were used.

REFERENCES

1. H. W. Knoebel, "The Electric Vacuum Gyro," Technical Report R-126, Coordinated Science Laboratory, University of Illinois, July 1961. (This report is unclassified. See also the confidential final report R-195 by H. W. Knoebel and D. O. Skaperdas, Feb. 1964).

2. B. Lange, "The Drag-Free Satellite," AIAA Journal, 2, 1590 (Sept. 1964).

3. Proposal to Develop a Zero-g, Drag-Free Satellite and to Perform a Gyro Test of General Relativity in a Satellite, submitted to NASA by Stanford University, Nov. 1962. See also Stanford University Semiannual Status reports under Research Grant NsG-582 from NASA.

4. K. G. Henize, "The Baker-Nunn Satellite-Tracking Camera," Sky and Telescope, p. 108, (Jan. 1957).

5. Research in Space Science, Special Report No. 74, Smithsonian Astrophysical Observatory, (Sept. 18, 1961).

6. Private Communication, Smithsonian Astrophysical Observatory.

4.1 Introduction

Gravity-gradient torque arises from the inverse-square law of gravitation. Different points in the same body have different gravitational forces which depend inversely on the squares of their respective distances from the center of the earth. In general, the net gravity-gradient effect on an orbiting satellite is a net torque which tends to bring the axis of minimum moment of inertia in alignment with the radius vector to the center of the earth. This effect has been used successfully to stabilize non-spinning earth satellites with one end always directed toward the earth. The gravity-gradient torque on an axisymmetric body is proportional to the difference between the maximum and minimum moments of inertia and is detrimental to a satellite which is supposed to be spin-stabilized. The following analysis describes the minimization of gravity-gradient effects on the proposed relativity satellite.

4.2 Gravity-Gradient Moment

Figure 4.1 illustrates a general orbit-spin-axis configuration. Standard derivations of the gravity-gradient moment on an axisymmetric satellite give the moment components in coordinate system [2], which relates the principal inertia axes of the satellite to the orbital plane. Reference 1 gives the components as

$$M_{x2} = -(3GM/R^3)(C-A)\sin\theta\cos\theta\sin^2\omega_o t \tag{1a}$$

$$M_{y2} = -(3GM/2R^3)(C-A)\sin\theta\sin 2\omega_o t \tag{1b}$$

$$M_{z2} = 0 \tag{1c}$$

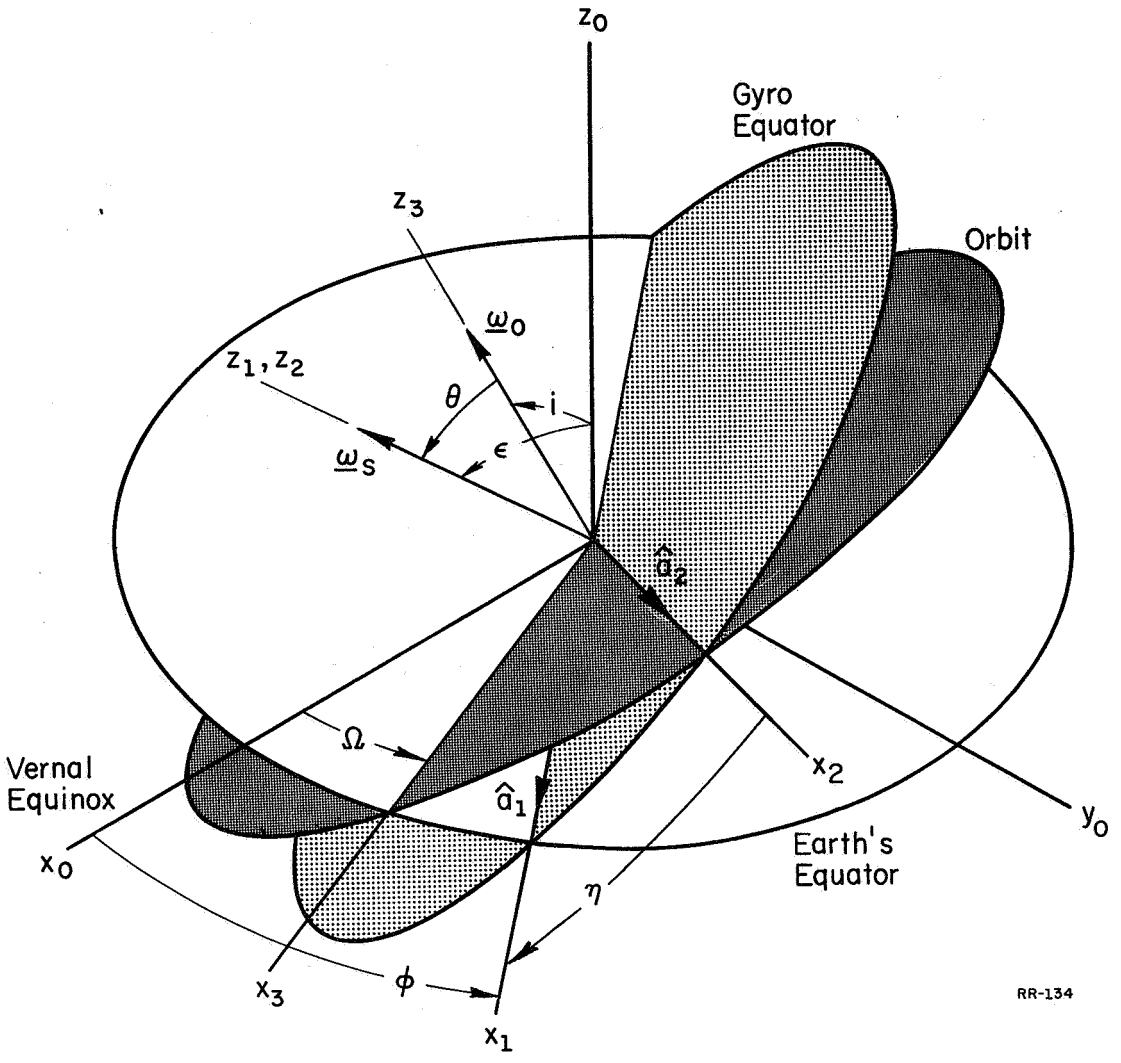

Figure 4.1 Orbit and gyro coordinate systems related to inertial coordinate system. The y_1, y_2 and y_3 axes have been omitted for clarity.

[0] - inertial system; z_o is the north pole of the earth.

[1] - satellite principal axes of inertia referred to inertial system.

[2] - satellite principal axes of inertia referred to orbital plane.

[3] - orbit axes referred to inertial system.

where M is the mass of the earth and R is the distance between the centers of the satellite and the earth; C and A are the polar and transverse moments of inertia of the satellite, respectively. It is assumed that any initial wobbling of the gyro has damped out, and that the spin vector $\underline{\omega}_s$ is colinear with the angular momentum vector and the C axis. With $\underline{\omega}_o$ defined as the orbital angular velocity vector, θ is the angle between the vectors $\underline{\omega}_s$ and $\underline{\omega}_o$. In the general case, the satellite's orbital plane will regress about the earth's polar axis at the rate of $\dot{\Omega}$ degrees per year[2] and will produce an additional change in θ.

The geometry involved in the general case of interest for regressing orbits is illustrated in Fig. 4.1. An earth-based coordinate system is fixed with z_o along the earth's north pole and x_o along the line of vernal equinox (i.e., the line of the nodes between the ecliptic and the earth's equatorial plane). The y_o axis completes an orthogonal right-handed system and, therefore, lies in the earth's equatorial plane. Coordinate system [1] is shown with z_1 also along the gyro spin axis, but with x_1 along the line of nodes between the earth's and gyro's equatorial planes. This is the most logical system in which to observe gyro motion with respect to the earth. The moment given for system [2] can be transformed through angle η to system [1] by the transformation

$$\begin{bmatrix} \cos\eta & -\sin\eta & 0 \\ \sin\eta & \cos\eta & 0 \\ 0 & 0 & 1 \end{bmatrix}$$

The moment components in system [1] are now given by

$$M_{x1} = -(3GM/R^3)(C-A)[\cos\eta\sin\theta\cos\theta\sin^2\omega_o t - \tfrac{1}{2}\sin\eta\sin\theta\sin 2\omega_o t] \qquad (2)$$

$$M_{y1} = -(3GM/R^3)(C-A)[\sin\eta\sin\theta\cos\theta\sin^2\omega_o t+\tfrac{1}{2}\cos\eta\sin\theta\sin 2\omega_o t] \quad (3)$$

$$M_{z1} = M_{z2} = 0. \quad (4)$$

Angle η is eliminated by vector manipulation[3], and the gravity-gradient moment can be written in system [1] for a general orbit of inclination i and right ascension Ω and a given spin axis direction defined by ϵ and φ. The instantaneous moment components are now

$$M_{x1} = (3GM/R^3)(C-A)\{[\sin i\cos\varepsilon\cos(\Omega-\varphi)-\cos i\sin\varepsilon]\cos\theta\sin^2\omega_o t-\tfrac{1}{2}\sin i\sin(\Omega-\varphi)$$
$$\times\sin 2\omega_o t\} \quad (5)$$

$$M_{y1} = (3GM/R^3)(C-A)\{\sin i\sin(\Omega-\varphi)\cos\theta\sin^2\omega_o t+\tfrac{1}{2}[\sin i\cos\varepsilon\cos(\Omega-\varphi)-\cos i\sin\varepsilon]$$
$$\times\sin 2\omega_o t\} \quad (6)$$

$$M_{z1} = 0. \quad (7)$$

4.3. Precession

The precession rate $\underline{\omega}$ of coordinate system [1] can be found from Euler's dynamical equation,

$$\underline{H}+\underline{\omega}\times\underline{H} = \underline{M}. \quad (8)$$

Inspection of Fig. 4.1 shows the components of $\underline{\omega}$ in system [1] to be

$$\omega_{x1} = \dot{\varepsilon} \quad (9a)$$

$$\omega_{y1} = \dot{\varphi}\sin\varepsilon \quad (9b)$$

$$\omega_{z1} = \dot{\varphi}\cos\varepsilon. \quad (9c)$$

Since the coordinate axes of system [1] lie along the principal axes of the body, the angular momentum vector $\underline{H}$ and its derivative are

$$H_{x1} = A\dot{\epsilon} \tag{10a}$$

$$H_{y1} = A\dot{\varphi}\sin\epsilon \tag{10b}$$

$$H_{z1} = C(\omega_s + \dot{\varphi}\cos\epsilon) \tag{10c}$$

and

$$\dot{H}_{x1} = A\ddot{\epsilon} \tag{11a}$$

$$\dot{H}_{y1} = A(\ddot{\varphi}\sin\epsilon + \dot{\varphi}\dot{\epsilon}\sin\epsilon) \tag{11b}$$

$$\dot{H}_{z1} = C(\dot{\omega}_s + \ddot{\varphi}\cos\epsilon - \dot{\varphi}\dot{\epsilon}\sin\epsilon). \tag{11c}$$

The angular rate of the gyro, ω_s, is typically more than ten orders of magnitude larger than $\dot{\varphi}$ or $\dot{\epsilon}$. As will be seen later $\ddot{\varphi}$ and $\ddot{\epsilon}$ are of the order of $\dot{\varphi}^2$ or $\dot{\epsilon}^2$. Therefore, substitution of (9),(10), and (11) into (8) and neglecting all terms on the left-hand side which do not contain the factor ω_s, shows that

$$\dot{\varphi} = M_{x1}/(C\omega_s\sin\epsilon) \tag{12}$$

$$\dot{\epsilon} = -M_{y1}/C\omega_s \tag{13}$$

Substitution of (5) and (6) into (12) and (13) will give instantaneous values of gravity gradient precession components, $\dot{\varphi}$ and $\dot{\epsilon}$.

If it be assumed that i, Ω, ϵ, and φ change much less rapidly than $\omega_o t$, average rates $\langle\dot{\varphi}\rangle$ and $\langle\dot{\epsilon}\rangle$ may be found by integrating over one orbital period, T:

$$\langle\dot{\varphi}\rangle = \frac{1}{T}\int_o^T \dot{\varphi}dt, \tag{14a}$$

$$\langle\dot{\epsilon}\rangle = \frac{1}{T}\int_o^T \dot{\epsilon}dt. \tag{14b}$$

For an elliptical orbit, the radius R from the center of the earth is

$$R = a(1-e^2)/[1+e\cos(\Psi-\alpha)],$$

in which a is the semi-major axis of the ellipse, e is the eccentricity, $\Psi=\omega_o t$ is the argument of the satellite, and α is the argument of perigee. Also, Kepler's law of areas provides the relation

$$\dot{A} = R^2\dot{\Psi} = \sqrt{[GMa(1-e^2)]},$$

so that

$$dt/R^3 = \dot{\Psi}dt/R\dot{A} = d\Psi/R\dot{A}.$$

Integration in time over one orbital period thus becomes integration in Ψ from 0 to 2π. The substitutions and integrations in (12) and (13) over one orbital period give the average rates of change of the spherical coordinates of the gyro spin axis direction as

$$\langle\dot{\varphi}\rangle = \Lambda[\sin i\cot\epsilon\cos(\Omega-\varphi)-\cos i]\cos\theta, \tag{15}$$

$$\langle\dot{\epsilon}\rangle = \Lambda[\sin i\sin(\Omega-\varphi)]\cos\theta, \tag{16}$$

where the gravity-gradient precession coefficient is defined as

$$\Lambda = 3GM(C-A)/[2a^3(1-e^2)^{3/2}C\omega_s], \tag{17a}$$

and cos θ may be written

$$\cos\theta = \sin i\sin\epsilon\cos(\Omega-\varphi)+\cos i\cos\epsilon. \tag{17b}$$

Equations (15) and (16) may be integrated with respect to time for any $i(t)$ and $\Omega(t)$ to give φ and ϵ as functions of time. The averages $\langle\dot{\varphi}\rangle$ and $\langle\dot{\epsilon}\rangle$ are both of the order of Λ, and therefore, this quantity must be small (specifically, $\Lambda/\omega_s \ll 1$) for the foregoing derivation to be valid. Furthermore, the time derivatives of (15) and (16) show that $\langle\ddot{\varphi}\rangle$, $\langle\ddot{\epsilon}\rangle$, and therefore $\dot{\omega}_s$ are of the order $\langle\dot{\varphi}\rangle^2$ or $\langle\dot{\epsilon}\rangle^2$, as assumed previously.

4.4 Order-of-Magnitude Minimization

The first step in reducing the gravity-gradient precession is to reduce the coefficient Λ to its lowest possible value. If it could be made much less than, say, 0.1 arcsec, the gravity-gradient precession could be regarded as of no problem to the gyroscope-satellite. However, limitations on the inertia difference ratio, (C-A)/C, and angular velocity, ω_s, prevent this possibility. The semi-major axis, a, of the orbital ellipse is limited for reasons of satellite visibility and the magnitude of the relativity effect, and for this analysis is assumed to be 7371 km, for an average altitude of 1000 km. A circular orbit is assumed, making e=0.

Let γ denote (C-A)/C. The smaller γ, the closer the body shape approaches a sphere. The centrifugal stress produced in a solid, homogeneous, elastic sphere is a maximum at its center and is given by[4]

$$S_s = \rho\omega_s^2 r^2 (3+2\nu)/(7+5\nu) \tag{18}$$

in which S_s is the stress at the center of the sphere, ρ is the density of the material, ω_s is the angular velocity in radians per second, r is the radius of the sphere, and ν is the Poisson's ratio for the material. A type of glass, such as Owens-Illinois' Cer-Vit, has been specified because of its low thermal expansion properties and high electrical resistance. For this material, ρ=2.5 gm/cm^3 and ν=0.25.

For Cer-Vit, the rupture stress is 13,000 psi, so that from equation (18), the rupture speed for a one-foot diameter sphere would be 1900 rad/sec., or 18,200 rpm. By comparison, ordinary plate glass may rupture at about 8000 psi. However, the minimum probable breaking stress over a long term may be only 1900 psi, according to reference 5. This estimate was substantiated by tests conducted at the Coordinated Science Laboratory on one-foot diameter disks made of plate glass. The disks were spun in their own plane in a simple test fixture at increasing angular velocities until they ruptured. The maximum stress, at the center of the disk, is given by

$$S_D = \rho r^2 \omega_s^2 (3+\nu)/8$$

and reached a value of about 3200 psi at a spin speed of 9000 rpm just before rupture, for the weaker of two specimens tested. No extensive materials testing program was carried out, but the experimental apparatus was shown to be adequate for centrifugal testing should any new material become available. The apparatus was dismantled before Cer-Vit was recognized as a promising material for the relativity satellite.

As a result of the spin tests made on the glass disks, the need for a large mechanical safety factor for any glass or ceramic material was emphasized. A tentative spin speed was set at 6000 rpm so that the maximum stress in a one-foot sphere made of Cer-Vit would be less than 1500 psi.

The centrifugal force also causes elastic deformation which tends to increase the inertia difference ratio, γ. Chree's[4] work describes in detail the elastic deformation at any point in a rotating solid sphere. At the surface of the sphere, the strain in the radial direction is

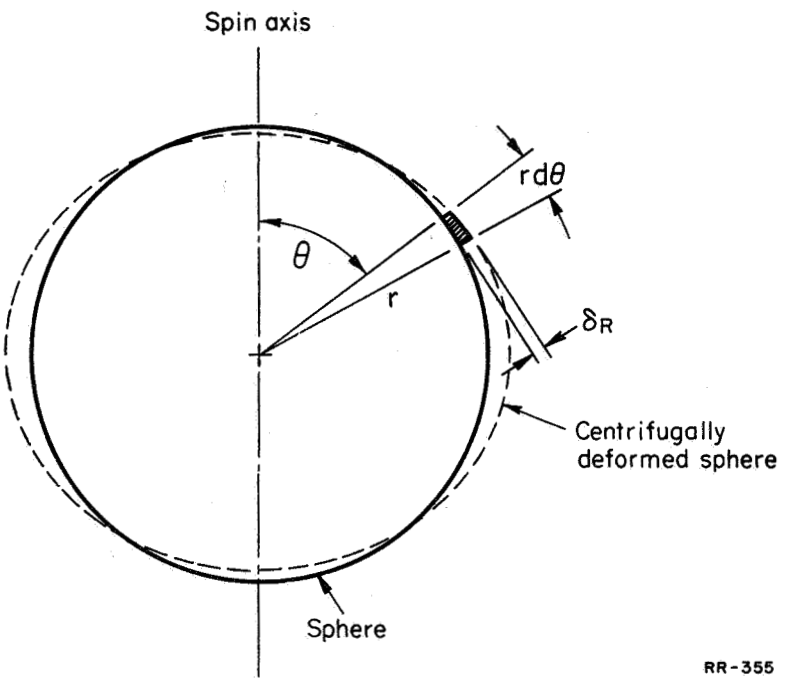

Figure 4.2

Solid sphere deformed by centrifugal acceleration.

$$\delta_R = (2/3E)\rho\omega_s^2 r^3(1+\nu)\{\nu_1[(3/2)\sin^2\theta - 1] + \nu_2\}, \tag{19}$$

in which E is the Young's modulus, θ is the angle from the spin axis, $\nu_1=(2+\nu)/(7+5\nu)$, and $\nu_2=(2/5)(1-2\nu)/(1+\nu)$.

The change in the moment of inertia about the spin axis can be calculated from equation (19). If the body is perfectly spherical when at rest, angular rotation produces, at an angle θ from the spin axis, a distortion in the radial direction which may be treated as a ring of mass dm on the outside of the spherical surface. From Fig. 4.2 it is seen that

$$dm = 2\pi\rho r^2 \delta_R \sin\theta\, d\theta \tag{20}$$

The change in the moment of inertia about the spin axis is obtained by multiplying (20) by $r^2\sin^2\theta$ and integrating with respect to θ. The result is

$$\Delta I = (4\pi/3E)\rho^2\omega_s^2 r^7(1+\nu)[(4/3)(\nu_2-\nu_1)+(8/5)\nu_1],$$

which can be simplified to

$$\Delta I = (4\pi/3E)\rho^2\omega_s^2 r^7(76/75)(0.60-\nu)(\nu+1.395)/(\nu+1.40).$$

This is approximately

$$\Delta I \approx (4\pi/3E)\rho^2\omega_s^2 r^7(0.6-\nu), \tag{21}$$

a linear function of Poisson's ratio. The increase in inertia difference ratio may be found by dividing (21) by the inertia of a sphere, $8\pi\rho r^5/15$, to obtain

$$\gamma_{CD} = \Delta I/I = (5\rho/2E)r^2\omega_s^2(0.6-\nu), \tag{22}$$

where the subscript CD means "centrifugal deformation". Thus the inertia ratio is also a function of spin speed. The method of spin axis readout requires a preferred spin-axis direction, i.e. a finite γ. Therefore, the gyro at rest cannot be perfectly spherical but must have $\gamma=\gamma_o>0$.

The gravity-gradient precession coefficient for a spinning satellite with a preferred spin axis may be represented by

$$\Lambda = (3GM/2)(\gamma_o+\gamma_{CD})/[\omega_s a^3(1-e^2)^{3/2}]$$

or

$$\Lambda = \{3GM/[2a^3(1-e^2)^{3/2}]\}[(\gamma_o/\omega_s)+(5\rho/2E)r^2(0.6-\nu)\omega_s]. \qquad (23)$$

It can now be seen that Λ is no longer a monotonic decreasing function of ω_s. Differentiating (23) with respect to ω_s and equating the result to zero gives the following condition for a minimum in Λ:

$$\omega_s^2 = (2E\gamma_o)/[5\rho r^2(0.6-\nu)],$$

or

$$\gamma_o = \gamma_{CD}.$$

Thus, Λ will have a minimum when the gyro spin speed is such that the deformation just equals the static inertia-difference ratio. For the Cer-Vit material already cited, a one-foot diameter solid sphere spinning at 6000 rpm would have $\gamma_{CD}=2.2\times10^{-4}$. Assuming $\gamma_o = \gamma_{CD}$, the minimum value of Λ would be about 27 arcsec/yr for a 1000-km orbit altitude.

4.5. Effects of Micrometeoroids

Barthel[6] has pointed out the danger in having the static inertia difference ratio, γ_o too small. Since the proposed satellite is unshielded, it will be subjected to the micrometeoroid flux of high-speed particles.

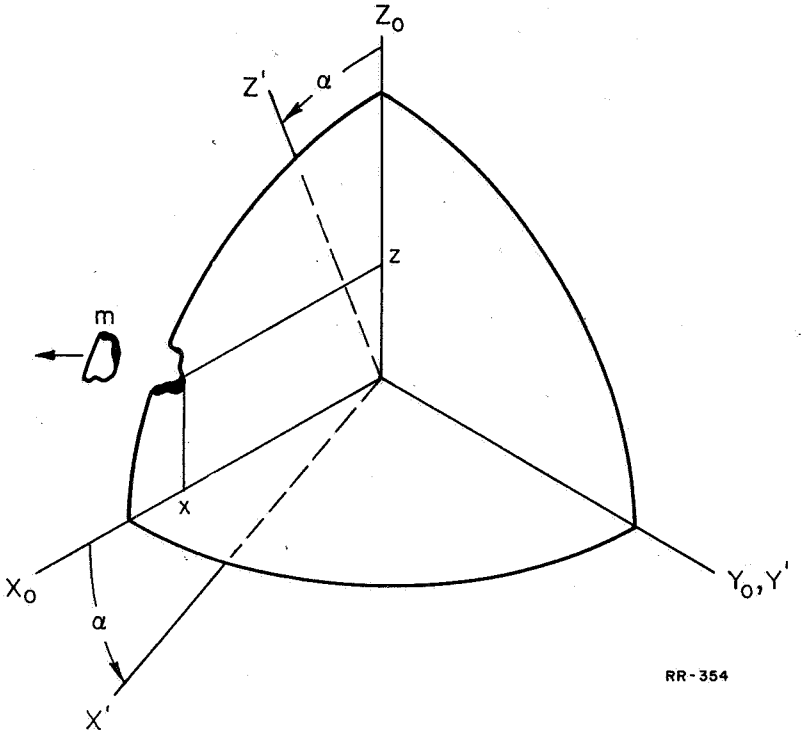

Figure 4.3

Rotation of principal axes of inertia caused by the removal of a small particle of mass.

A high-energy particle could melt away a portion of the gyro surface by the conversion of kinetic energy to heat. The analysis in Appendix 4A shows that perturbations of the angular momentum vector by meteoroid disturbances are negligible. If the bit of mass were removed from a perfect sphere, the immediate effect would be to produce a non-isoinertial body whose maximum moment-of-inertia axis would subsequently drift into the angular-momentum vector because of the cyclic strain-energy dissipation in the material. The maximum-inertia axis would shift directly to the point where the mass was removed if the body were perfectly spherical, but would rotate a smaller amount if $\gamma_o \neq 0$. The effect, as analyzed in Ref. 6 is as follows. The gyro, as manufactured, has an inertia tensor

$$I = \begin{bmatrix} A & 0 & 0 \\ 0 & A & 0 \\ 0 & 0 & C \end{bmatrix},$$

where A, A, and C > A are the moments of inertia about axes x_o, y_o, z_o respectively. If a small particle of mass m is removed from the body surface at coordinates (x,0,z), the resulting inertia tensor (refer to Fig. 4.3) becomes

$$I' = \begin{bmatrix} A-mz^2 & 0 & mxz \\ 0 & A-m(x^2+z^2) & 0 \\ mxz & 0 & C-mx^2 \end{bmatrix}.$$

The body's symmetry prevents any loss in generality in assuming the y-coordinate of the mass removed to be zero. The principal axes of inertia will then shift to axes x', y', z' by a rotation of angle α

about the y_o axis. Their transformation is given by the orthogonal nonsingular matrix

$$H = \begin{bmatrix} \cos\alpha & 0 & -\sin\alpha \\ 0 & 1 & 0 \\ \sin\alpha & 0 & \cos\alpha \end{bmatrix},$$

and may be used to find the new diagonalized inertia tensor I_D' by the equation

$$I_D' = H^{-1} I' H. \tag{24}$$

When the indicated matrix multiplication is performed, it is found that the new inertia tensor has the same vanishing components as in I', but the new diagonal elements are

$$I_{D11} = (A-mz^2)\cos^2\alpha+(C-mx^2)\sin^2\alpha+2mxz\sin\alpha\cos\alpha,$$

$$I_{D22} = A-m(x^2+z^2),$$

$$I_{D33} = (A-mz^2)\sin^2\alpha+(C-mx^2)\cos^2\alpha-2mxz\sin\alpha\cos\alpha,$$

replacing $A-mz^2$, $A-m(x^2+z^2)$, $C-mx^2$, respectively, and the new off-diagonal terms replacing mxz are each equal to

$$[C-A+m(z^2-x^2)]\sin\alpha\cos\alpha+mxz(\cos^2\alpha-\sin^2\alpha).$$

The required value of α, then, is to be found by requiring this last expression to vanish. With the help of double-angle formulas, this value of α is seen to be given by

$$\tan 2\alpha = -2mxz/[C-A+m(z^2-x^2)].$$

If the coordinates (x,z) be replaced by polar coordinates (r,β),

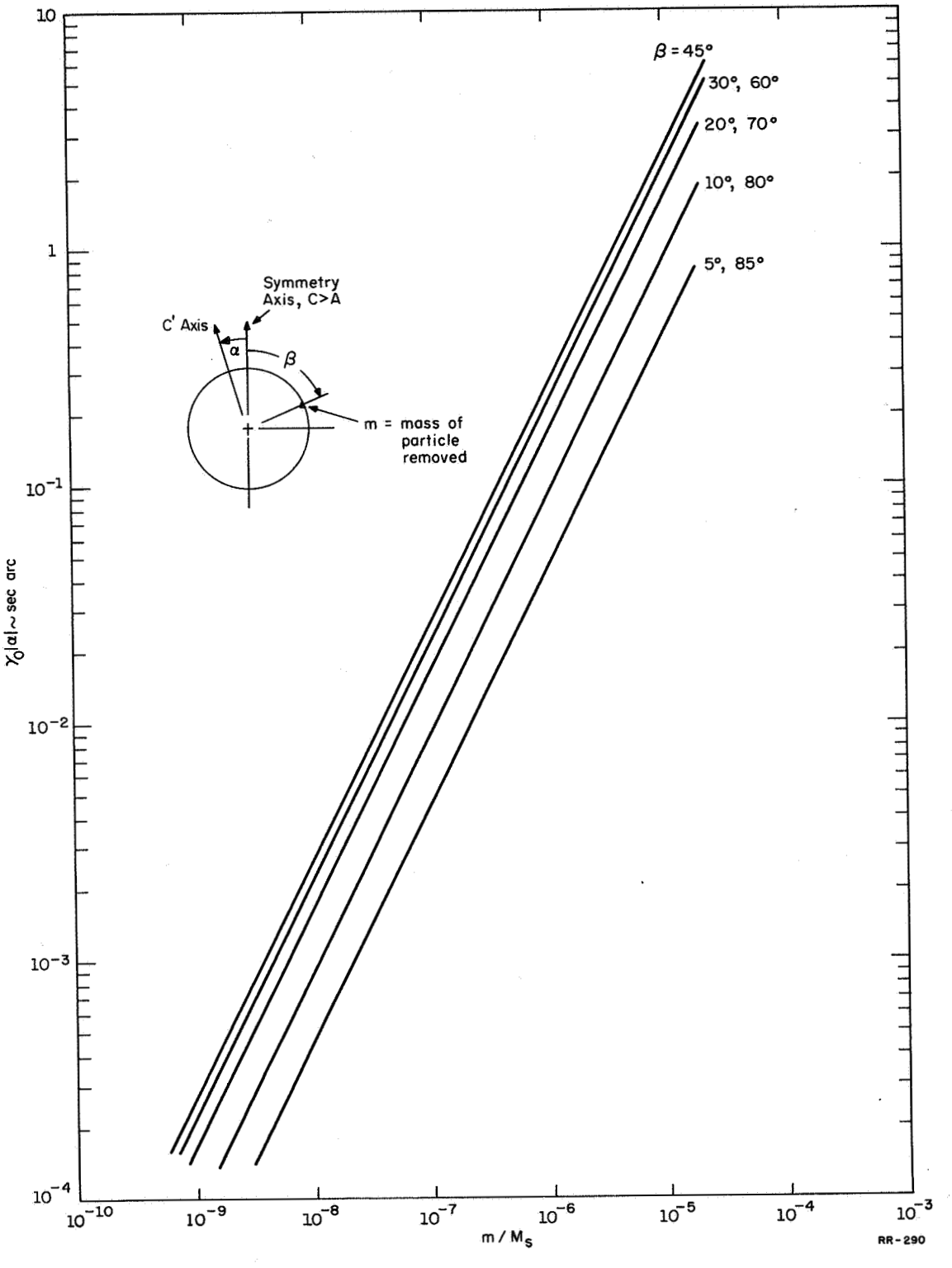

Figure 4.4

Normalized rotation of body axes vs. size of mass particle removed.

$\gamma_o = (C-A)/C$, M_s = mass of the satellite.

using $\sin\beta=x/r$ and $\cos\beta=z/r$, then α may be given by

$$\tan 2\alpha = -mr^2 \sin 2\beta / (C-A+mr^2 \cos 2\beta), \tag{25}$$

again with the help of double-angle formulas. For a spherically symmetric body, C=A, or

$$\tan 2\alpha = -\tan 2\beta,$$

which means that one of the "minor" axes rotates to the cavity left by the removed particle and becomes the maximum moment-of-inertia axis. If the satellite is nearly spherical with C>A, then $C \approx 2M_s r^2/5$ where M_s is the mass of the satellite. It will be shown that typically $\alpha \ll 1$ and $m/M_s \ll (C-A)/C$, so that when the numerator and denominator of the right side of (25) be divided by $2M_s^2/5$ and C respectively, the approximate angle of principle axis rotation is seen to be

$$\alpha = -(5/4)(m/M_s\gamma_o)\sin 2\beta. \tag{26}$$

Thus, given γ_o, m/M_s, the angle α has an absolute maximum when the mass particle is removed at an angle of 45^o from the spin axis. Fig. 4.4 gives the product $\gamma_o|\alpha|$ as a function of the relative size of mass removed from a nearly spherical body. The different curves also show the effect of location of the crater relative to the symmetry axis. For example, if a particle of mass $10^{-7}M_s$ is removed at 10^o or 80^o from either end of the symmetry axis of a body with $\gamma_o=0.001$, a principle axis shift of 9 arcsec would result.

As stated earlier in this section, the mechanism of mass

removal considered here is by the conversion of part of the kinetic energy of a micrometeoroid to the heat of fusion of the satellite material. The mass melted away is then

$$m = \eta m_m v_m^2 / 2\mathcal{E} \tag{27}$$

where η is the fraction of kinetic energy converted to heat of fusion, m_m is the mass of micrometeoroid, v_m is the velocity of micrometeoroid, and $\mathcal{E}$ is the heat of fusion of satellite material. The mass and velocity of meteoroids have been estimated by many researchers, and a number of different flux models have been developed. The majority of sources use an average velocity of 30 km/sec and a flux density of this form

$$\Phi = K m_m^{-k} \tag{28}$$

in which Φ is the number per square meter per second of particles of mass m_m grams and greater, and K and k are positive constants. The three models used in this report are summarized in Table 4.1.

Table 4.1

Model	Mass Range (gm)	Av.Vel.(km/sec)	Source	Ref.
$\Phi_1 = 1.3\times10^{-12} m_m^{-1}$	$10^{-5} \le m_m \le 10$	30	Whipple,57	8
$\Phi_2 = 1.3\times10^{-13} m_m^{-1}$	$10^{-7} \le m_m \le 1$	30	Whipple, Revised	8
$\Phi_3 = 10^{-17} m_m^{-1.7}$	$10^{-10} \le m_m \le 10^{-6}$	Distributed	Barthel	6,7

In the third model, Barthel used the data reported in Ref. 7 to develop a velocity distribution, divided into 5 equal parts with the following velocities: 15 km/sec, 22km/sec, 22km/sec, 38km/sec, and 68 km/sec.

The probability of a meteoroid striking a space vehicle is usually assumed to follow a Poisson distribution, with the probability of n hits in time t given by

$$P(n,t) = (1/n!)(Nt)^n e^{-Nt}, \tag{29}$$

in which N is the average frequency of hits determined from the flux model by

$$N = \Phi A_s S_f, \tag{30}$$

A_s is the surface area of the space vehicle, and S_f is the shielding factor of the earth, the fraction of the total solid angle, subtended at the satellite, that is obscured by the earth. Assume that a meteoroid of mass m_m, velocity v_m, strikes a nearly spherical mass at a position 45^o from the major axis of symmetry. Then, if (27) be substituted into (26) and solved for m_m, the mass necessary to cause a principal axis shift of $|\alpha|$ radians, at most, is found to be

$$m_m = (32\pi/15)(\mathscr{C}\rho r^3|\alpha|\gamma_o)/(\eta v_m^2). \tag{31}$$

If this equation be substituted into (28) and then into (30), the average frequency of hits large enough to shift the body axes by angle $|\alpha|$ is found to be

$$N_\alpha = 4\pi r^2 K S_f [(15/32\pi)(\eta v_m^2)/(\mathscr{C}\rho r^3 \gamma_o |\alpha|)]^k. \tag{32}$$

As an example, the average frequency of hits large enough to cause one arcsec shift will be calculated for the inertia ratio $\gamma_o = 2.2\times10^{-4}$, as determined in section 4.4. Flux model Φ_3 will be used, and a

pessimistic $\eta = 1$ will be assumed, along with the following parameters:

$$\mathcal{E} = 330 \text{ cal/gm}$$

$$\rho = 2.5 \text{ gm/cm}^3$$

$$r = 15 \text{ cm}$$

$$K = 10^{-17} \text{ gm}^{1.7}\text{m}^{-2}\text{sec}^{-1}$$

$$S_f = 0.75$$

$$k = 1.7$$

$$|\alpha| = 1 \text{ arcsec} = 4.8\times10^{-6} \text{ radian}$$

The smallest meteoroid mass needed, given by (31), is $m_m = 4.3\times10^{-8}$gm. The average frequency of particles of this size and larger hitting the satellite is then $N_\alpha = 220$ hits/year. Such a high frequency of disturbances would shift the body axes of the satellite much too often to obtain the required accuracy of spin axis readout, and a larger γ_o is indicated. Since an increase of γ_o leads to an increase in gravity-gradient moment, a balance must be reached such that the gravity gradient is minimized while still making the satellite somewhat immune to meteoroid disturbances. The readout requirements indicate the need for about one week of undisturbed data to determine the spin-axis direction to less than a half second of arc. To track the spin-axis drift, many sets of good data will be required. If body axis shifts of one second of arc could be limited to an average frequency of only one per year, the probability of zero disturbances in any one week would be from Eq. (29) just exp(-1/52) or 0.98. That is to say, the probability of one or more such hits per week would be 2 percent.

To see what effect this high probability of success will have on the gravity gradient moment, first Eq. (32) is to be solved for γ_o,

and the result inserted in Eq. (23) for the gravity-gradient precession coefficient. At the same time, the satellite rotational velocity is to be represented by the ratio of peripheral velocity, v, and radius r. The equation for Λ including both meteoroid damage probability and centrifugal deformation is

$$\Lambda = [3GM/2a^3(1-e^2)^{3/2}]$$

$$\times[(15/32\pi v)(\eta v_m^2/\varepsilon\rho|\alpha|)(4\pi KS_f/N_\alpha)^{1/K} \tag{33}$$

$$+(5\rho/2E)(0.6-\nu)vr].$$

In this form it is clear that once a choice is made of orbit altitude, satellite material, and frequency of hits N_α which produce a body axis shift $|\alpha|$, the gravity gradient can be minimized by adjusting peripheral velocity v and radius r. For $\gamma_o > \gamma_{CD}$, Λ decreases with increasing v, but the peripheral velocity is limited by the maximum allowable stress. For the 1500-psi limit set in 4.4, the peripheral velocity is about 100 meters per second. The dependence on radius is determined by the model of meteoroid flux which is used. If k=1, as in Φ_1 and Φ_2, then Λ is a linear function of r of the form

$$\Lambda = A_1 + A_2 r.$$

Thus, the smallest radius is most favorable. However, if k=1.7 as in Φ_3, equation (33) has the form

$$\Lambda = (A_1/r^{0.84}) + A_2 r$$

which clearly exhibits a relative minimum in r. Figure 4.5 is a plot

of gravity gradient precession coefficient vs gyro radius for two meteoroid flux models, Φ_2 and Φ_3, in which it is assumed that one hit per year causes a principal axis shift of one arcsec. The results for model Φ_1 are not shown because Φ_2 is a revised estimate of that model and was assumed to be a more accurate representation. Two curves are shown for each flux model, the upper curves in each model for a peripheral velocity of 100 meters per second, the lower ones for 150 meters per second, which would produce a maximum stress of 3800 psi. The ranges of meteoroid masses applicable to each model listed in Table 4.1 limit the regions of applicability to the solid portions of the curves shown in Fig. 4.3. The applicable ranges of gyro radius are summarized below:

Φ_2: 0.5 cm < gyro radius < 1600 cm,

Φ_3: 1.5 cm < gyro radius < 15 cm.

It is interesting to note that if Φ_3 were good for masses up to 10^{-5} gm, the curves could be used up to 103 cm. The minimum value of Λ, found by differentiating (33) with respect to r and equating to zero, would be 38 arcsec per year at a radius of 74 cm; for v = 150 m/sec, Λ would be 36 arcsec per year at a radius of 47 cm. This analysis has had the remarkable result that a rather broad optimum can be found for the gyro radius fairly close to the values of interest in the design of the relativity satellite, i.e. between 15 cm and 30 cm. By adhering strictly to the curves shown in Fig. 4.5, it would appear that 15 cm would truly give a minimum value for Λ, since that is the upper limit of the useful region of the Φ_3 curve as derived from Table 4.1.

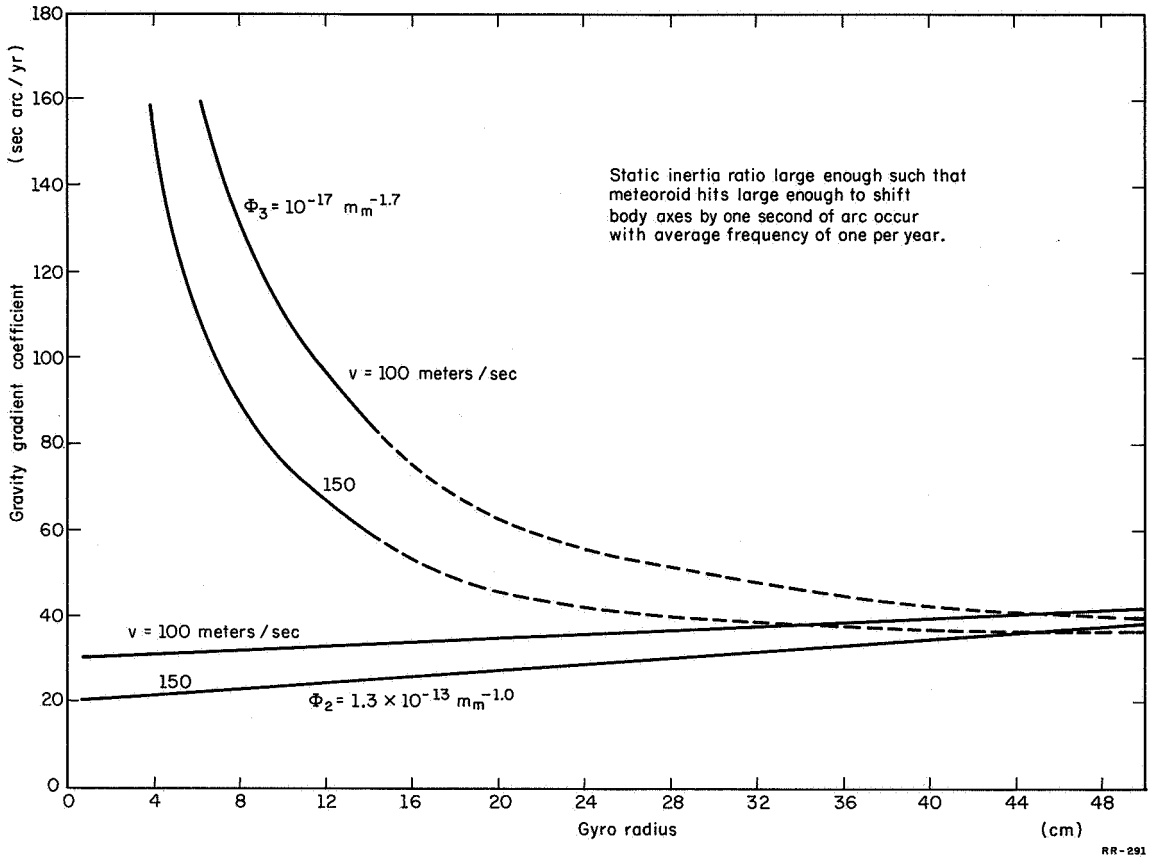

Figure 4.5

Minimum gravity gradient coefficient
vs. gyro radius.

In concluding this section, several observations can be made. The criterion for the satellite to be relatively immune from a meteoroid-produced axis shift was derived assuming that all of the kinetic energy of the incoming particle is converted to heat and that the crater is formed at an angle of 45^{o} from either end of the satellite spin axis, the worst possible place. If it is assumed that any point on the nearly spherical body is equally likely to be hit by a meteoroid, then the average angular shift of the principal axes caused by a given particle is about 65% of the maximum calculated by equation (26). The curves in Fig. 4.5 may therefore be regarded as somewhat conservative, and a 15 cm radius satellite designed with γ_o so large as to produce a maximum of 80 arcsec per year gravity-gradient precession will be virtually free from any noticeable meteoroid disturbances.

4.6 Special Orbits

Now that the gravity gradient precession coefficient has been minimized to a value of about 80 seconds of arc per year, it is necessary to consider how to reduce the actual gravity gradient precession rates, $\langle\dot{\varphi}\rangle$ and $\langle\dot{e}\rangle$, given by Eqs. (15) and (16).

The relativity drift rate of the gyro spin axis will be largest when the spin axis lies in the orbital plane. Therefore, two cases of special interest are an equatorial orbit and a polar orbit, because either of these orbits will allow the gyro spin axis to lie in the orbital plane for an extended period of time. For each of these special cases, Eqs. (15) and (16) may be simplified and integrated directly, as will be seen.

4.6.1. Equatorial Orbit

For an equatorial orbit, the inclination i will be assumed small so that

$$\sin i \approx i$$

$$\cos i \approx 1.$$

Also, it is assumed that,

$$\epsilon = \tfrac{1}{2}\pi + \delta_e$$

where δ_e is a small angle between the spin axis and the x_o, y_o plane, as shown in Fig. 4.6. From this figure are obtained

$$\sin\epsilon = \sin(\tfrac{1}{2}\pi+\delta_e) = \cos\delta_e \approx 1$$

$$\cos\epsilon = \cos(\tfrac{1}{2}\pi+\delta_e) = -\sin\delta_e \approx -\delta_e.$$

From Eq. (17b) there obtains

$$\cos\theta = \sin i\cos(\Omega-\varphi) - \delta_e \cos i.$$

Since i is also a small angle, this reduces to

$$\cos\theta \approx i\cos(\Omega-\varphi) - \delta_e.$$

Substituting these small angle approximations into Eqs. (15) and (16) results in the following:

$$\langle\dot{\varphi}\rangle = -\Lambda[i^2\delta_e\cos^2(\Omega-\varphi) + i\delta_e^2\cos(\Omega-\varphi) + i\cos(\Omega-\varphi) - \delta_e]$$

$$\langle\dot{\epsilon}\rangle = \Lambda[\tfrac{1}{2}i^2\sin 2(\Omega-\varphi) - i\delta_e\sin(\Omega-\varphi)].$$

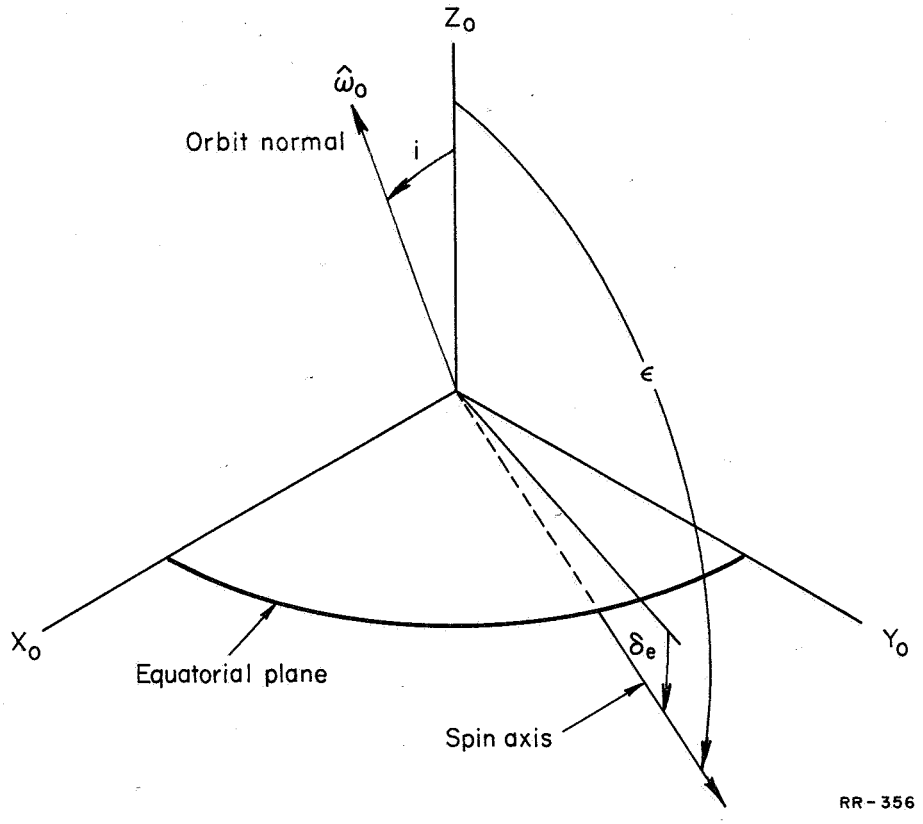

Figure 4.6

Orbit and spin axis configuration for a near-equatorial orbit.
The X_o axis is along the vernal equinox;
the Z_o axis is the north pole of the earth.

Since i and δ_e are both small, $\langle\dot{\varphi}\rangle$ is larger by at least one order of magnitude than $\langle\dot{\epsilon}\rangle$, and may now be simplified by dropping the higher order terms in i and δ_e:

$$\langle\dot{\varphi}\rangle \approx \Lambda[\delta_e - i\cos(\Omega-\varphi)]. \tag{34}$$

For near equatorial orbits, Ω changes at the rate of 6 to 9 revolutions per year. Therefore, Eq. (34) indicates that the average rate of change of φ is proportional to δ_e, the angle between the gyro spin axis and the earth's equatorial plane. Setting $\Omega=\Omega_o+\dot{\Omega}t$, Eq. (34) can be integrated with respect to time to give $\Delta\varphi$:

$$\Delta\varphi = \Lambda\{\delta_e t-(i/\dot{\Omega})[\cos(\Omega_o-\varphi)\sin\dot{\Omega}t+\sin(\Omega_o-\varphi)(\cos\dot{\Omega}t-1)]\}$$

By arbitrarily setting $\Omega-\varphi=\frac{1}{2}\pi$, this simplifies to

$$\Delta\varphi = \Lambda[\delta_e t+(i/\dot{\Omega})(1-\cos\dot{\Omega}t)] \tag{35}$$

A 1000-km-altitude orbit inclined at 10^o from the equator regresses at the rate of 2200 degrees per year. Thus, with Λ = 80 arcsec/yr, the periodic part of Eq. (35) has a maximum amplitude of about 0.36 arcsec. However, to keep the secular part of (35) less than 0.1 second of arc in one year requires

$$\delta_e < (1/800) = 0.072^o.$$

4.6.2. Polar Orbit

A true polar orbit (i.e., $i=\frac{1}{2}\pi$) is required for a nonregressing orbit plane. The nodal regression rate of the orbit line of

nodes is given in Ref. 2 by

$$\Omega = -(3J_2/2)(GM/a)^{\frac{1}{2}}(R_e^2/a^3)(1-e^2)^{-2}\cos i, \tag{36}$$

where $J_2 = 1.082 \times 10^{-3}$ is the coefficient of the second harmonic term in the earth's gravitational potential. (A more exact equation for nodal regression, also given in Ref. 2, contains terms three orders of magnitude smaller than Eq. (36) and will not be required in this analysis.) The right ascension of the orbit line of nodes will now be written $\Omega=\Omega_o+\dot{\Omega}t$, where Ω_o is the value of Ω at the time of injection of the satellite into orbit. Figure 4.7 shows a typical configuration for a near polar orbit right after injection. Here, δ_p is an error angle between the initial orbit line of nodes and the projection of the gyro spin axis on the earth's equatorial plane. It will be seen that the gravity gradient precession depends on this angle and on the regression rate, $\dot{\Omega}$.

From Fig. 4.7 it can be seen that

$$\Omega_o-\varphi = \tfrac{1}{2}\pi-\delta_p,$$

and, therefore,

$$\Omega-\varphi = \dot{\Omega}t+\tfrac{1}{2}\pi-\delta_p.$$

Using

$$\cos(\Omega-\varphi) = \sin(\delta_p-\dot{\Omega}t),$$

$$\sin(\Omega-\varphi) = \cos(\delta_p-\dot{\Omega}t),$$

and also, assuming that $i=\frac{1}{2}\pi+i'$, where i' is a small error in orbital inclination, we have

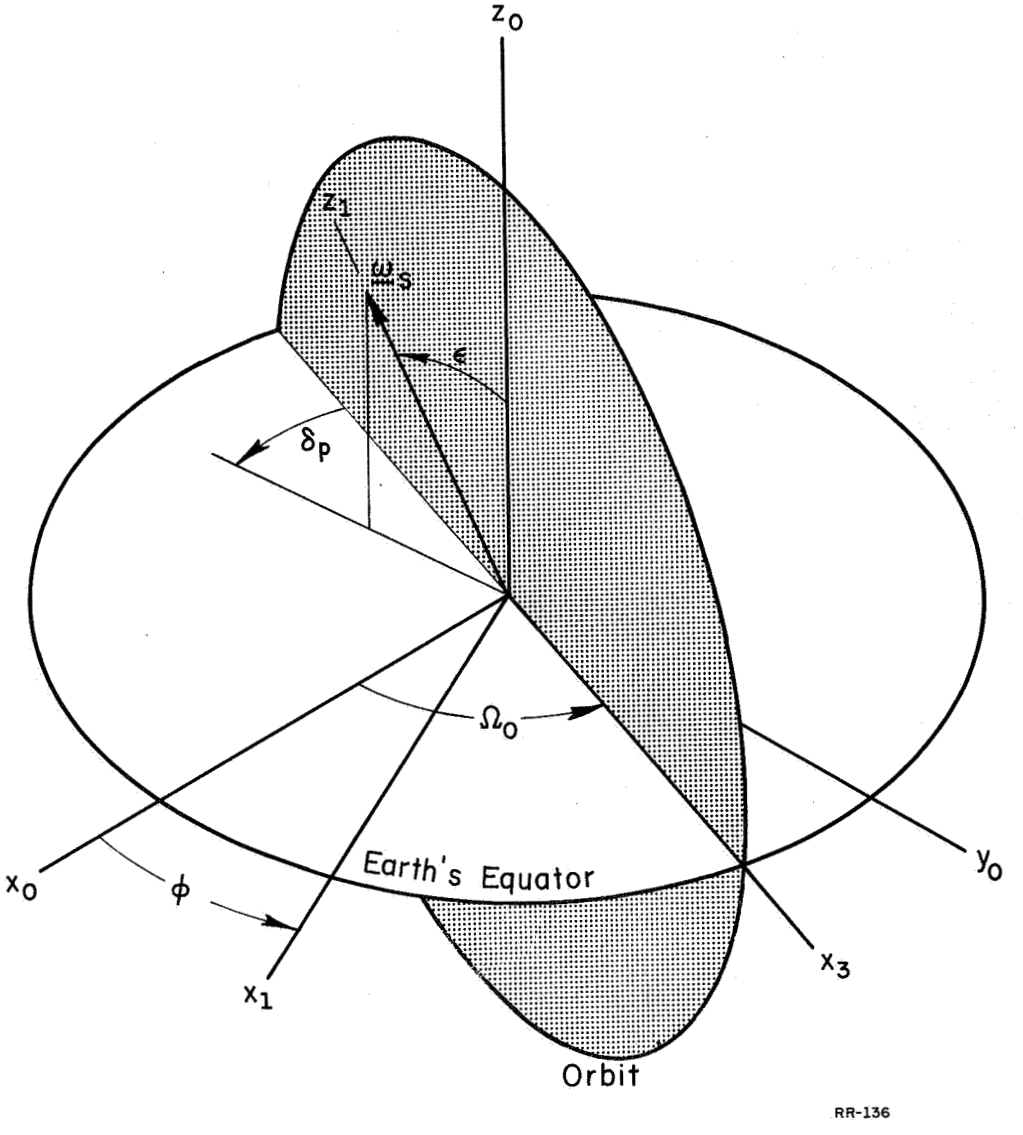

Figure 4.7

Initial orbit and spin axis conditions for a near-polar orbit. X_o is along the vernal equinox; Z_o is the earth's north pole.

$$\cos\theta = \sin\epsilon\sin(\delta_p - \dot{\Omega}t) - i'\cos\epsilon .$$

Equations (15) and (16) now become

$$\langle\dot{\varphi}\rangle = \Lambda[\cos\epsilon\sin^2(\delta_p - \dot{\Omega}t) - i'(\cos 2\epsilon/\sin\epsilon)\sin(\delta_p - \dot{\Omega}t) - i'^2\cos\epsilon], \tag{37}$$

$$\langle\dot{\epsilon}\rangle = \Lambda[\tfrac{1}{2}\sin\epsilon\sin(2\delta_p - 2\dot{\Omega}t) - i'\cos\epsilon\cos(\delta_p - \dot{\Omega}t)]. \tag{38}$$

These equations may be integrated with respect to time to give $\Delta\varphi$ and $\Delta\epsilon$ as functions of time:

$$\Delta\varphi = \tfrac{1}{2}\Lambda t\cos\epsilon\{1 - \sin 2\delta_p(1-\cos 2\dot{\Omega}t)/2\dot{\Omega}t - (\cos 2\delta_p \sin 2\dot{\Omega}t)/2\dot{\Omega}t$$

$$+4i'\cot 2\epsilon[\cos\delta_p(1-\cos\dot{\Omega}t)/\dot{\Omega}t - (\sin\delta_p\sin\dot{\Omega}t)/\dot{\Omega}t] - i'^2\} \tag{39}$$

$$\Delta\epsilon = \tfrac{1}{2}\Lambda t\sin\epsilon\{(\sin 2\delta_p \sin 2\dot{\Omega}t)/2\dot{\Omega}t - \cos 2\delta_p(1-\cos 2\dot{\Omega}t)/2\dot{\Omega}t$$

$$-2i'\cot\epsilon[\sin\delta_p(1-\cos\dot{\Omega}t)/\dot{\Omega}t + (\cos\delta_p\sin\dot{\Omega}t)/\dot{\Omega}t]\}. \tag{40}$$

If ϵ is allowed to vanish, these equations may give misleading results. However, it must be remembered that φ and, therefore, $\Delta\varphi$, are undefined if $\epsilon=0$ because the gyro spin axis becomes coincident with the z_o axis, as can be seen in Fig. 4.7.

It will be seen later that, for practical purposes, the nodal regression rate, $\dot{\Omega}$, should be less than 45 degrees per year and, therefore, Eq. (36) indicates that for 1000 km orbits, i' must be no larger than 1^o or .017 radian. Consequently, for such slow regression rates, Eqs. (39) and (40) may be simplified by dropping the terms

containing i'. The simplified expressions are

$$\Delta\varphi = \tfrac{1}{2}\Lambda t\cos\varepsilon[\,1-\sin 2\delta_p(1-\cos 2\dot{\Omega}t)/2\dot{\Omega}t-(\cos 2\delta_p \sin 2\dot{\Omega}t)/\dot{\Omega}t] \tag{41}$$

$$\Delta\varepsilon = \tfrac{1}{2}\Lambda t\sin\varepsilon[\,(\sin 2\delta_p \sin 2\dot{\Omega}t)/2\dot{\Omega}t-\cos\delta_p(1-\cos 2\dot{\Omega}t)/\dot{\Omega}t] \tag{42}$$

Some typical curves are plotted in Figs. 4.8 and 4.9 to show the variations of $\Delta\varphi$ and $\Delta\varepsilon$ as functions of the initial misalignment angle, δ_p, and the nodal regression angle, $\dot{\Omega}t$. In these curves, the nondimensional parameters $\Delta\varphi/(\Lambda t\cos\varepsilon)$ and $\Delta\varepsilon/(\Lambda t\sin\varepsilon)$ have been plotted. These curves illustrate the need to keep the nodal regression rate and δ_p as small as possible to avoid large values of gravity gradient precession.

4.7 Conclusions

The gravity gradient torque acting on a non-isoinertial spinning satellite can easily produce precession in the same direction as the predicted relativity precession. Centrifugal deformation of the satellite and the need for a preferred spin-axis direction relatively free from micrometeoroid cratering effects lead to a lower limit value of the inertia difference ratio, γ. This lower limit of γ is a function of the gyro size and material properties and of the model used for the meteoroid flux. By using this lower limit of γ in the gravity-gradient equation, the precession coefficient Λ can be minimized with respect to the gyro radius. A 15-cm-radius gyro with Λ = 80 arcsec per year, or a 30-cm-radius gyro with Λ = 50 arcsec per

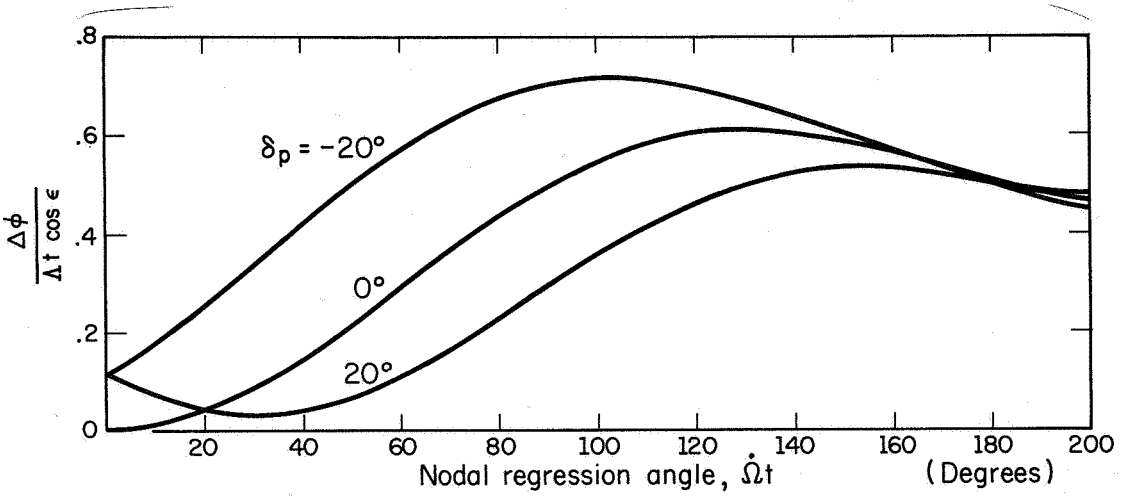

Figure 4.8 RR-187

Gravity gradient precession for regressing polar orbit; dimensionless equatorial plane component vs. regression angle.

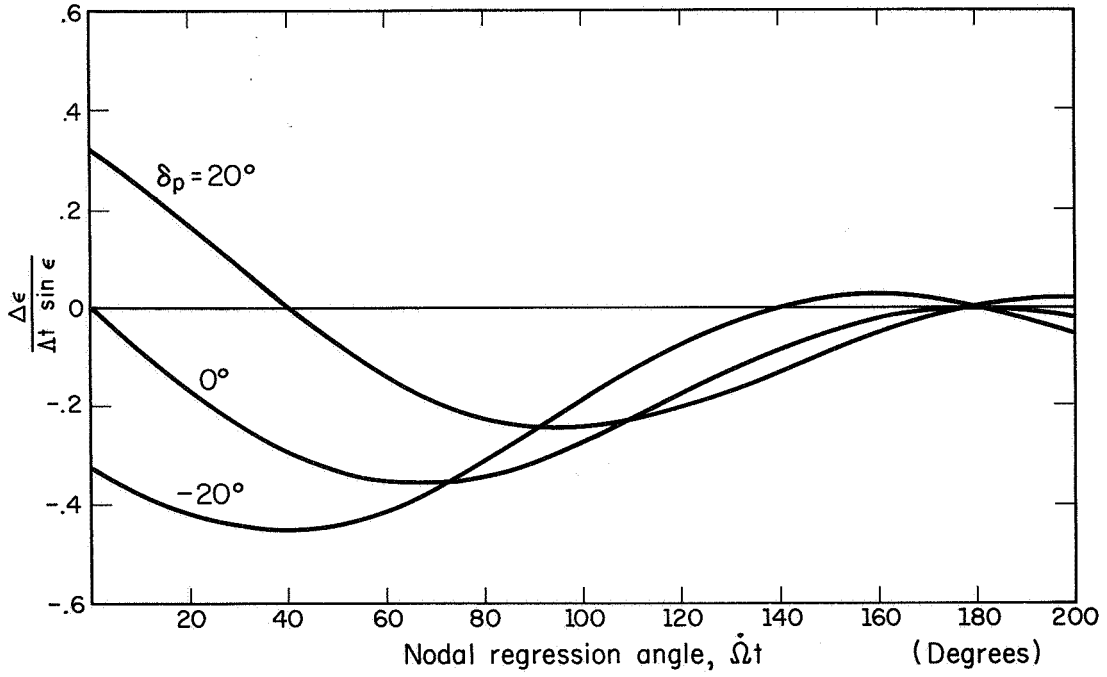

Figure 4.9 RR-188

Gravity gradient precession for regressing polar orbit; dimensionless component normal to earth's equatorial plane vs. regression angle.

year could be built with the same degree of meteoroid immunity as that of optimum radius, 74 cm, which would have Λ = 38 arcsec per year.

The final reduction of gravity gradient precession must be accomplished by precise initial alignment of the gyro spin axis. Eq. (35) indicates that for a near equatorial orbit, the secular precession rate in the same direction as that predicted by relativity theory is just Λ multiplied by the small misalignment angle between the gyro spin axis and the earth's equatorial plane. A misalignment of 0.07^{o} would produce a secular precession of 0.1 arcsec in one year for the 15-cm radius, whereas the same precession would obtain with the 30-cm radius for a misalignment of 0.11 degree.

Some softening of this need for precision in alignment would be possible if the value of Λ were accurately known. An estimate of Λ is available from the design of the gyro, and the prediction of its spin deformation. An estimate is also available from the peroidic component of the gravity-gradient precession. Both of these estimates will be made as a matter of course; the former is a necessary part of the design, and the latter is a necessary part of data analysis. If Λ may be known with an accuracy of 20 percent, then the secular part of the gravity-gradient precession would be known with a like accuracy, so that a five-fold greater error, than demanded above, could be tolerated in the alignment of the spin axis with the earth's equatorial plane.

4.8. Appendix--Momentum Transfer of Micrometeoroids

The degree to which the relativity satellite of the Coordinated Science Laboratory is immune to the momentum transfer of impacting meteoroids depends upon the model of the meteoroid flux. The best known, and also the most conservative, model of the meteoroid environment was developed by Whipple in 1957. This model can be represented by

$$\Phi_1 = 1.3 \times 10^{-12} m^{-1} ,$$

where Φ is the flux per meter^2 sec of particles with mass m grams and greater[8]. A 1961 evaluation of rocket and satellite data obtained

$$\Phi_2 = 10^{-17.0} m^{-1.70} ,$$

applicable for masses of 10^{-10} to 10^{-6} gm[8]. However, observations of meteors simulated by shaped-charge firings indicated that Whipple's 1957 estimate should be revised by an order of magnitude to give[8]

$$\Phi_3 = 1.3 \times 10^{-13} m^{-1} .$$

These are the three meteoroid models currently used, all subject to revision as more is learned of the space environment.

The number of particles hitting a given satellite in a given amount of time can be calculated, using the flux expression, to be

$$N = \Phi A T ,$$

where A is the area exposed to meteoroids, and T is the time of exposure. Assume, for calculation purposes, a possible CSL gyro satellite to be a solid, nearly spherical body of density 2.5 gm/cm^3, having a radius of 30 cm, spinning at 50 Hz and monitored for one year. A plot of the number of meteoroids striking the satellite versus the meteoroid mass is given in Fig. 4.10 using the above satellite radius and the three different flux estimates. Figure 4.10 reveals that large numbers of small meteoroids will hit the satellite while few meteoroids heavier than 10^{-5} grams are to be expected within a year's time.

The effect of a meteoroid hit will depend upon the momentum of the impinging particle. Visual observations of meteor showers indicate that large meteoroids have approximate velocities of 28 km/sec while smaller particles have a velocity of about 15 km/sec. The velocity distribution tabulated in Table 35 of Ref. 8 is used for calculations in this analysis. A conservative approach to the momentum-exchange analysis is to assume that the momentum vector of all impinging particles is perpendicular to the spin axis and intersects the spin axis. The impulsive angular displacement, δ, caused by one meteoroid hit would then be

$$\delta = mvr/C\Omega ,$$

where C is the moment of inertia, Ω is the spin rate, and mv is the momentum of the meteoroid acting at a distance r from the center of mass of the satellite. For a conservative calculation, let r be the radius of the satellite, R. The moment of inertia of the spherical gyro is

$$C = 8\pi\rho_s R^5/15$$

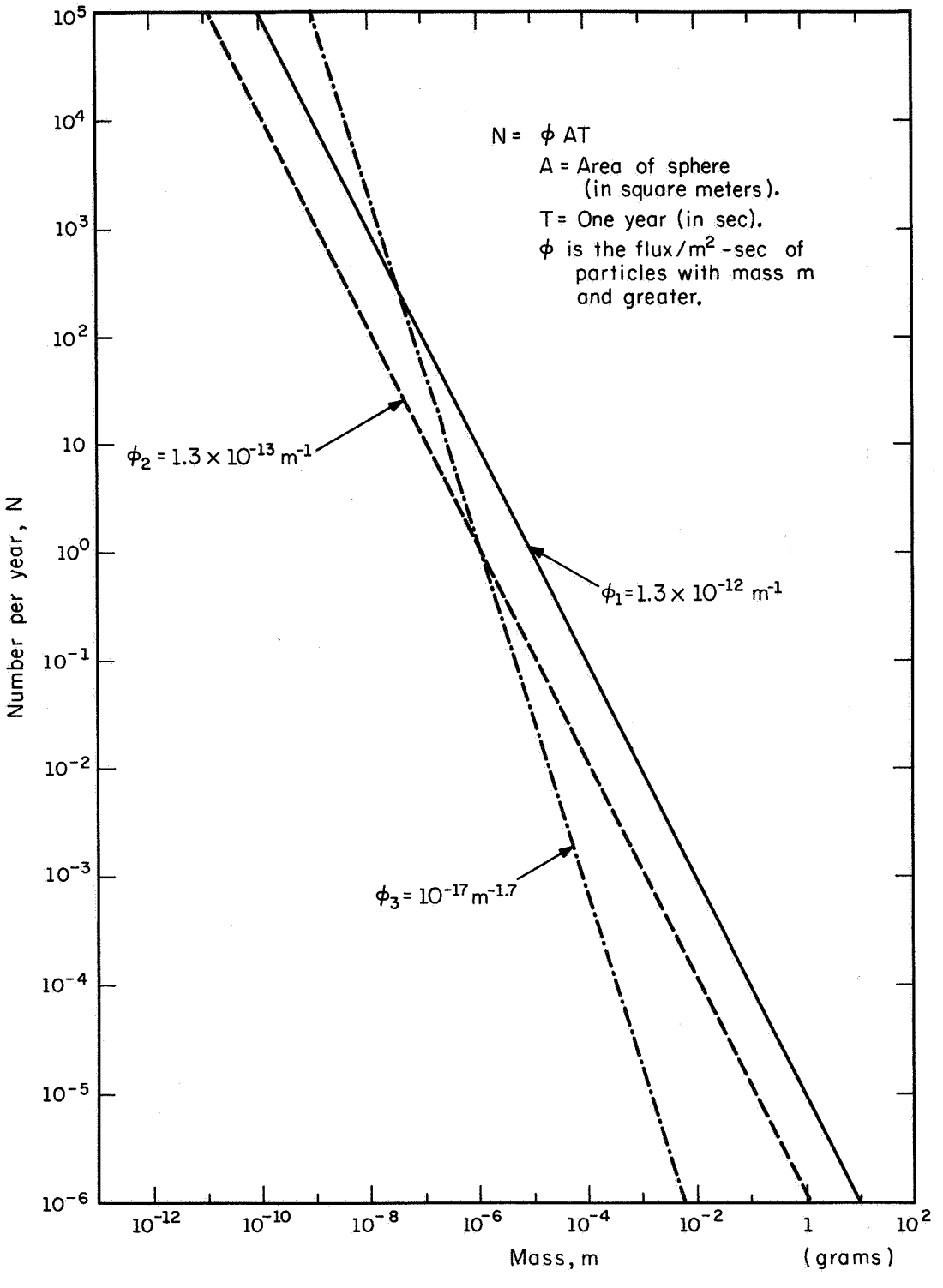

Figure 4.10

Number of meteoroids striking a spherical satellite of 30 cm radius vs. meteoroid mass. Three flux models are shown.

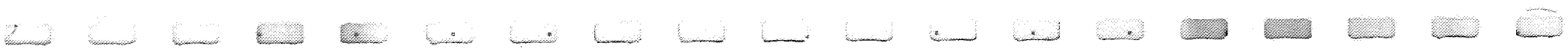

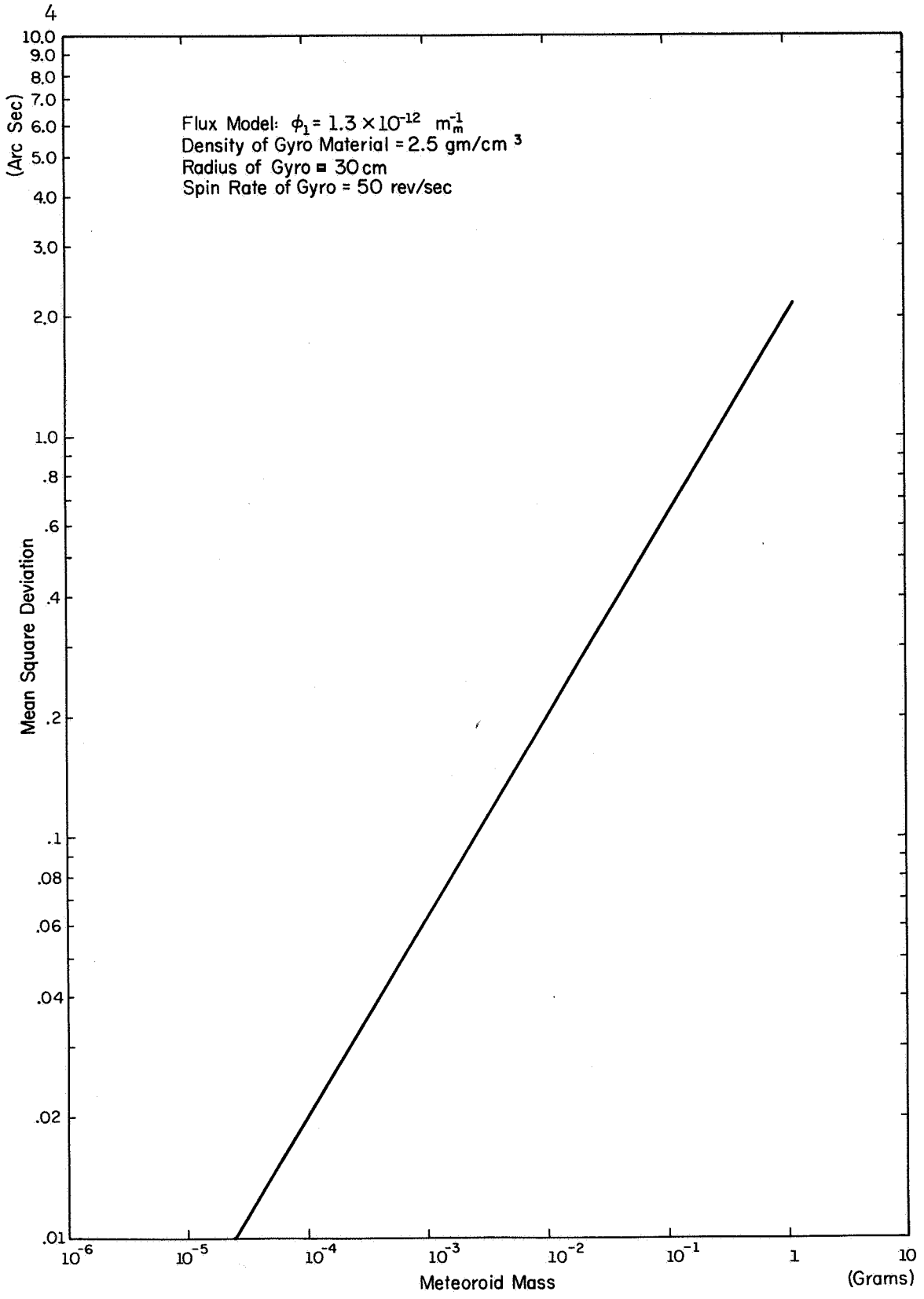

Figure 4.11

Mean square deviation of the satellite angular velocity vector vs. meteoroid mass.

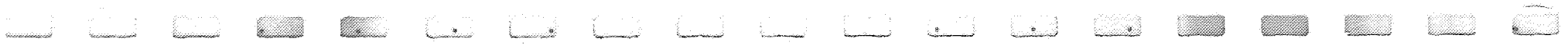

where ρ_s is the density, and the impulsive angular deviation due to one meteoroid hit becomes

$$\delta = (15/8\pi)(mv/\rho_s R^4\Omega).$$

A large satellite then would be less affected by meteoroid hits than a smaller one. However, a larger satellite is hit by a greater number of particles. This can be taken into consideration by assuming a mean square deviation of events along the spin axis and writing an expression for the net angular deviation, σ, of N hits,

$$\sigma = \delta\sqrt{N} .$$

This function is plotted versus meteoroid mass in Fig. 4.11 using the conservative 1957 Whipple estimate of meteoroid flux. Since the cross-sectional area of a sphere is πR^2, σ is inversely proportional to the radius cubed.

Figure 4.11 indicates that the larger meteoroids will be detrimental to the relativity experiment which requires spurious deviations of less than 0.1 sec of arc per year. However, the probability of being hit by the larger meteoroids is of course less than for the smaller particles. For a Poisson distribution of events, the probability of no impact, P(0), within a year by a meteoroid of a given mass is given by

$$P(0) = e^{-N}$$

where $N = \Phi AT$. Therefore, for a meteoroid of a given mass, the maximum impulsive precession due to its impact and the probability of not hitting the satellite can be calculated. A plot of P(0) versus δ

using the three meteoroid flux models is given in Fig. 4.12. This plot can be interpreted to give the probability of success of the experiment with reference to meteoroids if a maximum δ to be tolerated is defined. For the CSL relativity experiment this maximum δ would be 0.1 arcsec in a year which would correspond to better than 93% chance of success using the most conservative flux estimate.

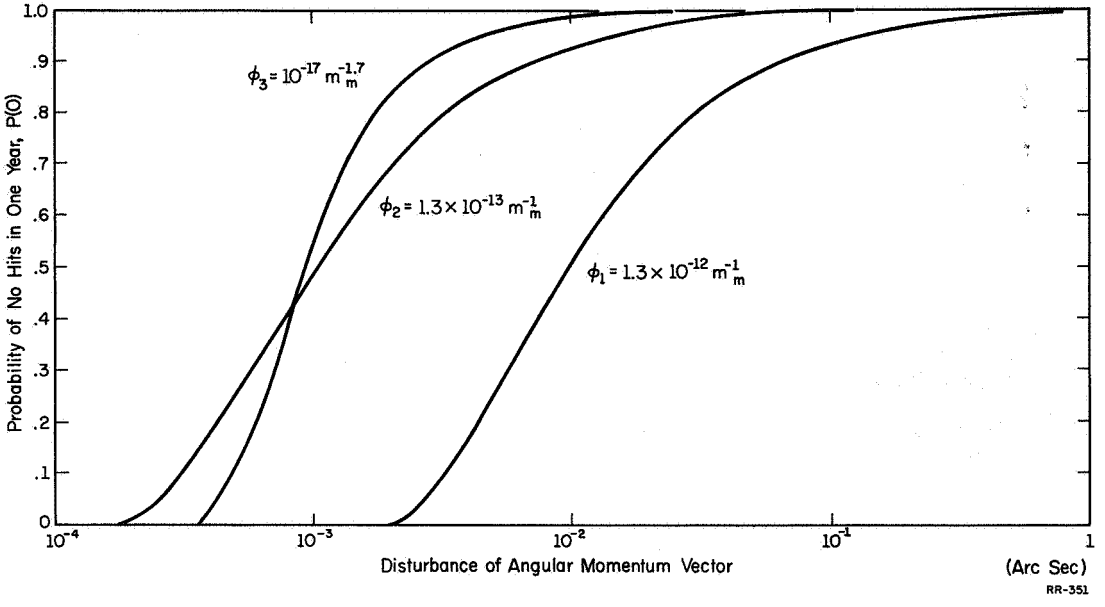

Figure 4.12

Probability of no disturbances of the satellite angular velocity vector due to meteoroid momentum exchange.

4.9. References

1. Scarborough, J. B., The Gyroscope, Theory and Applications, Interscience (1958).

2. Wolverton, R. W., (Editor), Flight Performance Handbook for Orbital Operations, John Wiley and Sons (1963).

3. Myers, J. L., Jr., The Effects of the Nodal Regression of the Orbit on the Gravity Gradient Precession of a Gyroscopic Satellite. Report R-309, Coordinated Science Laboratory, University of Illinois, (July, 1966).

4. Chree, C., The Equations of an Isotropic Elastic Solid in Polar and Cylindrical Coordinates, Cambridge Phil. Soc. Trans., Vol. 14, Part 3 (1889).

5. Shand, E. B., Glass Engineering Handbook, 2nd. Ed. McGraw-Hill, (1958).

6. Barthel, H. O., Effects of Micrometeoroid Cratering on the Direction of the Axis of Maximum Moment of Inertia, Report R-274, Coordinated Science Laboratory, University of Illinois, Feb., 1966.

7. Davison, E. H. and Winslow, P. C., Jr., Space Debris Hazard Evaluation, NASA TN D-1105, (Dec., 1961).

8. Orbital Flight Handbook, NASA SP-33, Vol. I, Part I. (1963), pp. II-46, 47.

5.1. Introduction

The unshielded relativity gyro will be subjected to aerodynamic torques due to atmospheric drag. The aerodynamic torque on a spinning spherical satellite has been studied by R. D. Palamara[1] and Nan Tum Po.[2] R. D. Palamara analyzed not only aerodynamic torque but also numerous other effects which cause torque on an unprotected spinning satellite. His study of the aerodynamic torque is, however, restricted in that the satellite spin axis is taken as being in the plane of the orbit. Nan Tum Po obtained a more general solution which he used to find the spin rate slowdown of a satellite having high surface area to mass ratio; however, his results are not applicable to the calculation of the precession rate of a solid spherical satellite which is given here.

This study consists of first obtaining the general analytical expression for aerodynamic torque which is found to depend upon the orientation of the satellite and the accommodation coefficient of the surface. Consideration is then given to the effect of nonuniform distribution of accommodation coefficient and orbital regression effects which cause a change in satellite orientation with time. When these results are applied to the spherical satellite, two conclusions are evident. First, a reasonable adjustment in the initial orbital parameters and satellite orientation can be made so as to reduce the aerodynamic effect to a value acceptable for the relativity experiment. Second, aerodynamic effect can also be

amplified to make possible a direct measurement of the accommodation coefficient of the satellite surface. The feasibility of performing a satellite experiment to measure the accommodation coefficient is investigated.

The obvious advantage the satellite method has over earthbound-laboratory methods of measuring the accommodation coefficient is that the measurements are made under actual orbital conditions.[3,4,5] This advantage coupled with the accuracy and unique simplicity of the proposed satellite provides an experimental method for the study of accommodation coefficients.

5.2. Analysis of Aerodynamic Torque on a Spinning Spherical Satellite

The design parameters of the proposed experiment correspond to a gyro of one foot in diameter, composed of solid glass and spinning at about 100 Hz. These parameters will be used in the analysis to present sample results. Although the satellite is polyhedral in design, it is assumed to be spherical for the purpose of analysis.

The satellite orbit must be restricted to altitudes of less than 1000 miles to produce a measurable relativity effect and also to provide sufficient brightness of reflected sunlight for data collection. This restriction to low orbits allows the assumption that random or thermal motion of gas molecules can be neglected in comparison with the relative velocity of the satellite;[6] therefore, the incident velocity of gas molecules can be taken to be equal to the orbital velocity of the satellite. The assumption of free molecular flow valid above 100 miles can be used in the altitude of interest here.[7]

The aerodynamic forces may be calculated by considering the incident and reflected molecules separately. The reflection of molecules is determined by the accommodation coefficient of the surface. In this analysis the classical Maxwell accommodation coefficient is used in which the accommodation coefficient, α_d, equals the percentage of impinging molecules that are diffusely reflected from the surface after being accommodated to the surface. The remaining percentage, $1 - \alpha_d$, is specularly reflected with no energy accommodation.

The torque caused by gas-surface interactions is analyzed by also considering the specularly and diffusely reflected molecules separately. The resultant force due to a specular reflection is normal to the surface; therefore, for a spherical surface, no torque about the center of mass results from specularly reflected molecules. For the diffusely reflected molecules, the torque is evaluated in the following way. First, the force due to the impingement of the molecule depends on the angle of the surface to the flow and in general causes a torque about the center of mass. After accommodation to the surface, the molecule is diffusely reflected with a velocity component normal to the surface. This component results in only a normal force as required by the definition of diffuse reflection. Since the molecules have been accommodated to the surface, each diffusely reflected molecule has also a component of velocity tangent to the surface and equal to the angular velocity of the surface at the point of reflection. The diffusely reflected molecules thus cause a normal force which produces no torque and a tangential force which produces a torque proportional to the angular velocity of the surface at the point of reflection. It is this mechanism which produces the precessional torque that causes the directional movement of the spin axis.

The coordinate systems to be used in the analysis are shown in Figs. 5.1 and 5.2. The X, Y, Z axis is the inertial set with Z toward Polaris and X along the vernal equinox. The x, y, z coordinate

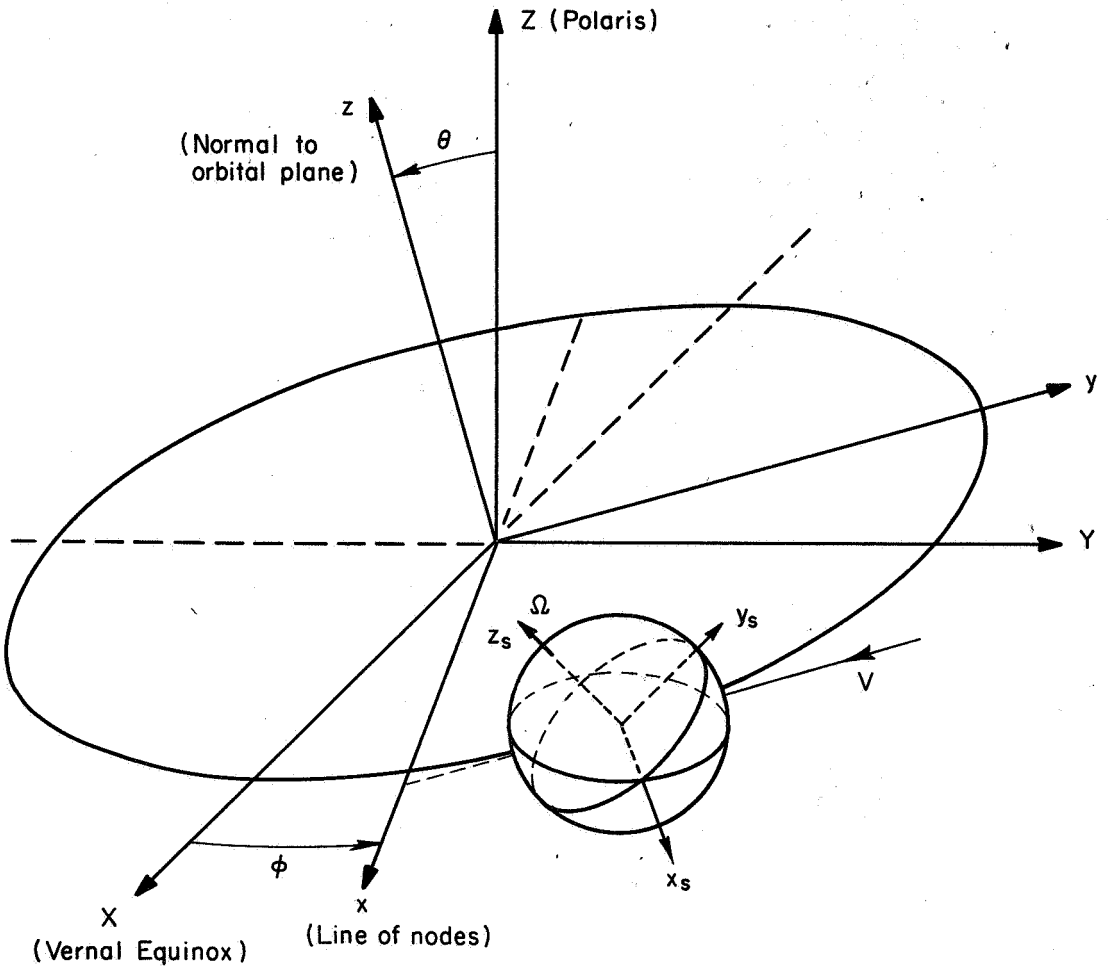

Figure 5.1

Arrangement of Coordinate systems.

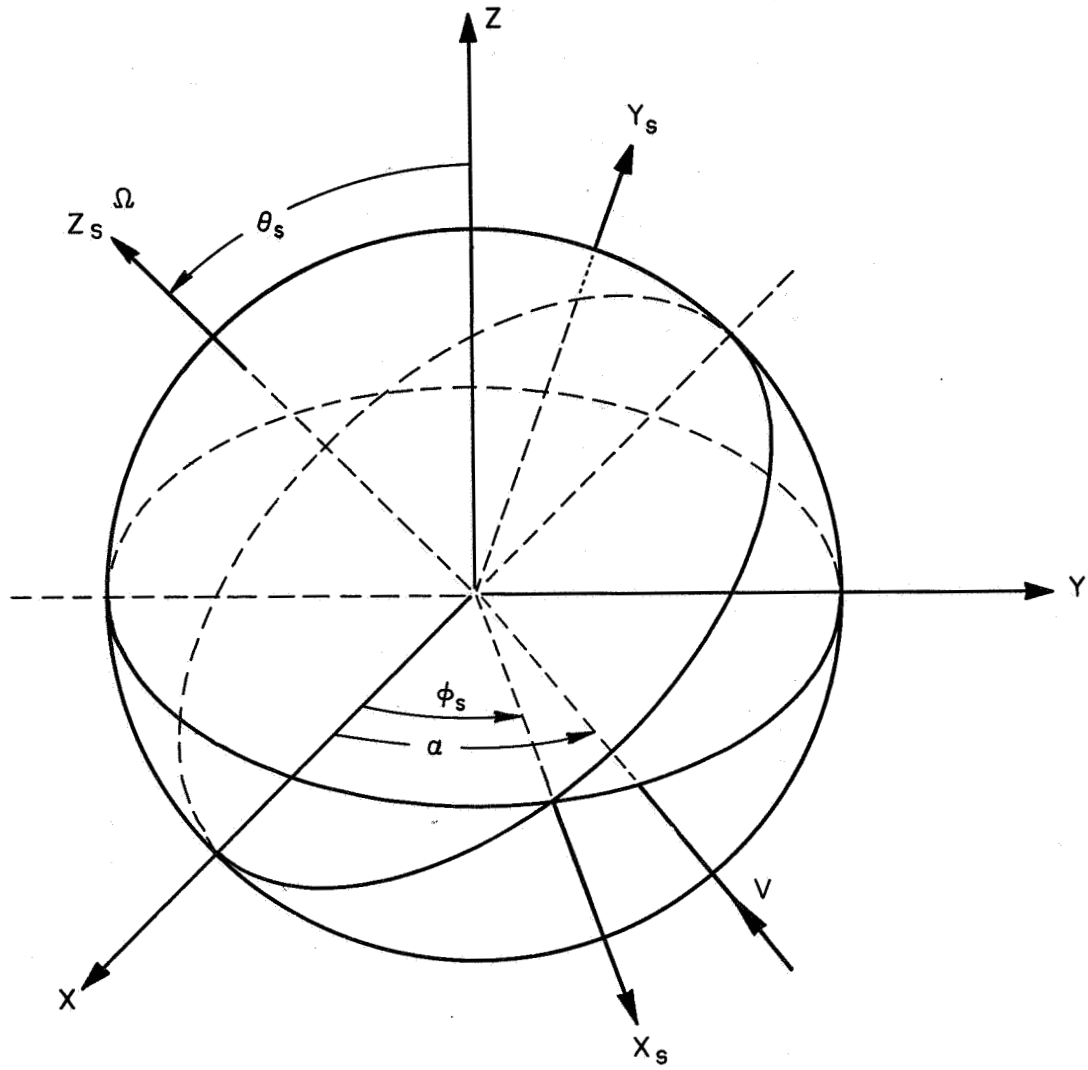

Figure 5.2

Coordinate systems transported to a common origin.

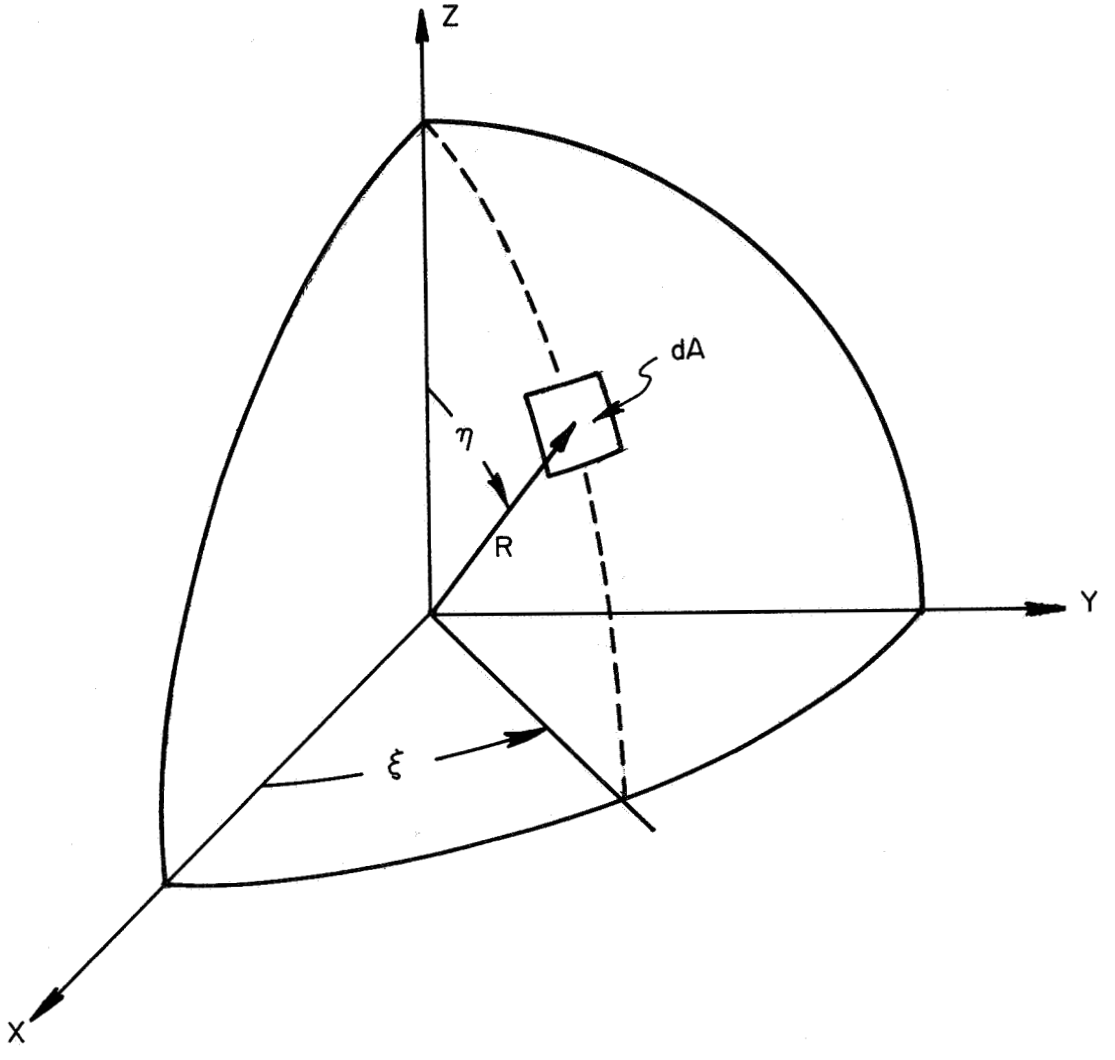

Figure 5.3

Coordinate system used for surface integration.

system is attached to the orbit with the z axis normal to the orbital plane and the x axis as the ascending node of the orbit. The x_s, y_s, z_s set is attached to the gyro and the x_s axis can be thought of as the line formed where the plane normal to the spin axis intersects the orbital plane. i, j, k, and i_s, j_s, k_s are unit vectors along the x, y, z and x_s, y_s, z_s axes respectively. Also shown in the figures is the gas flow velocity vector which is always in the x, y plane and can be thought to rotate about the center of the satellite at the orbital angular velocity. The velocity vector is tangent to the orbital path at all times. Fig. 5.3 illustrates the spherical coordinate system (η, ξ, R) used in the integration over the surface of the sphere.

The mass flux of gas molecules impinging upon an element of surface dA is

$$\rho \bar{V} \cdot \bar{n} \, dA \tag{1}$$

where ρ is the atmospheric density at the orbital altitude, $\bar{V}$ is the velocity vector equal to the orbital velocity, and $\bar{n}$ is the normal to the surface area dA.

Since only the diffusely reflected molecules enter in the torque analysis, we may ignore the specularly reflected ones. The impinging molecules exert a torque

$$- (\bar{R} \times \bar{V}) \, \alpha_d (\rho \bar{V} \cdot \bar{n} \, dA). \tag{2}$$

The reflecting molecules exert a torque

$$\bar{R}\times(\bar{\Omega}\times\bar{R})\ \alpha_d(\rho\bar{V}\cdot\bar{n}\ dA) \tag{3}$$

where $\bar{\Omega}$ is the spin vector of the gyro and $\bar{R}$ is the radius vector to the surface from the center of mass. The elemental torque $d\bar{L}$ produced by the complete interaction is then the sum of the above expressions, i.e.,

$$d\bar{L} = -\alpha_d[\bar{R}\times(\bar{V}-\bar{\Omega}\times\bar{R})(\rho\bar{V}\cdot\bar{n}\ dA)]. \tag{4}$$

Substituting the required vectors and integrating over only the surface in the velocity stream, we obtain the instantaneous torque which reduces to a function of the angles, α, θ_s, ϕ_s as

$$\begin{aligned} L = &-L_o[\sin\theta_s\sin\phi_s(\sin^2\alpha+2)+\sin\theta_s\cos\phi_s(\sin\alpha\cos\alpha)]i \\ &+L_o[\sin\theta_s\sin\phi_s(\sin\alpha\cos\alpha)+\sin\theta_s\cos\phi_s(\cos^2\alpha+2)]j \\ &+3L_o[\cos\theta_s]k \end{aligned} \tag{5}$$

where

$$L_o = \alpha_d\frac{\rho V\pi R^4}{4}\Omega. \tag{6}$$

If we now consider the orbit fixed in inertial space, the problem is similar to the classic top or gyro problem where the torque is defined with respect to a nonmoving frame. To find the resulting motion of the spin axis under the action of the above torque, we must express this torque referred to the x_s, y_s, z_s system. The torque referred to in this system, $\bar{L}_s$ becomes

$$\bar{L}_s = L_o[\sin\theta_s \sin\phi_s \cos\phi_s (\cos^2\alpha - \sin^2\alpha) + \sin\theta_s \sin\alpha \cos\alpha$$

$$(\sin^2\phi_s - \cos^2\phi_s)]i_s$$

$$+ L_o[\sin\theta_s \cos\theta_s \cos^2\phi_s (\cos^2\alpha + 2) + \sin\theta_s \cos\theta_s \sin^2\phi_s(\sin^2\alpha + 2)$$

$$+ 2\sin\theta_s \cos\theta_s \sin\phi_s \cos\phi_s \sin\alpha \cos\alpha - 3\cos\theta_s \sin\theta_s]j_s$$

$$+ L_o[-2\sin^2\theta_s \sin\phi_s \cos\phi_s \sin\alpha \cos\alpha - \sin^2\theta_s \cos^2\phi_s(\cos^2\alpha + 2)$$

$$- \sin^2\theta_s \sin^2\phi_s(\sin^2\alpha + 2) - 2\cos^2\theta_s]k_s \ . \qquad (7)$$

Since the spin rate of the gyro will be much higher than the angular movements of the spin axis, the Euler equations can be simplified by neglecting terms of small magnitude. The precession of the spin axis is then defined by the following:

$$\dot{\theta}_s = \frac{L_{y_s}}{I\Omega} \qquad (8)$$

$$\dot{\phi}_s \sin\theta_s = \frac{L_{x_s}}{I\Omega} \qquad (9)$$

where L_{y_s} and L_{x_s} are the y_s and x_s components of torque respectively, and I is the moment of inertia about the spin axis. The angular displacement for any time t becomes

$$\Delta\theta_s = \int_o^t -\frac{L_{y_s}}{I\Omega}\, dt \tag{10}$$

and

$$\Delta\phi_s = \int_o^t \frac{L_{y_s}}{\sin\theta_s\, I\Omega}\, dt\ . \tag{11}$$

Performing the integration, assuming a circular orbit and considering the trigonometric functions of θ_s and ϕ_s essentially constant during the time of integration, we obtain

$$\Delta\phi_s = 0 \tag{12}$$

$$\Delta\theta_s = \frac{n\pi L_o}{I\,\Omega\,\omega_o} \sin\theta_s \cos\theta_s \tag{13}$$

where n is the number of completed orbits. The movement of the spin axis is a precession causing the spin axis to move into the plane of the orbit if initially out of the plane. However, no precession exists if the spin axis is initially perpendicular to the orbital plane ($\theta_s = 0$) or if the spin axis is in the orbital plane ($\theta_s = \frac{\pi}{2}$). The maximum value of θ_s occurs when $\theta_s = \frac{\pi}{4}$.

Substituting in Eq. (13) the expression for L_o and the moment of inertia I (where I is expressed for a solid sphere of

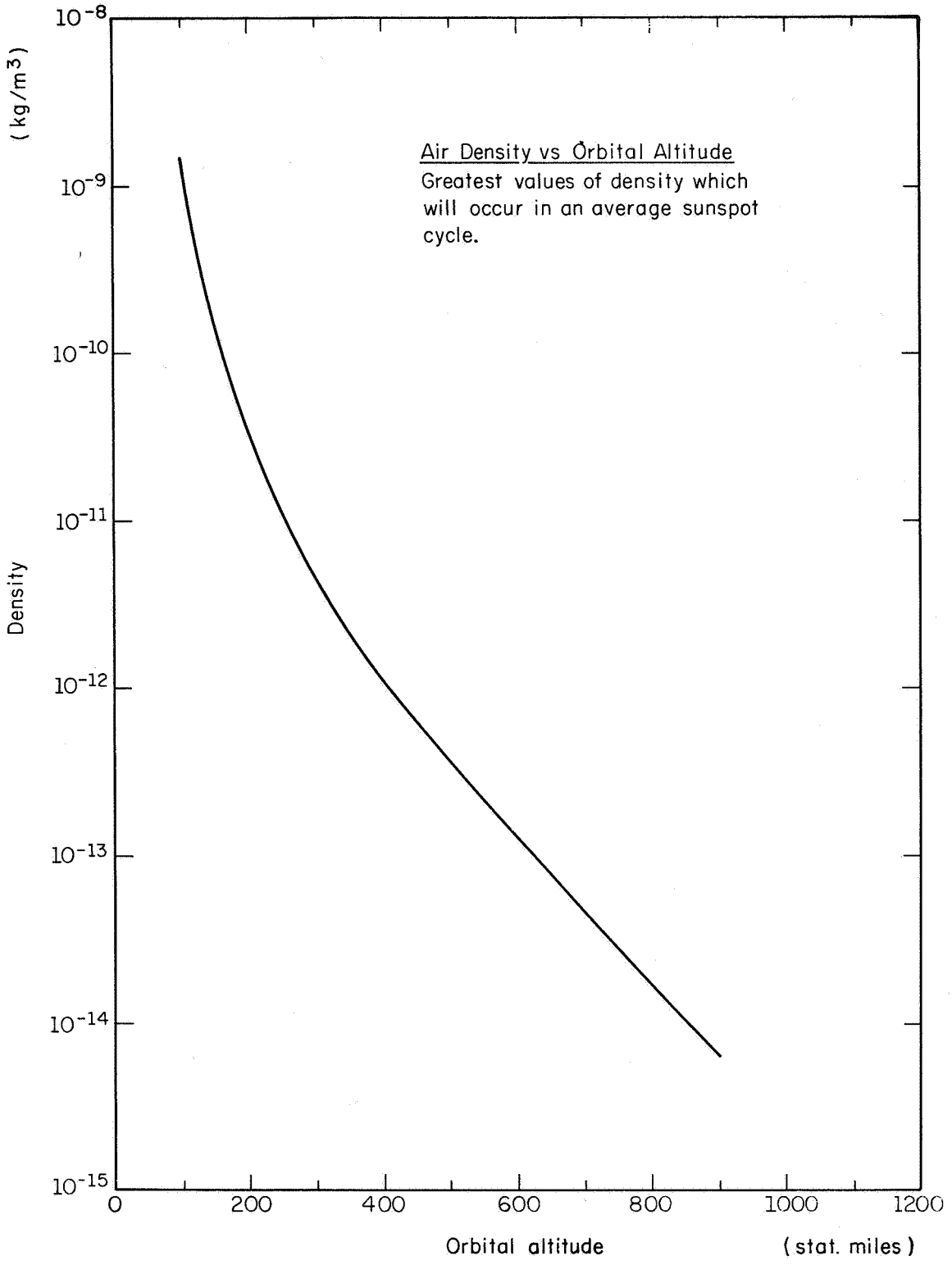

Figure 5.4

Air density vs. orbital altitude.

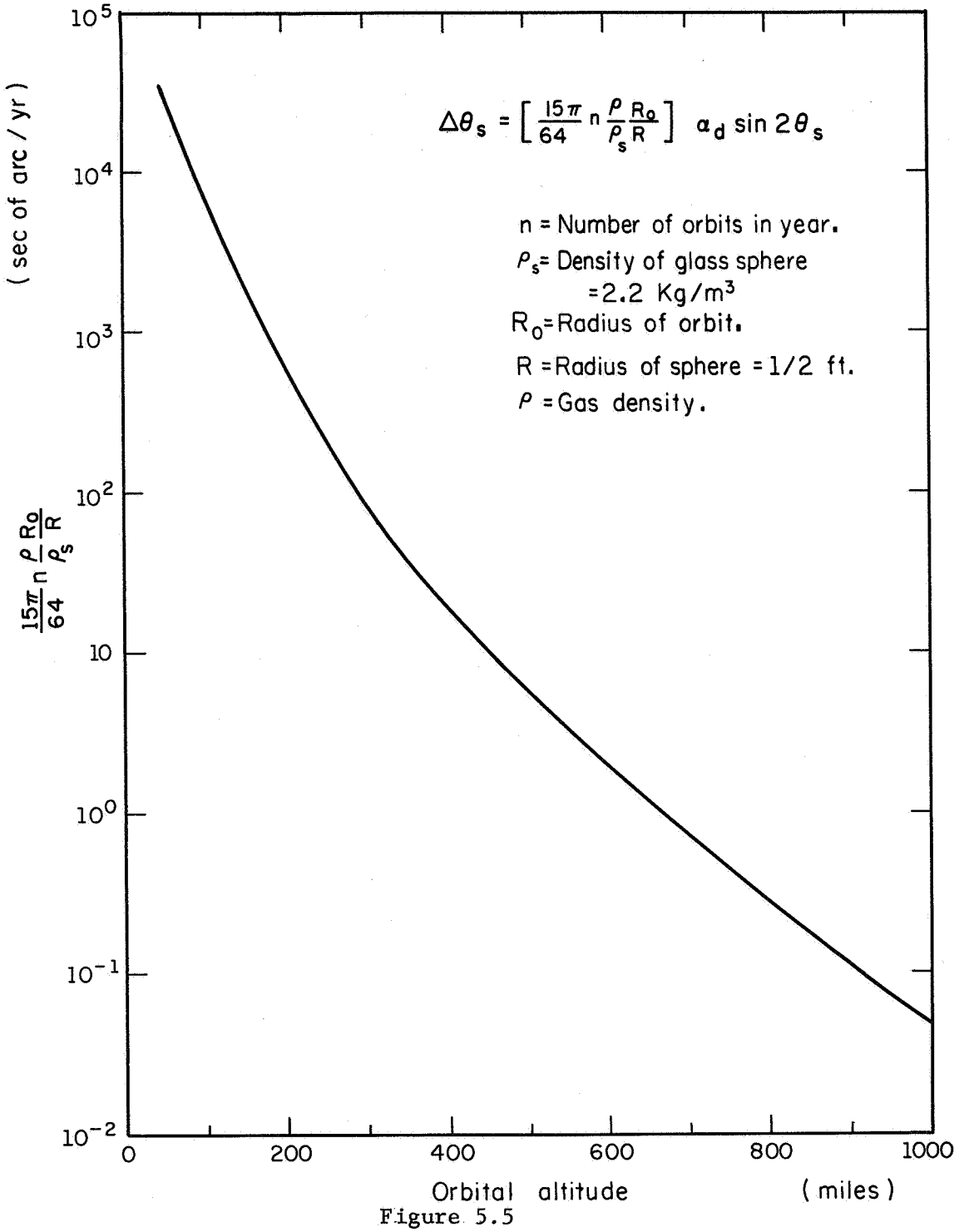

Figure 5.5

Coefficient of precession rate vs. altitude.

material density ρ_s and where the orbital velocity V is expressed as $R_o\,\omega_o$ where R_o is the radius of the orbit measured from the center of the earth), we obtain

$$\Delta\theta_s = n\alpha_d \frac{15\pi}{64} \frac{\rho}{\rho_s} \frac{R_o}{R} \sin 2\theta_s . \tag{14}$$

The final expression which is independent of Ω, is seen to be a function of various parameters but only two, ρ and θ_s, are significant in changing the value of $\Delta\theta_s$. If $87^o < \theta_s < 93^o$ (the spin axis between $\pm 3^o$ of the orbital plane), $\Delta\theta_s$ is reduced by an order of magnitude of its maximum value at $\theta_s = \pi/4$. The effect of atmospheric density is best illustrated by choosing, as a basis for calculation, a solid glass sphere of one foot diameter for which

$$\rho_s = 2.2\times10^3 \text{ kg/m}^3$$

$$R = 1/2 \text{ ft} = 1.5\times10^{-1} \text{m}.$$

The atmospheric density is taken as the maximum occurring during an average sunspot cycle and is plotted in Fig. 5.4.[8] With these values a plot of $\Delta\theta_s/\alpha_d \sin 2\theta_s$ versus orbital altitude is given in Fig. 5.5. The plot shows that the aerodynamic effect can be reduced to less than one sec of arc per year by orbiting the satellite at 600 miles and requiring the spin axis to be within 3^o of the orbital plane.

The magnitude of the aerodynamic effect is directly proportional to the accommodation coefficient of the satellite surface. This parameter can vary between zero and one and its value is dependent upon the surface properties. Most of the experimental data available predicts the accommodation coefficient to be almost one. However, no experimenters have been able to reproduce the orbital environment which requires a very high speed gas flow combined with an almost perfect vacuum. In view of the results obtained shown in Fig. 5.5, the possibility is presented of using a lower orbit to magnify the aerodynamic effect which would, in turn, provide an accurate measurement of the accommodation coefficient under the actual orbital conditions which are so difficult to achieve in the laboratory. A complete discussion of this possibility and the results of this analysis will be presented later.

The slow-down of the satellite spin rate is calculated as follows. The slow-down torque, L_{z_s}, is along the z_s axis and the expression for the slow-down rate from the Euler equation is

$$\dot{\Omega} = \frac{L_{z_s}}{I} \quad . \tag{15}$$

Therefore,

$$\Delta\Omega = \int_o^t \frac{L_{z_s}}{I}\, dt = \frac{n}{I\omega_o} \int_o^{2\pi} L_{z_s}\, d\alpha \quad . \tag{16}$$

Substitution of L_{z_s} from Eq. (7) and integrating

$$\Delta\Omega = \frac{n\pi L_o}{I\omega_o} (5 + \cos^2 \theta_s)$$

and using the substitutions for L_o, V, and I this becomes

$$\frac{\Delta\Omega}{\Omega} = - n \alpha_d \frac{15\pi}{64} \frac{\rho}{\rho_s} \frac{R_o}{R} (5 + \cos^2 \theta_s) . \quad (17)$$

The slow-down rate is seen to be of the order of the precession rate. Substitution of the various parameters at 600 miles yields

$$\frac{\Delta\Omega}{\Omega} \approx 3 \times 10^{-5}. \quad (18)$$

The slow-down effect will therefore be negligible for the altitudes and spin rates to be used in this experiment.

5.3. Consideration of Nonuniform Surface Distribution of Accommodation Coefficient

Effects such as roughing of the surface by dust particles, changing of surface properties due to radiation, and nonuniform heating of the surface could cause changes in the accommodation coefficient with respect to position on the surface of the satellite. To study this problem and the resulting motion of the satellite spin axis, we consider the satellite so oriented that the positive spin vector is directed towards the sun and assume that the spin axis lies in the plane of the orbit.

Under the above conditions, one-half the surface area of the satellite is in sunlight while the other half is not (see Fig. 5.6). The surface in the sunlight will then have a higher temperature than that not in sunlight. It may be assumed then that the effect of the nonuniform heating is to cause one-half the surface to have one accommodation coefficient α_d', and the other half to have accommodation coefficient α_d''. Since the spin axis is in the plane of the orbit, the satellite presents different parts of its surface to the velocity stream. At some points in its orbit the satellite presents both "hot" and "cold" surfaces to the velocity stream while at other points only a "hot" or a "cold" surface is subjected to molecular impingement. In view of the aerodynamic torque analysis presented earlier,[9] there is no torque about the spin axis when only a "hot" or a "cold" surface is exposed to the velocity stream (and the spin axis in the plane of the orbit). However, when both "hot" and "cold" surfaces are exposed to the velocity stream a torque will occur.

Since the spin axis is in the plane of the orbit and pointing towards the sun, the satellite must pass through the shadow of the earth. Assume that while the satellite is in the earth's shadow the temperature reaches an equilibrium value at all points on its surface. During the period the satellite is in the shadow, no aerodynamic torque acts on the spin axis. By referring to Fig. 5.6, we can visualize a net torque acting on the satellite spin

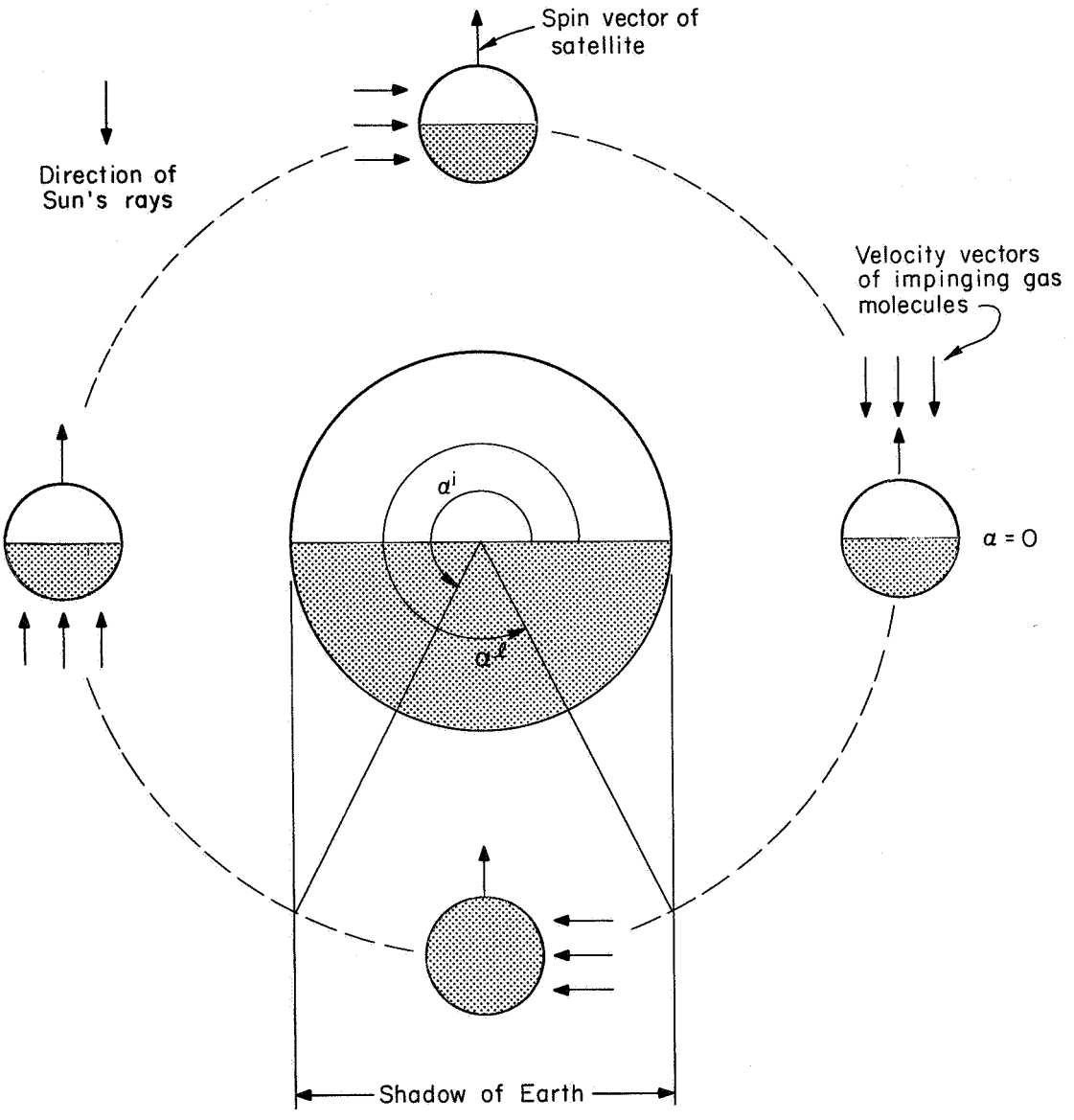

Figure 5.6

Diagram of nonuniform solar heating effect for satellite in equatorial orbit.

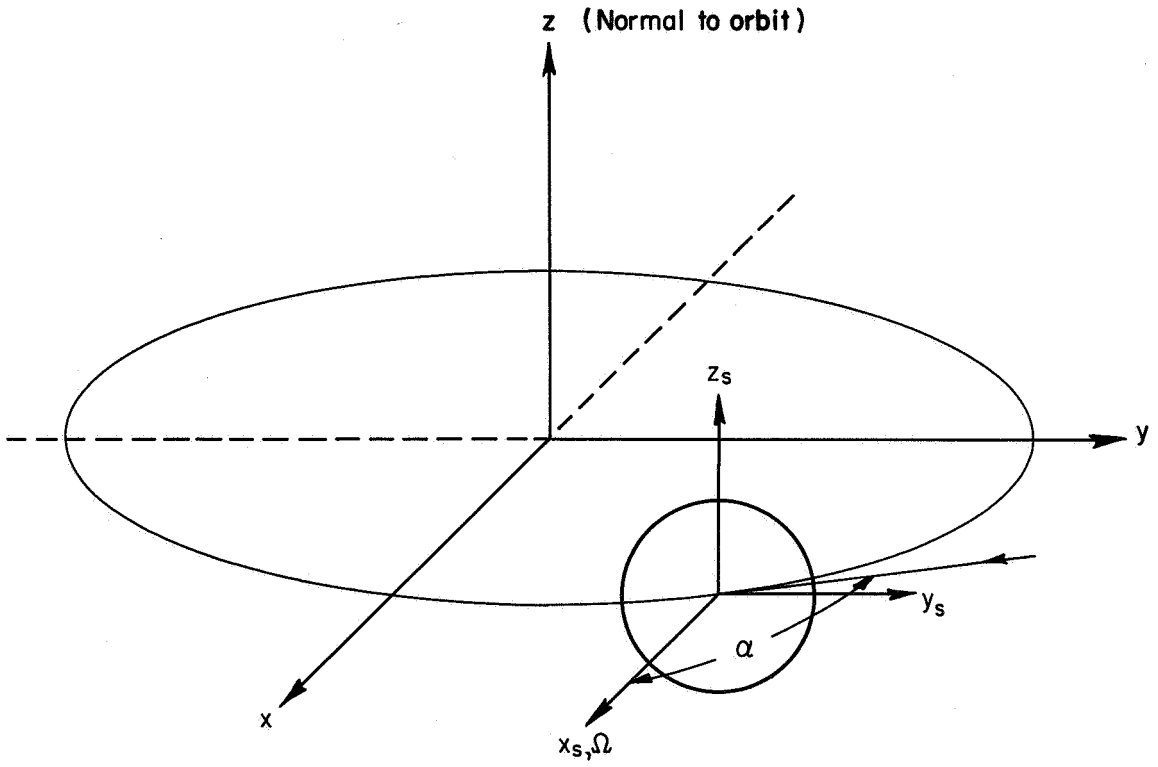

Figure 5.7

Coordinate system used for
nonuniform heating analysis.

axis every complete orbit. A significant angular displacement could occur after 10^3 such orbits in a year's time.

As before, the specularly reflected molecules do not enter into the torque analysis.[10] There are now two expressions for the elemental torque

$$d\bar{L} = -\alpha_d[\bar{R}\times(\bar{V} - \bar{\Omega}\times\bar{R})(\rho\bar{V}\cdot\bar{n}\,dA)] \tag{19}$$

(α_d' must be used for molecules impinging on one-half the surface area and α_d'' for the other where α_d is the accommodation coefficient), $|\bar{R}|$ is the radius of the satellite, $\bar{V}$, the orbital velocity, $\bar{\Omega}$ the satellite spin rate and ρ the gas density.

The coordinate systems (Fig. 5.7) have been set up so that the instantaneous torque on the satellite referred to the fixed inertial frame of the orbit has the same components when referred to the coordinates fixed with respect to the satellite; therefore, the result of integration of Eq. (19) can be applied directly to the Euler equations to find the precession. To describe the motion of the satellite under the action of this torque we introduce the reference angles ϕ_s and θ_s. Let θ_s be the angle between the normal to the orbit, z, and the spin axis, x_s. Initially then, $\theta_s = \frac{\pi}{2}$. Let ϕ_s be the angle between the line of nodes of the orbit, x, and the rising node of the satellite with respect to the orbit plane, y_s. Therefore, $\phi_s = \frac{\pi}{2}$ initially. The motion of the coordinate system attached to

the satellite is defined by

$$\omega_{x_s} = -\dot{\phi} \cos\theta$$

$$\omega_{y_s} = \dot{\theta} \tag{20}$$

$$\omega_{z_s} = \dot{\phi} \sin\theta .$$

With the usual assumption that the spin rate is much larger than $\bar{\omega}_s$, the Euler equations may be simplified as follows

$$L_{x_s} = I\,\dot{\Omega}$$

$$L_{y_s} = I\,\Omega\,\omega_{z_s} = I\,\Omega\,\dot{\phi}\sin\theta_s = I\,\Omega\,\dot{\phi} \tag{21}$$

$$L_{z_s} = -I\,\Omega\,\omega_{y_s} = -I\,\Omega\,\dot{\theta}_s .$$

The angular precession can now be found from

$$\Delta\phi_s = \int_o^t \frac{L_{y_s}}{I\Omega}\,dt = \int_o^\alpha \frac{L_{y_s}}{I\Omega}\,\frac{d\alpha}{\omega_o} \tag{22}$$

and

$$\Delta\theta_s = -\int_o^t \frac{L_{z_s}}{I\Omega} = -\int_o^\alpha \frac{L_{z_s}}{I\Omega}\,\frac{d\alpha}{\omega_o} \tag{23}$$

where ω_o is the orbital angular velocity and is a constant for a

circular orbit. Performing the integration of Eqs. (22) and (23) after substituting the expressions for L_{y_s} and L_{z_s} given from integration of Eq. (19) we obtain, for one complete orbit,

$$\Delta\phi_s = \frac{\pi}{4} \frac{\rho V R^4}{I \omega_o} \frac{R_e}{R_o} (\alpha_d' - \alpha_d'') \tag{24}$$

$$\Delta\theta_s = -\frac{1}{3} \frac{\rho V^2 R^3}{I\Omega \omega_o} (\alpha_d' - \alpha_d'')(\pi - 2\beta_s + \sin 2\beta_s) \tag{25}$$

where

$$\beta_s = \cos^{-1} \frac{R_e}{R_o} .$$

Substituting into these equations the expressions for the moment of inertia of a sphere, $I = \frac{8}{15} \rho_s \pi R^5$, and the velocity of the satellite $V = R_o \omega_o$, we obtain

$$\frac{\Delta\phi_s}{\alpha_d' - \alpha_d''} = \frac{15}{32} \frac{\rho}{\rho_s} \frac{R_e}{R} \tag{26}$$

and

$$\frac{\Delta\theta_s}{\alpha_d' - \alpha_d''} = \frac{15}{24} \frac{\rho}{\rho_s} \frac{\omega_o}{\Omega} \frac{R_o^2}{R} \frac{\pi - 2\beta_s + \sin 2\beta_s}{\pi} \tag{27}$$

where

$$\beta_s = \cos^{-1} \frac{R_e}{R_o} .$$

Since the orientation of the satellite spin axis with respect to the sun will change due to the motion of the earth about the sun, Eqs. (26) and (27) give the maximum angular displacement of the spin

axis that can occur in one orbit. One-quarter of a year after the spin axis was pointing at the sun, the position of the earth in its orbit will cause the satellite spin axis to be normal to the sun's rays. The accommodation coefficient will then be of constant value at all points on the surface because the satellite will have reached an equilibrium temperature at all points on the surface. $\Delta\theta_s$ and $\Delta\phi_s$ will be zero for one orbit since $(\alpha'_d - \alpha''_d) = 0$. To obtain the actual variation of $\Delta\theta_s$ and $\Delta\phi_s$ throughout the year would require knowledge of the variation of temperature distribution and accommodation coefficient which is not available. This variation is approximated by assuming $\Delta\theta_s$ and $\Delta\phi_s$ to decrease or increase linearly from its maximum value to zero in one-quarter year. From the plot of the known points shown in Fig. 5.8 one can easily determine that the total integrated angular displacement for one year would be zero; however, the maximum deflection from an initial value of zero would be large and measurable. This value is just the integrated angular deflection for the half year when $\Delta\theta_s$ and $\Delta\phi_s$ start from zero values, pass through the maximum and back to zero. This integral is approximated as the area of an equilateral triangle with base of 1/2 year and having vertices at the known points seen in Fig. 5.8,

$$(\phi_s \text{ or } \theta_s)(\text{maximum}) = \left(\frac{\text{number of orbits in 1/2 year}}{2}\right)\left(\frac{\Delta\theta_s \text{ or } \Delta\phi_s}{\text{one orbit}}\right).$$

A plot of the maximum total angular precession is given in Fig. 5.9

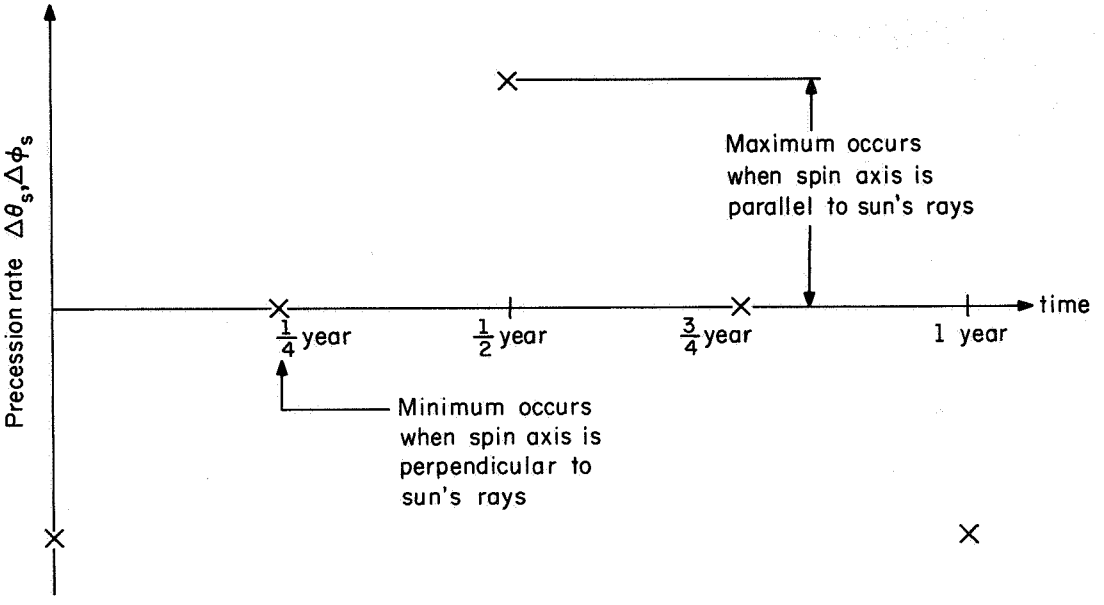

Figure 5.8

Diagram of known precession rate values during one year due to nonuniform heating.

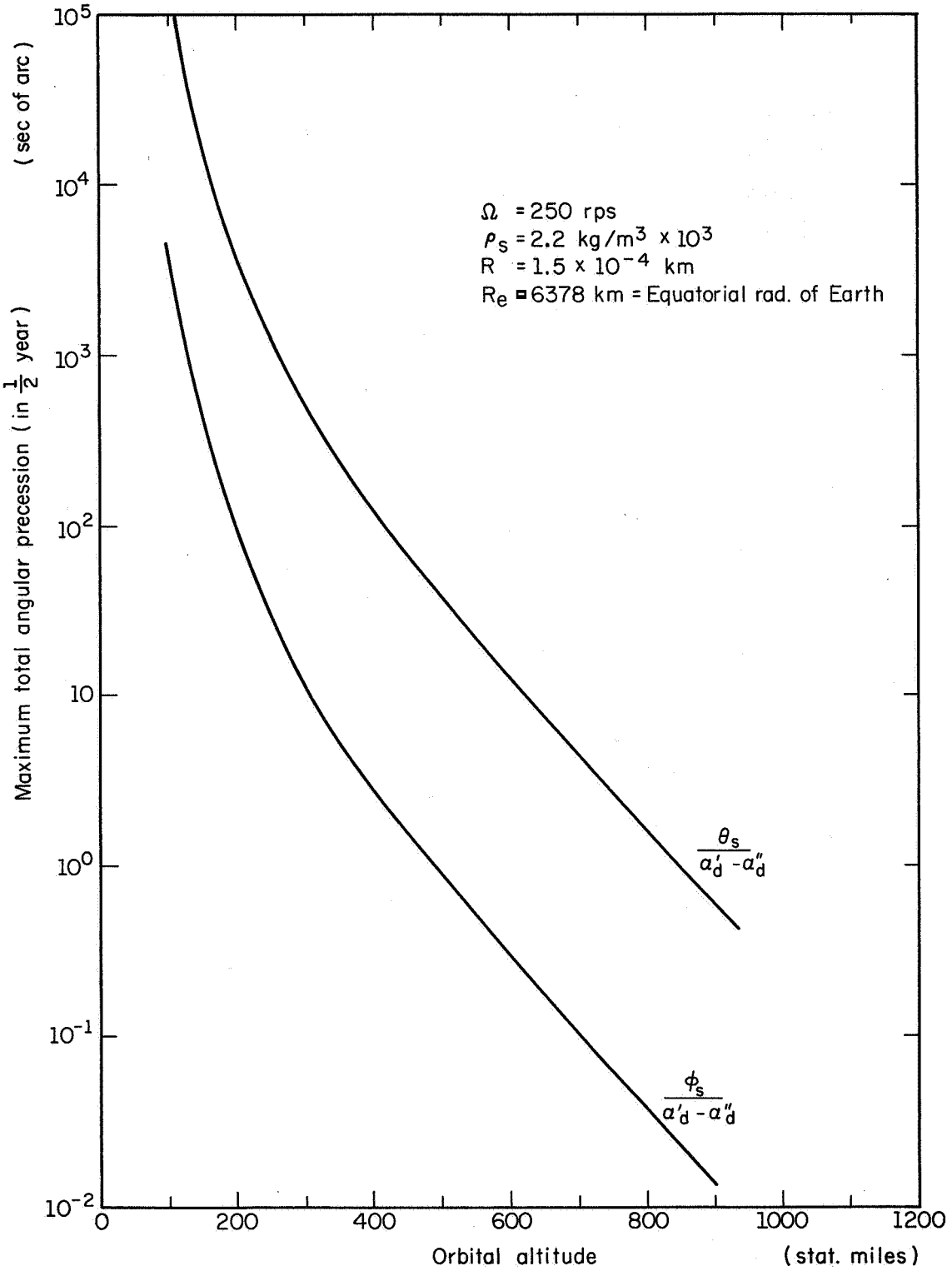

Figure 5.9

Aerodynamic precession due to
nonuniform solar heating vs. altitude.

where for purposes of calculation the spin rate, Ω, material density, ρ_s, and radius, R, of the gyro were taken to be 250 Hz., 2.2×10^{3} kg/m^3 and 1.5×10^{-4} km, respectively.

From Fig. 5.9 it is seen that the nonuniform solar heating effect could be significant at even 600 miles if the accommodation coefficient difference is largely due to the temperature difference. Fortunately, experimental data predicts an extremely small change in accommodation coefficient with temperature, if any at all. Very little work has been done in this area and valid experimental evidence of the dependence of accommodation coefficient on surface temperature is not readily available. An experiment by J. K. Roberts (1932) shows an increasing thermal accommodation coefficient with temperature of

$$\frac{\Delta\alpha}{\Delta T_w} \approx \frac{.01}{50^{\circ}C}$$

where T_w is the temperature of the surface. Some of the more reliable later experiments on thermal accommodation coefficient indicate a much smaller change of[11]

$$\frac{\Delta\alpha}{\Delta T_w} \approx \frac{.001}{50^{\circ}C} .$$

One study of normal momentum transfer by R. E. Stickney and F. C. Hurlbut show no change of accommodation coefficient with temperature;[12] however, their results with respect to temperature effect are not accurate enough to reveal a $\Delta\alpha/\Delta T_w$ of less than $.01/50^{\circ}C$.

If we take into account the experimental work that has been done on the temperature dependence of accommodation coefficient, it appears that the nonuniform heating at 600 miles altitude will not be detrimental to the relativity experiment.

We consider next the motion of the spin axis if the difference in accommodation coefficient is due to a distribution of surface roughness or other surface properties. Analogous to nonuniform heating analysis, we consider one-half the spherical surface to have a surface property such that its accommodation coefficient is α_d' and then the other half sphere to have a different surface property such that its accommodation coefficient is α_d''. If we assume the spin axis to be in the plane of the orbit, the equations of motion of the spin axis are the same as those for the nonuniform heating case with one notable exception. In the nonuniform heating case the accommodation coefficient difference went to zero when the satellite was in the earth's shadow. In the nonuniform surface property case the accommodation coefficient difference never goes to zero. When the integration over one orbit is evaluated, the expression for torque integrates to zero and no finite integrated motion could be observed for one orbit. The torque is also zero if one considers the spin axis to be in the plane which separates the two half-spheres having different accommodation coefficients.

From the discussion and calculated results for the nonuniform surface property effect, we conclude that the torque arising from a localized accommodation difference (such as a small area damaged by a meteoroid) would be much less than that resulting from the nonuniform

heating case, and therefore, the localized accommodation coefficient differences would be negligible in comparison to the torques resulting from other effects. This conclusion is also substantiated by the work of R. D. Palamara, who studied the effect of localized accommodation coefficient differences and arrived at the result that the maximum periodic precession would be less than 4.6×10^{-4} sec of arc per unit radian from variation in α_d on a surface element dA.[13]

5.4. Effect of Regression of Orbit on Satellite Motion

In the above analysis of drag, the satellite orbit has been assumed fixed in inertial space. In general, earth orbits are regressing orbits because the earth itself is not a perfect sphere. The principal effect of orbital regression is to change the orientation of the satellite with respect to the orbital plane. Since the aerodynamic torque depends upon this orientation, orbital regression will effect the motion of spin axis of the satellite as seen by an earth based observer. Also, if it is desirable to maintain a specific orientation of the satellite with respect to the orbital plane (say to maximize or minimize a torque), an orbital regression analysis must be made to determine the orbital parameters needed. For completeness the effect of regressing orbit is analyzed and sample results obtained to indicate the spin axis motion.

The general equation for precession can be found but there

are many different solutions possible depending upon the initial conditions on ϵ and ϕ, the Euler angles of the satellite spin axis with respect to an earth based inertial coordinate system, and the initial conditions on i and ϕ, the orbital inclination and angle of nodes, respectively. To illustrate the type of solutions expected when orbital regression is included, the near equatorial orbit will be used as an example. Then

$$\sin i \approx i$$

$$\cos i \approx 1 \ .$$

Also, require the spin axis to be nearly in the orbital plane, that is, let

$$\epsilon = \frac{\pi}{2} + \delta_e$$

where δ_e is a small angle. Then

$$\sin \epsilon \approx 1$$

$$\cos \epsilon \approx - \delta_e \ .$$

By using these assumptions in the general precession equations and neglecting terms of order higher than i or δ_e, we obtain the expression for precession for n orbits of

$$\Delta\epsilon = n \alpha_d \frac{15\pi}{64} \frac{\rho}{\rho_s} \frac{R_o}{R} \left[\mp \frac{2}{\dot{\Phi}T} i \sin \dot{\Phi}T - 2\delta_e\right] \qquad (28)$$

where ρ/ρ_s is the ratio of gas density to satellite material density, $\frac{R_o}{R}$ is the ratio of orbital radius to satellite radius, $\dot{\Phi}$ is the orbital regression rate and T is the elapsed time from the initial conditions.

The coefficient of the bracketed term is the same as found for the non-regressing orbit analysis and is plotted in Fig. 5.5. In fact, the second term

$$n\,\alpha_d\,\frac{15\pi}{64}\,\frac{\rho}{\rho_s}\,\frac{R_o}{R}\,(-2\delta_e)$$

is exactly the result one would expect if the orbit was non-regressing and $\theta_s = \frac{\pi}{2} + \delta_e$. The effect of regression is thus seen to add an oscillating term having the orbital regression frequency and magnitude dependent upon the orbital inclination.

At 600 miles for a solid glass satellite of one-foot diameter and time equal to one year

$$n\,\alpha_d\,\frac{15\pi}{64}\,\frac{\rho}{\rho_s}\,\frac{R_o}{R} \simeq 2\,\alpha_d \text{ sec arc}$$

$$\dot{\Phi} = 35\,\frac{\text{rad}}{\text{year}}$$

$$T = 1 \text{ year.}$$

Then, letting $\sin \dot{\Phi}T$ be maximum ($\pm$ 1), we have

$$\frac{\Delta\epsilon}{\alpha_d} \simeq 2[-2\,\delta_e \pm .056\,i]\text{arc sec.} \qquad (29)$$

This result shows that the effect of orbital regression for the condition used is small if δ_e is the same order as i. If i is allowed to be an order of magnitude greater than δ_e, the orbital regression effects could be of the same order as the aerodynamic effect.

The most important conclusion drawn from these results is that when orbital regression is included in the analysis, the results will be separable into two parts. One term will be of the same type as for the non-regressing orbit. The other part of the solution will contain terms of the orbital regression frequency. These last terms cannot in general be neglected because they will depend upon the orbital parameters and be of various magnitudes. Also, if it is desired to keep the spin axis fixed with respect to the orbital plane, the regression results will give the accuracy required on i, ϵ, and ϕ to retain a certain initial orientation.

5.5. Aerodynamic Effect on the Relativity Experiment

The experiment proposed to measure a general relativity effect consists of measuring the angular displacement of the satellite spin axis from its original position after a one-year period of time. The predicted angular displacement due to the relativity effect alone is 5 to 7 sec of arc per year. It is desirable in regard to the relativity experiment to reduce the aerodynamic effect to a value of

at least less than one-tenth the predicted relativity effect. From the results calculated in this report, the reduction of the aerodynamic effect is possible providing proper satellite orientation is maintained. Figure 5.5 shows that if the satellite is orbited at an altitude of 600 miles or more and the spin axis is restricted to lie within 3^{o} of the orbital plane, then an angular displacement of less than .2 sec of arc per year is to be expected. These are reasonable requirements since the experiment requires the spin axis to be nearly in the plane of the orbit to produce the relativity effect. The 600 mile altitude limitation is approximately the altitude originally proposed for the experiment and has since served as one of experimental parameters.

The nonuniform heating analysis was considered to be of importance to the relativity experiment because if an equatorial orbit were used there would be very little that could be done to prevent nonuniform heating of the surface of the solid satellite. The results shown in Fig. 5.9 indicate that nonuniform heating should not be of importance if the available experimental work on accommodation coefficient change with temperature can be relied upon. Taking the maximum $\Delta\alpha/\Delta T_N$ as $.01/50^{o}$ and assuming a pessimistic value of 50^{o} change in temperature, the precession rate at 600 miles due to nonuniform heating is less than .2 sec of arc per year. Therefore, the use of the equatorial orbit for the relativity experiment is permissible from aerodynamic considerations.

The orbital regression analysis is of importance because from it the orbital parameters are determined which allow the spin axis to remain relatively fixed with respect to the orbital plane. The fixing of the spin axis to the orbital plane for a period of a year is necessary not only to reduce the aerodynamic effect but also to maximize the relativity effect and minimize gravity gradient precession. Therefore, the requirement of near zero orbit inclination for the case of an equatorial orbit is compatible with the relativity experiment. This compatibility is to be expected for either the polar or equatorial orbits and the various initial conditions possible.

It can then be concluded that the aerodynamic effects can be reduced to less than one-tenth the relativity effect by orbiting at 600 miles or above and requiring the spin axis to be within 3^{o} of the orbital plane.

5.6. Measurement of Accommodation Coefficients and Atmospheric Gas Density

The results of the above analysis at low orbital heights have lead to a feasibility study for utilizing the aerodynamic effect to measure accommodation coefficients and atmospheric gas density. The inclusion as one of the primary objectives, that of the measurement of atmospheric density appears, at first, to be repetitious of the numerous orbital drag measurements of the past. However, after investigating

the parameters which influence the drag of a body in free-molecular flow, it is found that the conversion of aerodynamic drag to atmospheric density is not at all well known. (See, for example, ref. 15) In fact, the density values reported at present could be as much as 40% in error. This error in density is unimportant for the relativity experiment but is very important for low altitude satellites and reentry vehicles. The unknown quantity in drag measurement is the drag coefficient C_D. Drag is given by

$$D = C_D \tfrac{1}{2} \rho V^2 \bar{A} \tag{30}$$

where ρ is the atmospheric density, V the velocity of the satellite and $\bar{A}$ is a suitable reference area. The drag coefficient of a satellite is found to be strongly dependent upon the gas surface interaction parameters. For example, for a sphere

$$C_D \approx 2 + \frac{8}{9} \alpha_d (1-\alpha_T)^{\frac{1}{2}} \tag{31}$$

where α_d is the momentum accommodation coefficient as defined before. The thermal accommodation coefficient α_T is defined as

$$\alpha_T = \frac{T_w - T_i}{T_r - T_i} \tag{32}$$

where T_i is the temperature of the incident molecules, T_r the temperature of the diffusely reflected molecules, and T_w the temperature of

the satellite surface.

The plot of equation (31), Fig. 5.10, shows that the drag coefficient of a sphere can range from 2.0 to 2.89 depending upon the values for α_d and α_T. For drag measurements in the past, a value of 2.2 has been assumed which could lead to as much as 25% error in the density determination. Equations could be shown for cylinders, flat plates, cones, etc., in which errors as high as 40% are possible.

From the above discussion we see that an accurate measurement of the accommodation coefficients α_d and α_T would provide the information necessary to determine the density accurately. Unfortunately, there is no knowledge of these coefficients at the incident energies associated with near earth satellites. (See, for example ref. 16) The energy range of interest for satellite application is between 1 and 10 ev. and it is precisely this energy range in which no laboratory experiment has been able to obtain measurements with neutral molecular beams. In fact, none of the methods now in use to generate neutral molecular beams are believed capable of obtaining accurate data in the 1.0 to 10 ev. range. There will undoubtedly be methods developed in the future but these are believed to be as much as five or more years off.

The only state-of-the-art means of obtaining high energy molecular beams is then the satellite itself. Therefore, the experiment we propose will use the satellite velocity to generate the molecular beam. The results of the experiment will have immediate

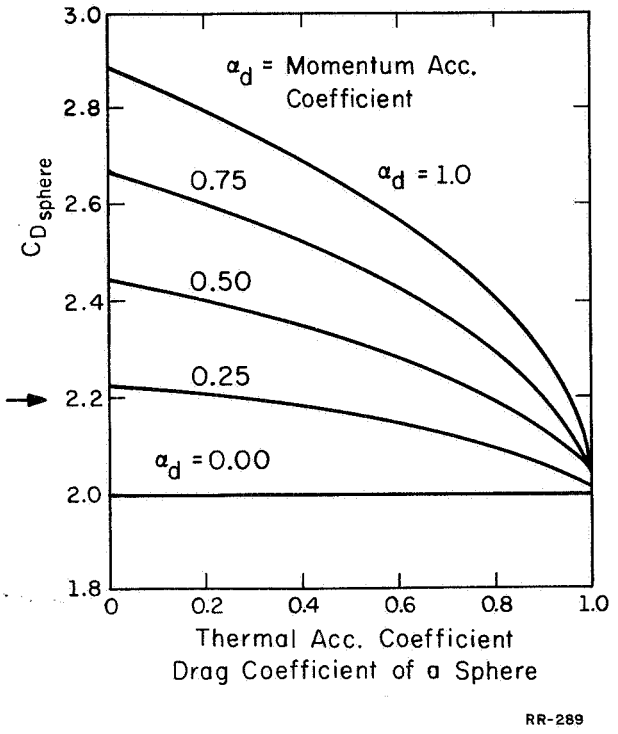
3.0
2.8
2.6
2.4
2.2
2.0
1.8
$C_{D\,sphere}$
α_d = Momentum Acc. Coefficient
α_d = 1.0
0.75
0.50
0.25
α_d = 0.00
0
0.2
0.4
0.6
0.8
1.0
Thermal Acc. Coefficient
Drag Coefficient of a Sphere
RR-289

Figure 5.10

engineering application to satellite and re-entry design analysis. Moreover, the experiment will be the first measurement of the accommodation coefficients ever performed in this energy range and would lead to a much greater understanding of the basic gas-surface interaction phenomena.

5.6.1. Theoretical Basis

5.6.1.1. Primary objectives

As a spinning satellite travels through the rarefied atmosphere it is acted upon not only by the drag force which changes the period of the orbit, but also by an aerodynamic torque. The aerodynamic torque can, in general, be divided into perpendicular and parallel components to the spin axis of the spin stabilized satellite. The torque parallel, T_{11}, causes slow down of the spin rate, while the perpendicular component of torque, $T_{\perp}$, causes precession of the spin axis in inertial space. Using the read-out system proposed by C.S.L., both the precession and spin rate of a passive satellite can be measured to high accuracy by using the sunlight reflected from mirrors on the satellite surface. Therefore, there are three measurable quantities of a passive spinning satellite; drag, T_{11}, and $T_{\perp}$.

In ref. 10, Karr has demonstrated that even a fully spherical satellite would have torque components both along and

perpendicular to the satellite spin axis of the form.

$$T_{\perp} = K_1 \alpha_d \rho$$

$$T_{11} = K_2 \alpha_d \rho$$

where K_1 and K_2 are constants dependent upon the size and weight of the sphere. The torque is seen to depend only upon the momentum accommodation coefficient and density and is independent of the thermal accommodation. The drag of a satellite, as mentioned before, is dependent upon α_d, α_T, and ρ. Since, for a spherical satellite, $T_{\perp}$ and T_{11} are proportional, a satellite of this shape is not suitable for measuring the proposed parameters independent of the gas density.

However, consider as an example a satellite composed of a cone and a sphere spinning about the axis of the cone. In general the measurable quantities for such a satellite will be of the form

$$\begin{aligned} D &= A_1 \rho + A_2 \alpha_d \rho + A_3 \alpha_d \rho \sqrt{1-\alpha_T} \\ T_{\perp} &= B_1 \rho + B_2 \alpha_d \rho + B_3 \alpha_d \rho \sqrt{1-\alpha_T} \\ T_{11} &= C \alpha_d \rho \end{aligned} \tag{33}$$

where the coefficients A, B, and C are known constants dependent

upon the shape, angle of attack, size and density of the satellite. The above equations must be independent for a solution to exist. This requirement of independence is expressed by the following relationship of the coefficients.

$$A_1 B_3 \neq A_3 B_1$$

This requirement is met for an appropriately orientated cone-sphere combination but is not met, as would be expected, for a sphere alone. Further, the magnitude of $(A_1 B_3 - A_3 B_1)$ is found to be of importance because of its relationship to the accuracy of the measurement of ρ, α_d, and α_T. In general, the larger the value of $(A_1 B_3 - A_3 B_1)$ the better the accuracy of the experiment. In a preliminary analysis, the cone-sphere combination was found to yield satisfactory experimental accuracy of the order of the accuracy of the drag and precession measurements. One of the purposes of the proposed study will be to find the satellite shape which will yield the best experimental accuracy.

5.6.1.2. Secondary objectives

Since ρ, α_d, and α_T can be determined accurately, the change in these parameters with time, if there is a change, could also be measured. In the early part of the experiment the degassing or desorption of adsorbed gases on the surface would most likely influence the accommodation coefficients. The change in these coefficients with time can be related to the degassing and desorption

rate of the surface which has not been measured for satellite surfaces.

If the satellite were orbited in high eccentricity orbit, the perigee point would travel through various altitudes and positions around the earth. The density could then be mapped from the date provided by the satellite. The accuracy of the data is, however, reduced because of the limited amount of time in which measurements can be made under approximately constant conditions.

If the orbit is high enough so that the lifetime of the satellite is not too short, the roughening of the surface by meteorites would cause a change in the accommodation coefficients with time. This effect would most likely occur long after the degassing and desorption effects, if indeed, degassing takes place at all.

5.6.2. Feasibility

The feasibility of performing an experiment of this type has been shown and there are no engineering problems beyond the present state of space technology. C.S.L. has determined that a passive sphere could be used where the spin axis precession could be determined to less than a sec of arc per year. The data for the measurement are obtained from sunlight reflected to a terrestial observer by mirrors placed on the satellite's surface. The spin rate is easily determined from the frequency of the flash of sunlight from the mirror. For an aerodynamic measurement, Karr found that the precession rate is well above 100 sec of arc per year for

spherical satellites. (See Fig. 5.5). A composite body satellite, such as the cone and sphere combination will yield precession rates of the order of 500 sec. of arc per month.

Therefore, using a single passive spinning satellite, the following three measurements can be made by the technique developed at the Coordinated Science Laboratory.

(1) Atmospheric drag

(2) Spin slow down rate

(3) Spin axis precession rate

From these three measurements, the following three parameters of prime importance for accurate orbital and re-entry analysis can be determined:

(1) The momentum accommodation coefficient of the satellite surface.

(2) The thermal accommodation coefficient of the satellite surface.

(3) The absolute orbital gas density.

In addition to the above principle objectives of the proposed satellite experiment, the following quantities of secondary importance could also be measured.

(1) The desorption and degassing rate of the satellite surface.

(2) Orbital gas density at various orbital altitudes.

(3) The change in accommodation coefficients with roughing of the surface by meteorites.

1. Palamara, R. D., Synthesis of a General Relativity Experiment (Thesis), June 30, 1964, pp. 53-74.

2. Po, Nan Tum, "On the Rotation Motion of a Spherical Satellite Under the Action of Retarding Aerodynamical Moments," NASA TTF-9630, January 22, 1965.

3. Evans, William J., "Aerodynamic and Radiation Disturbance Torques on Satellites Having Complex Geometry," Torques and Attitude Sensing in Earth Satellites, ed. S. Fred Siner. 1964, p. 85.

4. Wachman, Harold Y., "The Thermal Accommodation Coefficient: A Critical Survey," ARS Journal 32, January, 1962, p. 11.

5. McKeowan, "Surface Erosion in Space," Rarefied Gas Dynamics, Ed. J. A. Laurman, Supplement 2, Vol. I, 1963.

6. Wachman, op. cit., p. 2.

7. Evans, op. cit., p. 83.

8. National Aeronautics and Space Administration, Orbital Flight Handbook, NASA Sp 33, Part 1, 1963, p. II 34.

9. Karr, G. R., Coordinated Science Laboratory, University of Illinois, Report R-295, Thesis.

10. The justification for neglecting specularly reflected molecules when α_d changes with position may not be as clear as before when α_d was constant. The resultant force of a specular reflection still passes through the center of mass

of the satellite. This force is greater due to impingement on one surface than on the other. Therefore, the net effect is to cause an aerodynamic "lift" to the satellite, but no torque.

11. Wachman, op. cit.,

12. Stickney, R. E., and F. C. Hurlbut, "Studies of Normal Momentum Transfer by Molecular Beam Techniques, "Rarefied Gas Dynamics, et. J. A. Laurman, Vol. I, 1963, pp. 454-469.

13. Palamara, op. cit., p. 68.

14. Priester, W., Roemer, M., and Vollard, H. "The Physical Behavior of the Upper Atmosphere Deduced from Satellite Drag Data" Space Science Reviews ed. c. de Joger, Vol. VI, No. 6, May 1967.

15. Anderson, J. B., Andres, R. P., and Fenn, J. B. "High Intensity and High Energy Molecular Beams" Advances in Atomic and Molecular Physics ed. Bates and Estermann, Vol. 1, 1965.

Figure

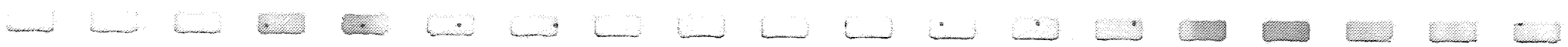

6.1. Introduction

The incident electromagnetic energy of radiation imposes a pressure upon an intercepting surface in much the same way as aerodynamic pressure. This follows from both the electromagnetic and quantum theories of light. At altitudes above 1000 km, the solar radiation pressure is higher than the aerodynamic pressure. In this chapter we will consider the solar-radiation-pressure induced torque on the C.S.L. relativity satellite described in previous sections.

Many authors have treated the problem of solar radiation pressure torque where the radiation disturbance torque arises from the asymmetry of the surface presented to the radiation source or from shielding of surfaces from radiation (see for example ref. 1). For the C.S.L. relativity satellite, shielding effects are non-existent and torques arising from asymmetry of the surface will be extremely small due to the nearly spherically symmetric configuration of the satellite. A calculation of this type for the C.S.L. satellite was presented in ref. 2, where a precession rate of about one sec of arc per year resulted from an asymmetry which caused the center of pressure to act at one millimeter from the center of mass.

Even when the surface is symmetrical with respect to the center of mass, a torque can exist because of differential reflectivity of the surface elements and variations in the direction of the surface normal. Different values of reflectivity for the various surfaces could arise from differential exposure to solar

radiation, meteorite cratering, manufacturing errors and other causes. Variations in the direction of the surface normal could arise from manufacturing errors and warpage of the surface due to deformation under centrifugal stress while spinning and thermal expansion by solar heating. This chapter will deal only with the precession caused by the larger of the above effects, differential reflectivity of the various surfaces.

6.2. Analysis of Solar Radiation Pressure Torque

6.2.1. Basic Equations

The satellite analyzed is the type proposed by the Co-ordinated Science Laboratory to measure a general relativity effect. The satellite parameters which will be used in this calculation are for the satellite configuration reported in ref. 3. Briefly, the configuration is a sphere modified by cubic-oriented flat surfaces. The spherical diameter is 30 cm and the flat to flat diameter is 24.50 cm. The six surfaces each have an area of 236 cm^2 and the angles of the surface normals relative to the spin axis are 42, 54, 71.36, 108.65, 126, and 138 degrees.

The basic equations for the torque caused by solar radiation can be found in many references (see for example ref. 4). The torque produced by radiation pressure on a finite plane surface at radius r_n from the center of mass of the body (see fig. 6.1) can be expressed as

$$\bar{L}_n = \bar{r}_n \times [P_o \Delta A_n (\bar{E} \cdot \bar{n}_n)\bar{E} + \eta_n P_o \Delta A_n (\bar{R}_n \cdot \bar{n}_n)(-\bar{R}_n)] \qquad (1)$$

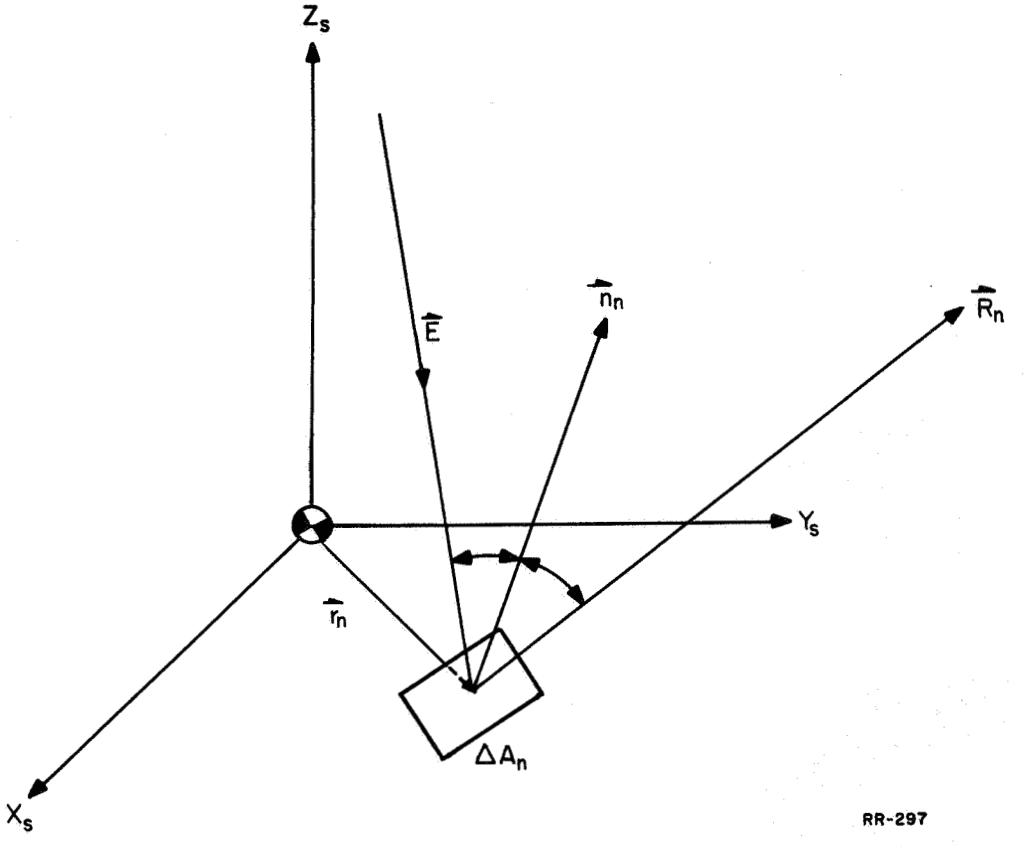

Figure 6.1

Reflection of solar radiation, $\vec{E}$, from a surface element, ΔA_n.

where P_o is the incident radiation pressure acting in the direction of the unit vector $\bar{E}$. ΔA_n is the surface element having the unit normal $\bar{n}_n$, $\bar{R}_n$ is the unit vector in the direction of the reflected radiation and η_n is the radiation adsorption coefficient which is equal to 1 for complete reflection and equal to zero for complete absorption.

Since $\bar{n}_n$, $\bar{E}$, and $\bar{R}_n$ are in the same plane, we can write the following

$$\bar{R}_n - \bar{E} = (-\bar{E} \cdot \bar{n}_n + \bar{R}_n \cdot \bar{n}_n)\bar{n}_n \tag{2}$$

Also, if we assume that the reflection is specular, then we have the angle of reflection equal to the angle of incidence or,

$$-\bar{E} \cdot \bar{n}_n = \bar{R}_n \cdot \bar{n}_n \tag{3}$$

Substituting (3) into (2) we have

$$\bar{R}_n = \bar{E} - 2(\bar{E} \cdot \bar{n}_n)\bar{n}_n \tag{4}$$

Using (4) in equation 1 we have for the instantaneous torque on the nth element of area

$$\bar{L}_n = P_o \Delta A_n(\bar{E} \cdot \bar{n}_n)\, \bar{r}_n \times [(1-\eta_n)\bar{E} + 2\eta_n(\bar{E} \cdot \bar{n}_n)\bar{n}_n] \tag{5}$$

Now, if we consider the elements of surface to all have normals in the same direction as the radius vector to the center of the surface from the center of the mass, we have

$$\bar{r}_n \times \bar{n}_n = 0 \tag{6}$$

This condition is very accurately met for the C.S.L. relativity satellite. Applying equation 6 to equation 5 we have

$$\bar{L}_n = P_o \Delta A_n (\bar{E} \cdot \bar{n}_n) \bar{r}_n \times \bar{E}(1 - \eta_n) \tag{7}$$

From equation 6 we can also write the following

$$\bar{n}_n = \bar{r}_n / |r_n| \tag{8}$$

Therefore, (7) becomes

$$\bar{L}_n = -P_o \Delta A_n |r_n| (1 - \eta_n) (-\bar{E} \cdot \bar{n}_n)(\bar{n}_n \times \bar{E}) \tag{9}$$

From Fig. 6.2 we can define the vectors $\bar{E}$ and $\bar{n}$.

$$-\bar{E} = \sin\alpha \sin\beta \, i_s - \sin\alpha \cos\beta \, j_s + \cos\alpha \, k_s \tag{10}$$

$$\bar{n} = \sin\theta_n \cos\phi_n \, i_s + \sin\theta_n \sin\phi_n \, j_s + \cos\theta_n \, k_s \tag{11}$$

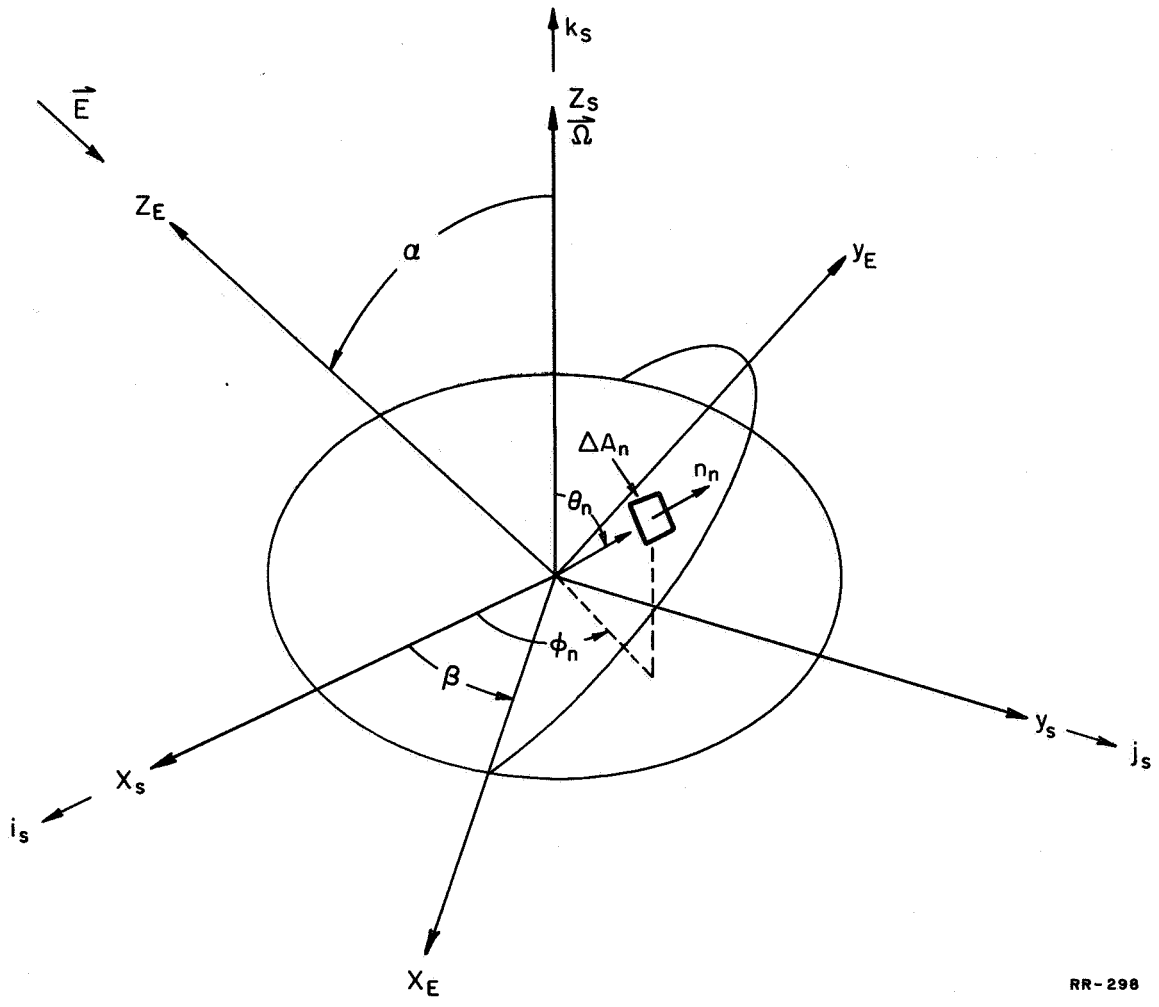

Figure 6.2

Orientation of solar radiation vector with respect to the satellite spin vector $\vec{\Omega}$.

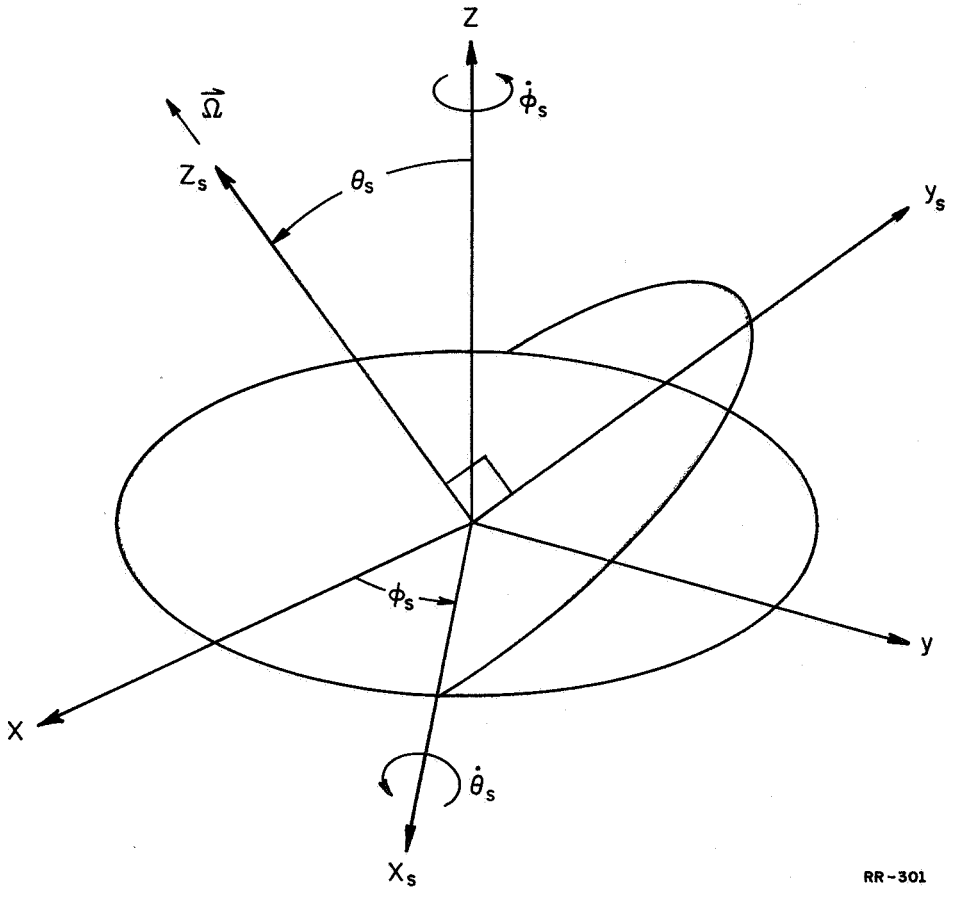

Figure 6.3

Orientation of satellite spin axis in the inertial reference system x, y, z.

where k_s is the unit vector in the direction of the positive spin vector. Substitution of eqs. (10) and (11) into (9) will yield the torque referred to the x_s, y_s, z_s coordinate system.

$$\bar{L}_n = L_{nx_s}\, i_s + L_{ny_s}\, j_s + L_{nz_s}\, k_s \tag{12}$$

where L_{nx_s}, L_{ny_s}, and L_{nz_s} are the components of the torque $\bar{L}_n$.

We are now prepared to find the motion of the satellite spin axis under the action of this torque. Since we want this precession referred to a coordinate system fixed in inertial space, we introduce the coordinate system shown in fig. 6.3 where the x, y, z system is the inertial system.

In this coordinate system we can write Euler's dynamical equations for the spinning satellite

$$\begin{aligned} L_{nx_s} &= I_1\, \dot{\omega}_{x_s} + (I_{z_s} - I_1)\, \omega_{z_s}\, \omega_{y_s} + I_{z_s}\, \omega_{y_s}\, \Omega \\ L_{ny_s} &= I_1\, \dot{\omega}y_s + (I_1 - I_{z_s})\, \omega_{x_s}\, \omega_{z_s} - I_{z_s}\, \omega_{x_s}\, \Omega \\ L_{nz_s} &= I_{z_s}\, (\dot{\omega}_{z_s} + \dot{\Omega}) \end{aligned} \tag{13}$$

Where we have assumed a body symmetric about the spin axis z_s. Ω is the spin rate, $I_1 = I_{x_s} = I_{y_s}$ the moment of inertia about the axis perpendicular to the spin axis. I_{z_s} is the moment of inertia

about the spin axis.

If the spin rate is large compared with the precession rates ω_{x_s}, ω_{y_s} and the slow down rate ω_{z_s}, as will be the case for the C.S.L. satellite, we can write equations 13 as

$$\begin{aligned} L_{nx_s} &= I_{z_s}\, \omega_{y_s}\, \Omega \\ L_{ny_s} &= -\, I_{z_s}\, \omega_{x_s}\, \Omega \\ L_{nz_s} &= I_{z_s}\, (\dot{\omega}_{z_s} + \dot{\Omega}) \end{aligned} \tag{14}$$

Referring to fig. 6.3 we can write

$$\begin{aligned} \omega_{x_s} &= \dot{\theta}_s \\ \omega_{y_s} &= \dot{\phi}_s \sin \theta_s \\ \omega_{z_s} &= \dot{\phi}_s \cos \theta_s \end{aligned} \tag{15}$$

Using equations 15 in equations 14, we find the precession components of the satellite spin axis, letting $I_{z_s} = I$

$$\dot{\phi}_s = \frac{L_{nx_s}}{\Omega\ I \sin \theta_s} \tag{16}$$

$$\dot{\theta}_s = \frac{L_{ny_s}}{I\ \Omega} \tag{17}$$

To find the precession of the satellite we must integrate equations 16 and 17 with respect to time. In general, the quantities α, β, ϕ_m, θ_s, and ϕ_s which appear in L_{nx_s} and L_{ny_s} are all functions of time. However, in one revolution of the satellite about its spin axis, all the quantities can be considered constant except ϕ_n. Therefore, we find the average precession of the spin axis for one revolution of the satellite by integrating only over ϕ_n from 0 to 2π. That is, the average precession can be expressed as

$$\tilde{\dot{\phi}}_s = \int_o^t \frac{L_{nx_s}}{I\,\Omega \sin\theta_s}\, dt/t$$

and

$$\tilde{\dot{\theta}}_s = -\int_o^t \frac{L_{ny_s}}{I\,\Omega}\, dt/t$$

now $\phi_n = \Omega t$ and for one revolution

$$t = \frac{2\pi}{\Omega}$$

$$dt = \frac{d\phi_n}{\Omega}$$

Therefore,

$$\tilde{\dot{\phi}}_s = \frac{1}{2\pi} \int_o^{2\pi} \frac{Lnx_s}{\Omega\ I\ \sin\ \theta_s}\ d\ \phi_n \tag{18}$$

$$\tilde{\dot{\theta}}_s = \frac{-1}{2\pi} \int_o^{2\pi} \frac{Lny_s}{I\,\Omega}\ d\ \phi_n \tag{19}$$

Before we can perform the integration of equations 18 and 19, we must take into consideration that for a given θ_n, the surface

associated with that angle may pass into the shadow or the back side of the satellite. Under that condition, no torque would act on the satellite. Therefore, we must use the shadow boundary as the limits of integration on ϕ_n. From fig.6.1, we see that the shadow is defined by

$$- \bar{E} \cdot \bar{n}_n = 0 \tag{20}$$

From equations 10 and 11 we find

$$- \bar{E} \cdot \bar{n}_n = \sin\alpha \sin\beta \sin\theta_n \cos\phi_n - \sin\alpha \cos\beta \sin\theta_n \sin\phi_n + \cos\alpha \cos\theta_n \tag{21}$$

We want to find the value of ϕ_n for a given θ_n when equation 21 is equal to zero. Denoting as ϕ_{n_s} the value of ϕ_n when the shadow boundary is reached, we find

$$\phi_{n_s} = \sin^{-1}\left(\frac{1}{\tan\alpha \tan\theta_n}\right) + \beta \tag{22}$$

We see that three situations for the shadowing of a surface at a given θ_n. First, the surface may be in the sunlight for one complete rotation of the satellite. For this case we integrate equations 18 and 19 from 0 to 2π on ϕ_n. Another case is when the surface is in the shadow for one complete rotation. Under these conditions we have zero torque. The third case is the most complicated.

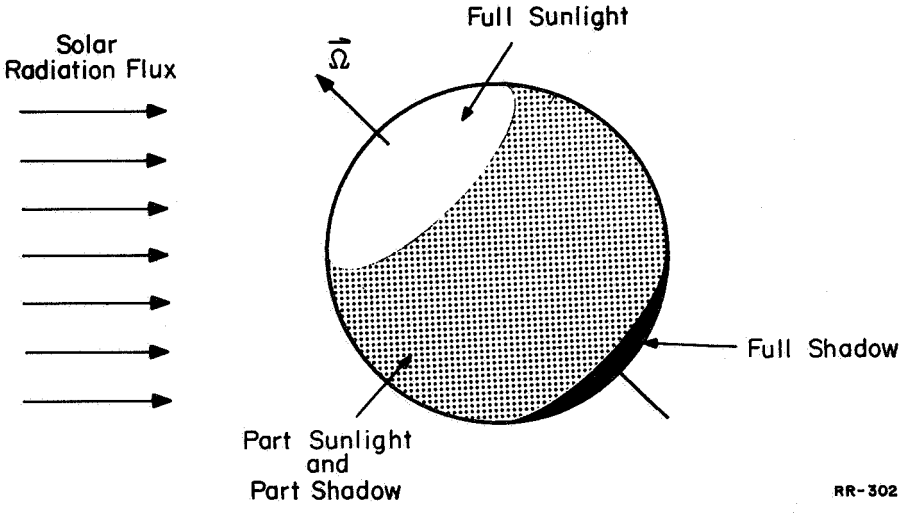

Figure 6.4

Three regions of solar coverage on a spinning sphere at an angle to the solar radiation flux.

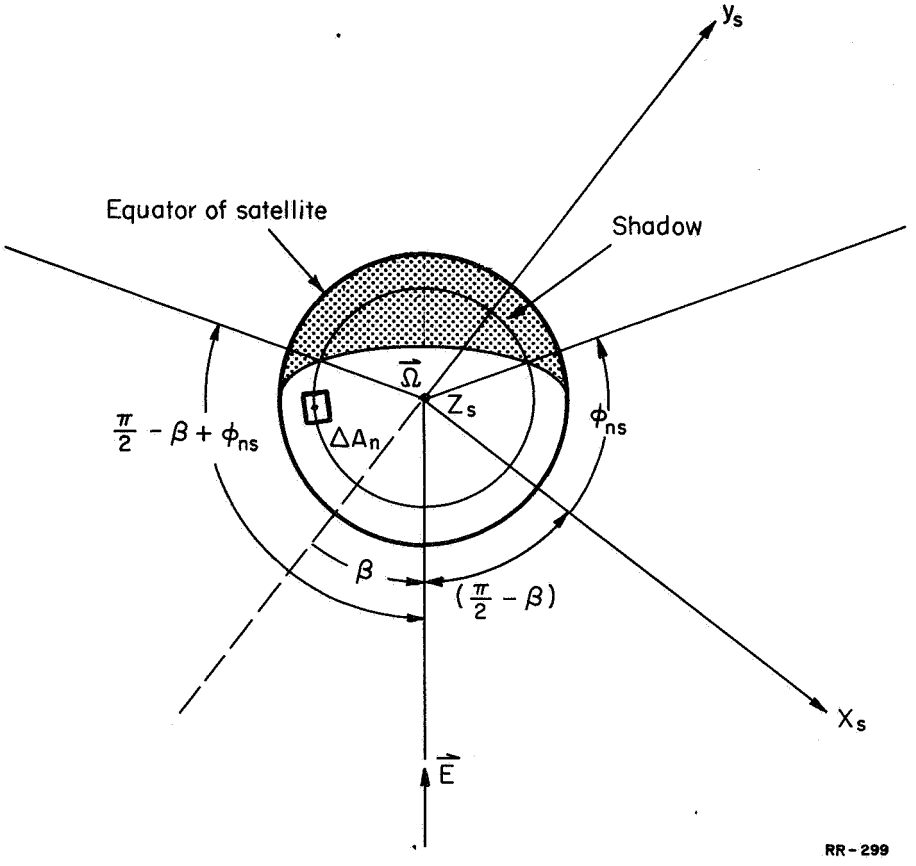

Figure 6.5

Top view of satellite with shadow; showing angular limits of shadow boundary for a surface ΔA_n.

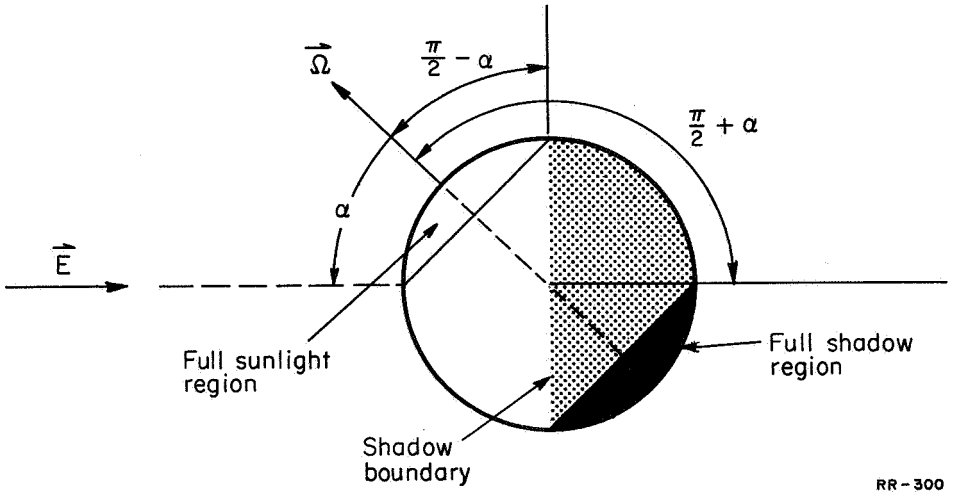

Figure 6.6

Side view of satellite with shadow;
showing angular limits of shadow regions.

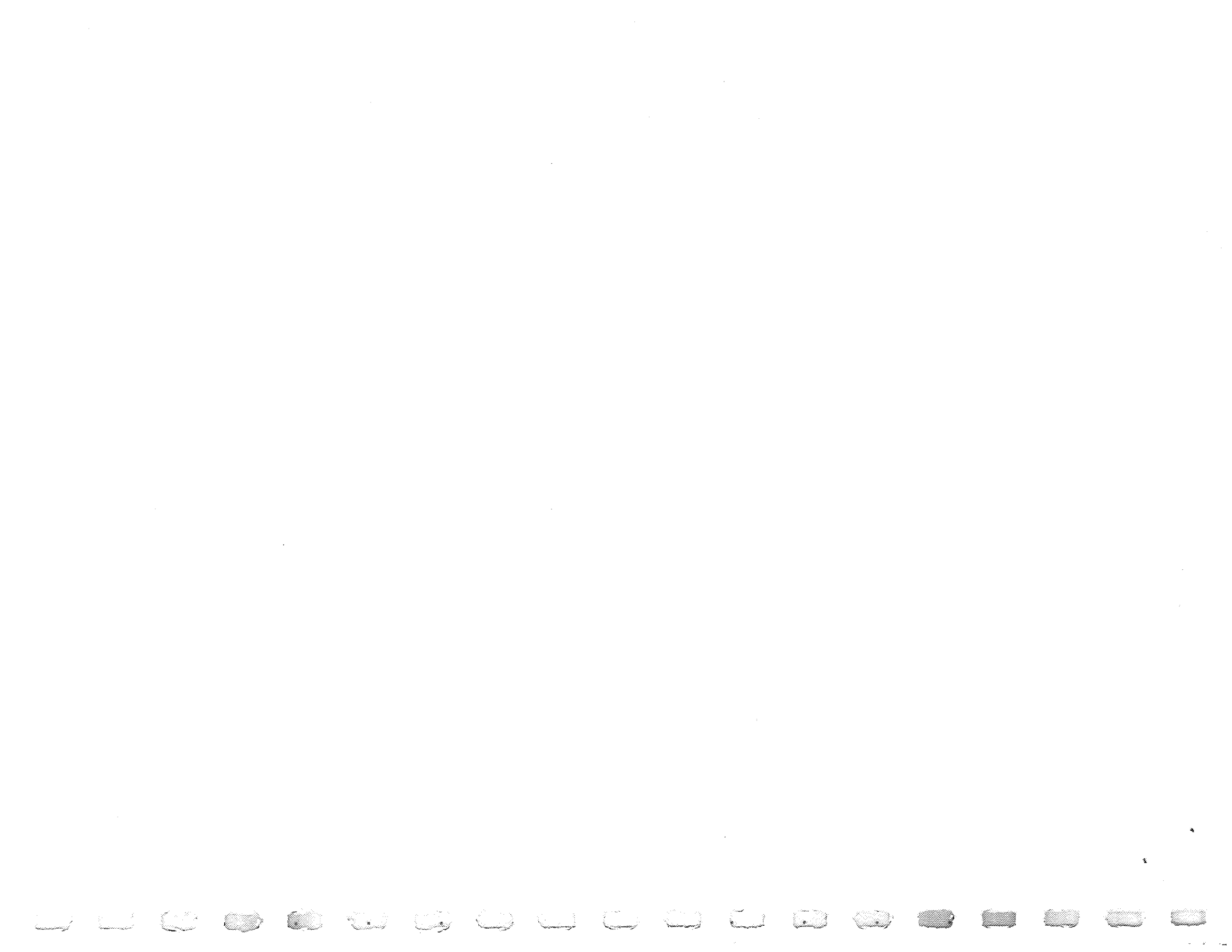

For this case the surface is in the sunlight for part of the rotation and then passes into the shadow. (see fig. 6.4). The geometry involved in this third case is shown in fig. 6.5.

Case I. Full sunlight; $\theta_n < \frac{\pi}{2} - \alpha$

A surface at angle θ_n from the spin axis will be in full sunlight for one complete rotation if $\theta_n < \frac{\pi}{2} - \alpha$ (see fig. 6.6). Integrating equations 18 and 19 from θ to 2π we have

$$\tilde{\dot{\phi}}_s = \frac{-L_o}{2\Omega I \sin\theta_s}\left[\sin\alpha\cos\alpha\cos\beta(2\cos^2\theta_n - \sin^2\theta_n)\right] \qquad (23)$$

$$\tilde{\dot{\theta}}_s = \frac{-L_o}{2 I \Omega}\left[\sin\alpha\cos\alpha\sin\beta(\sin^2\theta_n - 2\cos^2\theta_n)\right] \qquad (24)$$

where $L_o = P_o \Delta A_n |r_n| (1 - \eta_n)$

Case II. Full shadow; $\theta_n > \frac{\pi}{2} + \alpha$

For this case no torque acts on the satellite, therefore,

$$\tilde{\dot{\phi}}_s = 0$$

$$\tilde{\dot{\theta}}_s = 0$$

Case III. Part sunlight, part shadow; $\frac{\pi}{2} - \alpha < \theta_n < \frac{\pi}{2} + \alpha$

From fig. 6.5 we see that the limits of integration should be from $(-\pi - \phi_{n_s} + 2\beta)$ to ϕ_{n_s}. Integrating equations 18 and 19 using these limits instead of from 0 to 2π we have

$$\tilde{\dot{\phi}}_s = \frac{-L_o}{2\pi\,\Omega\,I\sin\theta_s}\left\{\frac{D\cdot F}{2}\sin^2\theta_n\left[\sin^2\phi_{n_s} - \sin^2(\phi_{n_s} - 2\beta)\right]\right.$$

$$- G\cdot F\sin^2\theta_n\left[\frac{\pi}{2} - \phi_{n_s} - \beta - \frac{1}{4}\left(\sin 2\phi_{n_s} - \sin 2(\phi_{n_s} - 2\beta)\right)\right]$$

$$+ F^2\sin\theta_n\cos\theta_n\left[-\cos\phi_{n_s} - \cos(\phi_{n_s} - 2\beta)\right]$$

$$+ D\cdot G\sin\theta_n\cos\theta_n\left[\sin\phi_{n_s} - \sin(\phi_{n_s} - 2\beta)\right]$$

$$+ G^2\sin\theta_n\cos\theta_n\left[\cos\phi_{n_s} + \cos(\phi_{n_s} - 2\beta)\right]$$

$$\left. + G\cdot F\cos^2\theta_n\,(\pi - 2\phi_{n_s} - 2\beta)\right\} \qquad (25)$$

$$\tilde{\dot{\theta}}_s = \frac{-L_o}{2\pi\,\Omega\,I}\left\{-D^2\sin\theta_n\cos\theta_n\left[\sin\phi_{n_s} - \sin(\phi_{n_s} - 2\beta)\right]\right.$$

$$- D\cdot G\sin\theta_n\cos\theta_n\left[\cos\phi_{n_s} + \cos(\phi_{n_s} - 2\beta)\right]$$

$$- D\cdot F\cos^2\theta_n\,(\pi + 2\phi_{n_s} - 2\beta)$$

$$+ D\cdot F\sin^2\theta_n\left[\frac{\pi}{2} + \phi_{n_s} - \beta + \frac{1}{4}\left(\sin 2\phi_{n_s} + \sin 2(\phi_{n_s} - 2\beta)\right)\right]$$

$$- \frac{G\cdot F}{2}\sin^2\theta_n\left[\sin^2\phi_{n_s} - \sin^2(\phi_{n_s} - 2\beta)\right]$$

$$\left. + F^2\sin\theta_n\cos\theta_n\left[\sin\phi_{n_s} - \sin(\phi_{n_s} - 2\beta)\right]\right\} \qquad (26)$$

where $L_o = P_o\,\Delta\,A_n\,|r_n|\,(1 - \eta_n)$

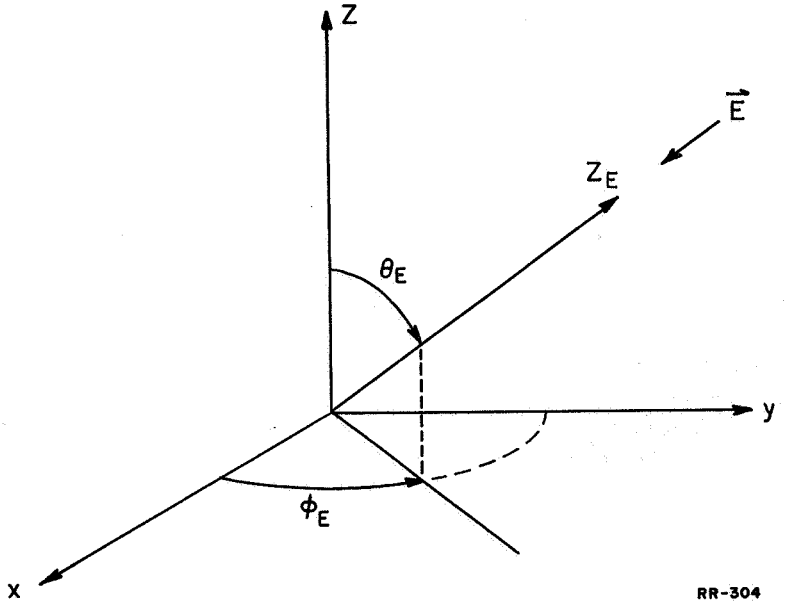

Figure 6.7

Orientation of solar radiation flux vector
in the inertial reference system.

and

$$D = \sin\alpha \sin\beta$$

$$G = \sin\alpha \cos\beta \tag{27}$$

$$F = \cos\alpha$$

We now have but one more modification of the above equations before we can solve problems. As the equations are written, the solar radiation vector $\bar{E}$ is referred to the satellite coordinate system. It is more advantageous for computational purposes to refer the solar radiation vector to the inertial system, x, y, z. The angles involved are defined in fig. 6.7. Therefore, referred to the x, y, z system we have

$$-\bar{E} = \sin\theta_E \cos\phi_E \, i + \sin\theta_E \sin\phi_E \, j + \cos\theta_E k \tag{28}$$

With this equation and equation (10) we can find D, G, and F (eq. 27) in terms of θ_E and ϕ_E. Therefore, equations 27 become

$$D = A \cos\phi_s + B \sin\phi_s$$

$$G = A \cos\theta_s \sin\phi_s - B \cos\theta_s \cos\phi_s - C \cos\theta_s \tag{29}$$

$$F = A \sin\theta_s \sin\phi_s - B \sin\theta_s \cos\phi_s + C \cos\theta_s$$

where

$$A = \sin \theta_E \cos \phi_E$$

$$B = \sin \theta_E \sin \phi_E \qquad (30)$$

$$C = \cos \theta_E$$

Now, with equations 23, 24, 25, 26, and 29 we are prepared to find the precession of the satellite spin axis referred to an inertial coordinate system of our choosing. In practice one might choose the orbital plane of the satellite or the earth's north pole as the basis for the inertia system. Since we are considering satellite orbits which regress during the year, we have chosen the earth fixed system. In this way the system of equation defining A, B, C (eq. 30) correspond to the motion of the sun referred to the earth. The equations defining the rotation of the sun with respect to various coordinate systems can be found in other reference. See for example ref. 5.

6.2.2. Earth Shadow Effect

In our calculation of the precession, we assume that the average precession rates, $\tilde{\dot{\theta}}_s$, and $\tilde{\dot{\phi}}_s$, are constant over one complete orbit of the satellite. This is an accurate assumption considering that the sun's position does not change greatly in the spproximately 90 minutes it takes for one complete orbit. Therefore, for one

complete orbit

$$\Delta\theta_s = t_s \frac{2\pi}{\omega_o} \tilde{\dot{\theta}}_s$$

and

$$\Delta\phi_s = t_s \frac{2\pi}{\omega_o} \tilde{\dot{\phi}}_s \tag{31}$$

where ω_o is the orbital angular velocity of the satellite. The quantity t_s is a correction factor needed to correct for the effect of the earth's shadow. If the satellite passes through the earth's shadow, no solar torque will act. The quantity t_s is described as follows

$$\text{For } \sin\nu \leq \sqrt{1-(R/r_s)^2}$$

$$t_s = 1$$

$$\text{For } \sin\nu > \sqrt{1-(R/r_s)^2}$$

$$t_s = \frac{180-\phi}{180}$$

where

$$\cos\phi = \frac{\sqrt{1-(R/r_s)^2}}{\sin\nu} \tag{32}$$

R = radius of the earth and r_s = radius of the satellite orbit measured from the earth's center. The angle ν is the angle between the Earth-sun line and the normal to the orbit plane. This angle is

found from solar and orbital parameters from the following:

$$\begin{aligned}\cos \nu = &\cos \Theta \sin \Omega_o \sin i \\ &- \sin \Theta \cos i_\theta \cos \Omega_o \sin i \\ &+ \sin \Theta \sin i_\theta \cos i\end{aligned} \tag{33}$$

where Θ is the ecliptic angle of the sun from equinox and i_θ is the obliquity angle equal to 23.4^o. Ω_o is the angle of the ascending node of the satellite and i is the orbital inclination. The above relations are only correct for circular near-earth orbits and can be obtained from simple geometric considerations. The error committed when one treats small eccentricity orbits ($e < 1$) is, however, quite small.

6.2.3. Orbital Regression Effect

A regressing orbit is not fixed in inertial space. The satellite in this orbit does, however, remain relatively fixed in inertial space while the orbit can be thought to regress under it. Since a regressing orbit does not effect the orientation of the sun relative to the satellite, the inclusion of regression effects is straight forward. The principle effect of orbital regression is to alter the amount of time the satellite remains in the earth's shadow. The change in the orbit's position with respect to the earth is

$$\Delta\Omega_o = -3\pi\ J_2(R/P)^2 \cos i \tag{34}$$

in units of radius per second where R is the radius of the earth, P is the semi-latus rectum, i the orbital inclination, and J_2 is the second coefficient of the potential function. The quantity Ω_o is the angle of node for the orbit which appears in equation (33). Therefore, after each orbit, the regression can be calculated and substituted into equation 33 to give a new ν. This ν is then used in equation 32 to find a new shadow time, t_s.

6.2.4. Advance of Perigee

Besides orbital regression, the asymmetry of the earth also causes an advance of perigee. This effectively changes the time required for the satellite to complete one orbit. The equation for advance of perigee is

$$\Delta\omega = 3\pi J_2 (R/P)^2 (2\text{-}5/2 \sin^2 i) \qquad (35)$$

where $\Delta\omega$ has units of radius per sec and the other quantities have been defined in section 6.2.3. Equation (35) can then be used to calculate a coefficient to multiply equation (31) to modify the original time for one orbit.

6.3. Computational Procedure

In all the results that will be discussed, the precession of

the C.S.L. satellite as described at the beginning of section II is calculated. This precession and the manner in which it varies over one year is calculated and plotted. In order to obtain maximum use of the computer program, each of the six surfaces of the C.S.L. satellite was treated separately but calculations were done simultaneously. A surface at a given θ_n was considered to have a coefficient of reflectivity of zero ($\eta_n = 0$) while the remaining surfaces were assumed to have an $\eta_n = 1$. This was done for each of the n surfaces. Therefore, the results give the precession for six different satellites. Each curve shows the precession of the whole satellite due to that one surface being non-reflective. Of course, one may add the precessions together to obtain the precession for two or more surfaces being non-reflective at the same time. If all the six surfaces were non-reflective, then we should obtain zero torque because of the symmetry of the surface placement. This can be seen from the results by noting that at each position in time, the total torque (the sum of all the curves) is approximately zero. The sum is not exactly zero because we are treating six different satellites rather than one satellite with six different surfaces.

With this in mind, a brief step by step procedure used in the computer program for calculating the precession will be given

1. Read in initial data on satellite and orbit parameters.
2. Calculate eqs. 34 and 35. These values remain constant because i does not change. The value from equation 34

will be used in equation 33 to find a new shadow time after each orbit.

3. Find position of the sun. (Eqs. 30).
4. Find the sun's position relative to the satellite. (Eqs. 29). From this calculation we find the angles α and β which are need in the integration limits.
5. Calculate the average precession rate $\tilde{\dot{\theta}}_s$ and $\tilde{\dot{\phi}}_s$ for each of the six surface angles θ_n(Eqs. 23, 24, or 25, 26.) Case I, II, or III.
6. Calculate the precession over one orbit of the satellite (Eqs. 31) for each of the six surfaces including the effects of earth shadow and advance of perigee.
7. Re-calculate the sun's position and orbital position and proceed starting at step 4.

This procedure is followed for each orbit over a period of time of one year. For the orbits we are considering, altitudes of about 600 miles or 1000 km, there are about 5000 orbits in a year. The results, which will be discussed in the next section, are calculated and plotted by the computer. The computer time involved is about 20 min. on C.S.L.'s own CDC 1604 computer. This time includes the time needed for print out of the data.

6.4. Discussion and Analysis of Results

Samples of the computer solution results are presented in figures 6.8 through 6.13. Each curve represents the precession of the C.S.L. satellite with only that surface at the given angle θ_n being completely non-reflective. For all of the plots presented, certain basic satellite and orbital parameters remained the same. These are as follows.

1. Surface areas - The C.S.L. satellite has six plane surfaces of equal area.

$$\Delta A_n = 0.236 m^2; \quad n = 1, 6$$

2. Radial distance of surface from center of mass - All six surfaces of the C.S.L. satellite have equal radial magnitudes.

$$|\bar{r}_n| = .1225m \; ; \quad n = 1, 6$$

3. Coefficient of reflectivity

$$\eta_n = 0 \; ; \quad n = 1, 6$$

4. Angular position of radius vector of each surface with respect to the satellite spin axis.

$\theta_1 = 42^o$ $\qquad$ $\theta_4 = 108.65^o$

$\theta_2 = 54^o$ $\qquad$ $\theta_5 = 126^o$

$\theta_3 = 7.35^o$ $\qquad$ $\theta_6 = 138^o$

5. Radius of satellite orbit - Due to constraints on the maximum and minimum orbital altitudes, we have chosen a 600 mile, approximately 1000 km, altitude. Therefore

$$r_s = 7.345 \times 10^6 m$$

6. Moment of inertia - It is proposed that the C.S.L. satellite be made from a non-conductive material such as glass or ceramic. For computational purposes, we have chosen a material specific gravity of 2.2 which corresponds to glass. The moment of inertia was calculated assuming a spherical body of radius half way between the spherical diameter and flat to flat diameter of the C.S.L. satellite, .13625m.

$$I = .1725 \text{ kg } m^2$$

7. Spin rate of satellite - Due to constraint on the maximum and minimum spin rate possible, we have chosen

$$\Omega = 100 \text{ cycles/sec} = 628 \text{ rad/sec}$$

8. Incident solar radiation pressure assumed constant at Earth's orbit (see ref. 4).

$$P_o = 0.3 \text{ dynes/m}^2 \; 20.3 \times 10^{-6} \; \frac{\text{Kg}}{\text{m sec}^2}$$

9. Initial position of sun - The starting time was consistently chosen to be at the vernal equinox.

$$\Theta = 0.98563\ d$$

where d is the number of days past vernal equinox.

Although the above parameters have remained constant throughout our calculations, the computer program is adaptable to any number of different satellite shapes and dynamic properties. With the above parameters fixed, we have then five parameters which we have varied in the results presented. These are

1. Initial satellite orientation with respect to the inertial coordinate system

$$\theta_s \text{ and } \phi_s$$

2. Initial orbital parameters

   i - orbital inclination

   Ω_o - angle of ascending node

   e - eccentricity of orbit (less than 0.1)

Since we have chosen the inertial reference frame to be earth centered, the angles θ_s and ϕ_s are measured with respect to the north pole of the earth and the line of Aries, respectively (see fig. 6.3).

Although the plots are self explanatory, a brief description of each would be given.

Fig. 6.8 and 6.9. These figures give the precession component for an equatorial orbit with the satellite spin axis in the orbital plane but 65.6^{o} out of the ecliptic plane.

Figs. 6.10 and 6.11. These are for an orbit inclined at 30^{o} with a small eccentricity of .01. The satellite spin axis is initially in the orbital plane and 5^{o} out of the ecliptic plane.

Figs. 6.12 and 6.13. These are for an equatorial orbit. The satellite spin axis is, however, perpendicular to the ecliptic plane. These results also simulate to some degree a polar orbit with the satellite spin axis in the orbital plane.

From these plots we find that there are both secular and periodic precession rates. The maximum precession is less than 5 sec of arc for a surface which is completely non-reflective and the satellite spin axis perpendicular to the ecliptic plane. Magnitudes of the order of 1 to 2 sec of arc are representative of the precession expected for the completely non-reflective surfaces. Since the surfaces of the C.S.L. satellite are to be highly reflective, we can expect possibly a .1 to .2 sec of arc precession, at most, with a 10% degradation of one surface.

The plots are instructive in showing the precession for a specific surface having a given reflectivity. The precession is found

to vary widely for the sample cases presented. Although this detailed knowledge is useful, a more general analysis of the data will prove to be more useful for design purposes.

Even if the reflectivity of the surfaces were initially balanced, the space environment effects of meteorites, cosmic rays, dust particles, and others can be expected to degrade the surface reflective properties. Although there is some data on these degrading effects from recent satellite experiments, the degrading process and rates are not known well enough so that they can be designed into the satellite. Furthermore, the degrading of the reflective properties cannot be expected to be uniform over the surface of the satellite. The satellite will obtain an average reflectivity with time, but it is expected that the reflectivity from surface to surface will vary around this average value. To be able to obtain some idea of these effects, we perform an analysis of these surface variations using a stochastic model following the work by Robert E. Roberson in ref. 4.

Consider that each surface has the same nominal value for the reflectivity, η^*, such that the total torque on the satellite is zero. This nominal value of reflectivity could be the average reflectivity. Now we consider that due to the non-uniform manner in which the space environment effects erode the surfaces, each surface will have, actually, a value of reflectivity given by

$$\eta_n = \eta^* + \delta\eta_n \tag{34}$$

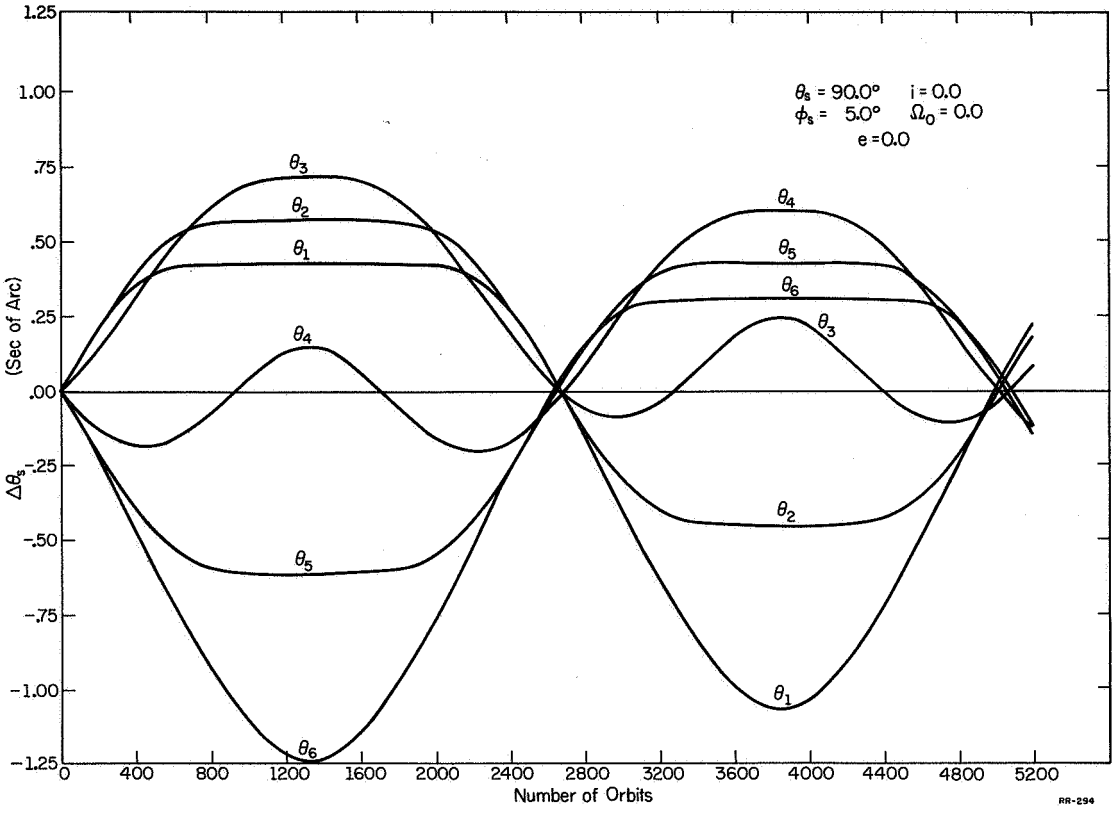

Figure 6.8

$\Delta\theta_s$ vs. number of orbits for equatorial orbit with spin axis in the orbital plane.

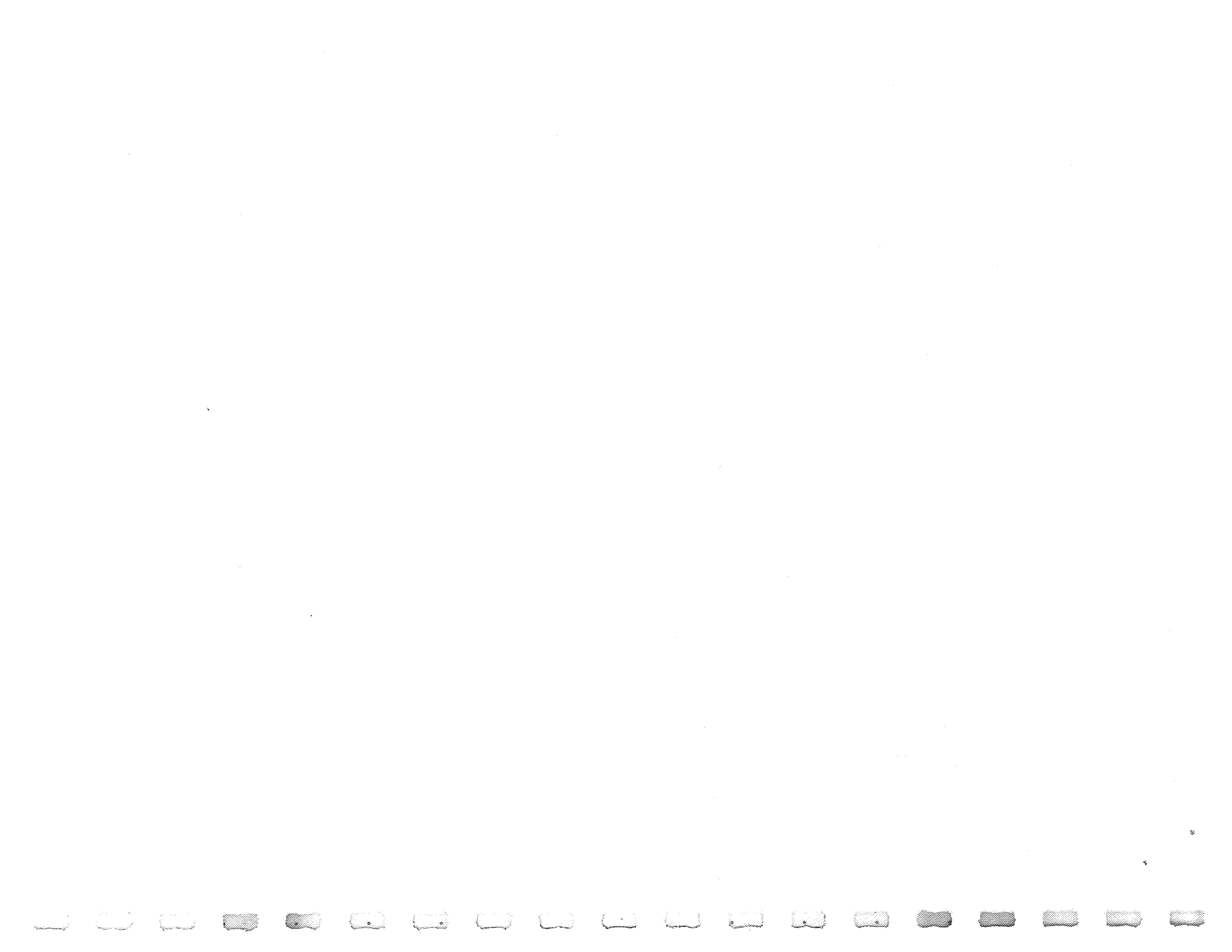

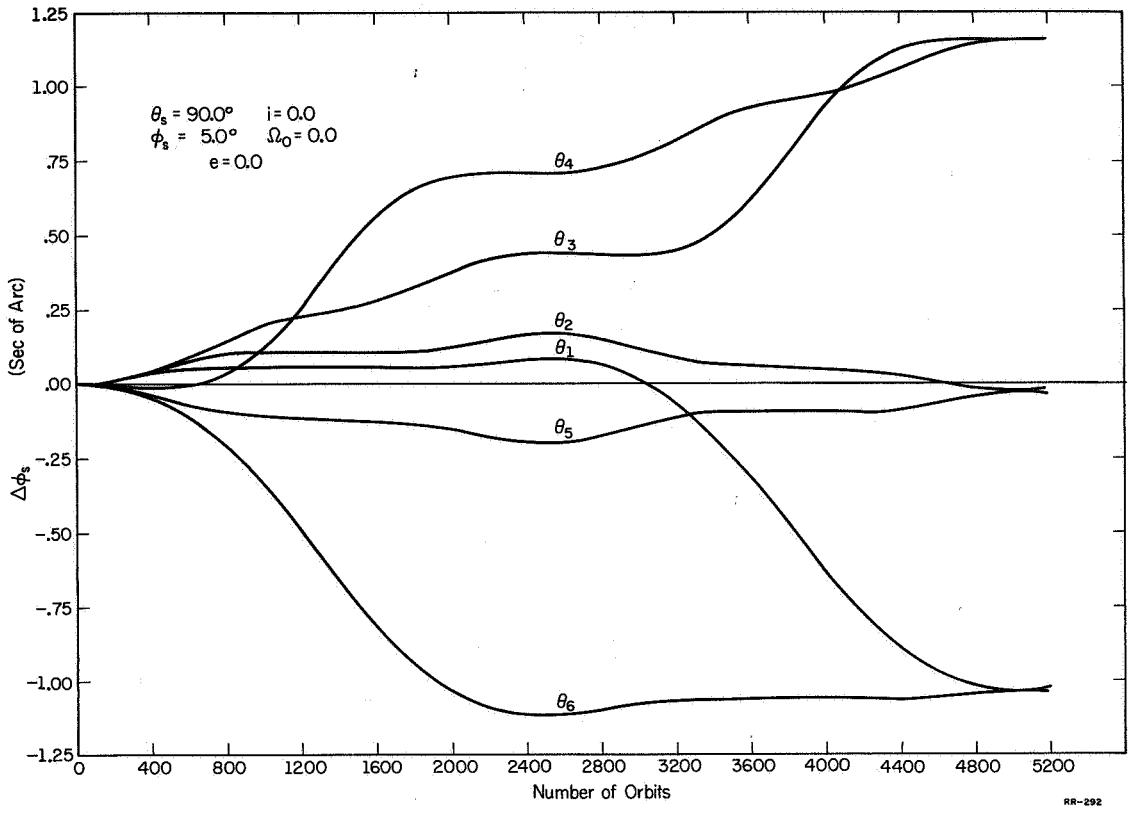

Figure 6.9

$\Delta\phi_s$ vs. number of orbits for an equatorial orbit with spin axis in the orbital plane.

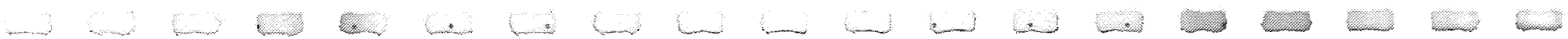

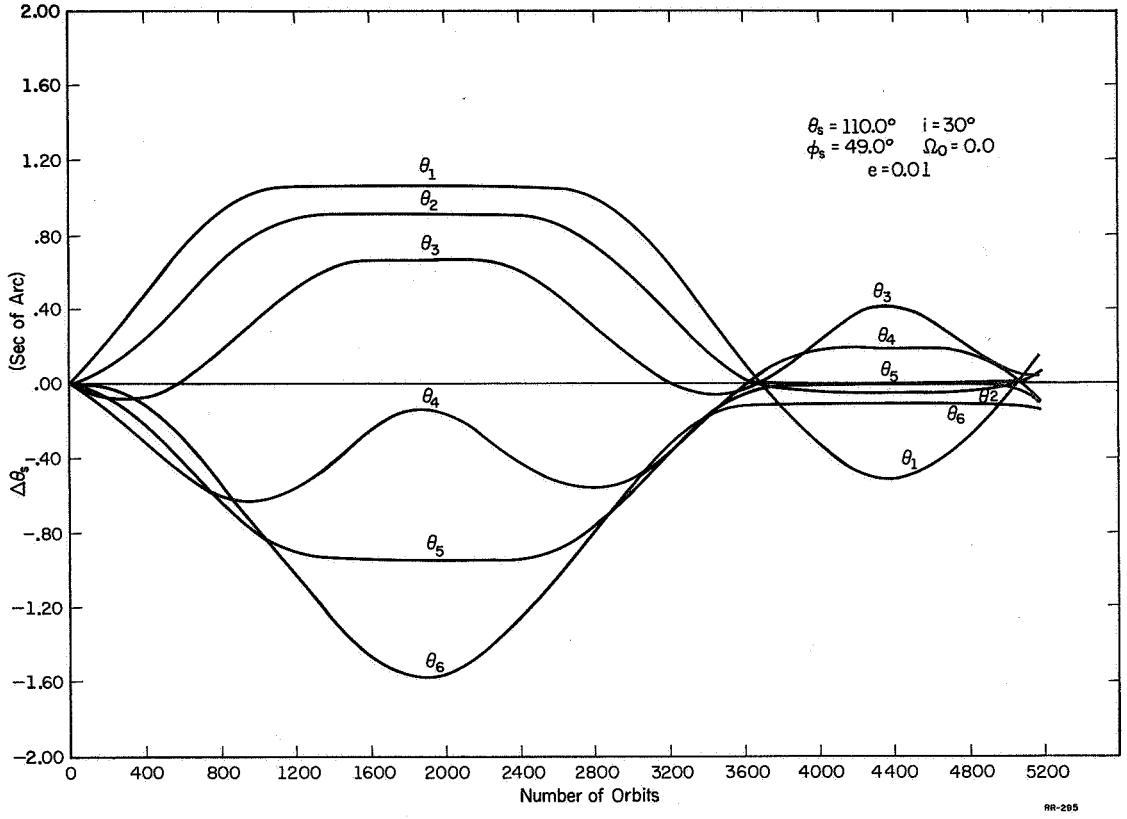

Figure 6.10

$\Delta\theta_s$ vs. number of orbits for satellite orbit of 30° inclination and eccentricity of 0.01. The spin axis is in the orbital plane.

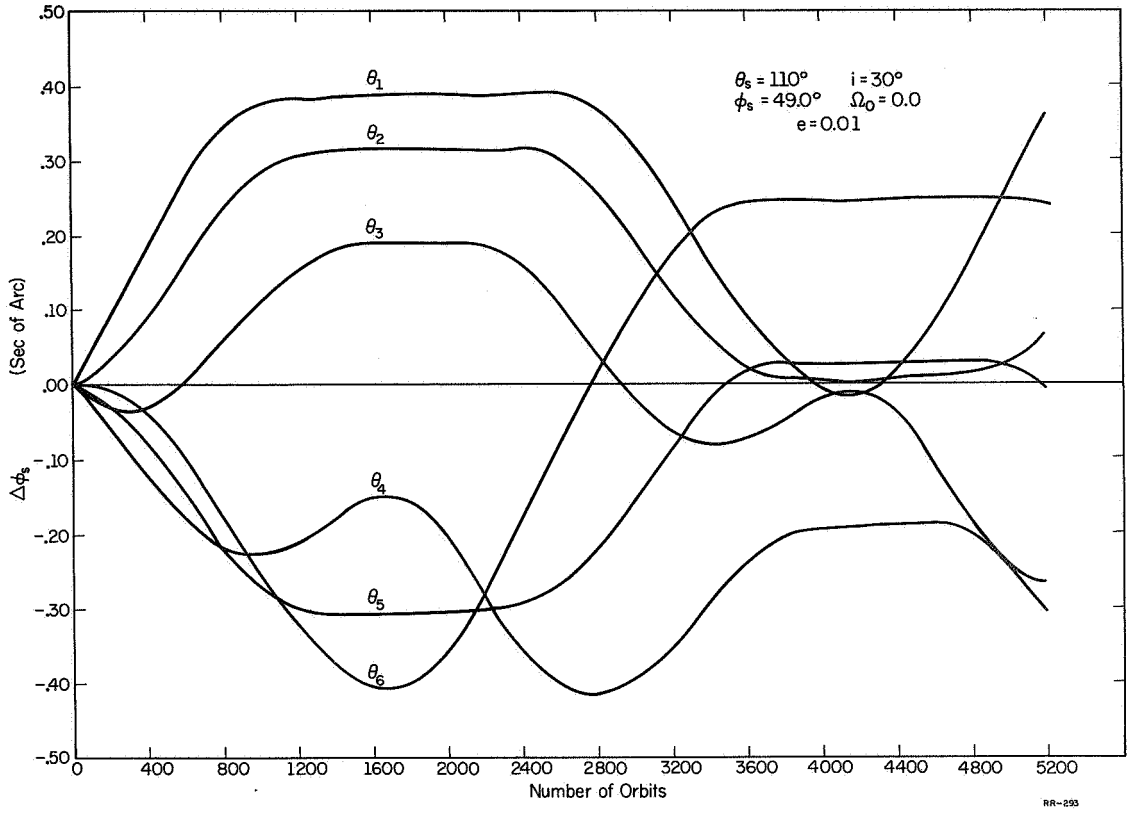

Figure 6.11

$\Delta\phi_s$ vs. number of orbits for satellite orbit of 30° inclination and eccentricity of 0.01. The spin axis is in the orbital plane.

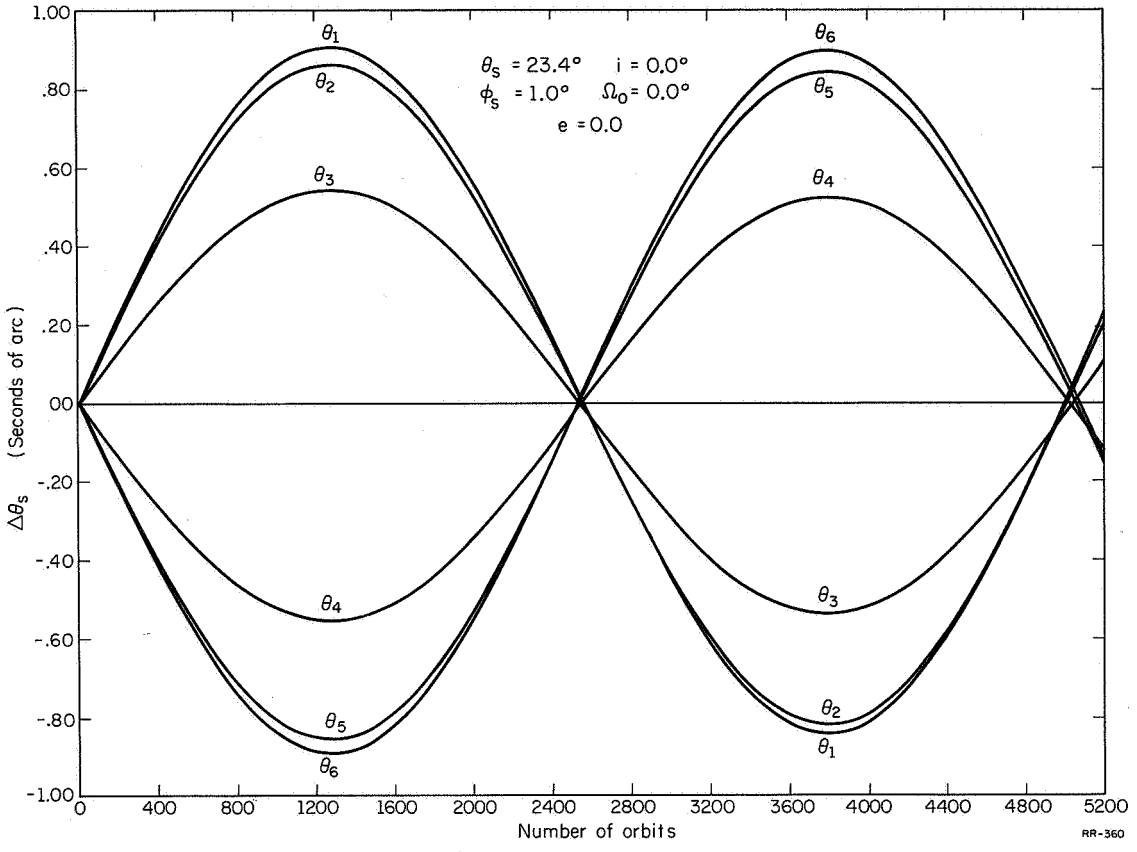

Figure 6.12

$\Delta\theta_s$ vs. number of orbits for an equatorial orbit.
The satellite spin axis is perpendicular to the ecliptic plane.

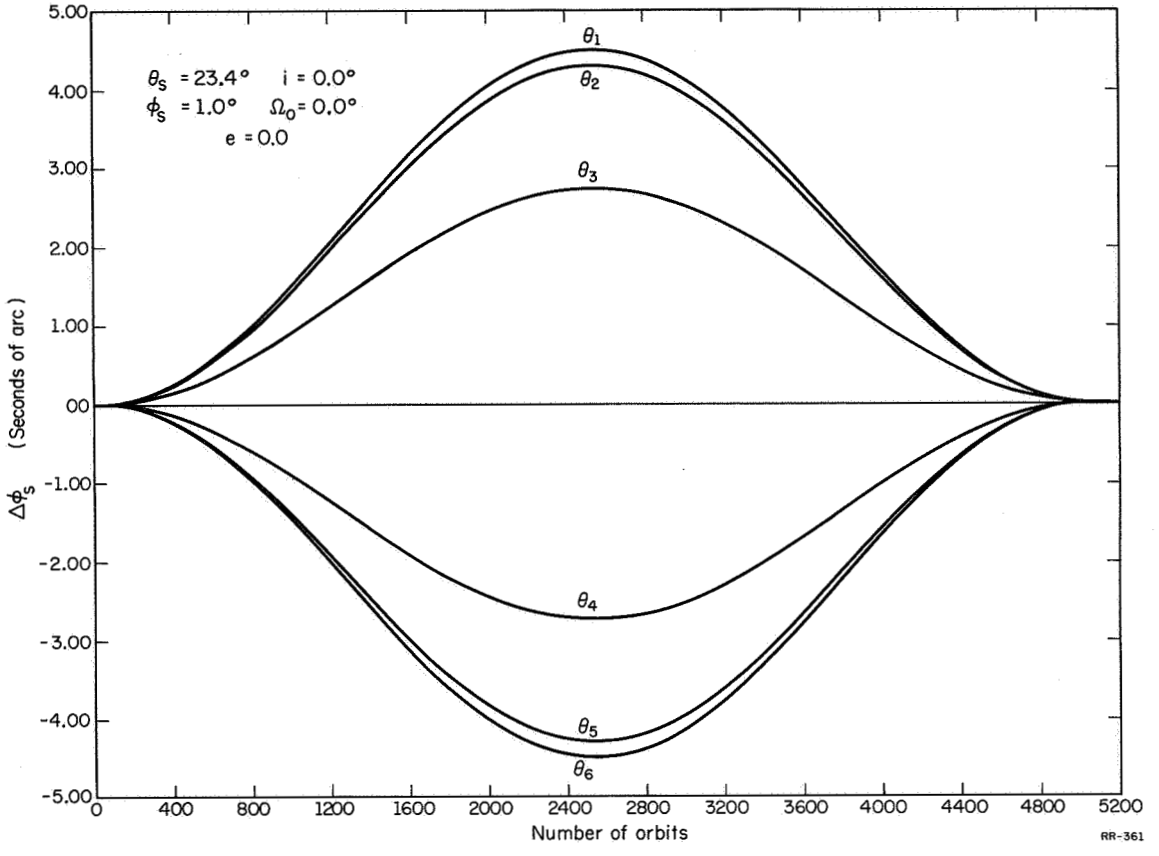

Figure 6.13

$\Delta\phi_S$ vs. number of orbits for an equatorial orbit.
The satellite spin axis is perpendicular to the ecliptic plane.

where $\delta\eta_n$ is a small variation, positive or negative, from the nominal value of reflectivity η^* for which the satellite would be balanced. Using equation 34 in the torque and precession equations, we find that the variation in the total precession component is given by

$$\delta\theta_s = \sum_n \Delta\theta_{s_n} \delta\eta_n$$
$$\delta\phi_s = \sum_n \Delta\phi_{s_n} \delta\eta_n \tag{35}$$

where $\Delta\theta_{s_n}$ and $\Delta\phi_{s_n}$ are the vaults of equations 31 evaluated for a specific θ_n and η^*.

If we consider $\delta\eta_n$ to be a random variable with zero mean, we find that the expected values of $\delta\theta_s$ and $\delta\phi_s$ is also zero. If, however, we suppose that the reflectivity variations in the different surface elements is uncorrelated, we can write

$$\overline{\delta\eta_n \, \delta\eta_k} = \sigma_\eta^2 \, \delta_{nk} \tag{36}$$

where σ_η equals the rms variation in surface reflectivity. The overbar denotes expected values over the probability distribution for the variable in question. With this assumption, we can derive the precession component correlation functions from equations 35.

$$\overline{\delta\theta_s \, \delta\theta_s} = \sum_n (\Delta\theta_{s_n})^2 \sigma_\eta^2$$
$$\overline{\delta\phi_s \, \delta\phi_s} = \sum_n (\Delta\phi_{s_n})^2 \sigma_\eta^2 \tag{37}$$

From equations 37 we can find the rms values of the precession components for the various cases we have plotted in the results. To obtain a conservative estimate we will use the relative maximma of the $\Delta\theta_{s_n}$ and $\Delta\phi_{s_n}$ values over the period of one year for which the results were plotted. Therefore,

$$\text{rms } \delta\theta_s = \left[\sum_n (\Delta\theta_{s_n})^2_{\max} \right]^{\frac{1}{2}} \sigma_\eta \tag{38}$$

$$\text{rms } \delta\phi_s = \left[\sum_n (\Delta\phi_{s_n})^2_{\max} \right]^{\frac{1}{2}} \sigma_\eta \tag{39}$$

Equations 38 and 39 are plotted in figs. 6.14 and 6.15 respectively. The maximum values of $\Delta\theta_{s_n}$ and $\Delta\phi_{s_n}$ were obtained from the appropriate plots in figs. 6.8 through 6.13 with the exception of the line labeled, "Ω11 to lines of Aries, i = 0" and the line labeled "Ω 5° out, i = 15°," which were obtained from data not presented graphically.

Figure 6.14 shows that there is little change in the rms of $\delta\theta_s$ for the various orbital and satellite orientation parameters chosen. The values are generally higher than for the rms of $\delta\phi_s$. The out - of - equatorial - plane component of precession is, however, not considered of great importance to the relativity experiment. The precession caused by the general relativity effect is directed only in the equatorial plane. Therefore, the out - of - plane motion of the spin axis will not effect the accuracy of the relativity experiment.

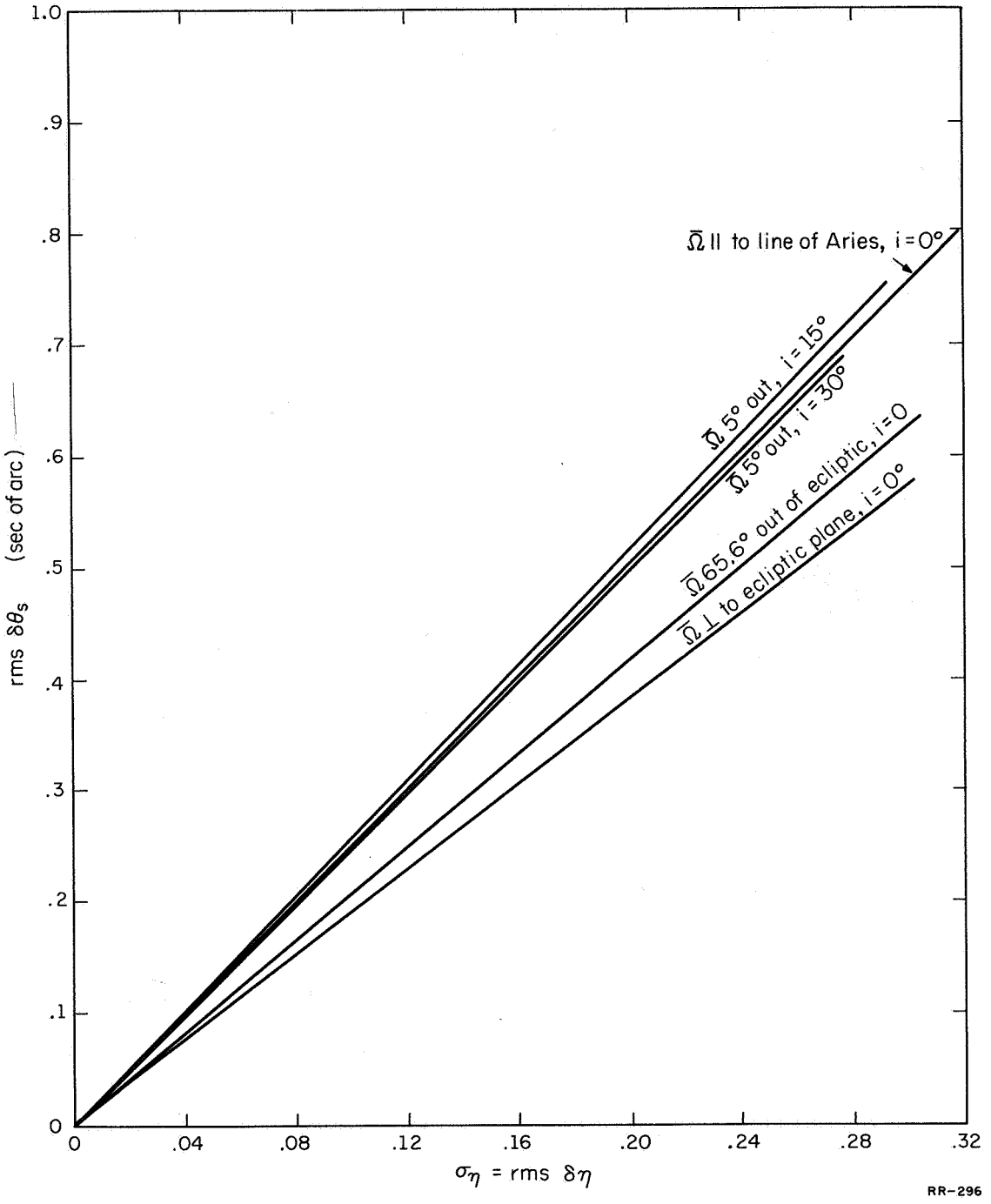

Figure 6.14 The root-mean-square of the out-of-equatorial-plane precession component vs. root-mean-square of surface reflectivity.

Figure 6.15 is then the more important plot with respect to the relativity experiment. This plot shows conclusively that the best orientation for the satellite is one in which the spin axis is nearly in the ecliptic plane. Of secondary importance is the orbital inclination, assuming the spin axis is initially in the orbital plane and also in the ecliptic plane. Future work will investigate more thoroughly the effect of orbital parameters in hopes of finding the best orbit and satellite orientation.

Figure 6.15 shows that we can keep the rms value of the in-plane - precession to less than .1 sec of arc in one year with as much as 10% variation in surface reflectivity if the satellite spin axis is nearly in the ecliptic plane. A 10% variation should be the maximum that one might expect from the space enviornment degrading effects. Only a 1% variation could be allowed for the case where the spin axis is perpendicular to the ecliptic plane for the same rms value of precession.

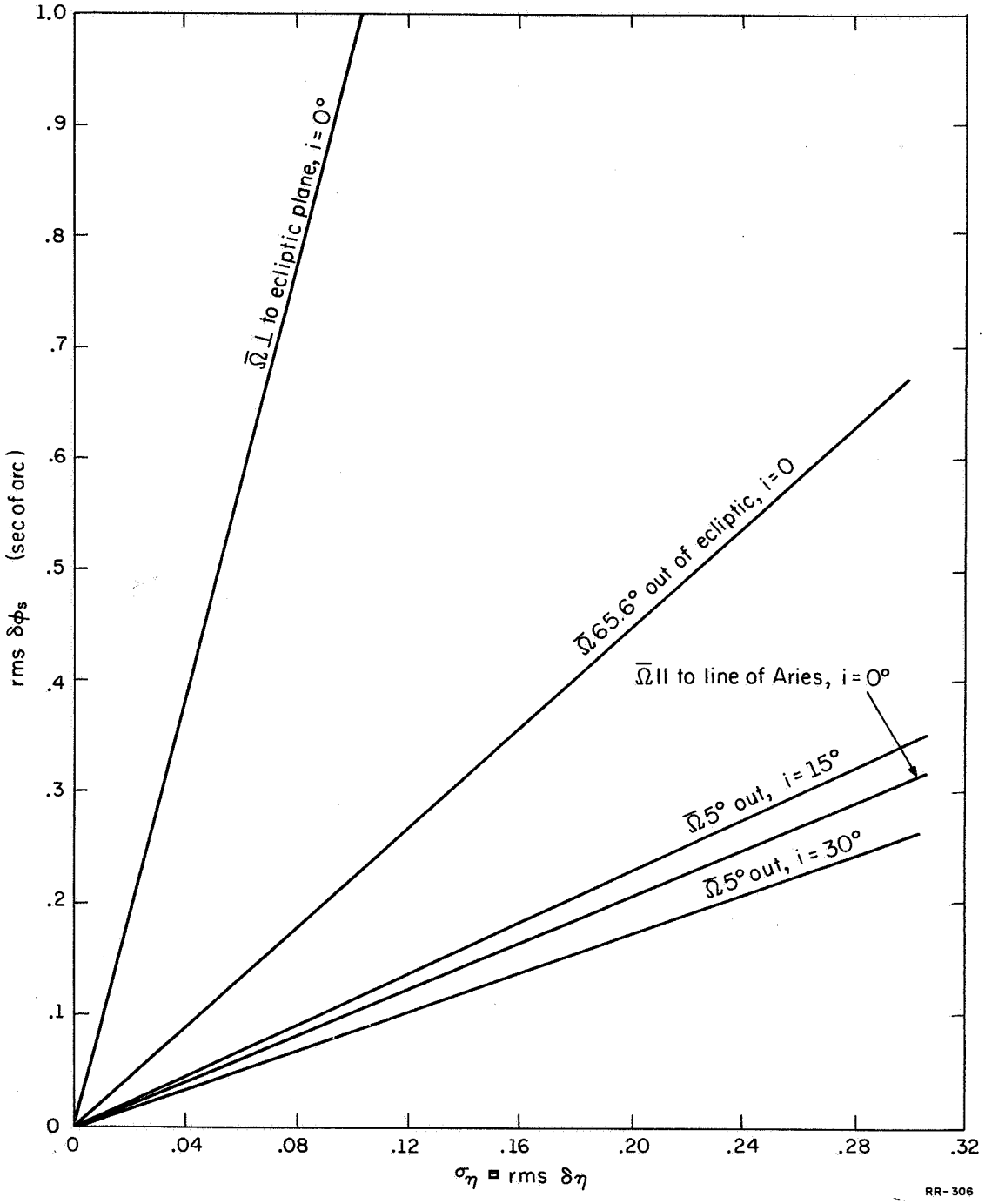

Figure 6.15 The root-mean-square of the in-equatorial-plane precession component vs. the root-mean-square of surface reflectivity.

ΔA_n	area of surface element.
$\bar{E}$	unit vector defining position and direction of solar flex.
i	orbital inclination.
i_Θ	obliquity of sun, 23.4^o.
I_1, I_{z_s}, I	moment of inertia
J_2	potential expansion coefficient.
$\bar{n}_n$	outer unit normal vector to surface element.
$\bar{L}, \bar{L}_n$	vector torque.
p	semilatus rectum of orbit
P_o	incident solar radiation pressure.
$\bar{r}_n$	radius vector to center of surface element.
r_s	radius of satellite orbit from center of earth.
R	radius of earth.
t_s	fraction of orbital period which is in shadow.
α, β	angles defining orientation of sun with respect to the satellite (see fig. 6.2).
η	coefficient of reflectivity.
ν	angle between earth-sun line and normal to the orbital plane.
Θ	ecliptic angle of sun.
θ_E, ϕ_E	angles defining orientation of sun with respect to the inertial reference from (see fig. 6.7).
θ_n, ϕ_n	angles defining position of surface element ΔA_n with respect to the satellite centered coordinate system (see fig. 6.2).
θ_s, ϕ_s	angles defining satellite spin axis with respect to the inertial reference frame (see fig. 6.3).
ϕ_{n_s}	the angle ϕ_n for which the surface element ΔA_n at angle θ_n passes into the shadow of the satellite.
δ_{nk}	Kronecker delta

ω	angle of perigee.
ω_o	orbital angular velocity.
$\omega_{x_s}, \omega_{y_s}, \omega_{z_s}$	components of satellite precession rate.
Ω	satellite spin rate
Ω_o	angle of ascending node of satellite measured from line of Aries in the equatorial plane.

References

1. William J. Evans, "Aerodynamic and Radiation Disturbance Torques on Satellites Having Complex Geometry", Torques and Attitude Sensing in Earth Satellites ed. by S. Fred Singer, pp. 83-98, 1964.

2. Progress Report for June, July, and August, 1965, Coordinated Science Laboratory. University of Illinois, Urbana, Illinois, pp. 17-20.

3. Progress Report for March-August, 1966, Coordinated Science Laboratory, University of Illinois, Urbana, Illinois, pp. 105-111.

4. Robert E. Roberson, "Radiation Pressure Torques from Spatial Variations in Surface Properties" Journal of Spacecraft, Vol. 2, No. 4, July - Aug., 1965, pp. 605-607.

5. Orbital Flight Handbook, NASA sp. 33, part 3, 1963.

In this section it is shown that all spurious torques due to electric, magnetic and electromagnetic effects (with the exception of solar radiation, the effects of which are described in chapter 6) can be readily controlled to sufficiently small values. This control is obtained by choosing appropriate values of the volume electrical resistivity for the gyro material.

The larger torques will be considered first. In order to avoid drift torque due to localized charge on a sphere in an electric field the charge must be uniformly distributed within a maximum specified time. Consider a rotating sphere of radius r located in an electric field E with a fixed charge q localized to give the maximum electric dipole moment (see fig. 7.1). From the figure we can write the expression for torque T and drift rate ω_d:

$$T = qE\ r \sin\theta$$

$$\omega_d \approx \frac{T}{I_\omega} = \frac{qE\ r \sin\theta}{2/5\ mr^2\ \omega}$$

$$\omega_d = \frac{15}{8\pi} \frac{q\ E \sin\theta}{\rho_n\ r^4\ \omega}$$

where ω is the spin rate and ρ_n is the mass density. To estimate the charge, assume that the sphere is at the potential V. The charge due to that potential is assumed to be localized by some undefined process to give a maximum dipole moment. Since $q = CV$ where $C = 4\ \epsilon r$ and $\epsilon = \epsilon_o \epsilon_r$

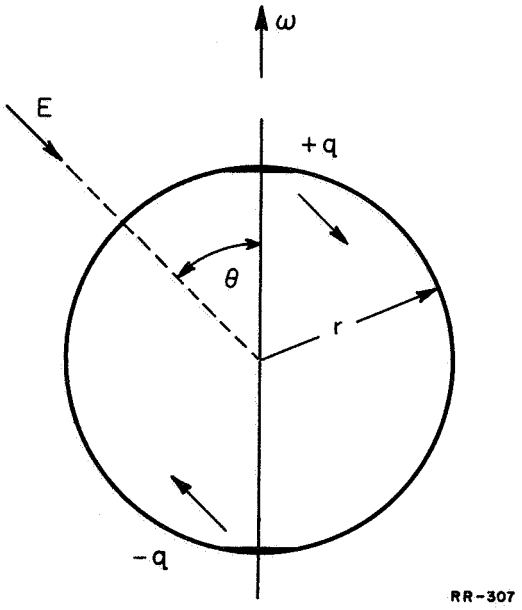

Figure 7.1

Charged Sphere in an Electric Field

$$\omega_d = \frac{15}{2} \frac{\varepsilon_o \varepsilon_r VE}{\rho_m r^3 \omega} \sin\theta \qquad (1)$$

$$\rho = 2.5 \times 10^3 \text{ kgm/m}^2$$

$$\omega = 2\pi \ 100 \text{ rad/sec}$$

$$r = 0.30\text{m}$$

$$\varepsilon_o = 8.85 \times 10^{-12} \text{ farad/m}$$

$$\varepsilon_r = 1$$

$$\theta = 90^o \text{ for the worst case.}$$

What value of potential V should be used? Reference 1 states that "the accumulated charge on the outside of the satellite may be fairly large, corresponding to a potential of several (or in a few cases, several hundred) volts." In reference 2 potentials of about -6 volts on a satellite at an altitude of 795 km were measured, which were about seven times the calculated values. Satellite potentials of the order of -0.15 volts were calculated and observed for the Explorer II satellite, as described by N. C. Jen.[3] Let us take V = 10 volts.

Uncertainties also exist for exact values of the earth's electric field at altitudes of 600 km; however, references indicate an upper bound of about 0.1 volt/m.

Substituting these values into equation (1) one obtains as the worst case (i.e., where $\theta = 90^{o}$ during all orbits);

$$\omega_d = 1.2 \times 10^{-14} \text{ rad/sec.}$$

$\approx$ 0.08 arc sec/year, which is approximately one-hundredth of the first-order relativity effect.

In order to safeguard against possibly more pessimistic space conditions, a charge-relaxation time τ (in which a localized charge is distributed to reduce its initial values ρ to ρ/e in time τ) is specified. From Ohm's law, the equation of continuity and one of Maxwell's equations the following is obtained:

$$\vec{i} = q\vec{E}$$

$$\nabla \cdot \vec{i} = -\frac{\partial q}{\partial t} = \sigma \nabla \cdot E = \frac{\sigma q}{\epsilon}$$

$$-\frac{\partial q}{\partial t} = \frac{1}{\rho_e \varepsilon}$$

where ρ_e is the volume electrical resistivity. The solution is

$$q = q_o e^{-t/\rho_e \varepsilon}$$

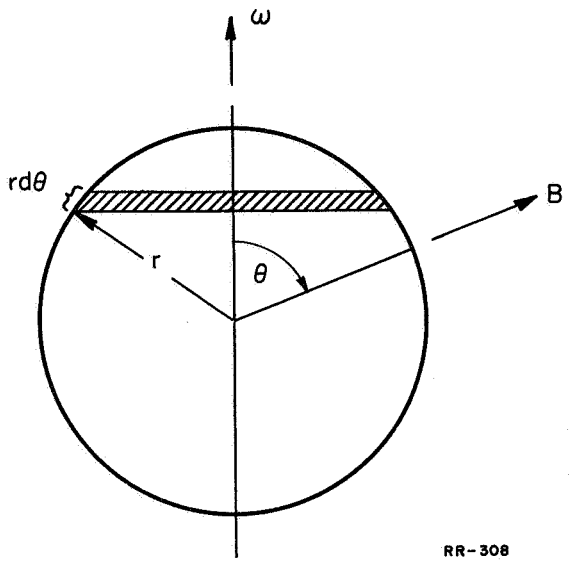

Figure 7.2

Rotating, Uniformly Charged Sphere
in a Magnetic Field

and hence the relaxation time τ is

$$\tau = \rho_e \epsilon \cdot = \rho_e \epsilon_r \epsilon_o \tag{2}$$

If the gyro were made of Cer-Vit, a very low thermal expansion glass fabricated by Owens-Illinois, the charge-relaxation time would depend on the glass resistivity which in turn is dependant on the gyro satellite temperature. A chart of satellite temperature T, ρ_e and τ is given below

T-^oC	ρ_e-ohm-meter	τ-sec
90	8×10^8	.018
0	8×10^{12}	173
-25	3×10^{14}	6,800

By means of solar reflective coatings on the satellite gyro the equilibrium temperature and hence the charge-relaxation time can be selected over a fairly wide range. The choice of maximum relaxation time imposes an upper bound on the volume electrical resistivity.

The case of a uniformly charged gyro rotating in a magnetic field B is next considered. Let the total charge Q be uniformly distributed over the solid spherical gyro (see fig. 7.2). The charge per unit area is $Q/4\pi r^2$. The area of the zone shown in fig. 2 is

$2\pi r^2 \sin\theta \, d\theta$. The magnetic moment μ due to this zone is

$$d\mu = (di)\ (\text{area about which the current element di circulates})$$

$$= \frac{(\text{Charge per unit area})(\text{area of zone}).(\text{Area about which di circulates})}{(\text{Period of revolution})}$$

$$= (Q/4\pi r^2)(2\pi r^2 \sin\theta \, d\theta)\ f\ (\pi r \sin\theta)^2$$

$$\mu = \frac{\omega Q}{4} r^2 \int_o^{\pi} \sin^3\theta \, d\theta$$

$$\mu = \frac{\omega Q r^2}{3}$$

$$\omega_d \approx \frac{|\bar{\mu} x \bar{B}|}{I\omega} = \frac{(\omega Q r^2/3)(B\sin\phi)}{\omega(2mr^2)/5} = \frac{5QB\sin\phi}{6m}$$

$$= \frac{5CVB\sin\phi}{6(4\pi r^3 \rho_m/3)}$$

But $C = 4\pi\varepsilon_o r$

$$\omega_d = \frac{15\,\varepsilon_o VB\sin\phi}{6r^2\rho_m} \qquad (3)$$

The most pessimistic values of gyro potential V (= 1000 volts) for a glass gyro of radius r = 0.15m in the earth's magnetic field, $B = 0.5 \times 10^{-4}$ webers/m^2, with μ always perpendicular to B gives a worst case value of drift rate ω_d approximately equal to 0.1 arc sec per year, a negligible value. Hence, there is no need to do an exact integration of the torque over the orbital path.

The maximum volume electrical resistivity was set by the relaxation time τ, which depends on the satellite temperature. Let us take $\rho_e \approx 10^{12}$ ohm meter as a maximum value. A minimum value

of ρ_e is established by considering the torque due to induced currents of a conductive sphere rotating at approximately 100 cps in the earth's magnetic field. The torque depends on the depth of penetration which, for values of ρ_e as small as 1 ohm meter, is greater than the gyro diameter. Under this condition it is shown in Appendix A that the drift rate ω_d is

$$\omega_d = \frac{B^2 x 10^{-9}}{8\ \rho_e\ \rho} \tag{4}$$

where ω_d is in radians/sec., B is in gauss, ρ_e is in ohm cm and ρ is in gm/cm^3. B is 1/2 gauss for the earth's magnetic field, ρ = 2.5 gm/cm^3 for glass and, setting a maximum drift rate of 0.1 arc sec/year, the lower limit of volume electrical resistivity is obtained from (4) as $\rho_e > 835$ ohm cm $\approx$ 10 ohm meter.

Hence, the resistivity range has been tentatively established as

$$10^{12} > \rho_e > 10 \text{ ohm meter.} \tag{5}$$

An approximate worst case calculation for a sphere spinning in an electric field which induced charges slide along the resistive spherical surface as the sphere rotates shows that a negligible drift torque exists for ρ_e within the range shown in equation (5). This approximate calculation is shown in Appendix B.

The Satellite Gyro can acquire an electric charge because of collisions with ions and electrons during its trajectory (electro-hydrodynamic effect). For comparable electron and ion temperatures the thermal velocities of the electrons are higher than those of the ions or the velocity of the satellite; therefore, the electron flux hitting the satellite is much greater than that of the ions. A negative satellite potential is thus generated which builds up to an equilibrium value V_{eq} such that the electron and ion collision rates with the satellite are equal. Calculated values[2] of V_{eq} are approximately -0.8 volts whereas observed values of -6 volts have been measured. It has been shown that the larger value of V_{eq} produces negligibly small values of drift due to interaction with the earth's electric and magnetic fields. The effect of Coulomb drag on the drift rate will be investigated following the procedure of reference 4.

The Coulomb drag results from the Coulomb force between the negatively charged satellite and deflected or non-colliding ions and from the change in collision rate because of the Coulomb force between the colliding ions and charged satellite. As the satellite moves across the earth's magnetic field, it becomes polarized so that the cross-section for ion collision is increased in the region of the negative pole and decreased in the region of the positive pole. Ion deflection is also no longer symmetrical because of the polarized satellite. The resultant Coulomb drag force vector due to scattering acts at the center of the satellite gyro and hence causes no torque. The portion of the Coulomb drag due to non-symmetrical ion

collision does cause a torque, however, which is estimated as follows. Again, worst case conditions are taken. Reference 4 states that, for a 4-meter sphere at 1500 km. due to increased ion collision, the effective collision area is 10% larger than the projected area of the sphere while the Coulomb drag due to increased ion impacts is 2.3% of the drag of the uncharged sphere.

The increased effective diameter of the original one foot gyro is 12.6 inches. Assuming maximum effect, the center of the effective collision area is displaced 0.3 inches from the gyro center. The drag of the uncharged sphere at 900 miles altitude is, at worse $D \approx \frac{3}{2}\rho V^2 A = 3/2(2\times10^{-16}\ \text{kgm/m}^3)(50\times10^6\text{m/sec}^2)\pi(.15)^2\ \text{m}^2 \approx 10^{-9}$ newtons. The Coulomb drag is $.025\ D \approx 2.5 \times 10^{-11}$ newtons, which is applied 0.3 inches off center of the gyro. This gives a torque $T = 2.5 \times 10^{-11}\ (0.3 \times 10^{-2})(2.54) = 19 \times 10^{-14}$ newton meter. The worse case drift rate becomes $\omega_d = T/I\omega = 19 \times 10^{-14}/(0.3)(2\pi)(100) \approx 9.5 \times 10^{-16}$ rad/sec, an insignificant amount.

The optical method for determining the spin-axis orientation requires good reflective surfaces on the flat portions of the polygonal glass gyro. If conductive materials are used on the surface to satisfy the required high optical reflectivity, there would be an induced torque due to these metal surfaces rotating in the earth's magnetic field caused by interaction with the eddy current flow in the plates. Such torques could cause very high drift rates even though the conductive, vapor-deposited surfaces were very thin (in the region of 1000Å). One solution is to reduce the effective

eddy current loop areas by scribing narrow lines across the metallic surfaces. Another solution is to vapor deposit relatively high resistance, optically reflective surfaces such as germanium, silicon or tin-tin oxide on the glass gyro surface. The following analysis determines the maximum area of the effective current loops for a given surface resistivity and maximum allowable drift rate. To simplify the calculations worst case conditions will be assumed, resulting in an ample safety factor. It will be shown that aluminum surfaces require breaking up into smaller areas whereas surfaces of germanium, silicon, tin-tin oxide and other similar high resistance, high optical reflectance materials do not require this.

Consider a square loop of side a rotating with an angular velocity ω about axis Z, as shown in figs. 7.3 and 7.4. Let the magnetic field B make an angle α with respect to axis Z. The induced emf e for the sides labelled 1 and 2 are:

$$e_1 = B(\sin\alpha)a\omega r \cos(\theta-\phi) = Ba\omega r \sin\alpha(\cos\theta\cos\phi + \sin\theta\sin\phi)$$

$$e_2 = B(\sin\alpha)a\omega r \cos(\theta+\phi) = Ba\omega r \sin\alpha(\cos\theta\cos\phi - \sin\theta\sin\phi)$$

$$\Delta e = e_1 - e_2 = 2Ba\omega r \sin\alpha \sin\phi \sin\theta$$

But $\sin\phi = a/2r$.

$$\therefore \Delta e = Ba^2\omega \sin\alpha \sin\theta \qquad (1)$$

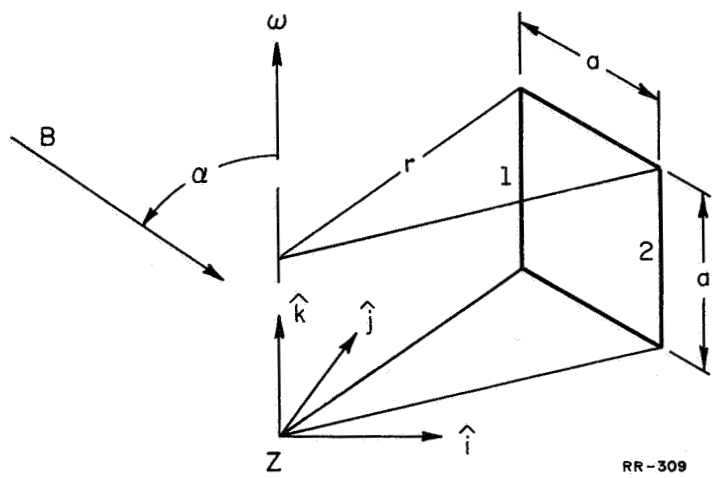

Figure 7.3

Loop Rotating in a Magnetic Field

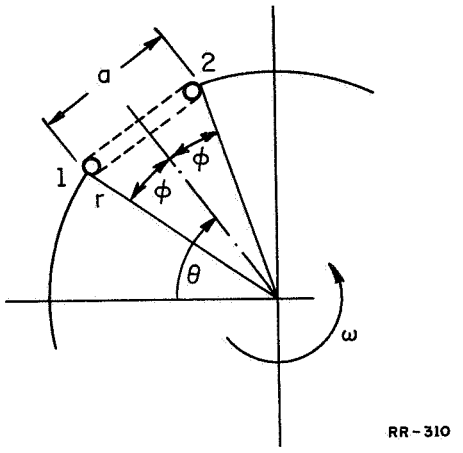

Figure 7.4

Loop Rotating in a Magnetic Field

Top View

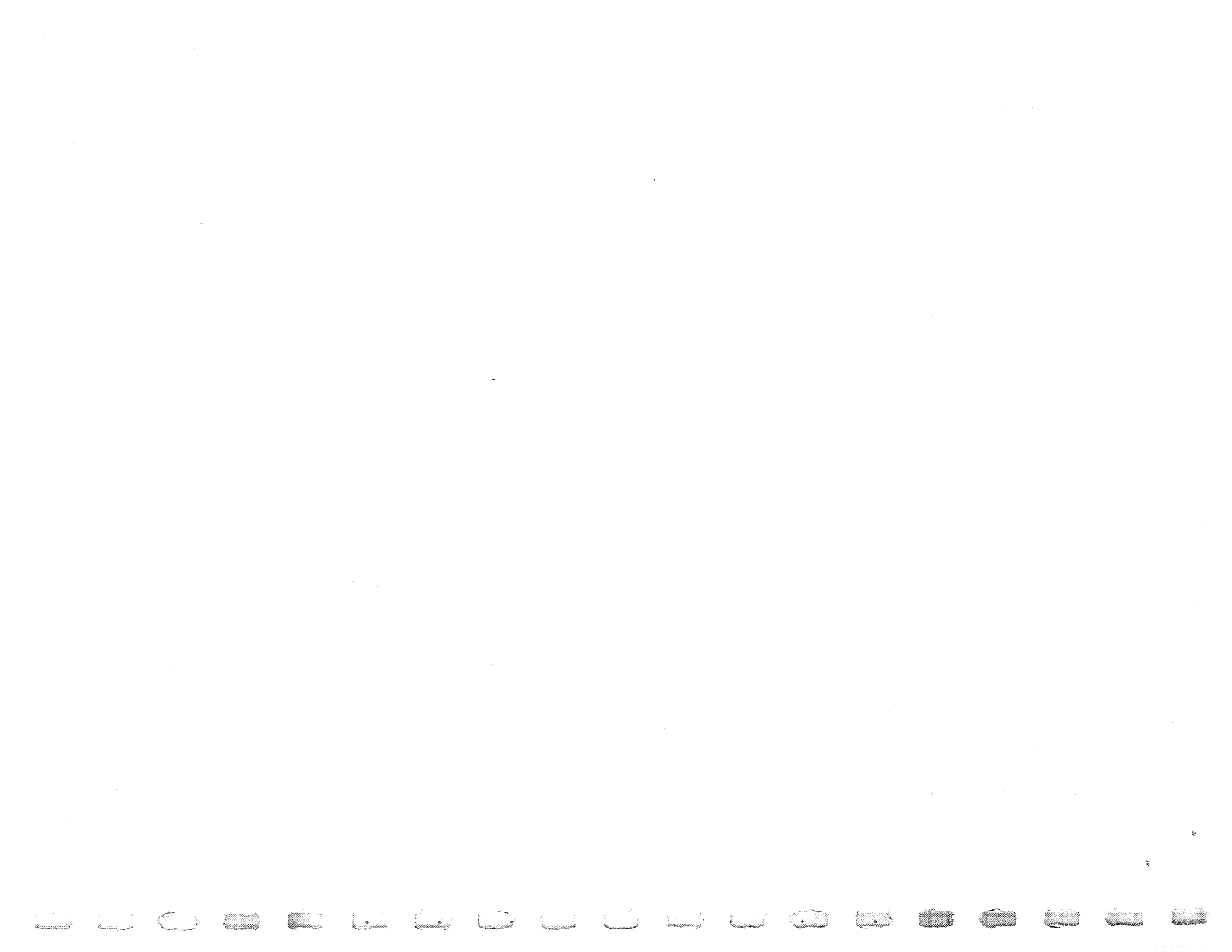

Making another simplification which provides a further safety factor in the end result, let the resistance of this loop be determined by considering the loop to be a flat plate of width a, path length 2a and effective cross sectional area ab/2. Therefore, $R = \rho\ell/A = \rho(2a)(2/ba) = 4\rho/b$ where b is the plate thickness. For the rotational frequency involved (100 cps), the skin depth for a good conductor is much greater than the plate thickness (1000 $\mathring{A}$). Since $\theta = \omega t$,

$$i = \Delta e/R = (Ba^2\omega b/4\rho) \sin\alpha \sin\omega t.$$

The magnetic moment μ becomes

$$\mu = ia^2 = (Ba^4\omega b/4\rho)\sin\alpha \sin\omega t = \mu_o \sin\omega t$$

The torque on this loop is $\bar{T} = \bar{\mu} \times \bar{B}$, and if we consider $\mu_o \sin\omega t$ as being equivalent to $\hat{i}\,\mu_o \cos\omega t + \hat{j}\,\mu_o \sin\omega t$ we have

$$T = \mu_o B \begin{vmatrix} \hat{i} & \hat{j} & \hat{k} \\ \cos\omega t & \sin\omega t & 0 \\ \sin\omega t & 0 & \cos\omega t \end{vmatrix} .$$

$$\bar{T} = \hat{i}\,\mu_o B\cos\alpha\sin\omega t - \hat{j}\,\mu_o B\cos\alpha\cos\omega t - \hat{k}\,\mu_o B\cos\alpha\cos\omega t.$$

The $\hat{k}$ torque component causes slowdown whereas the $\hat{i}$ and $\hat{j}$

components cause precession. From the previous equation, the maximum torque occurs when $\alpha = 45^{o}$.

$$T_{max} = \sqrt{2}\ \mu_o B \approx (0.3B^2a^4\omega b/4\rho)$$

The drift rate ω_d is obtained from the relation $\omega_d = T/I\omega$ where I is the gyro moment of inertia.

$$\therefore \omega_d = 0.3B^2a^4b/4I\rho. \qquad (2)$$

Consider the loop of fig. 7.1 cut up into n^2 smaller, adjacent but separate loops of side a/n. For simplification, assume that the plane of each loop is equidistant from axis Z, as in fig. 7.5. The induced potential of the i'th loop is, from equation (1)

$$\Delta e_i = B(a/n)^2\ \omega \sin\alpha \sin\theta_i$$

The resistance $R = \rho\ell/A = \rho(2a/n)(2n/ab) = 4\rho/b$

so that

$$i_i = (Ba^2\omega b/4n^2\rho) \sin\alpha \sin\omega t,$$

and if we let the currents from all the loops be in time phase the total magnetic moment from the n^2 elements is,

$$\mu = n^2 i_i (a/n)^2 = i_i a^2 = (Ba^4\omega b/4n^2\rho) \sin\alpha \sin\omega t.$$

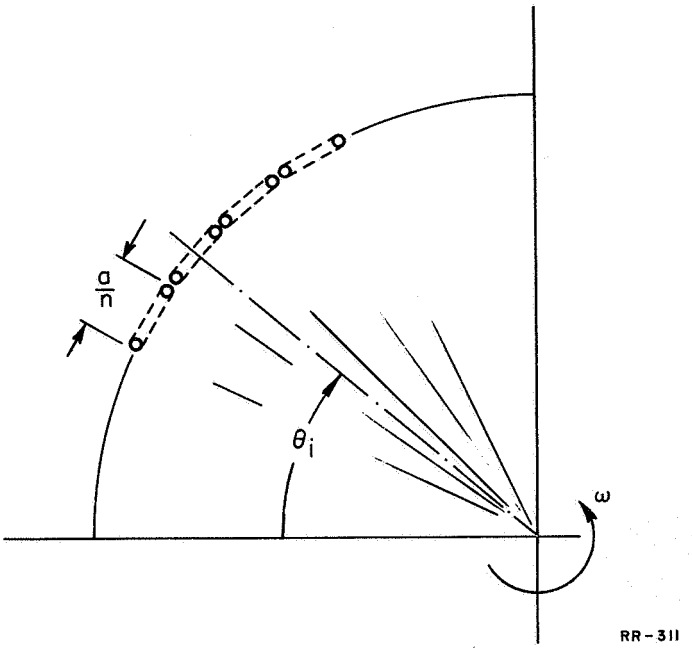

Figure 7.5

Loops Rotating in a Magnetic Field

Top View

The drift rate becomes $\omega_d \approx 0.3B^2a^4b/4n^2I\rho$ which is smaller than that of the original loop of side a by a factor of $1/n^2$. The worse-case drift rate will be calculated for each original gyro facet, then multiplied by the number of facets to obtain the resultant drift rate. If the drift rate is not negligible, a division by n^2 could make it so. The value of n determines the maximum size of the current loop areas and hence the distance between scribed lines on the facet surfaces.

One of the proposed gyro configurations is a sphere modified by cube oriented flats in which the area of the flats comprise half the area of the sphere. Chapter 9 describes this gyro in more detail. The diameter of each of the six facets is approximately 0.17 meter.

Consider the case of aluminum vapor-deposited to a thickness of 1000 $\mathring{A}$ onto the glass gyro surface. Substituting a = 0.17 meter, $B = 0.5 \times 10^{-4}$ weber/m^2 (earth's magnetic field). $\rho = 3\times10^{-8}$ ohm meter and I = 0.2 kgm-m^2 into equation (2), the drift rate for one facet becomes $\omega_d = 2.5 \times10^{-11}$ rad/sec. = 167 arc sec/year. Taking the worst case that the torques from each six facets are in space and time phase and that the resultant torque always causes the maximum precession, $\omega_d = 6 \times 167 \approx 1000$ arc sec/yr. To reduce this value to less than 0.1 arc sec/yr., n^2 must be larger than 10,000 or n must be at least 100. This means that at least 100 X 100 lines must be scribed on the surface of each facet, a laborious task.

On the other hand, vapor deposited germanium has a resistivity of about 10^5 larger than that of aluminum. This would cause a maximum drift rate of only 0.01 arc sec/year. Drift rates due to silicon and tin-tin dioxide surfaces would be even less.

Two other torques causing negligible drift rates are discussed in reference 1. These are the Barnett effect in which a rotating body develops a small magnetic dipole moment due to the revolving electronic systems within the atoms, and its inverse, the Einstein-de Haas effect, in which a body experiences a small torque due to a charging magnetic field.

7.1. Appendix A--Precession Due to the Interaction of a Rotating Sphere with a Constant Magnetic Field.

Part of this derivation closely follows Smythe[5], who treats the case of a conducting sphere in an alternating field. The magnetic field $\bar{B}$ may be defined in terms of a vector potential $\bar{A}$ so that

$$\bar{B} = \nabla \times \bar{A} \tag{A-1}$$

From Maxwell's equations and Ohm's Law, then it is shown that the solution of a magnetic field problem is equivalent to the solution of the following linear partial differential equation involving the vector potential:

$$\nabla^2 \bar{A} = \frac{\mu_o}{\rho_e} \frac{\partial \bar{A}}{\partial t} \tag{A-2}$$

where:

μ_o is the permitivity of free space (assumed equal to the material)

ρ_e is the resistivity of the rotor material

As a result of the linearity of this equation it is possible to introduce complex notation in its solution. That is, let

$$\bar{A} = R_e\left(\hat{\bar{A}}(x_i,t)\right)$$

$$\hat{\bar{A}}(x_i,t) = \hat{\bar{A}}(x_i)e^{i\omega t} \tag{A-3}$$

where

x_i represents the coordinates of the system

t is time, and

ω is the angular velocity of the rotor

$i = \sqrt{-1}$

Equation 2 now becomes

$$0 = (\nabla^2 - i\omega\mu_o/\rho_e)\ \hat{\bar{A}}$$

Note that $\omega\mu_o/\rho_e$ has dimensions of reciprocal length squared. Let

$$\delta = \sqrt{2\rho_e/\omega\mu_o}$$

The quantity δ is called the depth of penetration.

Finally, the equation that we wish to investigate is

$$0 = (\nabla^2 - 2i/\delta^2)\ \hat{\bar{A}} \qquad \text{(A-5)}$$

The general solution to the problem of the interaction between the rotating sphere and the magnetic field may be obtained by assuming suitable boundary conditions on equation (A-5). Figure 7.6 shows a sphere of exterior radius a and internal radius b whose spin axis vector makes an angle α with the magnetic field vector $\bar{B}_o$. The rotor is assumed to have a resistivity ρ_e and permeability

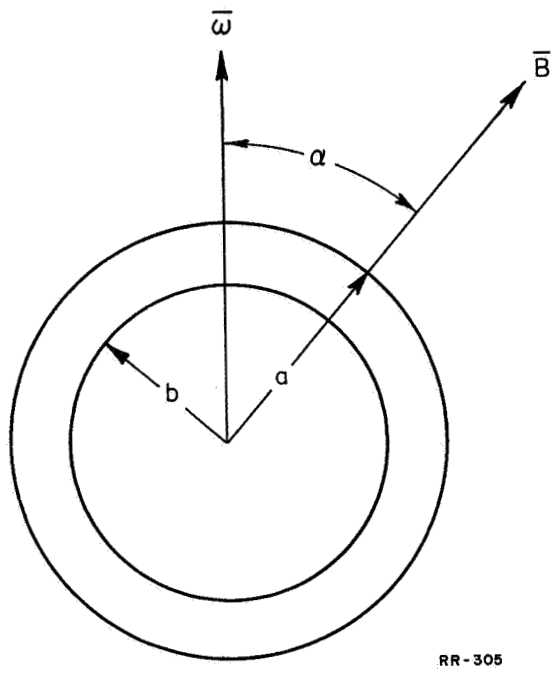

Figure 7.6

Shell Rotating in a Magnetic Field

μ_o (that of free space) and is rotating at an angular velocity ω. Thus the depth of penetration, δ, is uniquely defined by equation A-5. An appropriate set of boundary conditions is that both the vector potential and the magnetic field be continuous at both boundaries. The magnetic field is continuous because of the simplifying assumption that the permitivity of the conductor is the same as that of free space - certainly valid for all conductors except those which are ferromagnetic.

In a coordinate system fixed to the rotating sphere, the magnetic field with respect to the sphere is

$$\bar{B}_o = B_o(\hat{i} \sin\alpha \cos\omega t + \hat{j} \sin\alpha \sin\omega t + \hat{k} \cos\alpha)$$

where r, the radius vector from the rotor center, is large. By inspection the magnetic vector potential is

$$\bar{A} = \frac{1}{2}B_o\Big[\hat{i}(-y\cos\alpha - z \sin\alpha \sin\omega t) + \hat{j}(x\cos\alpha - z\sin\alpha \cos\omega t)$$

$$+ \hat{k}(x\sin\alpha \sin\omega t + y\sin\alpha \cos\omega t)\Big]$$

Transforming each of the components into a spherical coordinate system, (r, θ, ϕ), the vector potential becomes (considering only the time-dependent terms)

$$\hat{\bar{A}}_o = \frac{1}{2}B_o r\sin\alpha \; \bar{\Phi} \; e^{i\omega t} \qquad \text{(A-6)}$$

where

$$\bar{\Phi} = (\hat{i}i-\hat{j})\cos\theta-\hat{k}i\sin\theta e^{i\phi}$$

The form of the vector potential at infinity suggests a solution of the form

$$\hat{\bar{A}} = \frac{1}{2}B_o \sin\alpha e^{i\omega t} R(r)\bar{\Phi}(\theta,\phi)$$

Substitute into equation (A-5) and separate variables for each component in the usual manner. It can then be ascertained that the radial part (Rn), must satisfy the following differential equations in the shell:

$$\frac{d^2R}{dr^2} + \frac{2}{r}\frac{dR}{dr} - \left(\frac{i}{\delta^2} + \frac{2}{r^2}\right) R = 0$$

and in free space:

$$\frac{d^2R}{dr^2} + \frac{2}{r}\frac{dR}{dr} - \frac{2}{r^2} R = 0$$

The equation in free space has solutions r and r^{-2}. The variables in the differential equation in the shell are changed as follows:

$$V = V(r) = \sqrt{i}\, r/\delta$$

$$R = r^{-\frac{1}{2}} I$$

This equation can then be recognized as Bessel's modified differential equation

$$\frac{d^2I}{dV^2} + \frac{1}{V}\frac{dI}{dV} - \left(1 + \frac{9}{4}\frac{1}{V^2}\right) = 0$$

The radial solution may be written as follows:

$$R = Cr + Dr^{-2} \qquad r > a$$

$$R = r^{-\frac{1}{2}}\left[EI_{3/2}(V) + F\, I_{-3/2}(V)\right], \qquad a > r > b$$

$$R = Gr \qquad b > r > 0$$

Where $I_{3/2}(V)$ and $I_{-3/2}(V)$ are the modified Bessel functions of order 3/2 and -3/2 and C, D, E, F, and G are constants (possibly complex) to be determined by the boundary conditions. Note that the condition that the magnetic field B be continuous is equivalent to the condition that the derivative of A with respect to r be continuous. The important constants are those which determine the field inside the spherical shell. After a large amount of algebraic manipulation, the vector potential inside the shell in phasor notation is

$$\hat{\bar{A}} = \frac{1}{2}B_o \sin\alpha e^{i\omega t} R(r)\, \bar{\Phi}$$

where

$$R = \frac{3a}{V(r)^2}\Big[\Big\{V(r)\left[3+V(b)^2\right] - 3V(b)\Big\}\cosh\left[V(r)-V(b)\right] + \Big\{3V(b)V(r) - \left[3+V(b)^2\right]\sinh\left[V(r)-V(b)\right]\Big\}\sinh\left[V(r)-V(b)\right]\Big] \Big/ \text{Denom.}$$

where Denom = $3V(b)\cosh[V(a)-V(b)]+[3+V(b)^2]\sinh[V(a)-V(b)]$

7.1.1. The Precessional Torque

The torque which tends to precess the rotor is due entirely to the interaction of the current rings and the $\hat{k}$ component of the magnetic field. This can be ascertained by looking at the form of the vector Φ. From the form it is seen that the induced current flow lines are circles whose planes are parallel to the k axis. The precession torque is proportional to the triple vector product

$$\bar{r} \times (\bar{j} \times \bar{B}_o),$$

$$\bar{j} = \frac{1}{\rho_e} \frac{d\hat{\bar{A}}}{dt}$$

integrated over the volume of the shell. Thus

$$\bar{T} = \int_V [\bar{r} \times (\bar{j} \times B_o)] \, dV$$

which, after performing the angle integrations, reduces to

$$\bar{T} = Re \int_b^a r^3 R(r) dr \; . \; (\pi\omega B_o^2 \sin 2\alpha)/3\tau . \; (-\hat{i} + \hat{j}i)$$

And finally the torque for the shell is

$$\bar{T} = \frac{\pi B_o^2 \sin 2\alpha}{3\mu_o} R_e\Big[(-\hat{i}+\hat{j}i) \times 3a\delta^2\Big\{[[3+V(b)^2][3+V(a)^2]-9V(a)V(b)]\sinh[V(a)-V(b)]$$

$$+ 3[V(a)-V(b)][V(a)V(b)-3]\cosh[V(a)-V(b)]\Big\} \Big/ \text{Denom }]] \qquad \text{(A-6)}$$

where $\text{Denom} = 3V(b)\cosh[V(a)-V(b)]+[3+V(b)^2\sinh[V(a)-V(b)]$

The relation for the solid rotor is obtained by setting $b = 0$ in equation (A-6). After separating reals and imaginaries, the following form results

$$\bar{T} = \frac{\pi B_o^2 a^3 \sin 2\alpha}{\mu_o}\left\{3\hat{i}\left[\frac{\delta^2}{a^2} - \frac{\delta\sinh(\sqrt{2}a/\delta)+\sin(\sqrt{2}a/\delta)}{\sqrt{2}a\cosh(\sqrt{2}a/\delta)-\cos(\sqrt{2}a/\delta)}\right]\right.$$

$$\left. + \hat{j}\left[1 - \frac{3\delta}{\sqrt{2}a}\,\frac{\sinh(\sqrt{2}a/\delta)-\sin(\sqrt{2}a/\delta)}{\cosh(\sqrt{2}a/\delta)-\cos(\sqrt{2}a/\delta)}\right]\right\} \qquad \text{(A-7)}$$

The high frequency limit ($\delta << a$) is

$$\bar{T} = \hat{j}\,\frac{\pi B_o^2 a^3 \sin 2\alpha}{\mu_o}$$

The low frequency limit ($\delta >> a$) is

$$\bar{T} = \hat{i}\,\frac{\pi a^5 \omega B_o^2 \sin 2\alpha}{15\,\rho_m}$$

Thus, we see that at the high frequency limit the torque is independent

of the sphere material and is only a function of the field and the spherical volume. At the low frequency limit, since ωa^5 is proportional to the angular momentum, the precession rate is independent of the size of the rotor and dependent only on the density, the magnetic field and the resistivity of the rotor. The precession rate for this case is

$$\Omega = \frac{B_o^2}{8\rho_e\rho_m} \times 10^{-9}$$

where

B is in gauss

ρ_e is in ohm cm

ρ_m is in gm/cm^3

A suitable precession rate may be obtained by the use of a semiconductor material with a resistivity of the order of 1-10 ohm cm.

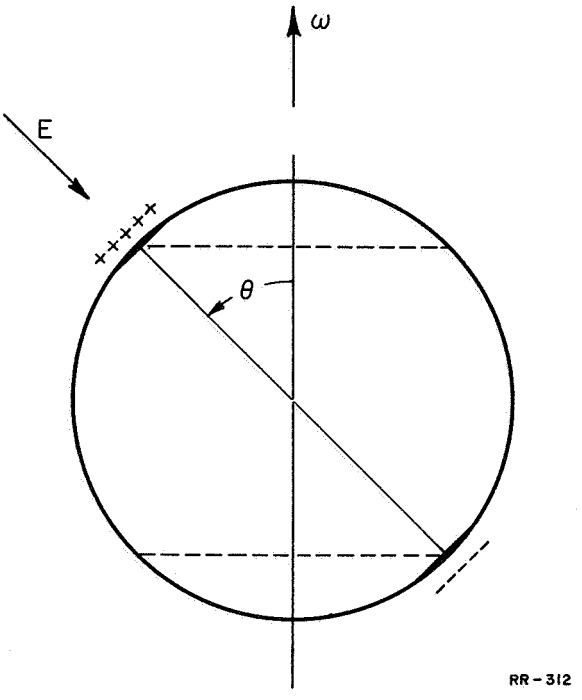

Figure 7.7

Conductive Sphere Spinning
in an Electric Field

7.2. Appendix B-- Approximate Worst Case Drift Calculation Due to Induced Charges Sliding Along a Spinning Sphere in an Electric Field.

In order to calculate the maximum current flowing on the surface, the sphere will be considered as a good conductor. To get the maximum power consumption P and hence the torque, the largest resistivity will be used with the maximum current to obtain the worst case. This drift is shown to be negligible.

Given a spinning sphere of radius a immersed in an electric field E making an angle θ with the spin axis, as shown in fig. 7.7. The induced charge Q is obtained from

$$Q = \epsilon \oint_A \bar{E} \cdot d\bar{A}$$

where the projected area of the sphere is used for $d\bar{A}$.

$$\therefore Q = \epsilon \, E\pi a^2$$

It is shown in field theory that the electric field distribution on the spherical surface is sinusoidal. We assume that the charge is also sinusoidally distributed, and take an equivalent width of about 1/3 of the half-circumference in which the charge density is considered constant. Let this charge travel the average path shown by the dotted lines.

$$\therefore i = Q/t = fQ = \omega Q/2\pi$$

$$\therefore \rho = 2i^2R = \frac{2\omega^2Q^2}{4\pi^2}\frac{\rho\ell}{A}$$

where $\ell = 2\pi a \sin\theta$

A = width w x depth of penetration δ

$w = \pi a/3$,

$\delta = \sqrt{2/\omega\mu\sigma}$

μ = permeability of vacuum = $4\pi \times 10^{-7}$

$\sigma = 1/\rho e$

$$\therefore P = \frac{3\omega^2Q^2}{\pi^2}\sqrt{\frac{\omega\mu P_e}{2}}$$

But $\rho = \bar{F}\cdot\bar{v} = \bar{T}\cdot\bar{\omega}$

Hence $T = P/\omega\sin\theta$

For the worst case, $\theta = 90^o$, so that $T = \rho/\omega$.

$\omega_d \approx T/I\omega$, where $I = 2ma^2/S$

$$\therefore \omega_d \approx \frac{45}{8\pi}\frac{\epsilon^2E^2}{a\,\rho_m}\frac{\omega\mu\rho e}{2}$$

where ρ_n is the mass density and ρ_e is the electrical resistivity.

Substituting the values $E = 100$ v/n, $\rho_n = 2.5 \times 10^3$ kgm/m^2, $a = 0.15$ m, $\rho_e = 10^{-14}$ ohm meter, $\mu = 4\pi \times 10^{-7}$ henry/m and $\epsilon = 8.85 \times 10^{-12}$ farad/m, the value of ω_d becomes approximately 0.001 arc sec/year, a negligible value.

1. Lange, B., "The Drag-Free Satellite," A.I.A.A., Journ., Vol. 2, No. 9, p. 1602 (1964).

2. Chopra, K. P., "Interactions of Rapidly Moving Bodies in Terrestrial Atmosphere, Rev. Mod. Phys., Vol. 33, No. 2, 1961, p. 160.

3. Jen, N. C., "Satellite Potential in an Ionized Atmosphere," A.I.A.A. Journ., Vol. 3, No 4, p. 714 (1965).

4. Hohl, F., and Wood, G. P., "The Electrostatic and Electromagnetic Drag Forces on a Spherical Satellite in a Rarefied Partially Ionized Atmosphere," Vol. II, Supplement 2, 1963, Advances in Applied Mechanics, Academic Press, N. Y.

5. Smythe, W. R., "Static and Dynamic Electricity," McGraw Hill, 1950, p. 397 ff.

8.1. Introduction

The relativity satellite, as proposed at C.S.L., will be tracked photographically by the network of Baker-Nunn satellite tracking cameras operated by the Smithsonian Astrophysical Observatory. Both orbital elements and spin axis direction must be obtained by means of photographs against the stellar background. The physical size and reflectivity of the satellite are prescribed in part by the input exposure requirements of the Baker-Nunn camera, which are explained in Chapter 9 of this report.

To optically track a passive satellite three conditions of observability must be satisfied.

(1) The observing station must be in darkness so that the sunlight reflections will be visible in the night sky. For this study, it was assumed that the sun must be at least 10^{o} below the horizon for any observation to be made.

(2) The satellite must appear above the horizon at the observing station in question. In general, there is some lower limit on the elevation angle of satellite photographic equipment, and the Baker-Nunn camera has a lower limit of about 14.5^{o}. The maximum elevation angle for a given orbit and observing station depends on the satellite altitude and the angle between the earth station and the plane of the orbit. Assuming circular orbits, Fig. 8.1 shows the maximum elevation angle vs. the angle between the observing station and the orbital plane for orbital altitudes from 200 km to 1200 km. This angle may be interpreted as the station north or south latitude if the orbit and

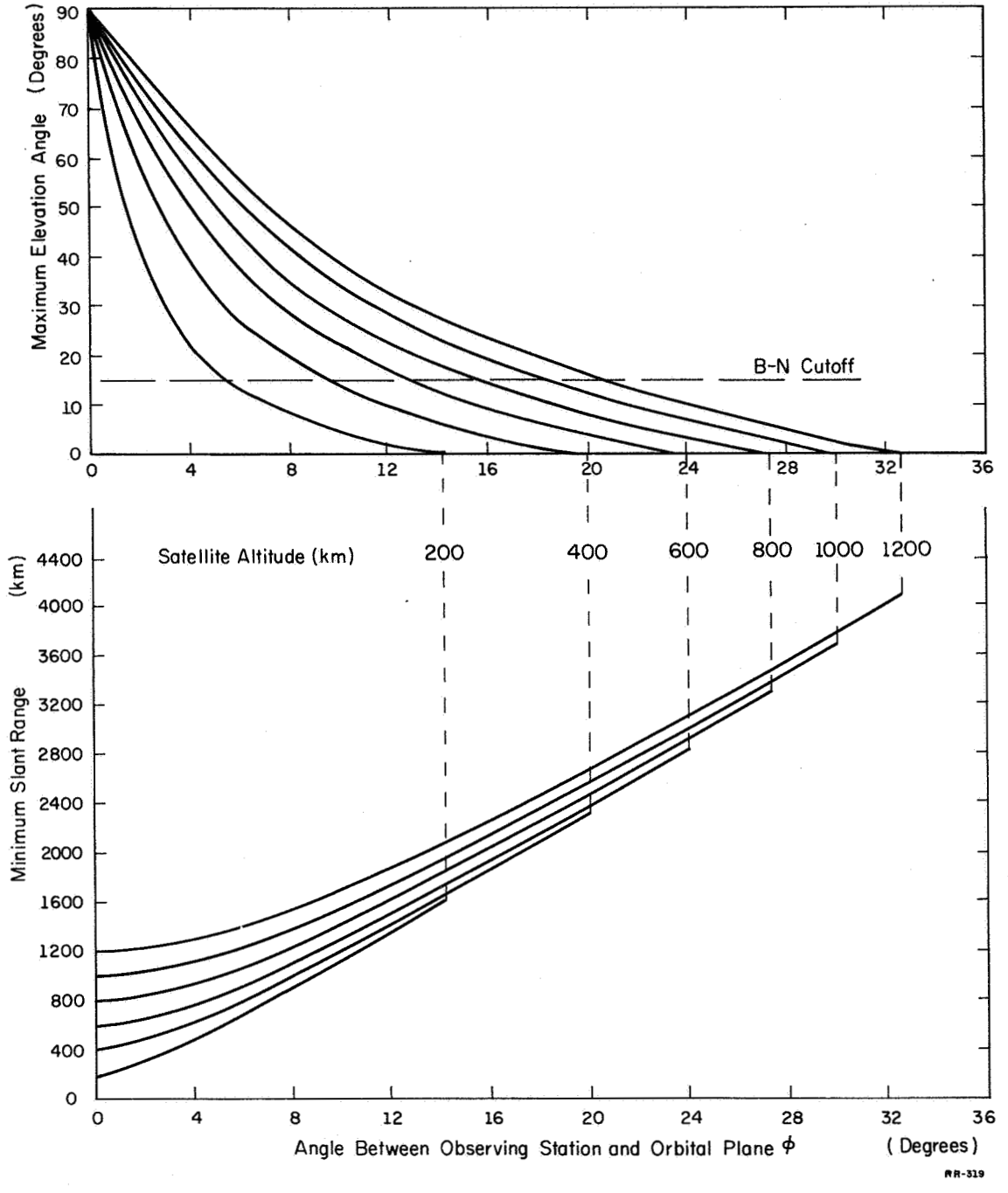

Figure 8.1

Elevation angle and slant range of a satellite whose radius vector makes angle φ with the radius vector to a terrestrial tracking station.

the earth's equator are coplanar. When the satellite appears at its maximum elevation angle, the slant range to the observing station is a minimum. The minimum slant ranges are also shown in Fig. 8.1. Thus a satellite at an altitude of 1000 km in an equatorial orbit could be photographed by a Baker-Nunn camera from any station within 18^{o} latitude, and the minimum slant range would be between 1000 km and 2400 km.

(3) The satellite must be in sunlight.

To obtain spin axis orientation data an additional requirement is that sunlight be reflected from at least one of the plane mirror facets on the satellite during a pass over a given station. Digital computer simulations written at C.S.L. and run on the CDC 1604 computer have been used to determine the best locations of mirrors on the gyroscope-satellite.

Two basic programs have been used. Program SATOBS (satellite observation) simulates each orbital pass which can possibly be observed from a given station and determines a useable range of mirror normals for each pass. Program ENVO (envelope of observability) computes an envelope of the observable mirror normals by using a minimizing technique and runs about 10 times faster than SATOBS; however, its use is limited to circular orbits.

8.2. Programs SATOBS and COUNT

Two digital computer programs have been written for the CDC 1604 computer at C.S.L. to simulate a passive satellite in orbit around the earth and to graphically depict the expected observation times and, in particular, the distribution of mirror normal angles which would reflect sunlight to given earth stations over a period of one year. In the satellite observation (SATOBS) program, radius vectors from the earth's center to the sun, earth station, and satellite are computed at fixed intervals of time, usually every three minutes, until the three observability conditions are satisfied. The first of these conditions, station in darkness, is satisfied whenever

$$\frac{\underline{R}}{|\underline{R}|} \cdot \hat{R}_s < \cos 100^\circ \tag{8.1}$$

where

$\underline{R}$ = radius vector to observing station

$\hat{R}_s$ = unit vector to sun

That is, the sun must be at least 10° below the horizon. The second condition, satellite above horizon, is satisfied whenever

$$\frac{\underline{R} \cdot \underline{S}}{|\underline{R}|\,|\underline{S}|} \geq \cos 75^\circ \tag{8.2}$$

where

$\underline{S} = \underline{r} - \underline{R}$ = slant range vector

$\underline{r}$ = radius vector to satellite.

Eq. (8.2) specifies that the angle measured from zenith to the satellite must be less than or equal to 75^{o}, thus assuring that the satellite is at least 15^{o} above the horizon. The third condition may be specified by inspection of the sketch of the plane containing

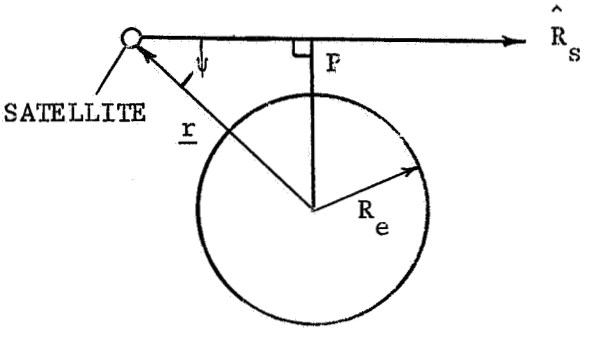

PLANE OF SUN, SATELLITE AND CENTER OF THE EARTH

the sun, satellite, and earth center. For sunlight to reach the satellite, it is necessary that P, the perpendicular from the earth center to the satellite-sun line, be greater than R_e, the radius of the earth. This is assured if

$$|r| \sqrt{1 - \cos^2 \psi} > R_e \tag{8.3}$$

$$\text{where } \cos \psi = \hat{R}_s \cdot \frac{\underline{r}}{|r|}$$

A "pass" of the satellite is defined as that period of time when all three conditions are satisfied. At the time instant when the three conditions (8.1)-(8.3) are first satisfied, the computer "backs up" one time increment, shortens the increment to 20 seconds, and proceeds to compute the radius vectors during an observable pass of the satellite. During a pass, additional computations at each time instant

determine the unit vector normal to a flat mirror on the satellite which would reflect sunlight to the ground station, and the "flash angle" or angle from the satellite spin axis to the mirror normal is calculated. In general, the flash angle may vary as much as 70^{o} in a given pass, and may have a relative maximum or minimum. Fig. 8.2 shows the flash angle variation computed by SATOBS through four passes of a satellite in a 1000 km equatorial orbit over a tracking station on the earth's equator. The plot shows that flashes could be obtained twice in one pass from each plane mirror whose normal makes an angle of say 50^{o}, 60^{o}, 110^{o}, or 120^{o} from the satellite spin axis. The maximum duration of any pass is somewhat more than 1000 seconds, or about 16 minutes. SATOBS stores flash angle data on magnetic tape and program COUNT reads the data and counts the number of times any specified mirror normal angle would produce flashes for a given orbit and station location. To save time and tape storage space, only the values of flash angle and time at the endpoints and at flash angle extremes for each pass are stored.

Program COUNT also produces calcomp plots of flash angle data for a whole year, in which the time scale is greatly compressed relative to that shown in Fig. 8.2, and each pass appears as a vertical line. Computer plots of flash angle data for the Baker-Nunn station at Curacao and a satellite in 1000 km orbit at inclinations of 0^{o}, 5^{o}, and 10^{o} are shown in Fig. 8.3 (a), (b) and (c); the satellite spin axis is directed at the vernal equinox. These plots show the dates of observation of any mirror on the spinning satellite.

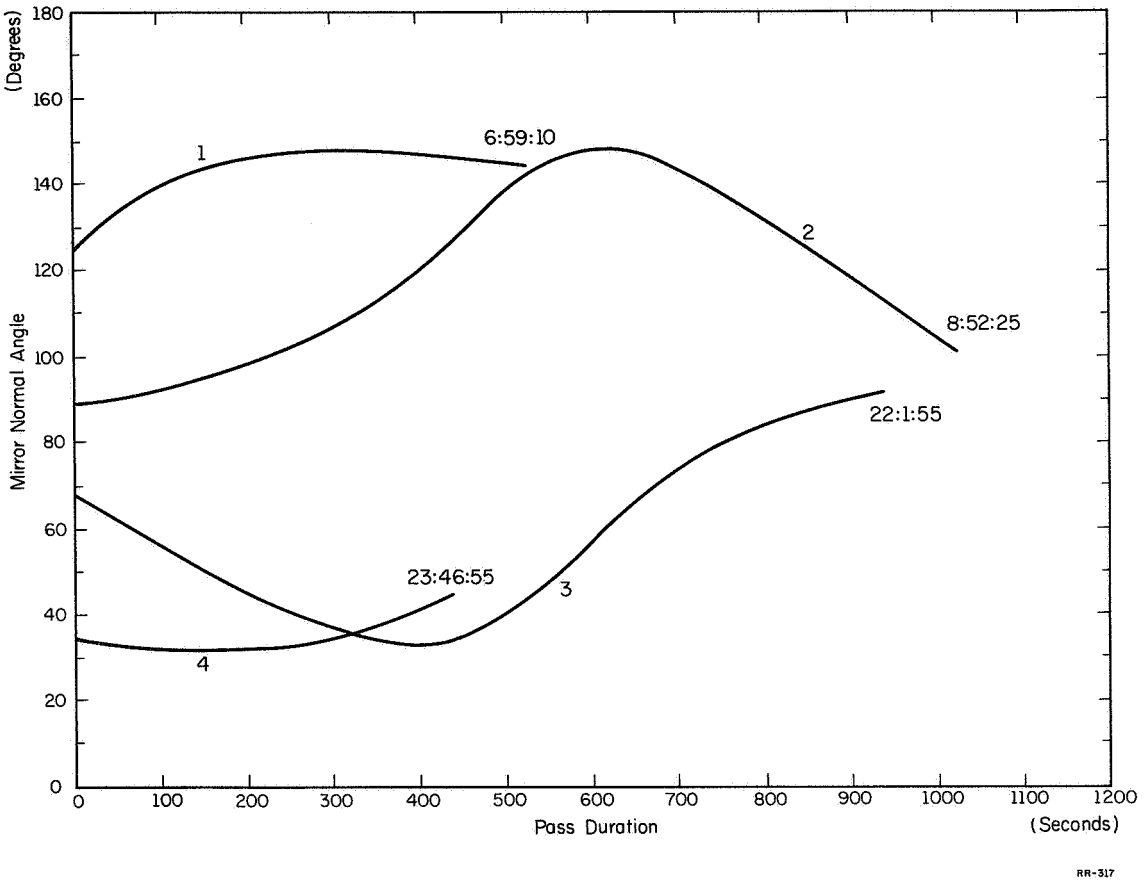

Figure 8.2

Angle from satellite spin axis to the vector normal to mirror which reflects sunlight to tracking station vs. time. Four passes in one day are shown of satellite in 1000 km equatorial orbit over fictitious tracking station located on the earth's equator. Greenwich mean time is listed at the end of each pass. The satellite spin axis is directed toward the vernal equinox.

It appears that flashes reflected from a mirror on either end of the spin axis (flash angle = 0^{o} or 180^{o}) are almost nonexistent, and mirror normals between 40^{o} and 140^{o} from the spin axis will be sighted most frequently. The average frequency of passes over the station is about two per day and if the satellite has six mirrors at angles of 42^{o}, 54^{o}, 71^{o}, 109^{o}, 126^{o}, 138^{o} (six faces of a cube), many of the passes will produce reflections from more than one mirror.

Comparison of Fig. 8.3(a) with Figs. 8.3(b) & (c) illustrates the effects of the regression of the orbit line of nodes due to the earth's oblateness. For zero inclination the node line is undefined, but for any finite inclination, the minimum angle between the station and satellite radius vectors occurs at varying positions relative to the sun line. Therefore, if the inclination is too large, there will be times when the satellite is not visible at the observing station at night time. The critical inclination can be found from Fig. 8.1 and the station latitude. In this figure, it can be seen that depending on satellite altitude, there is a certain maximum angle ϕ_m between the station and satellite such that observation is not possible from a Baker-Nunn tracking station. For example, at satellite altitudes of 800, 1000, and 1200 km the ϕ_m are 16^{o}, 18.6^{o}, 20.8^{o} respectively. Consequently, morning or evening observations can be made continuously only if the sum of station latitude and orbit inclination is less than ϕ_m. For the case of the 1000 km orbit being sighted from Curacao, latitude 12^{o}n, the critical inclination is $18.6^{o}-12^{o} = 6.6^{o}$. This explains the modulated effect on the flash angle distributions

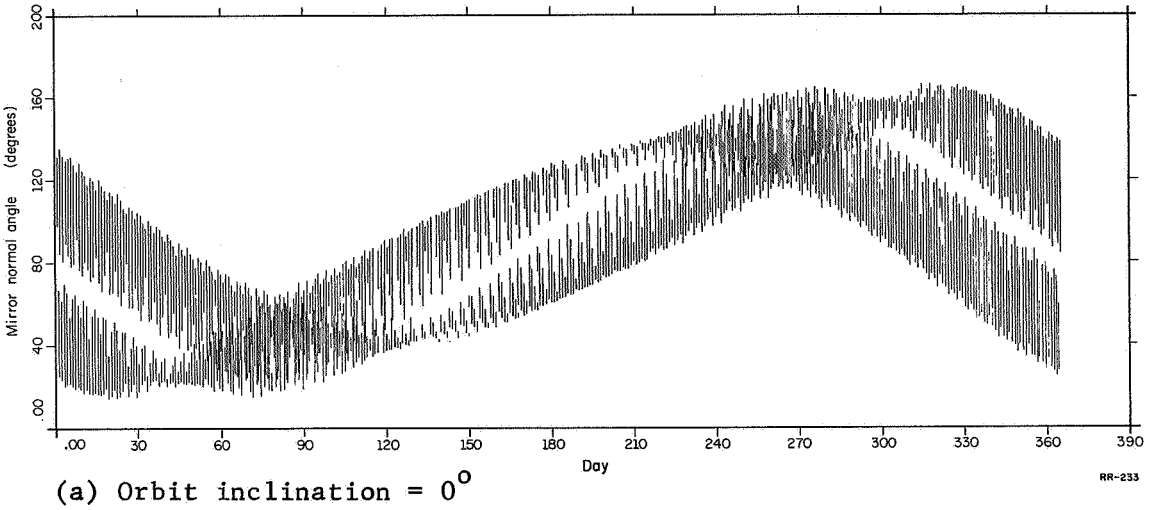

(a) Orbit inclination = 0^{o}

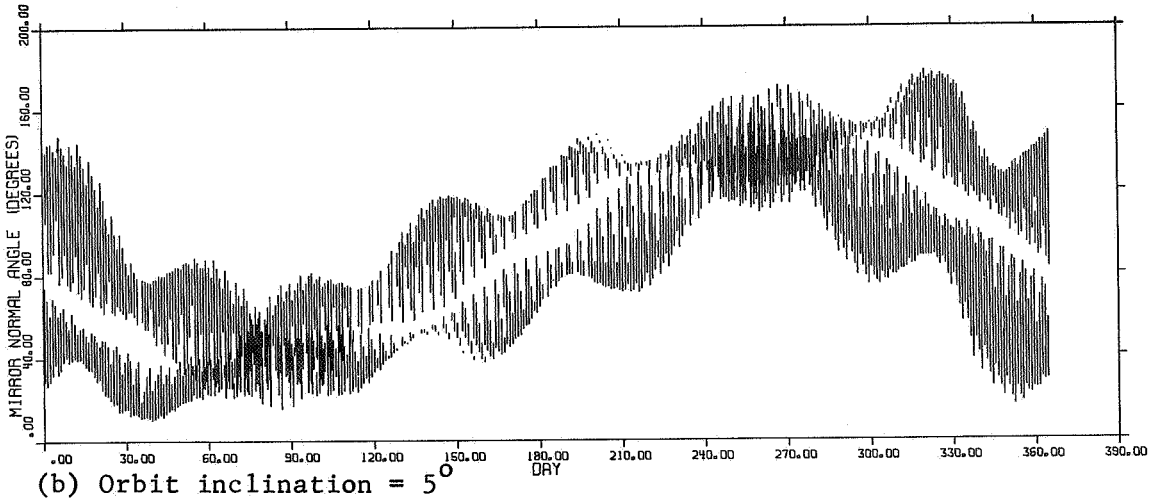

(b) Orbit inclination = 5^{o}

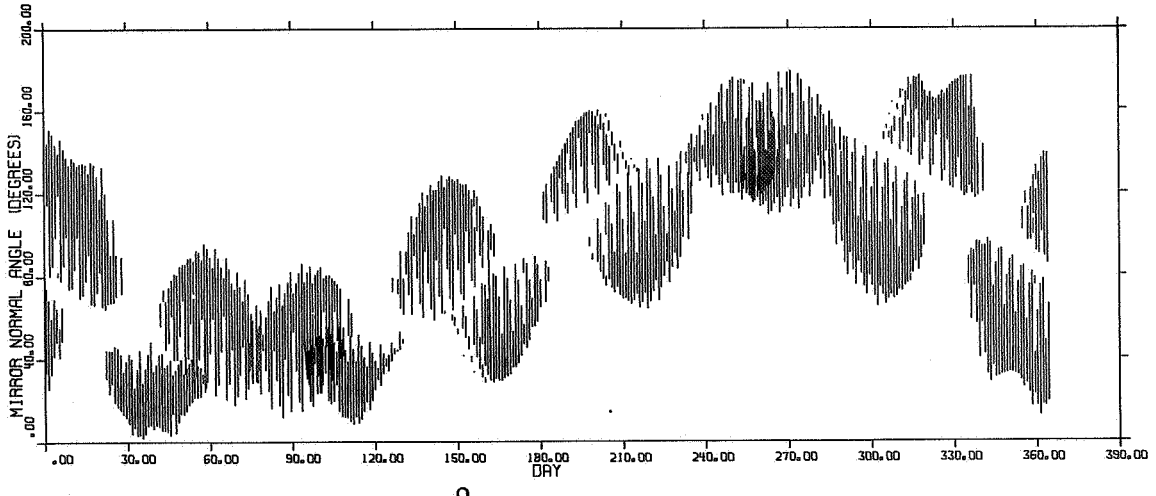

(c) Orbit inclination = 10^{o}

Figure 8.3

Flash angle distributions for tracking station Curacao, position 12^{o}N, 291^{o}E. The data are for circular orbits of 1000-km altitude, satellite spin axis along the vernal equinox line.

exhibited in Fig. 8.3(b) and (c) and the gaps in the pattern of Fig. 8.3(c), since $i = 10^{o}$. The modulation frequency is about seven cycles per year, the sum of six cycles per year nodal regression and, in the opposite direction, one cycle per year of the earth's rotation about the sun.

Fig. 8.4 shows the number of sightings accumulated over a year's time as a function of mirror normal angle. The data for this plot were obtained from the flash angle distributions shown in Fig. 8.3. It is seen that on the average, the number of sightings from the Curacao station decreases as the orbital inclination increases.

The satellite in a 1000 km equatorial orbit would not be visible from stations above 18.6^{o} latitude and since only two of the SAO network stations (Curacao and Arequipa, Peru, lat 16^{o} s) could be used to track the equatorial orbit, it was desired to check the feasibility of inclining the orbit so that other stations could be used. Fig. 8.5 shows the flash angle distributions for the tracking station at Maui, Hawaii for orbits of 5^{o} and 10^{o} inclinations. As could be expected, the sighting frequency at this station increases with the orbit inclination, and will reach a maximum at some particular inclination. However, the orbit cannot be inclined so much that the relativity effect is appreciably diminished (by the factor $(1 + \cos 2i)/2$) or that extraneous torques become more of a problem. The optimization of the orbit parameters for the relativity experiment is the subject of a Ph.D. thesis to be published by J. L. Myers.

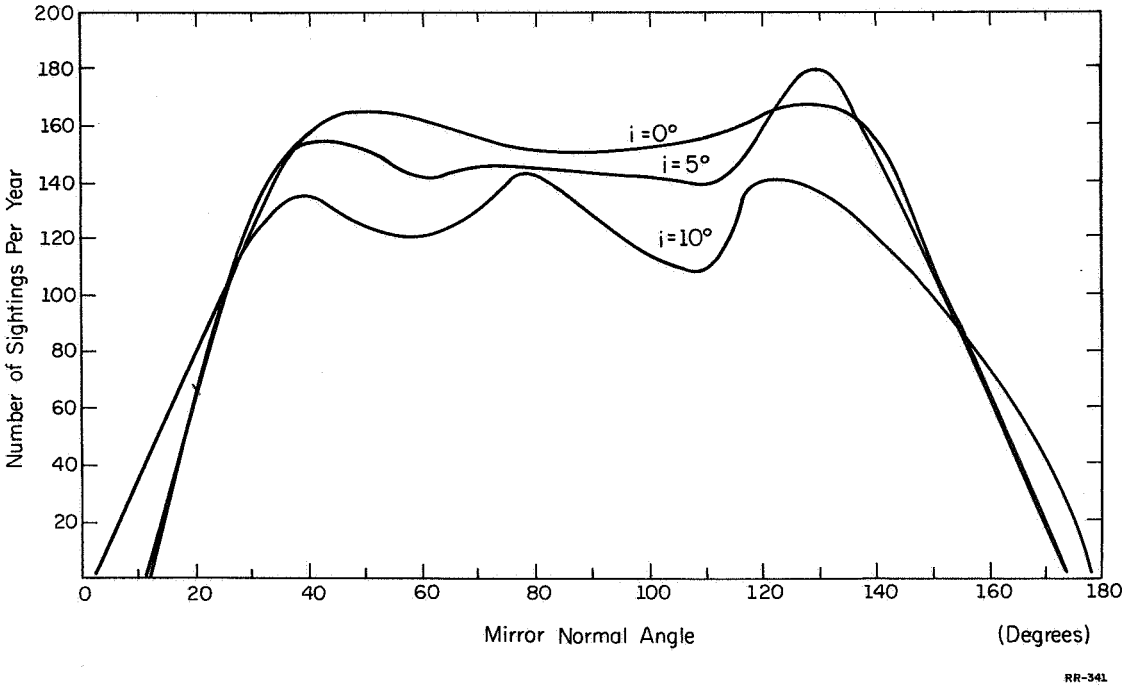

Figure 8.4

Cumulative number of satellite sightings per year vs. mirror normal angle. Orbit and tracking station are the same as those listed in Fig. 8.3.

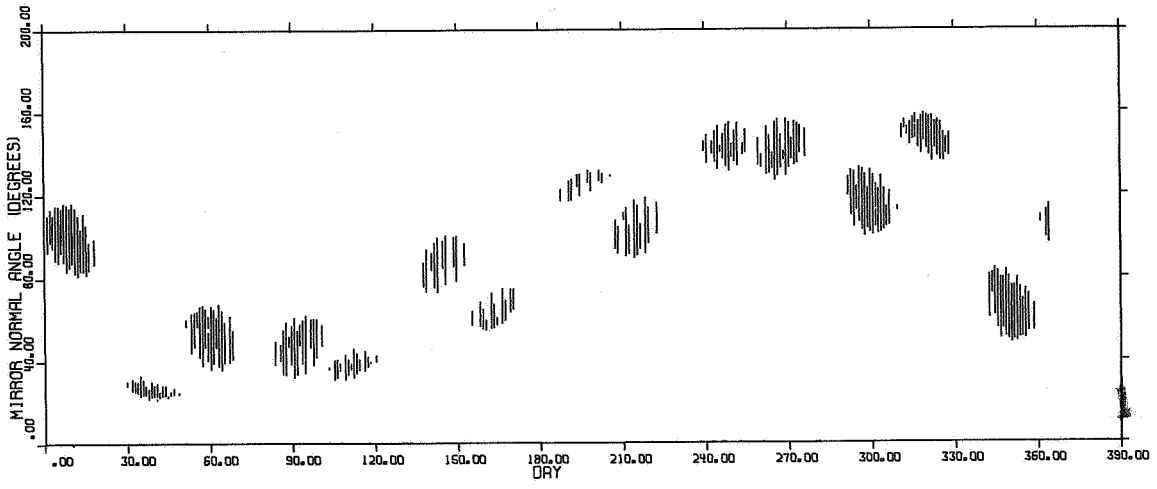

(a) Orbit inclination = 5^{o}

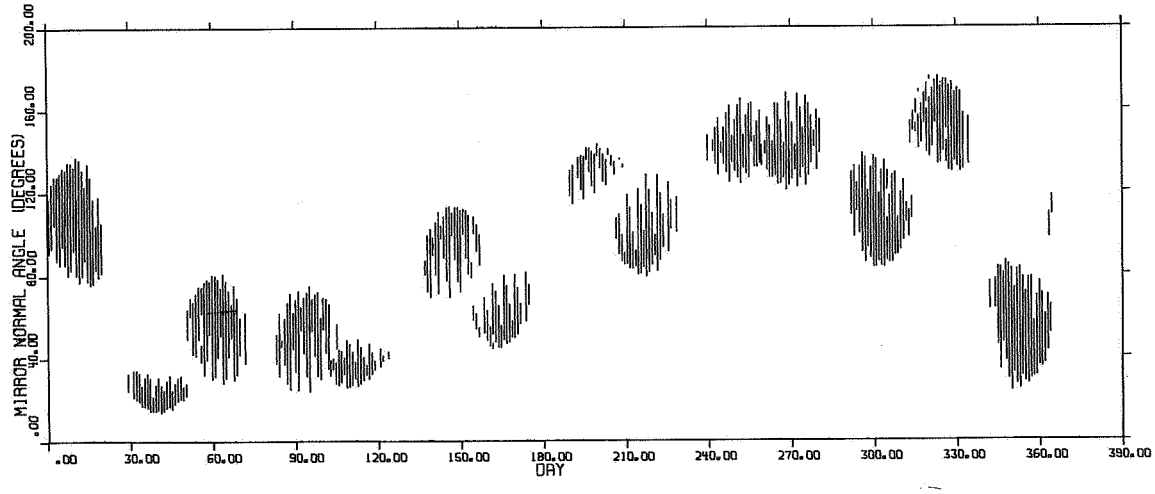

(b) Orbit inclination = 10^{o}

Figure 8.5

Flash angle distributions for tracking station Maui, Hawaii, position 20.7^{o}N, 203.7^{o}E. Data are for circular orbits of 1000-km altitude, satellite spin axis along the vernal equinox line.

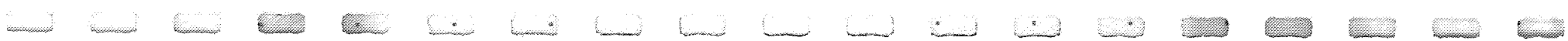

The flash angle distributions may be illustrated another way by plotting the projection of the mirror normal in the plane perpendicular to the gyro spin axis.

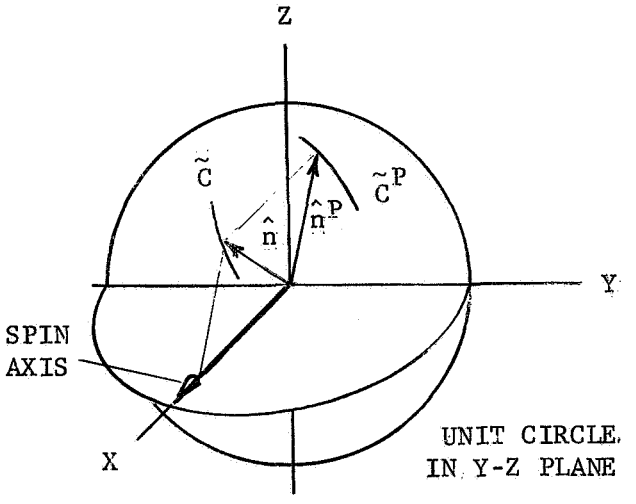

$\hat{n}$ = MIRROR NORMAL
$\hat{n}^P$ = PROJECTION OF $\hat{n}$ IN Y-Z PLANE
$\tilde{C}$ = TRAJECTORY OF MIRROR NORMAL ON SURFACE OF UNIT SPHERE
$\tilde{C}^P$ = PROJECTION OF $\tilde{C}$ ON Y-Z PLANE

Since the spin axis is assumed to be pointed at the vernal equinox, the mirror normal projection lies in the Y-Z plane in inertial space. The mirror normal is a unit vector, and the length of its projection is equal to the sine of the flash angle. Mirror normal distributions have been plotted in this way in Fig. 8.6 for one-week periods of observation from stations at Curacao and Peru. The orbital conditions are the same as those listed in Fig. 8.3(a), with the patterns in the upper half of each picture visible from Curacao, and those in the lower half visible from Peru. In each frame, circles have been drawn showing the paths of unit vectors on the spinning satellite which correspond to fixed mirror normals of 42^o, 54^o, and 71^o. Wherever a circle is crossed by the path of a projected mirror normal, an actual observation is indicated. The dotted paths denote mirror normal angles

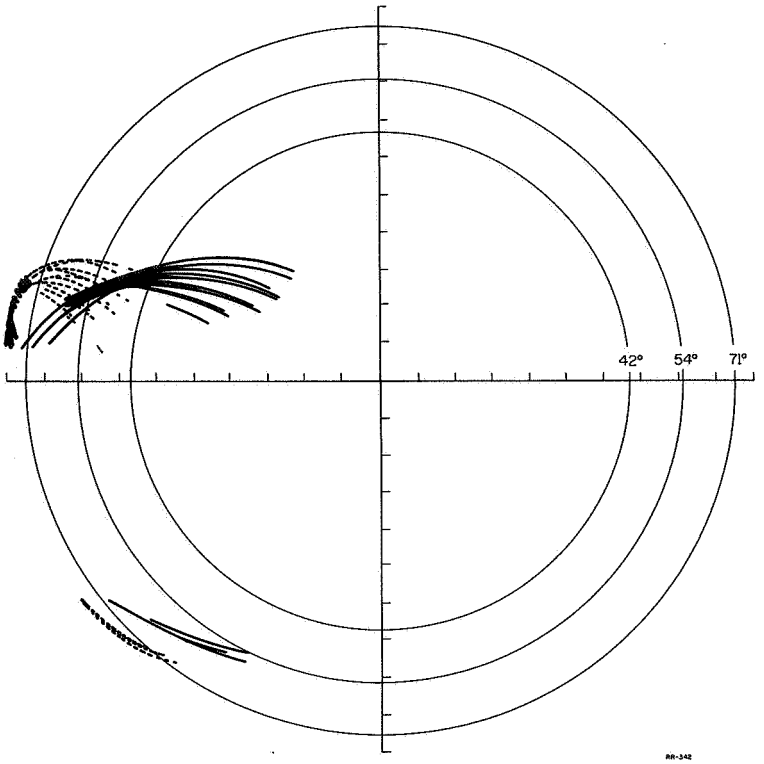

(a) First week of January

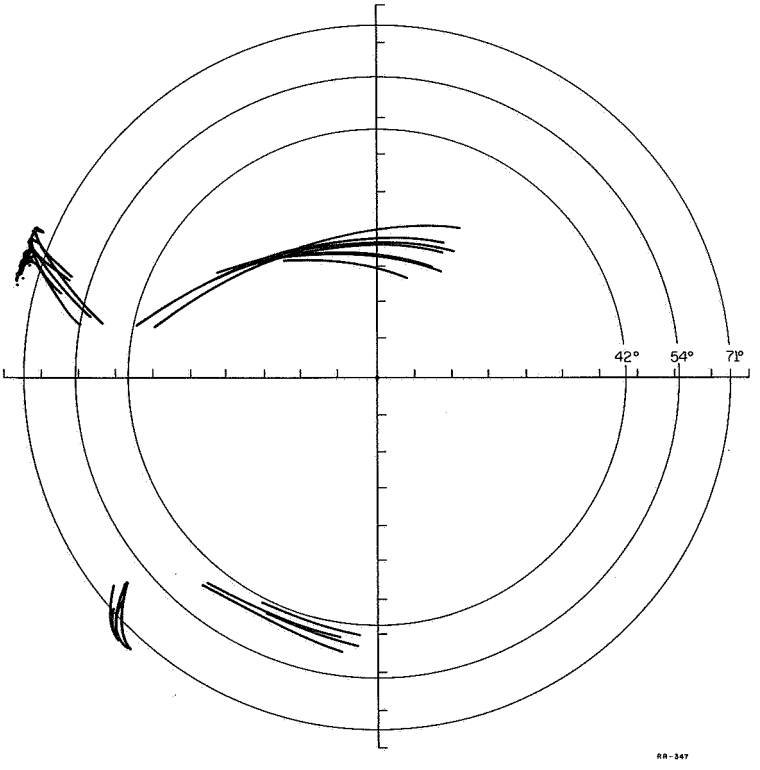

(b) First week of February

Figure 8.6

Projections of mirror normal unit vectors on the Y-Z plane of inertial space, i.e., perpendicular to the vernal equinox. The horizontal line represents an edge view of the earth's equatorial plane. The data shown are for a satellite in a 1000-km altitude circular orbit observed from Curacao and Peru.

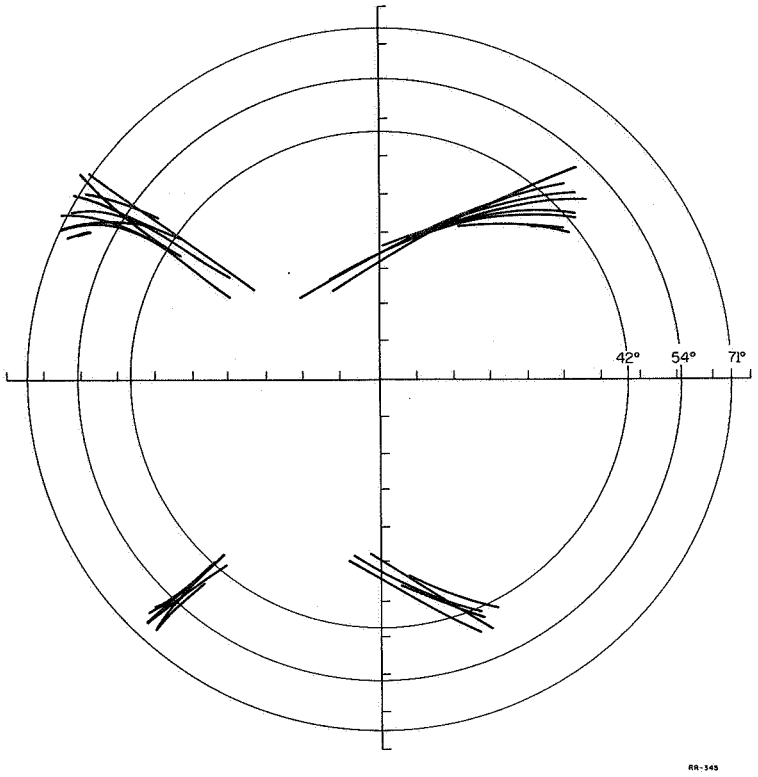

(c) First week of March

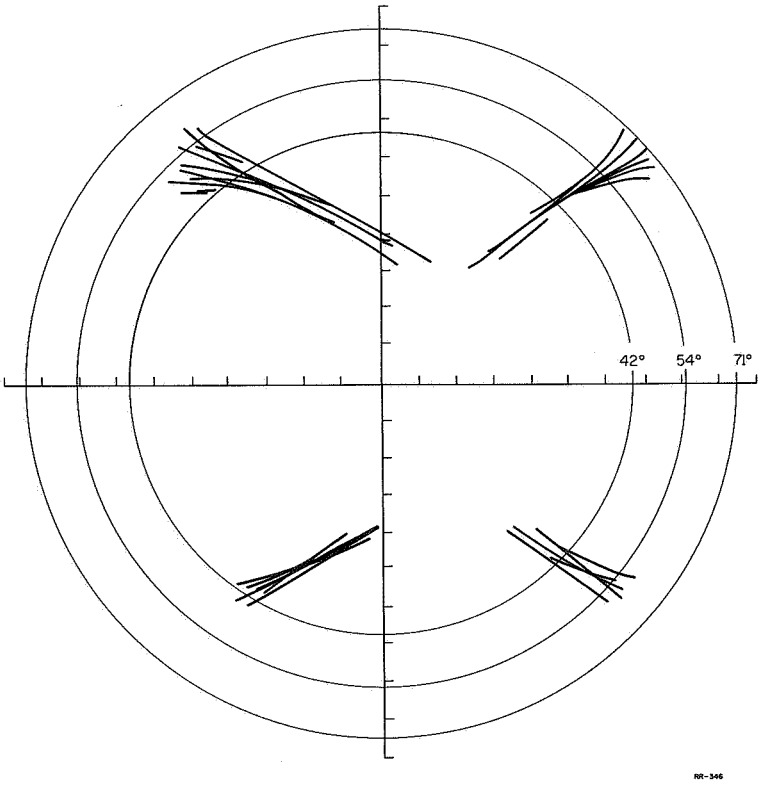

(d) First week of April

Figure 8.6 (continued)

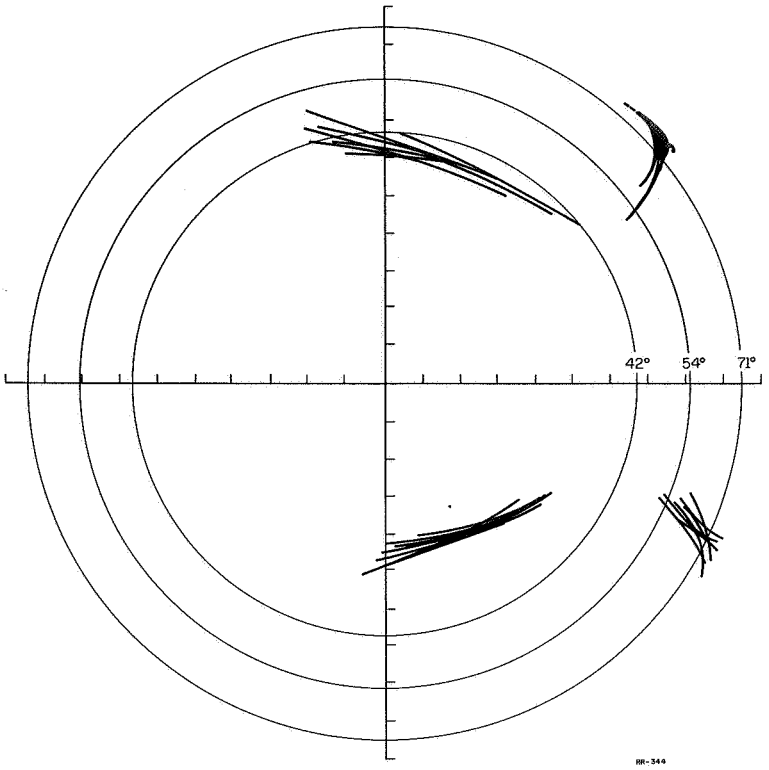

(e) First week of May

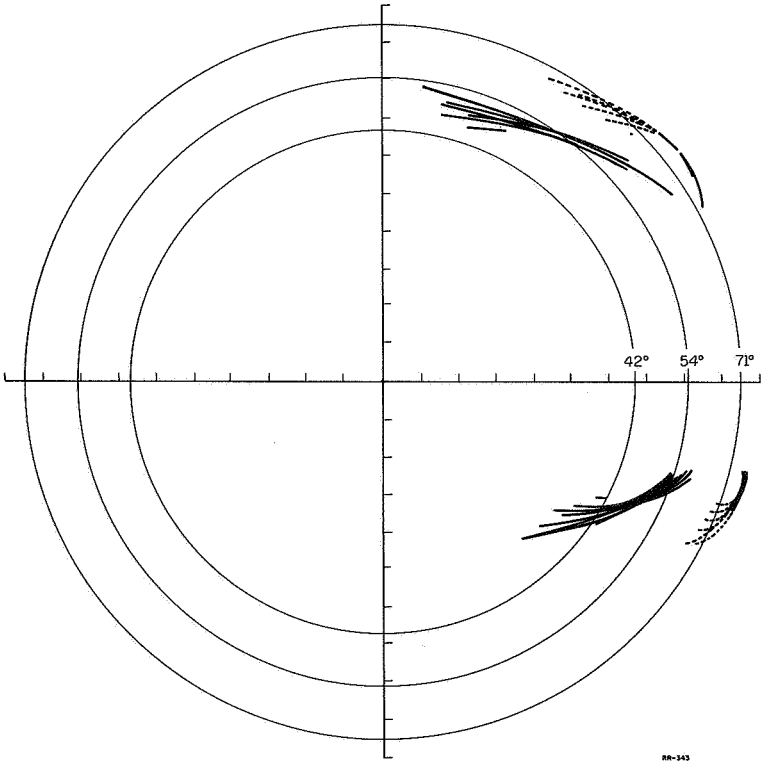

(f) First week of June

Figure 8.6 (continued)

of more than 90° and crossing a circle indicates a reflection from one of the supplementary fixed mirrors diametrically opposite those listed above. This presentation shows that there will usually be enough angular diversity of the mirror normals actually sighted to produce good estimates of the spin axis orientation.

8.3. Envelope of Observability: Program ENVO

An inspection of Figs. 8.3 and 8.5 shows that the flash angle distribution patterns are bounded by envelopes. The boundaries may be determined by finding the maximum and minimum values of the flash angle as a function of time. The resulting envelope is called the envelope of observability (EO) because observations giving spin-axis data are possible only from mirrors whose normal angles lie inside the envelope. A digital computer program, ENVO, has been developed to find the EO for any given orbit and station conditions. The program takes about five minutes to run a complete case on the CDC-1604 computer at CSL, compared to 30-40 minutes for program SATOBS to run the same case. The EO is computed in the following manner: given the station latitude, satellite orbit altitude, inclination, initial right asscension, spin-axis direction, and time, radius vectors are computed from the center of the earth to the sun, satellite, and earth station. At a given time instant, the cosine of the flash angle is computed and maximized with respect to two angles,

x_1, the station longitude measured from the vernal equinox line and x_2, the argument of the satellite, measured in the orbital plane from the line of nodes. All other angles are fixed by the initial conditions and time. At the same instant of time, the minimum of the cosine is also determined. These two extremes give the minimum and maximum of the flash angle.

Of course, the optimization of the cosine function is constrained by the same three conditions necessary for an observation as were used in SATOBS, namely earth station in darkness, satellite in sunlight and station-to-satellite line of sight more than 15^{o} above the horizon. In ENVO, these three constraints are formulated as penalty functions which are added to the authentic trigonometric expression whenever one or more of the constraint angles are outside the prescribed limits.

In general, observations are possible in the morning and evening of each day and thus two envelopes are produced. The initial conditions on x_1 and x_2 determine which of the two envelopes is to be followed. Figure 8.7 is an EO produced by ENVO, with points computed about four times a month, or every 7.5 days. These envelopes compare reasonably well with the SATOBS output in Fig. 8.3(a).

Either the flash angle distribution of Figs. 8.3 and 8.5 or the EO of Fig. 8.7 may be used to determine the effectiveness of a particular mirror mounted on a spinning satellite. In the former case one simply counts the number of vertical lines intersected in a year's time by the chosen flash angle. The same results can be obtained by

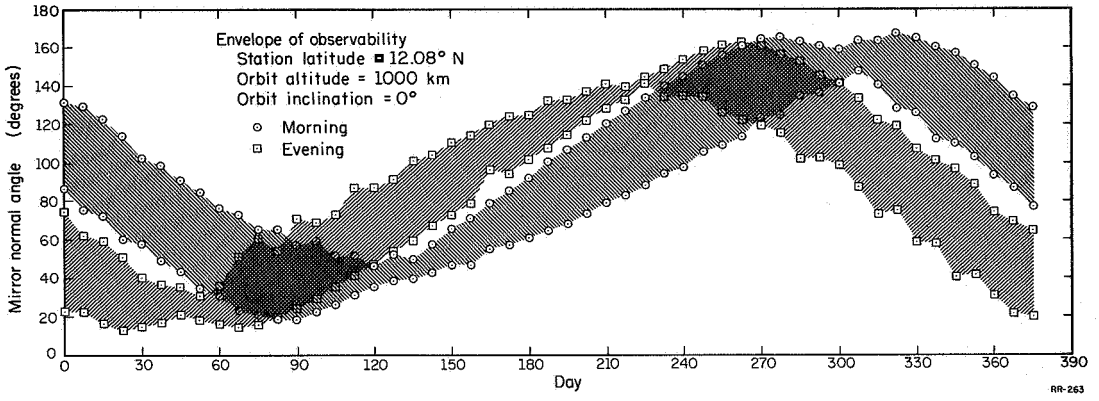

Figure 8.7

Envelope of observability of a satellite in circular orbit. Tracking station is Curacao.

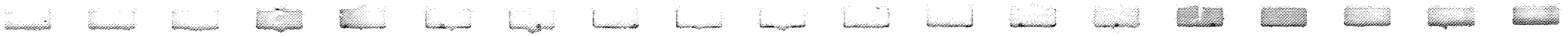

counting the number of days the particular flash angle is within the EO and multiplying by the average number of passes per day. As stated earlier, ENVO runs nearly 10 times as fast as SATOBS, so the EO method will be pursued in the optimization of orbital parameters for the relativity satellite.

Program ENVO is not as versatile as SATOBS because it is limited to circular orbits of low inclination. However, additional constraints will be easier to implement with ENVO, using a Lagrange multiplier technique. The constraints will be based on the brightness of flashes received at a tracking camera and are discussed in the next section.

8.4. Geometrical Factors Affecting Brightness of Flashes

The input exposure necessary to produce a photographable image in the Baker-Nunn camera is about 10^{-10} lumen sec/m^2. The luminous intensity of sunlight reflected from a perfect plane mirror to an earth station is

$$E_R = E_s A_m \cos\sigma / A_e \tag{8.4}$$

where

E_R = reflected luminous intensity ~ lumens/m^2

E_s = luminous intensity of sun's rays on earth ~ lumens/m^2

A_m = area of mirror

σ = angle of incidence = angle of reflection

A_e = area covered by reflected light at earth's surface in a plane normal to slant range vector

$$= \pi\left(\frac{.53^o}{2}\frac{\pi}{180^o}S\right)^2$$

S = slant range from earth station to satellite

The geometry of the reflected sunlight is shown in Fig. 8.8 (a). The mirror, mounted on a spinning satellite, sweeps through the sun's disc from limb to limb during a pass, giving the longest exposure time τ when it sweeps through the solar diameter. This exposure time is given by

$$\tau = .53^o \left(\frac{\pi}{180^o}\right)/|\dot{\hat{S}}| \tag{8.5}$$

where $|\dot{\hat{S}}|$ is the absolute value of the time rate of change of the unit vector from the satellite to the observing station. Referring to Fig. 8.8 (b), the time rate of change of $\hat{S}$ is

$$\dot{\hat{S}} = 2\left[\underline{\omega}_s \times \hat{n}(\hat{n} \cdot \hat{R}_s) + \hat{n}(\underline{\omega}_s \times \hat{n} \cdot \hat{R}_s)\right] \tag{8.6}$$

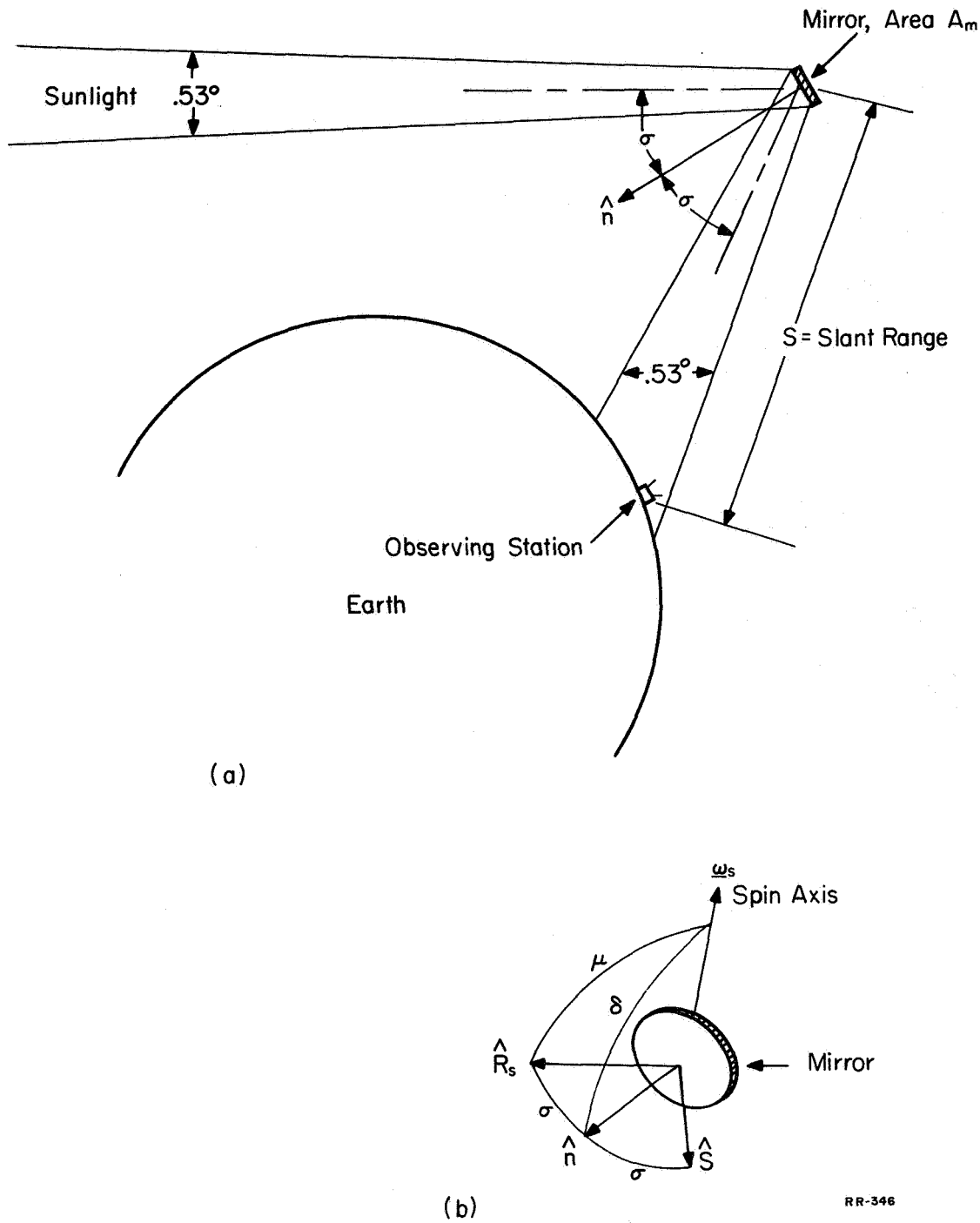

Figure 8.8

Geometrical factors which determine the photographic brightness of reflected solar radiation.

(a) Slant range S and angle of incidence-reflection, σ.

(b) Mirror normal angle δ, solar aspect angle μ, and incidence-reflection angle σ. R_s is the unit vector in the direction of the sun, $\hat{S}$ is the unit vector in the direction of the terrestrial tracking station, as seen from the satellite.

where

$\underline{\omega}_s$ = angular velocity vector

$\hat{n}$ = mirror normal unit vector

$\hat{R}_s$ = unit vector toward sun

Eq. (8.6) can be solved in terms of the sides of the spherical triangle, μ, σ, and δ in Fig. 8.8(b), and the result is

$$|\dot{\hat{S}}| = 2\omega_s[\sin^2\delta - (\cos\delta\cos\sigma\cos\mu)^2]^{\frac{1}{2}} \tag{8.7}$$

where

δ = flash angle = angle between spin axis and mirror normal

σ = angle of incidence

μ = solar aspect angle

Now, the input exposure per flash is just

$$\mathcal{E} = E_R \tau = 1.87 \times 10^9 \frac{A_m}{S^2} \tau\cos\sigma \tag{8.8}$$

where the value 1.25×10^5 lumens/m^2 has been used for the sun's luminous flux. The factor $\tau\cos\sigma$ may be regarded as an effective flash duration time, since it includes the fraction by which the mirror area is reduced by a reflection through an angle of 2σ.

Using Eq. (8.7) in (8.5), the effective flash time is

$$\tau\cos\sigma = \frac{6.7 \times 10^{-5} \cos\sigma}{\omega_s\left[\sin^2\delta - (\cos\delta\cos\sigma - \cos\mu)^2\right]^{\frac{1}{2}}} \tag{8.9}$$

The denominator of this equation cannot be zero or imaginary because the law of cosines for spherical triangles requires that

$$(\cos\delta\ \cos\sigma - \cos\mu)^2 \leq \sin^2\delta\ \sin^2\sigma$$

When the equality sign holds in this expression, (8.9) is a maximum:

$$(\tau\cos\sigma)_{max} = \frac{6.7 \times 10^{-5}}{\omega_s \sin\delta} \tag{8.10}$$

The minimum of (8.9) is realized when $\cos\mu = \cos\delta\ \cos\sigma$:

$$(\tau\cos\sigma)_{min} = \frac{6.7 \times 10^{-5}}{\omega_s}\ \frac{\cos\sigma}{\sin\delta} \tag{8.11}$$

Some typical curves have been plotted in Fig. 8.9 showing the effective flash duration from mirrors on a satellite spinning at 50 revolutions per second. The principal flash angles have been used, and the variation is shown as a function of solar aspect angle and incidence angle. In all cases, the highest likelihood of the maximum effective flash duration occurs near $\mu = 0$ or at the time of the vernal equinox assuming the satellite spin axis to be aligned in that direction. The

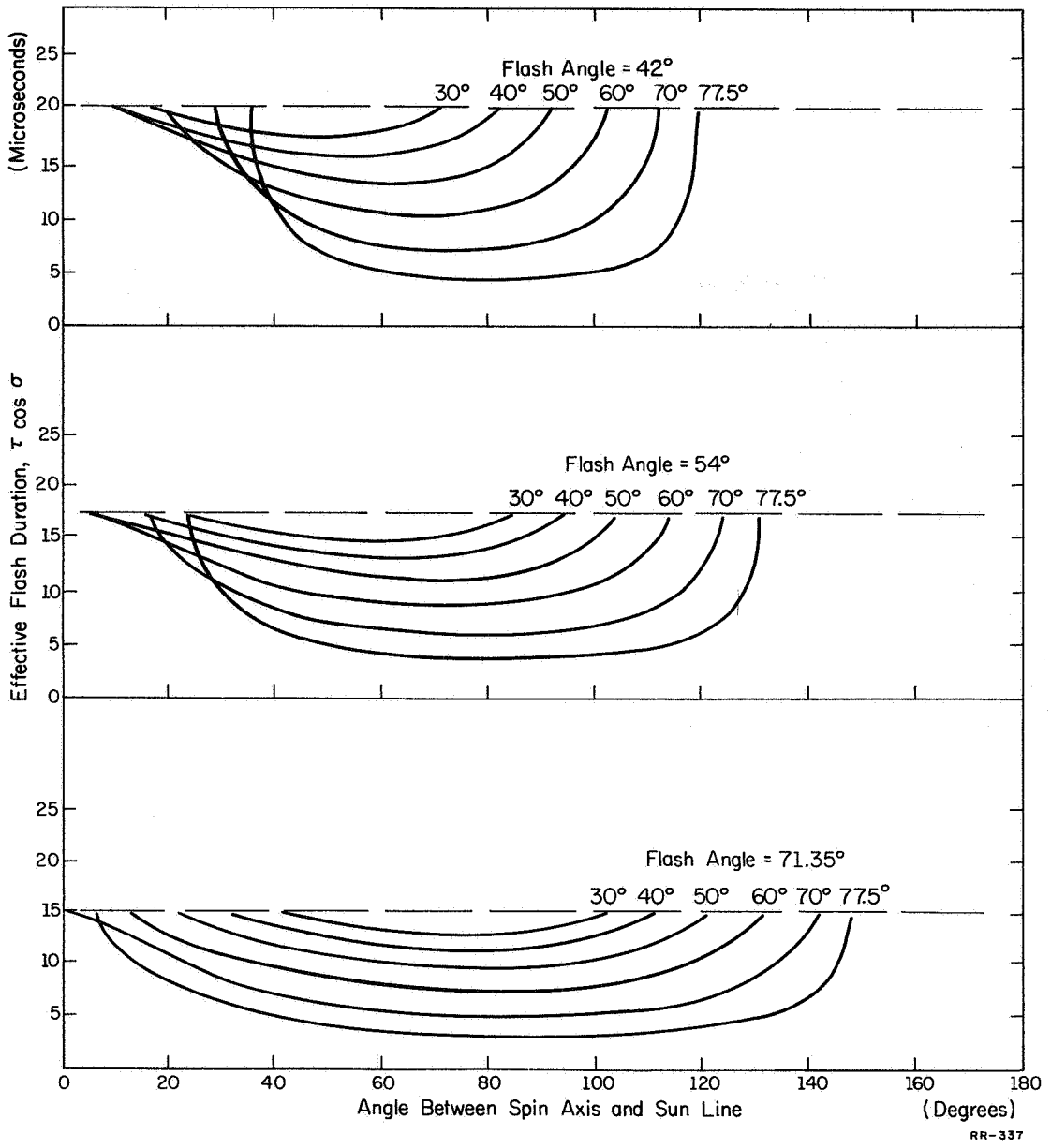

Figure 8.9

Effective flash duration $\tau \cos \sigma$, of individual flashes from mirrors on a satellite spinning at 50 hz. The flash angle is the angle between the satellite spin axis and the mirror normal.

mirror incidence angle is limited to 77.5° because of the limits set by the first three conditions of observability. The sketch below will clarify this limitation.

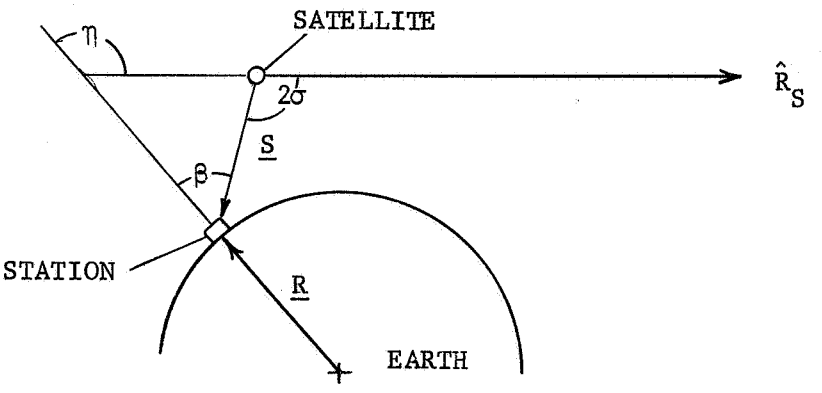

It is seen that $2\sigma = \pi + \beta - \eta$ and that σ will be maximum when β is maximum and η is minimum. But η is the angle between the earth station and the sun line, and cannot be less than 100°, by Eq. (8.1), and β can be no larger than 75° by condition (8.2). Therefore, the result is $\sigma_{max} = 77.5^{\circ}$ for any observable pass of the satellite and Eq. (8.11) gives the minimum effective flash duration as

$$(\tau \cos\sigma)_{min} = \frac{1.45 \times 10^{-5}}{\omega_s \sin\delta}$$

Now, with the help of Fig. 8.1 and Eq. (8.8), it becomes possible to estimate the effective flash duration necessary to produce a photographable image in the Baker-Nunn camera. Again, assuming a 1000 km orbit, Fig. 8.1 indicates a maximum slant range of 2400 km. With the mirror area chosen as 944 cm^2 and necessary

exposure $\mathcal{E} = 10^{-10}$ lumen sec/m^2, Eq. (8.8) gives $\tau\cos\sigma = 2.9\ \mu$ sec. Thus, it appears from Fig. 8.9 that, for a satellite spinning at 50 cycles per second, it is possible for the peak input exposure during any pass to be above the threshold of the Baker-Nunn camera. However, a factor of five above the threshold exposure may be possible only with the four mirrors whose normals are 42° and 54° from the spin axis.

8.5. Conclusions

The present results of studies of opportunities for observing the passive gyroscope satellite indicate that a .6 meter diameter satellite, spinning at 50 cycles per second and with the spin axis aligned toward the vernal equinox will produce photographable flashes from most of its 6 facets, each having an area of 944 cm^2. With the satellite in a 1000 km equatorial orbit, two Baker-Nunn stations in the SAO network, located at Curacao and Arequipa, Peru, would be capable of producing spin axis data about three times per day, weather permitting.

The expected observation frequencies were obtained from computer-simulated satellite orbits with no limitations on the individual flash brightness. The envelope of observability, which gives essentially the same information, will be modified to utilize a brightness criterion based on Eq. (8.8) to get a better estimate of the number of useable passes.

9. READOUT ACCURACY FOR THE BAKER-NUNN IMAGES

9.1. Introduction

The goal of the studies to be reported in this Chapter has been to determine the photographic brightness to be demanded of the relativity satellite so that satisfactory images may be recorded by the Baker-Nunn Satellite-Tracking Cameras[1] of the Satellite Observing Network operated by the Smithsonian Astrophysical Observatory. There are two kinds of images to be considered and, thus, two kinds of criteria defining "satisfactory." The reason is that there are two kinds of reflective facilities to be provided on the satellite*, illustrated in Fig. 9.1.

One of these facilities is the spherical surface. It was desired to "round-off" the space between the reflective facets, and it was decided to use this rounded-off part, following a suggestion by J. Bardeen, to provide a facility for tracking the satellite's orbital motion between the times at which the mirror flashes would be observable. In this way, orbital-motion data, in addition to spin-axis-motion data, could be obtained by methods each best suited to its own purpose, and "100% observability," over a much wider range of geometric conditions than demanded by the flat mirrors, could

---

*A third facility, the small polar facets, are not considered in this report because of the necessity to use a specially-located, possibly mobile, observing station. Because of the long "on time," the polar flashes would make very modest demands upon camera sensitivity, however. The feasibility of using these facets has not been examined in detail.

conceivably be assured.

The spherical-surface reflection is much weaker, being spread over 4π stereradians, than is that of the flats. On the other hand, it is essentially continuous, being interrupted with a duty cycle of about 50% by the flats. Thus, comparatively long exposures may be made by causing the camera motion to follow the satellite to record a point image. The brighter background stars then leave image trails which are periodically interrupted by the shutter in the camera. This is one of the standard modes of operation of the Baker-Nunn camera in tracking satellites, and it provides temporal and angular data of standard accuracy (1.1 arcsec in angle) for orbital determinations. The brightness criterion to be examined in Section 9.2, then, is that the exposure be well above a threshold value for standard methods of image measurement without demanding unreasonable precision (to obtain sufficiently long exposure times) in tracking the satellite's motion. A percent or less of error in matching the camera's angular velocity to that of the satellite is regarded as reasonable.

When it is desired to obtain spin-axis-orientation data, it is necessary for the camera motion to be sidereal to track the stars, which then register as point images, and the satellite's image is to be allowed to "trail." Under these circumstances, the photographic exposure produced by the spherical surface would be reduced by some two orders of magnitude and should fail to be recorded, so that the only possible record would be that produced by the flashes

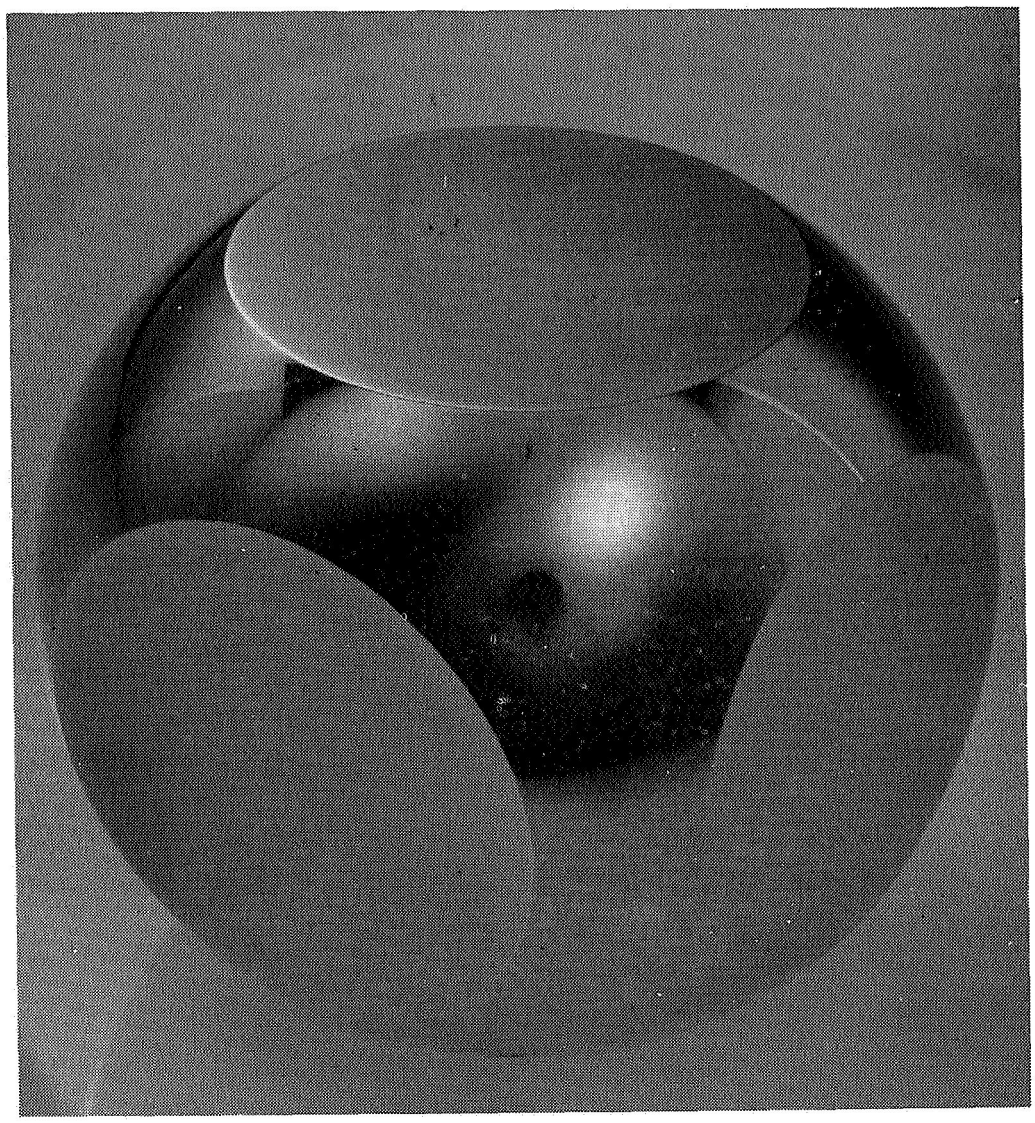

Figure 9.1

Model of the 60-cm relativity satellite. The two optically reflective facilities consist of the polished spherical surface and the six optical flats or glitter facets. The spherical surface provides for the observation of the orbital motion, while the flats provide for the observation of the spin-axis motion.

of sunlight from the other reflective facility, the large optical flats. Such a mode of operation would not be used unless it could be anticipated that all the geometric conditions described in Chap. 8 would be fulfilled for that pass of the satellite. Also, the cyclic mode of shutter operation is not to be used in the photography of the flat-mirror flashes, because the timing information to be obtained need not be more accurate than a few seconds of time.

In the early days of the experiment, the ability to anticipate the exact opportunity to record flash observations would be faulty to some extent, so that it might be necessary to leave the camera shutter open for longer intervals than the minimum needed to record the whole of the flash pattern. Although the camera is extremely tolerant of pointing errors, the longer exposures could result in excessive exposure to the night-sky background. As more data are obtained, however, the exposure time could be reduced to the 3 seconds or so necessary to record the whole image at the greater slant ranges.

The Baker-Nunn Satellite-Tracking Camera[1] is a Schmidt-type camera with a focal length of 0.5m (20 inches), an aperture of f:1.0, a field of view of 5^{o}X30^{o}, and a resolution spot-size on red-extended Royal-X Pan film (55mm Cinemascope base) of about 25 microns, corresponding to 10 arcsec, or about 50 microradians. The "threshold" sensitivity of the camera with this film, reciprocity conditions favoring fractional-second exposure times, and the standard processing established for the Satellite Observing Network,

is 0.8×10^{-10} lumen sec/m^2 measured at the input aperture of the camera for a point source having the same spectral properties as the sun seen through the Earth's atmosphere. This exposure produces a density increment of 0.35 ± 0.05 above that produced by a 1 sec exposure to night sky.[2] Experiments have established that "hard-edged" images, shutter-induced breaks in star trails, for example, may be located on the film with reference to other such images, or point images, with a standard error of 1.1 arcsec, i.e., to within about 1/9 of the resolution-spot size.[3]

Since the flash-pattern image to be obtained from the relativity satellite will resemble that of Fig. 9.2, which does not appear to be hard edged, it is necessary to determine the extent to which it may be expected that such images may be located to within the standard accuracy of 1.1 arcsec, with reference to neighboring stellar images on the same film. The image is trail-like, but, instead of having uniform density along its length and terminating abruptly, the density tapers toward either end and seems to "fade out."

This tapering may be known *a priori*, as it turns out, so that one could conceive of matching an observed taper against the predicted one to locate the center. Such a procedure cannot be expected to attain any arbitrarily desired accuracy, however, because, at the very least, there are also random density fluctuations along the image. These fluctuations are characteristic of the inherent graininess of the film, and they will always "fool" a matching

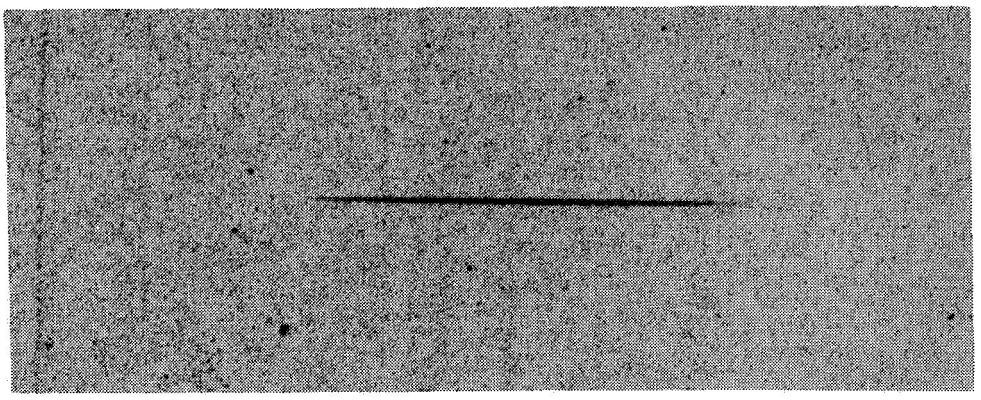

Figure 9.2

Enlarged photograph of film image simulating that which would be recorded by the Baker-Nunn camera for unresolved glitter flashes. The original image was 4.6 mm long, the same as would appear in the camera, and the film was of the same type, developed in the same manner, as used in the Smithsonian network of these cameras. The simulation used the anamorphic camera shown in Fig. 9.5.

procedure to a certain extent, so that an error in center estimation will result. The problem comes down to one of estimating that error and determining the exposure level at which the error is equal to the standard one of 1.1 arcsec, because it is that exposure level which must be met by the satellite design, and feasibility could turn upon the question as to whether such a design is at all reasonable. For the present eminently-reasonable 0.6-m diameter, it will be seen that the standard accuracy is in fact obtainable, and that the estimation methods need not involve detailed matching to a priori density patterns.

In the sections that follow, the photographic brightness of both the spherical and flat reflectors are surveyed and shown capable of producing quite dense images on the Baker-Nunn (B-N) film. The major part of the discussion is devoted to reporting our studies of the images obtainable from the flat reflectors, a flash-pattern image. The exposure structure of that image is discussed, following which the means used of photographically simulating such an image in the unresolved-flash case, together with analog trials at estimation of its center by means of weighted-aperature photometry are described. The experimental measurements of film noise and the mathematical modeling of that noise as needed for computer simulation of flash-pattern images is described, followed by a discussion of maximum-likelihood as well as "practical" weighting schemes of image-center estimation. The "practical" schemes were implemented in computer

trials for study, by which it was possible to show that the prescription turns out to be a very simple one for images of practical interest, and that these are the ones which demand exposures only 5-fold greater than threshold and that are capable of yielding the full accuracy inherent in the B-N camera, 1.1 arcsec.

9.2. Photographic Brightness of the Spherical Surface.

When the B-N camera tracks the satellite, the effective exposure time is limited by the error in matching the angular rate of the camera's motion to the apparent angular rate of the satellite's orbital motion, because this error will cause the satellite's image to creep along the film, eventually moving into previously-unexposed territory by virtue of having moved a distance equal to the diameter of the resolution spot. The image will move an angular distance θ in a time equal to $\theta r/v$, if r be the slant range to the satellite, and v be its linear orbital velocity, if the camera not be tracking. If it tracks with a percentage error ϵ, this time will be extended by the ratio $100/\epsilon$. Setting θ to be the resolution of the camera, 50 μrad, and r to be a value near the maximum for slant ranges, 2500 km, then, with an orbital speed of 7.4 km/sec, the effective exposure time is 1.7 sec for an ϵ of 1%.

With the present satellite, the spherical-surface reflection is interrupted by the flats, reducing the effective exposure time.

Since half the area of this surface has been devoted to the flats, it seems reasonable to use a duty factor of 50% to adjust the effective exposure time to be 0.85 sec, even though it would remain necessary to allow the camera to take the full 1.7 sec to record the image.

The luminous flux, F, at the satellite may be taken to be the value of the solar constant measured at the surface of the Earth, to allow for atmospheric absorption. This value in photometric units is $F = 1.25 \times 10^{5}$ lm/m^2. The part intercepted by the satellite of diameter d is $\pi d^2 F/4$, and this is scattered uniformly over a solid angle of 4π stererad, so that the luminous flux reflected to the camera is $\pi d^2 F/4$ divided by $4\pi r^2$, in which r is the slant range to the satellite. The result is that the received luminous flux is $(d/4r)^2 F$. Setting d=0.6 m and r=2500 km, the value $3.6 \times 10^{-15} F = 4.5 \times 10^{-10}$ lm/m^2 is obtained. For the calculated effective exposure time of 0.85 sec, the input exposure is $E = 3.82 \times 10^{-10}$ lm sec/m^2, which is above the threshold value of 0.8×10^{-10} lm sec/m^2 by the factor 4.8.

From studying the sensitometric curve[2] shown in Fig. 9.3, it may be deduced that exceeding the threshold-exposure value* by a

*This threshold exposure value for the B-N camera, defined in section 9.1, is based on utilization criteria and is not necessarily a standard sensitometric concept, such as the inertia point defined by Hurter and Driffield. For a discussion of photographic sensitometry, see Ref. 4, especially pages 72-119 and 409-436. The reciprocity conditions for this sensitivity measurement favor exposure times ranging from fractional seconds to a second or so. The manufacturer's literature, however, rates the film as having an excellent reciprocity law for exceedingly short exposure times. Consequently, no reciprocity corrections will be made here or in Section 9.3.

factor 4.8 will bring the density increment to 1.1 above night sky instead the threshold increment of 0.35. On the other hand, the standard night sky reference is based on an exposure of 1 sec, whereas some 2 sec is needed to record the image. With reference to this more heavily exposed background the density increment would still be 0.9. Since density increments of 0.35 are regarded as useful for the purpose of measurement, there seems to be provided an ample margin of sensitivity. Upon inspecting the overall equation for the above exposure calculation, with a duty factor ½,

$$E = \tfrac{1}{2}(100/\epsilon)(\theta r/v)(d/4r)^2 F,$$

it would appear, for example, that tracking errors of some 4% to 5% could be tolerated, or more at the shorter ranges, especially since the background exposure would then be reduced. Such questions are of no great importance except as demonstrating the ample sensitivity margins available.

9.3. Photographic Brightness of the Optical Flats.

The sun subtends an angle viewed from the earth of 0.93×10^{-2} rad, corresponding to a solid angle of $\pi/4$ times the square of that quantity, or 0.69×10^{-4} stererad. On the other hand, a mirror of area 1000 cm^2=0.1 m^2 subtends, at a slant range of 2500 km=2.5×10^6 m,

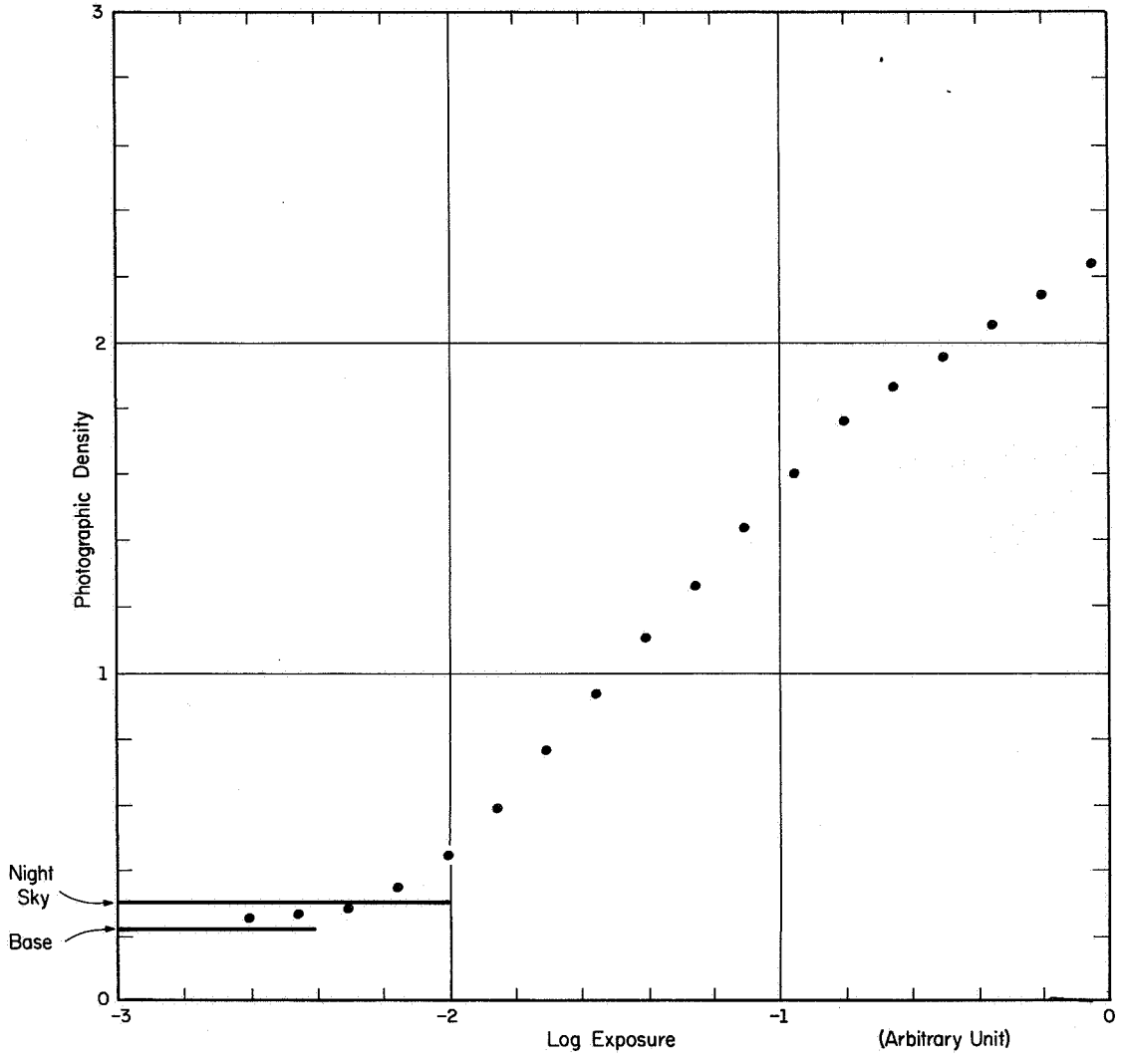

Figure 9.3

Sensitometric data for the type of film and development used for the Smithsonian network of Baker-Nunn cameras. The exposure scale may be calibrated from the information that a density increment of 0.35 ± 0.05 above night sky requires an exposure of 0.8×10^{-10} lm sec/m^2 at the input aperture of the camera for point images.

a solid angle of $[0.1/(2.5)^2]\times10^{-12}=1.6\times10^{-14}$ stererad. Through the aperture represented by such a mirror, then, only a fraction equal to $(1.6/0.69)\times10^{-10}=2.32\times10^{-10}$ of the solar disc may be seen. The interposition of such an aperture would reduce the luminous flux from its value given by the solar constant 1.25×10^{5} lm/m^2 to the value $2.32\times1.25\times10^{-5}=2.90\times10^{-5}$ lm/m^2.

The exposure time for a given flash depends upon the length of the chord across the solar disc that is scanned and upon a number of other geometrical factors indicated in Chapter 8. For the present purpose, let the time be that required for the satellite to turn through half the angular diameter of the disc, namely 0.46×10^{-2} rad, the factor ½ because the mirror normal bisects the angle between incident and reflected ray. For a rotation rate of 50 rev per sec or 314 rad/sec, this time is $(0.46/0.314)\times10^{-5}=14.8$ μsec. The exposure would then be $2.90\times1.48\times10^{-10}=4.29\times10^{-10}$ lm sec/m^2, a value which exceeds the "threshold" value of the B-N camera, 0.8×10^{-10} lm sec/m^2 by the factor 5.36.

This calculation serves the purpose of a base value, from which calculations for other slant ranges, other effective projected mirror apertures, or other exposure times may be made. Taking "rounder" numbers, it may be quoted that an aperture of 1000 cm^2, transmitting sunlight from a slant range of 2500 km, and open for 15 μsec, will produce an exposure greater than the B-N threshold value by the factor 5.44, and this represents a nominal value for the brightness of the optical flats on the satellite.

9.4. Flash-Pattern Structure.

As the satellite moves in its orbit at the rate of 7.38 km/sec, a mirror will come into reflecting position 50 times per second so that the flashes will have a spacing of 148 m along the orbit. At a slant range of 2500 km, however, the 50 μrad resolution-spot diameter of the B-N camera projects to 50X2.5=125 m. Thus it appears that the flashes would be individually resolved on the film at this and all shorter ranges. The spin rate would have to be increased, in fact, to about 60 Hz to make a continuous image, such as that shown in Fig. 9.2 at this essentially maximal range. At the time at which there was an interest in simulating flash pattern images, such faster spin rates, e.g., in the neighborhood of 100 Hz, were being considered.

The computed flash spacing, however, subtends an angle of $(148/2.5)\times10^{-6}$=59 μrad, so that in the 9.3 mrad angular width of the sun there would appear (9300/59)=158 flashes, which, at the rate of 50 per second, would be formed in a span of 3.16 seconds of time. On the film, the flash spacing would appear to be 30 microns and the total pattern width would be 4.6 mm because of the half-meter focal length of the camera's optics. At nearer slant ranges, the flash spacing would subtend larger angles and the image would be coarser. Its overall width, however, is fixed by the angular width of the sun, so that the image would contain fewer flashes, also, at the nearer ranges. For example, at 1000 km there would be only 63 flashes at 75 microns spacing over the same 4.6 mm on the film, and these would be recorded in 1.26 seconds of time.

In Section 9.3, exposure values for a central flash in the image were computed. For flashes away from the center of the image, the reflected line of sight scans along a chord of the solar disc of a length that becomes progressively less the nearer the chord to the limb of the solar disc. It is the length of this chord that determines the exposure time for the disc, so that the exposure value varies across the pattern as the length of a chord varies in its successive positions across a circle. Thus, a plot of exposure along the flash-pattern image would be a semicircular (or more generally a semielliptical) curve. From this knowledge, and a knowledge of the H & D sensitometric curve, the curve shown in Fig. 9.3, the resulting curve given by a densitometer tracing along the long axis of the image, such as the image of Fig. 9.2, for example, may be determined. In the case in which the flashes would be individually resolved, such a curve would be periodically "chopped", but otherwise would resemble that of Fig. 9.4, in which the irregularities reflect the random grain structure of the film.

9.5. Analog Image Simulation.

The image of Fig. 9.2 was formed by an anamorphic camera to produce a distorted image of the solar disc. The camera is shown in the schematic drawing of Fig. 9.5. The principal distorting element is the cylindrical mirror of which three were used to project three

images upon the 35mm red-extended Royal-X panchromatic film in the 35mm camera body. These anamorphic elements image the disc as a long narrow ellipse. The mirror-to-lens distance was chosen so that the minor axis of the ellipse would project on the film as considerably less than 25 microns, while the lens to film distance was chosen to match the half-meter focal length of the B-N camera.

The lens was chosen to have a spherical component with a focal length of 0.5m also, so that the length of the elliptical image would be the same as the length of the flash pattern image in the B-N camera. With this lens, the ends of the elongated image would be sharply focused. However, the closely spaced sides of the image would not be focused because the location of the virtual image for that dimension would fall only a small fraction of an inch behind the cylindrical surface. To focus this dimension, it was necessary for the lens to have a cylindrical component as well. The focal specifications for this lens fell in the range of those that are common for astigmatic spectacle lenses, and one such was procured from an optical dispensary. This lens exhibited chromatic aberration that was to be controlled by using color filters, since there was never to be any difficulty in obtaining intense enough images for photography with this very sensitive film, quite the contrary, in fact.

The focus of the camera for the ends of the image could be adjusted by moving the lens relative to the film, and that for the

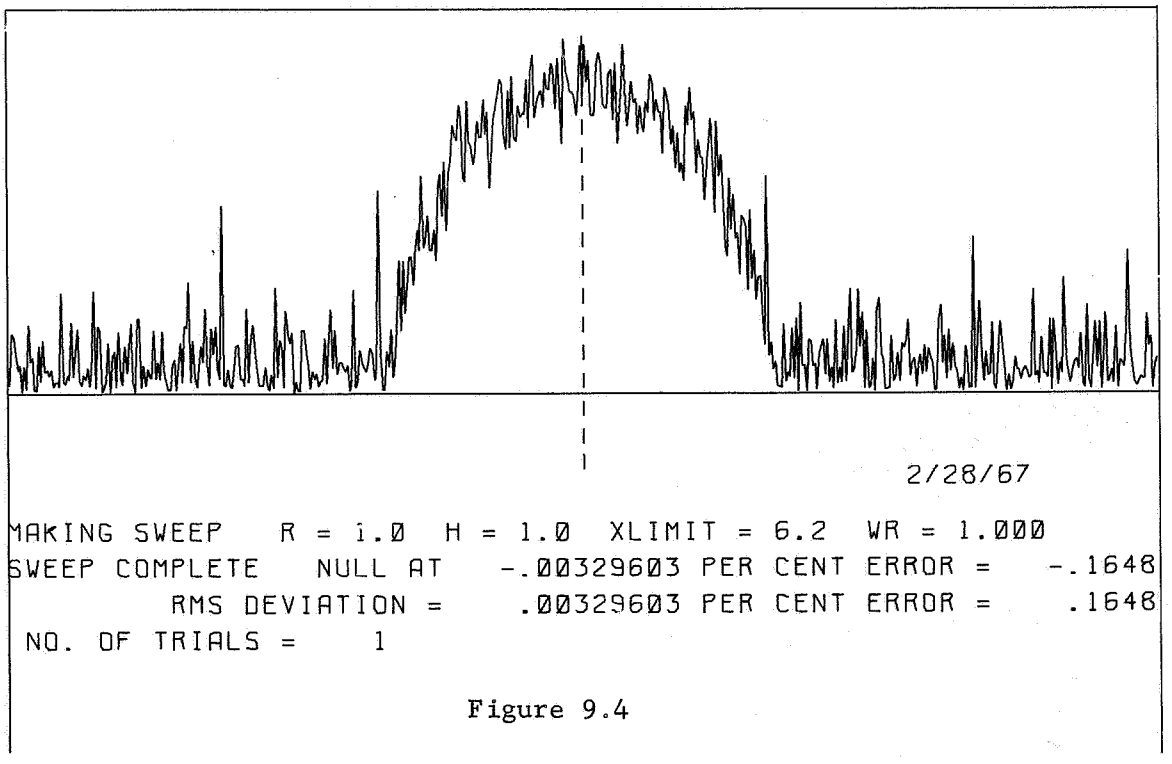

Figure 9.4

Computer-simulated densitometer tracing along the long axis of the flash-pattern image of Fig. 9.2. The simulation used a random-number generator obeying a law that was caused to vary along the image in accordance with models developed from a statistical analysis of the measured graininess noise characteristic of the film used in the Baker-Nunn cameras. Actual tracings closely resemble these.

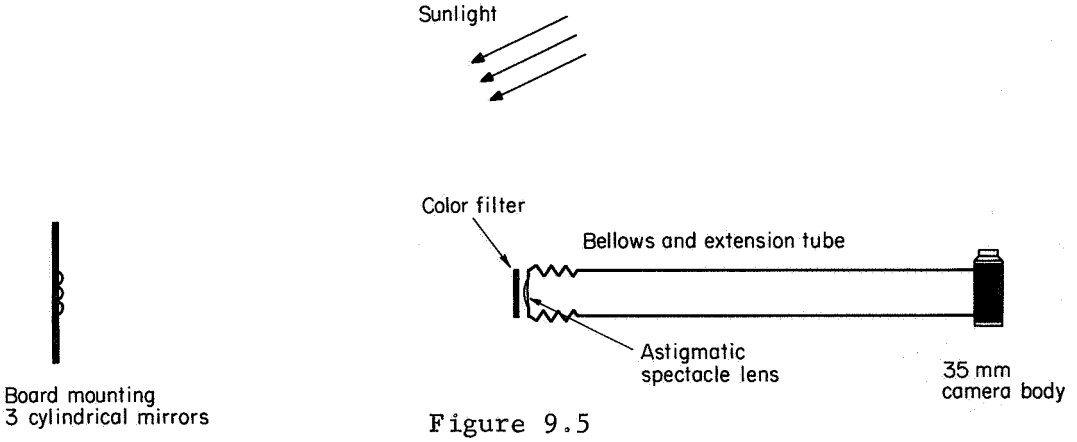

Figure 9.5

Schematic diagram of anamorphic camera used to form images simulating the unresolved flash patterns to be recorded by the Baker-Nunn camera, as in Fig. 9.2. The anamorphic elements are the cylindrical mirrors which form narrow images of the sun's disc. The spectacle lens has a cylindrical focal component to compensate for the astigmatism of the mirrors and a spherical component matching the optics of the Baker-Nunn camera. The color filter eliminates chromatic aberration.

sides by moving the cylindrical mirrors. With this latter adjustment, the image could be diffused to be 25 microns wide uniformly along its length so that the exposure value would vary as the width of the solar disc along that same dimension. The adjustments for the image of Fig. 9.2 approximate these conditions.

A great number of images were photographed with this camera for the purpose of making experimental trials of image-center estimation, using analog techniques. These estimation techniques were to be patterned after the modified center-of-gravity techniques being explored in a parallel study using digital-computer simulation.

A projection microdensitometer setup, based on the Jarrel-Ash projection microdensitometer owned by the U. of I. Astronomy Department, was used, in which the standard photomultiplier was replaced by one in a special housing. The special housing was fitted with provision for precision mounting of a density wedge in two positions, differing in orientation by 180°. The arrangement is schematically shown in Fig. 9.6. The density wedge in its two positions could weight each half of the image in a manner approximating a center of gravity weight. When the transmission through the two halves were equal, a center estimation could be read from the code wheels for the Mann-comparator lead screws driving the film transport.

Though it was known that a true center-of-gravity weighting was not optimal, trials were made using density wedges roughly of that sort, pending further specification of more nearly optimal weights as

the result of computer simulation. Statistical analysis of the results indicated that image centers could be estimated to within an rms error of about 0.6% of image width, or about 11 arcsec, considerably larger, as might have been expected from the make-shift character of the arrangement, than the errors found from computer simulation. The arrangement also made the estimation procedure very tedious to execute because of the painstaking care required.

Plans to provide for a more elaborate setup to obviate the necessity for making so many time-consuming adjustments, and to make a larger number of measurements with more-nearly-optimal-weighting wedges, were abandoned because of limitations in funds and staff. It has since been found, as a result of the computer simulation, moreover, that simpler estimation procedures will suffice for image-center estimation with an rms error of less than 0.06% of image width, or about 1.1 arcsec.

9.6. Measurement of Film-Noise Statistics.

For the purpose of developing mathematical models of film-noise statistics, experimental studies were undertaken to measure statistical properties of film noise in order to determine which measurable parameters would adequately characterize that noise. From specimens of B-N film, both as exposed in the camera, and as

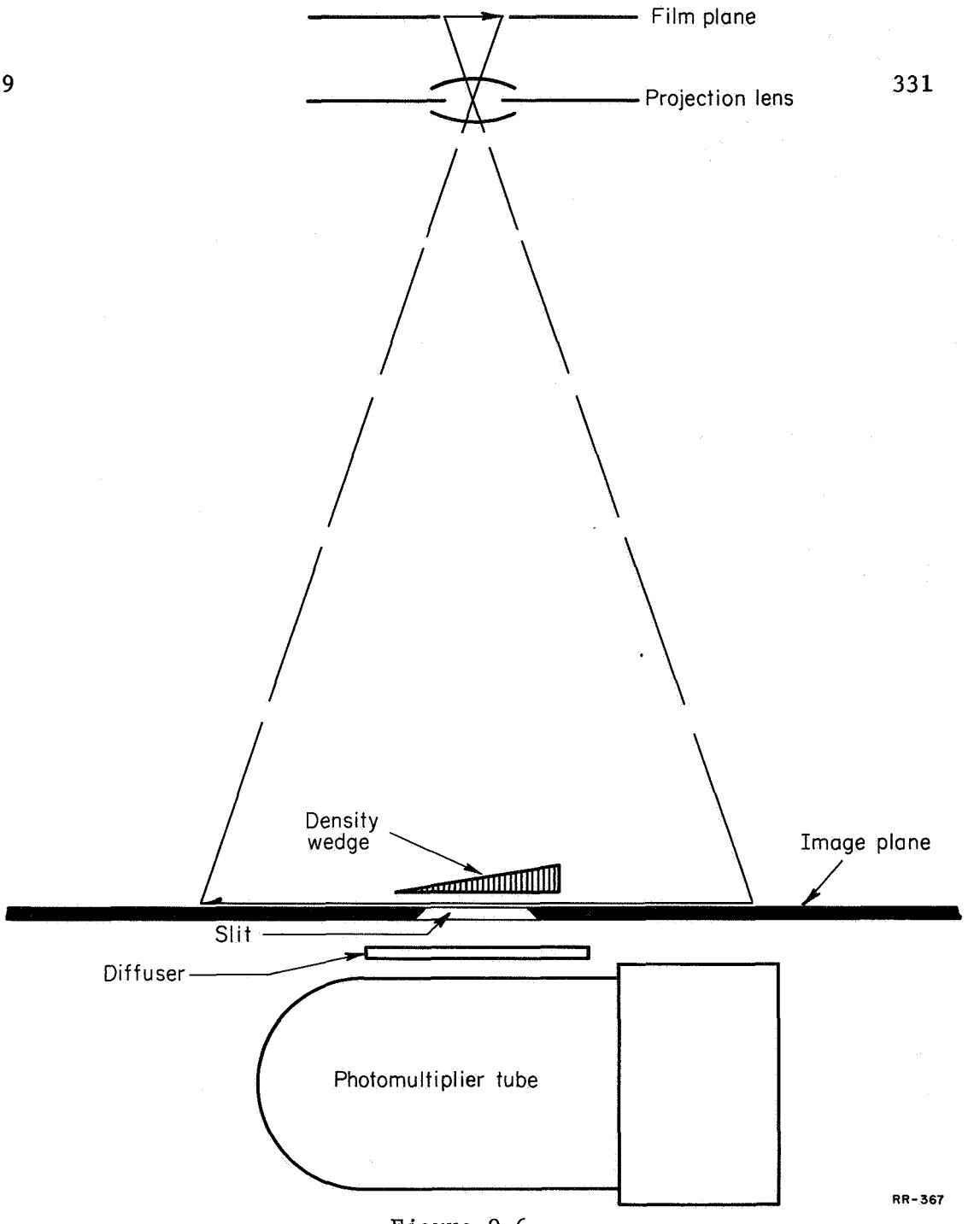

Figure 9.6

Weighted-aperture projection microdensitometer (schematic diagram). The light source and monitoring photomultiplier of the Jarrel-Ash instrument are not shown. By allowing half the image, of a type shown in Fig. 9.2, to enter the slit, noting the transmission, then moving the image to bring the other half over the slit with the wedge turned through 180°, and positioning the image to obtain exactly the same transmission, a center-of-gravity type of estimate of image center may be made. Later studies have shown that much more convenient estimation procedures may be used.

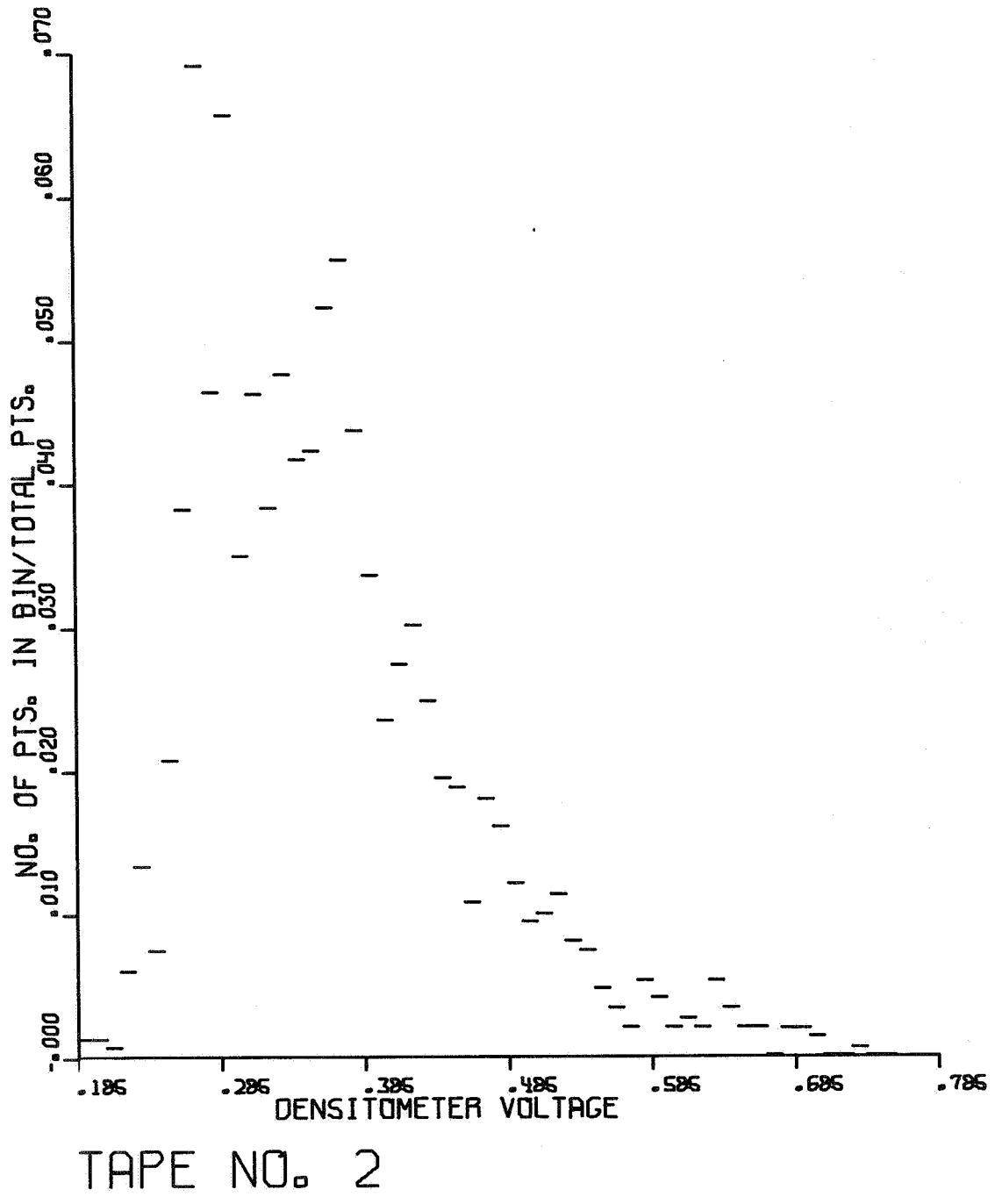

Figure 9.7

Measured probability distribution (noncumulative) of graininess noise in density of Baker-Nunn film. The average (specular) density is 0.36. The distribution is roughly characterized as skewed gaussian, except for a slight tendency for a double peak probably due to a drift in the calibration of the Ansco projection microdensitometer.

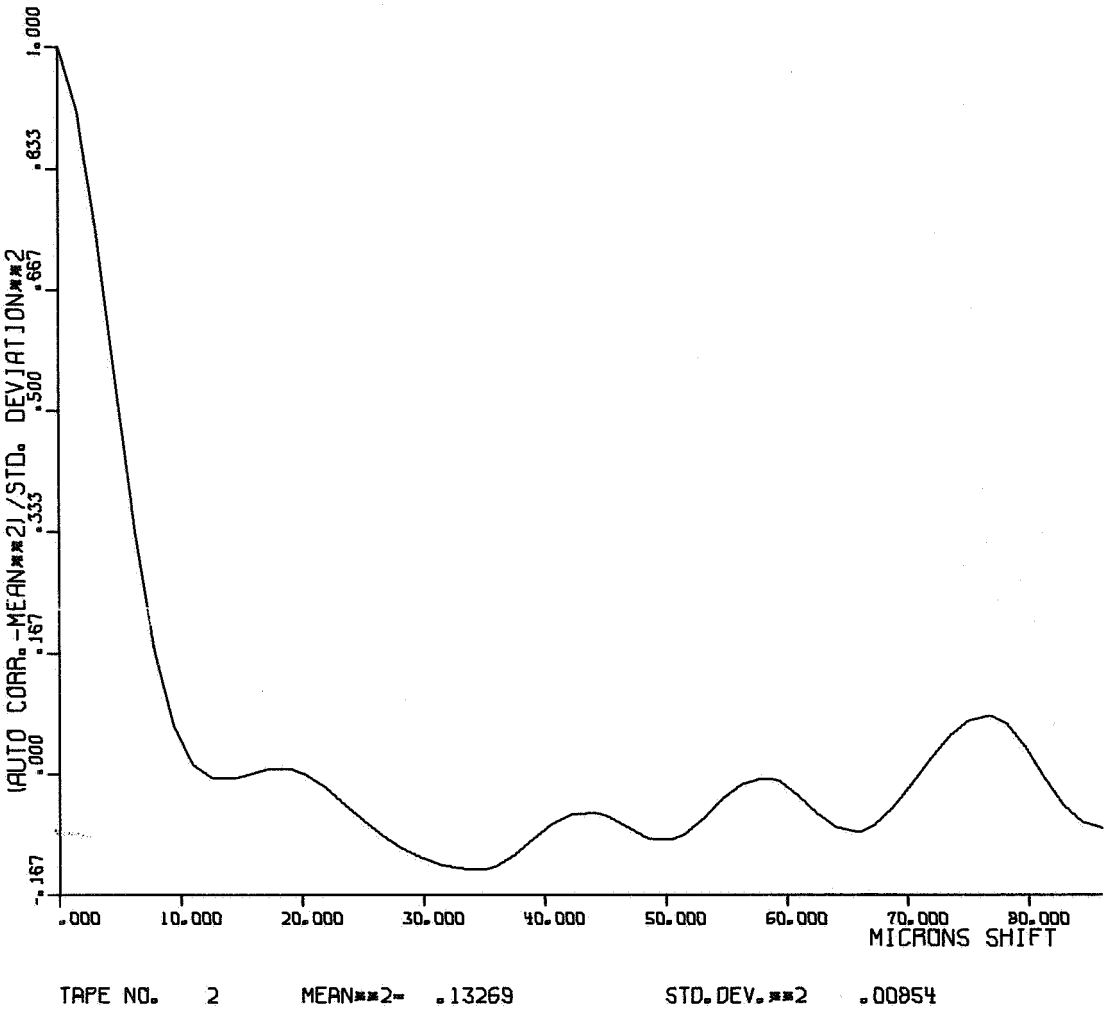

Figure 9.8

Measured autocorrelation values plotted versus separation along the film of the noisy density values for the same data as in Fig. 9.7. It is seen that for points separated by 10 microns (the width of the aperture in the Ansco projection microdensitometer) or more, the density fluctuations are essentially uncorrelated.

exposed to sensitometric step wedges, kindly supplied by the Smithsonian Astrophysical Laboratory,[2] microdensitometer tracings were obtained and studied.

Prior to our making arrangements with the U. of I. Astronomy Department to use their Jarrel-Ash machine, D. C. O'Connor, temporarily with Photogrammetry and Geodesy in the U. of I. Department of Civil Engineering, volunteered to make microdensitometer tracings for us with the Ansco machine at Ft. Belvoir.[5] These tracings were made of the density step wedges and were recorded graphically. Successive values on the graph were read at equal intervals and transcribed to coded paper tape for computer analyses. Calcomp plots of the transcription were compared against the original tracings to check for errors. These data were analyzed in two ways, and examples of the results are shown in Fig. 9.7 and 9.8.

The first of these, Fig. 9.7, shows a plot of the probability distribution (noncumulative) of the density values for an average density of 0.36, using a microdensitometer aperture of 10 μm. The indication is that of a roughly gaussian distribution, except for the clear evidence of skewness. At larger apertures, the general experience with such distributions is that they approach more nearly to gaussian distributions, but there is always some evidence of skewing.[6] For greater values of mean density than shown here, the distribution is also less strongly skewed.

Autocorrelation analysis was also undertaken, based on

values read from the tracing at micron intervals. An example of the autocorrelation function so obtained is plotted in Fig. 9.8, also for a mean density of 0.36. It is evident that the correlation is negligible for density values spaced more than 10 μm apart. Since this distance is the diameter of the aperture in the microdensitometer, the characteristic grain size must be somewhat smaller than that, and certainly smaller than the resolution-spot size of the B-N camera, 25 μm. In the planned simulation of B-N images with the computer, in which the image samples would be spaced a distance of 25 μm, these data indicate that the noise at each sample could be taken to be statistically independent of the noise at every other sample.

The mathematical models of film noise, to be described in Section 9.7, require the specification of only two parameters, the mean value and the standard deviation of the noise. The specification of the mean value was to be made to suit the needs of the digital-computer simulation program, so that the remaining parameter, the standard deviation, is the one to be determined by film-noise measurements. The exact form in which this was desired was that of the standard-deviation values, as a function of the mean. These were to be determined as transmission values, the reciprocal of that for opacity values, and the logarithm of the latter for density values.

For making these measurements, the Jarrel-Ash projection densitometer was used, including a facility for automatically punching

coded transmission values on paper tape. Using a 20 μm aperture, short scans within each step of the step-wedge specimen of B-N film were made and transmission values spaced more than 20 μm apart were punched. Though many data points were desired, it was necessary to make very short runs to minimize the risk of a lapse of focus, a condition which would increase the effective aperture size and lead to a low estimate of the standard deviation. As a further precaution, runs were made along the axis of film curl, despite the fact that the holder allowed very little curl. A Calcomp plot of a typical tracing is shown in Fig. 9.9. The data used for each density step was a composite of many such runs.

The transmission values obtained in this way are the so-called specular transmission values. Since the diminution of transmission by photographic film results in large part from a scattering of light, the transmission values depend in large measure upon the solid angle of acceptance of the forward-scattered light. When this solid angle is small, one is dealing with specular values, in contrast to the standard values obtained by placing a diffusing screen (opal glass) in contact with the specimen and measuring the light transmitted from that screen; these latter are called diffuse values and involve the acceptance of scattered light over more nearly 2π steradians. The calibration of the projection densitometer in terms of diffuse values was by a procedure involving a measurement of the Callier Q factor[7] for each density level to provide a conversion of

specular densities to diffuse densities by way of reference to a standard calibrated Welch step wedge. Diffuse values were desired so that the measured densities could be compared to those obtained in the sensitometry. The calibration procedures and statistical-analysis procedures were implemented on the CDC-1604 computer.

The resulting plot of the standard deviation in opacity, σ_ω, versus mean opacity, ν_ω, is shown in Fig. 9.10. The straight line fit obeys

$$\sigma_\omega = (\nu_\omega/6)^{4/3}. \tag{1}$$

Laws of this form have been examined by Finley and Marshall.[8] They find that the variance in transmission can be fitted to the law

$$\sigma_t^2 = \alpha t^b \tag{2}$$

in which b has the value 1.5 for a great variety of conditions and t is the transmission. Writing σ_t as a differential, this is

$$dt = \beta t^{b/2}, \tag{3}$$

into which there may be inserted $t=1/\omega$ and $dt=d\omega/\omega^2$ to obtain

$$d\omega = \beta\omega^{(2-b/2)}, \tag{4}$$

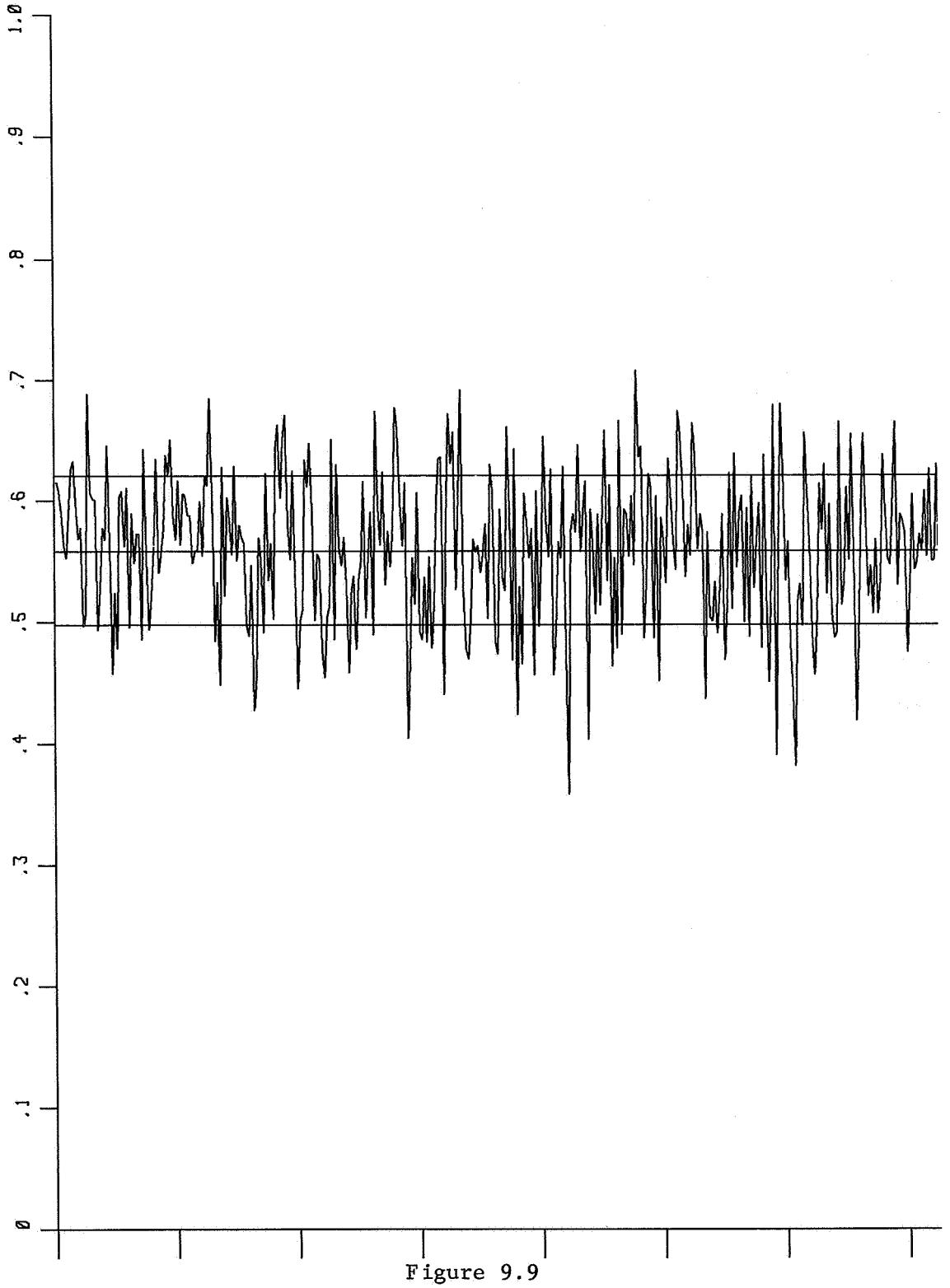

Figure 9.9

Calcomp plot of sequence of transmission values measured at intervals greater than 20 microns (the aperture diameter) along a constant-density portion of Baker-Nunn film using the Jarrel-Ash projection microdensitometer.

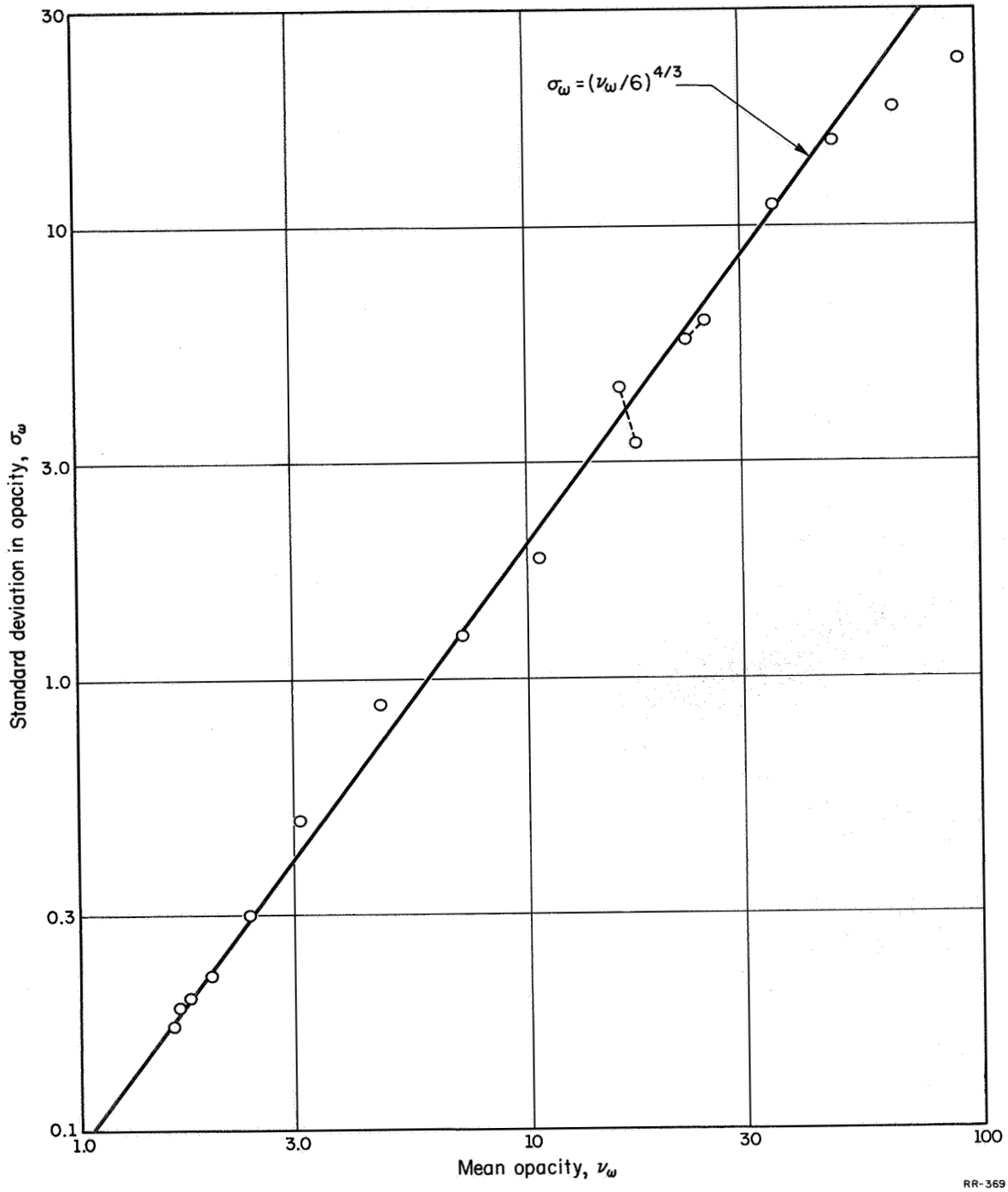

Figure 9.10

Measured standard deviation in opacity plotted versus mean opacity, adjusted to represent measurements on a diffuse basis. The fitting to a Callier Q-factor type of curve for this adjustment was made in batches. The overlap of one batch with another is indicated by the points connected by dashed lines, which points may be interpreted as providing a notion of the reproducibility of the data. The straight-line fit shown here represents the law to be used in the computer simulations.

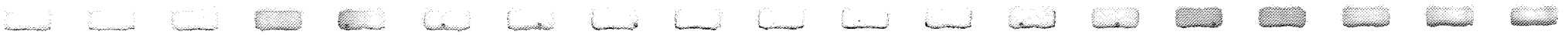

in which the exponent 2-b/2 may be compared with the exponent in Eq. (1). For example, the value b=1.5 is equivalent to an exponent value of 1.25 in Eq. (4), and this compares favorably with the value 1.33 in Eq. (1), as measured here. In some early runs covering a small range in opacity, an indication of an exponent of 1.0 was obtained for Eq. (4), with a β value of 0.1. Some of the digital-computer estimation trials were based on these early parameters, but the analyses for high-density images used the parameter values shown in Eq. (1).

9.7. Mathematical Models of Film Noise.

In order to construct numerical specimens of simulated densitometer tracings, as in Fig. 9.4, of noisy Baker-Nunn images of the flash pattern, it is necessary to develop mathematical models of the probability distribution of film noise. For economical simulation, the models must be simple in their parametric structure to facilitate allowing the parameter values to vary with position along the image to reflect variations in mean value, standard deviation, and skewness. At the same time, the models must be adaptable to the formation of random numbers obeying those models, starting from random numbers u uniformly distributed over $0 \leq u < 1$, since such are the ones most easily generated in a digital computer.

It is clear that perfectly symmetrical distributions are

out of the question, whether for transmission values, $t=I/I_o$, the ratio of transmitted to incident light, for opacity values, $\omega=1/t$, or density values $\delta=\log\omega$. For transmission values bounded to the finite interval $0\leq t\leq 1$, the distribution must vanish at 0 and 1 and be appropriately skewed as the mean crowds close to either bound. Opacity values are bounded to the semi-infinite range $1\leq\omega<\infty$, and density values are similarly bounded to $0\leq\delta<\infty$. Models need be developed only for opacity, but the same form of model, might, with suitable fitting, serve also for density. The model must be most strongly skewed when the mean is a short distance, measured in units of the standard deviation, from the lower bound, and become more nearly gaussian as the mean is farther from that bound.

The model to be chosen should be finite only for positive values (accommodation to the range 1 to ∞ can be obtained by shifting) and should involve 3 parameters: mean, standard deviation, and skewness. A one-parameter model was actually chosen, since dilation of the scale can be introduced as a second parameter, and since an arbitrary, but reasonable, relation between skewness and the ratio of standard deviation to mean was thought to be adequate in order not to place too great a burden upon the experimental measurements. The measurements were found to be sufficiently difficult, even for very modest demands for reliability, that this decision proved to be most fortunate.

The model chosen was the chi-square distribution

$$f_{\ell p}(\lambda)d\lambda = [\Gamma(p+1)]^{-1}e^{-\lambda}\lambda^{p}d\lambda \tag{1}$$

governing a random variable $0\leq\ell_p<\infty$, with mean value $\nu_{\ell p} = p+1$ and standard deviation $\sigma_{\ell p} = \sqrt{(p+1)}$, in which $\Gamma(\ )$ denotes the well-known gamma function. For $p\gg1$, this model does tend to a gaussian form, and it has a skewness deemed appropriate for the present purposes as may be seen from the plots of Fig. 9.11. Given arbitrary values of mean and standard deviation ν_x and σ_x, then p is specified via

$$p = (\nu_x/\sigma_x)^2-1, \tag{2}$$

and the random variable x is represented by

$$x = \sigma^2_x\ell_p/\nu_x, \tag{3}$$

for an x variable to be bounded as $0\leq x<\infty$, as, for example, density. For opacity, the p value is

$$p = [(\nu_\omega-1)/\sigma_\omega]^2-1, \tag{4}$$

and the random variable ω is

$$\omega = 1+\sigma_\omega^2 \ell_p/(\nu_\omega - 1), \tag{5}$$

in order to accommodate the lower bound at 1.

The plan of generation of these random variables, then, is to compute the ℓ_p random variables, given the specified p values via Eq. (2) or (4), and then to apply these scaling and shifting formulas Eqs. (3) or (5) as appropriate. The ℓ_p values themselves are to be calculated from uniformly distributed random numbers u. The way in which this last may be most economically done depends upon the value of p, whether $p=0$, $0<p<1$, $1\leq p<10$, and $10\leq p$.

For $p=0$, the distribution (1) is just the exponential distribution for which the cumulative form is

$$F_{\ell 0}(\lambda) = \int_0^\lambda e^{-\lambda} d\lambda = 1-e^{-\lambda}, \tag{6}$$

which is readily inverted to form

$$\lambda = F_{\ell 0}^{-1}(F) = \ln(1-F). \tag{7}$$

This form provides for a very simple generation of ℓ_0 as

$$\ell_0 = F_{\ell 0}^{-1}(u) = -\ln(1-u) \tag{8}$$

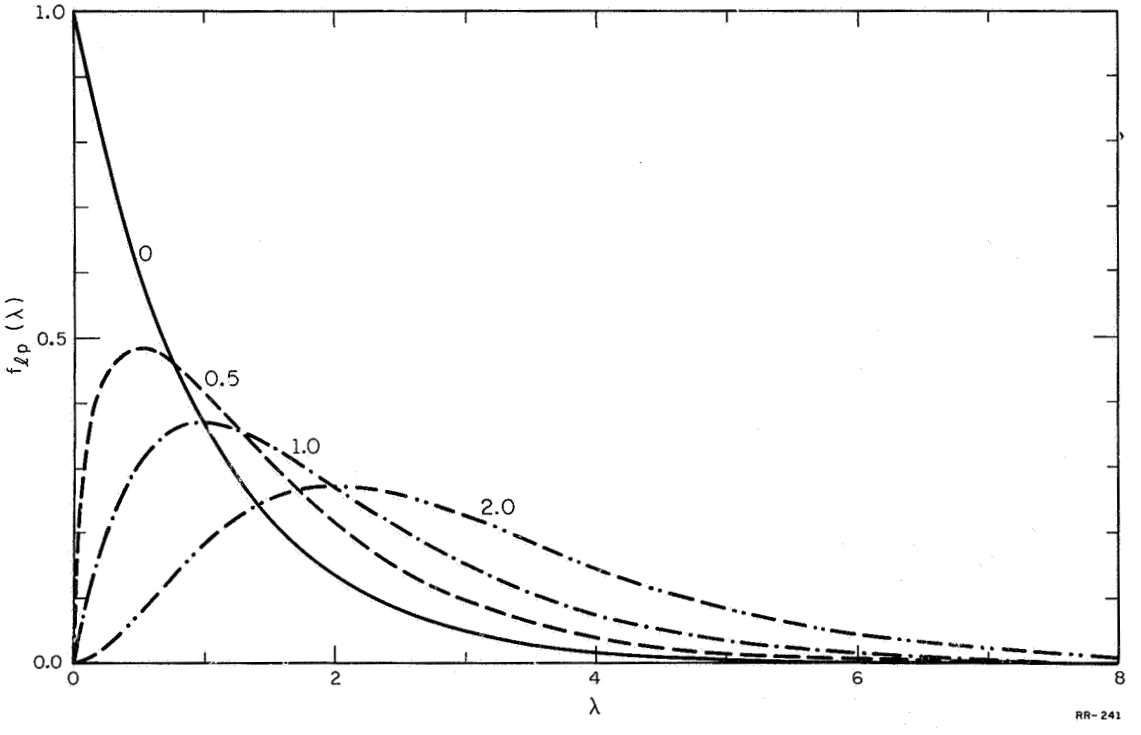

Figure 9.11

Plot of the mathematical models of film-noise probability distributions. These models are adapted to fitting to measured values of mean and standard deviation and have the property that the skewing depends, in approximately the correct manner, upon the distance of the mean, in standard-deviation units, from the lower bound. The parameter labels are values that are functions of the ratio of mean to standard deviation.

from the uniform random variables u. When p is not 0, this inversion of the cumulative distribution is very costly of computer time, especially if p be not an integer, and other algorithms must be used.

For $0<p<1$, the uniform random variable u is tested against a second, independent, uniform, random variable v, and the value of u is accepted as a suitable value for ℓ_p provided it satisfies

$$v \leq e^{-u} u^p. \tag{9}$$

Otherwise, the values of u, v are interchanged, and the test repeated. Failing both tests, the values of u, v are discarded and a new pair is generated, proceeding in this manner until a success is obtained. The range of the variables for this test are suitably scaled so that about 99.9% of the area under the curve specified by Eq. (9) is covered.

For $1\leq p<10$, the value of p is analyzed into a fractional part $0\leq p_f<1$, together with an integral part $p_i=n$. Since it may be shown that

$$\ell_p+\ell_0 = \ell_{p+1}, \tag{10}$$

for ℓ_p and ℓ_0 independent, it is sufficient to sum n independent generations of ℓ_0 to obtain ℓ_n and to also generate ℓ_p for $p=p_f$, adding that to ℓ_n.

For $10 \leq p$, the gaussian approximation is justified. The gaussian generation is done via a stored-table lookup using

$$\ell_p - (p+1) = F_g^{-1}(u)\sqrt{(p+1)}, \tag{11}$$

in which F_g^{-1} is the inverse of the cumulative gaussian distribution for zero mean and unit standard deviation.

The program for generating these random numbers has been tested, with satisfactory results for various values of p, by exercising it to generate a great many numbers, sorting these into value intervals, and comparing the empirical distributions so obtained with curves such as those shown in Fig. 9.11.

This program has also been incorporated into a larger program whereby the mean value ν, representing an image intensity, could be caused to vary in accordance with the sequence of exposure values along the simulated image, while the standard deviation was suitably dependent on the mean value, e.g., as in Eq. (1) of the preceding section. In this manner, data of the form of Fig. 9.4 was generated. This particular figure was made for density values in which the value of σ_δ was independent of ν_δ, a law of variation that was representative of early experimental data (in which σ_ω appeared to be proportional to ν_ω). Also, the nonlinearity of the H & D sensitometry curve, Fig. 9.3, was not used. The appearance of the more realistic image plots do not greatly differ from this one, however.

9.8. Estimation of Image Center by Maximum Likelihood.

The data representing a noisy image, such as that shown in Fig. 9.4, may be regarded as a sequence of n random variables which have taken on the values $y_1, y_2, \ldots, y_n$. If it is known how the probability distribution depends on the position θ_i in the sequence with respect to a central position θ_o, then the probability of obtaining any particular sequence can be expressed as a conditional probability, or likelihood function, the condition being that the central position be given by θ_o. Schematically, this likelihood function may be written

$$L = L\{y_1, y_2, \ldots, y_n | \theta_o\}. \tag{1}$$

These data may be thought to be "explained" with maximum likelihood by finding the value of θ_o which maximizes the value of L, i.e., by solving

$$\partial L/\partial \theta_o = 0 \tag{2}$$

to obtain that value of θ_o. It is often convenient to deal with the logarithm of the likelihood function

$$\Lambda = \ln L, \tag{3}$$

in which case, Eq. (2) is equivalent to

$$\partial\Lambda/\partial\theta_o = 0. \tag{4}$$

The value, obtained by solving Eq. (2) or Eq. (4), is called the maximum likelihood estimate[9] of the parameter θ_o, the center of the image.

In the present instance, the logarithm of the likelihood function is, from Eq. (1) of the preceding section,

$$\Lambda = -\Sigma_i \ln[\Gamma(p_i+1)] - \Sigma_i y_i + \Sigma_i p_i \ln y_i, \tag{5}$$

in which p_i is to be a function of $\theta_i-\theta_o$, the distance of the image point i from the image center θ_o, and the summation index i is to range over all points in the image. In this, y_i stands for the random value (density or opacity) that obtains at the point i. These y_i are fixed measured values, not to be regarded as functions of θ_o in calculating the derivative indicated in Eq. (4), except that they may be related to the values of interest (density or opacity) by way of θ_o-dependent parameters of proportionality.

Consider the differentiation of the first term on the right in Eq. (5). It is

$$-\Sigma_i(\partial/\partial\theta_o)\ln[\Gamma(p+1)] = \Sigma_i(\partial/\partial\theta_i)\ln[\Gamma(p_i+1)]. \tag{6}$$

In the approximation in which the summation is equivalent to an integration, the value of (6) is just the difference in the values of $\ln[\Gamma(p+1)]$ to the left and right of the image where p=0, i.e., the value of Eq. (6) is zero. (Apart from this approximation, the zero is also obtained for p being an even function of $\theta_i-\theta_o$.)

Also, if y is to represent an opacity value, then, according to Eq. (5) of the preceding section, y_i should be replaced by

$$y_i = (\omega_i-1)(\nu_i-1)/\sigma_i^2, \tag{7}$$

upon making adaptation to the present notation. The last term of Eq. (5) then becomes

$$\Sigma_i p_i \ln(\omega_i-1) + \Sigma_i p_i \ln[(\nu_i-1)/\sigma_i^2], \tag{8}$$

of which the last term may also be discarded by the same argument concerning Eq. (6). There remains only

$$\Sigma_i(\partial q_i/\partial\theta_i)(\omega_i-1) - \Sigma_i(\partial p_i/\partial\theta_i)\ln(\omega_i-1) = 0, \tag{9}$$

in which

$$q_i = (\nu_i-1)/\sigma_i^2 \tag{10a}$$

and

$$p_i = (\nu_i - 1)^2/\sigma_i^2 \tag{10b}$$

serve as local values of the signal-to-noise ratios.

The solution of Eq. (9) may be described. The function $\Omega=\partial q/\partial\theta$ is a function of $\theta_i-\theta_o$, that is to say, it is a weighting function for the values of ω_i-1, and its center θ_o is to be adjusted so as to make the first term of (9) vanish. Similarly, the function $\Delta=\partial p/\partial\theta$ is a weighting function for the values of $\ln(\omega_i-1)$ whose central location is to make the last term vanish. If these do not vanish separately, then, according to Eq. (9), θ_o must be chosen to make their difference vanish. When the index value c is assigned to the center of the weighting functions, the problem is seen to be the determination of c such that

$$\Sigma_i \Omega_{i-c}(\omega_i - 1) - \Sigma_i \Delta_{i-c} \ln(\omega_i - 1) = 0 \tag{11}$$

In the computer, this would be done by computing these weighted sums for successive values of c until the value were found for which (11) were satisfied. Actually, however, c need not be one of the indexed values, but, as a practical matter, it could be assumed to be such until neighboring values for which (11) would be positive for one and negative for the other were found, and then the true value of c could be estimated by interpolation.

The maximum-likelihood estimator was not thought to be adaptable to practical application, however, so that the formulae given here were not developed and studied until very late in this program of work. This judgment is borne out by the fact that this estimator requires the simultaneous weighting of opacity and its logarithm and is, on that account, nonlinear. The exact nature of the nonlinearity, in general, will depend upon the specific probabalistic model assumed; it is fully linear for gaussian models. This last observation was made quite early in the program, and it was the inspiration for the study of linear estimators. These are the "practical" ones with which the experience described in the next section was obtained.

In the experience with practical estimators, it was found that, for reasonably large image densities, the most nearly optimal weighting functions required zero weight over a very wide central portion of the image. On comparison with the weights that may be calculated from Eqs. (10), it was seen that this characteristic could rather accurately have been foretold, that only the edgemost 2% or 3% of the image would be of value, except for the possibility of very small negative weights in the central part being indicated. The significance of this comparison will be indicated in a later section, but it is premature to indicate in any great detail the role that a maximum likelihood estimator might play in the actual conduct of an experiment until further study is made.

9.9. Practical Center-Estimation Procedures.

The center-estimation procedures for which extensive trials were conducted in the computer using computer-simulated images, employed the so-called practical weighting scheme

$$\Sigma_i w_{i-c}(\omega_i - 1) = 0, \tag{1}$$

in which w_i is always positive for index values i of one sign and always negative for the other. The scheme is "practical," because it is one that could be implemented with a two-aperture densitometer in which the two apertures are suitably weighted by density wedges and equality between the signals obtained from the two apertures is to be sought.

The images constructed, as in Fig. 9.4, consisted of an interval representing night-sky exposure, a central interval representing the exposure pattern for the solar flashes, followed by a night sky interval. These three intervals were of nearly equal length, but the central interval was represented by 180 equally-spaced samples corresponding to a sample spacing equal to the resolution of the B-N camera, 10 arcsec, for a flash pattern 1800 arcsec long, i.e., the solar disc was taken to be exactly 0.5 deg. wide. The exposure values were programmed to follow the predicted "semi-circular" envelope (actually elliptical for arbitrary choice of scale) with a peak or central value that was specified in terms of

a density increment above night sky *via* computer interpolation in the sensitometric data of Fig. 9.3. Using these sensitometric data, the mean opacity value for each point of the image was computed, and, for each such point, the standard deviation of opacity was also determined using the law deduced from the measurements as in Fig. 9.10. Using the probabalistic models described in Section 9.7, these parameters governed the selection of the actual noisy opacity for each point.

Having constructed the ω_i sequence, the computer also generated the w_i sequence according to rules specified by the programmer. Then it computed the value of the weighted sum, the left-hand side of Eq. (1) for a short sequence of c values bracketing 0. On finding a neighboring pair of c values such that the sum was positive for one and negative for the other, the computer used linear interpolation to estimate more accurately the c value satisfying Eq. (1). Having stored this c value, the computer then proceeded to generate a new image to the same specifications, but using independent random numbers, to determine a c value, and to store that one also, repeating the process again and again until the specified number of statistically independent trials had been completed. It then computed the mean and standard deviation of its center determinations for printout as percentages of the solar-image width.

The results of many sets of trials are shown in Figs. 9.12 and 9.13. For these, the rule used was that the standard deviation

in opacity was 10% of the opacity value as indicated by early measurements. In later sets, the 4/3-power rule was used. Each datum of Fig. 9.12 is based on 100 trials, and the error symbol shown for one of the points represents the 10% rms statistical uncertainty. In Fig. 9.13, each datum represents 1000 trials and the statistical uncertainty is about equal in size to that of the plotting symbols used.

The data of Fig. 9.12 were obtained to explore the efficacy of various kinds of weighting curves for computing w_i. The center-of-gravity weight, open diamonds, is seen to be superior to weights that show discontinuities or provide uniform weights near the edges of the image. On the other hand, weights which are zero for the central part, but are free of discontinuities (though vanishing outside the image) are superior to center of gravity. Weighting curves such as shown by the open circles and that obey a second-order curvature have a clear advantage, especially if a central interval is zero (solid circles).

The data of Fig. 9.13 were obtained to explore the effect of reducing the number of flashes in the image. To this end, runs were made using 180 image points and also using 90 image points by the simple expedient of alternately replacing the opacity values for half the points by a constant value. In this way, the night-sky opacity fluctuations that would occur between resolved flashes is ignored, a proper procedure for actual estimation also, if weighting

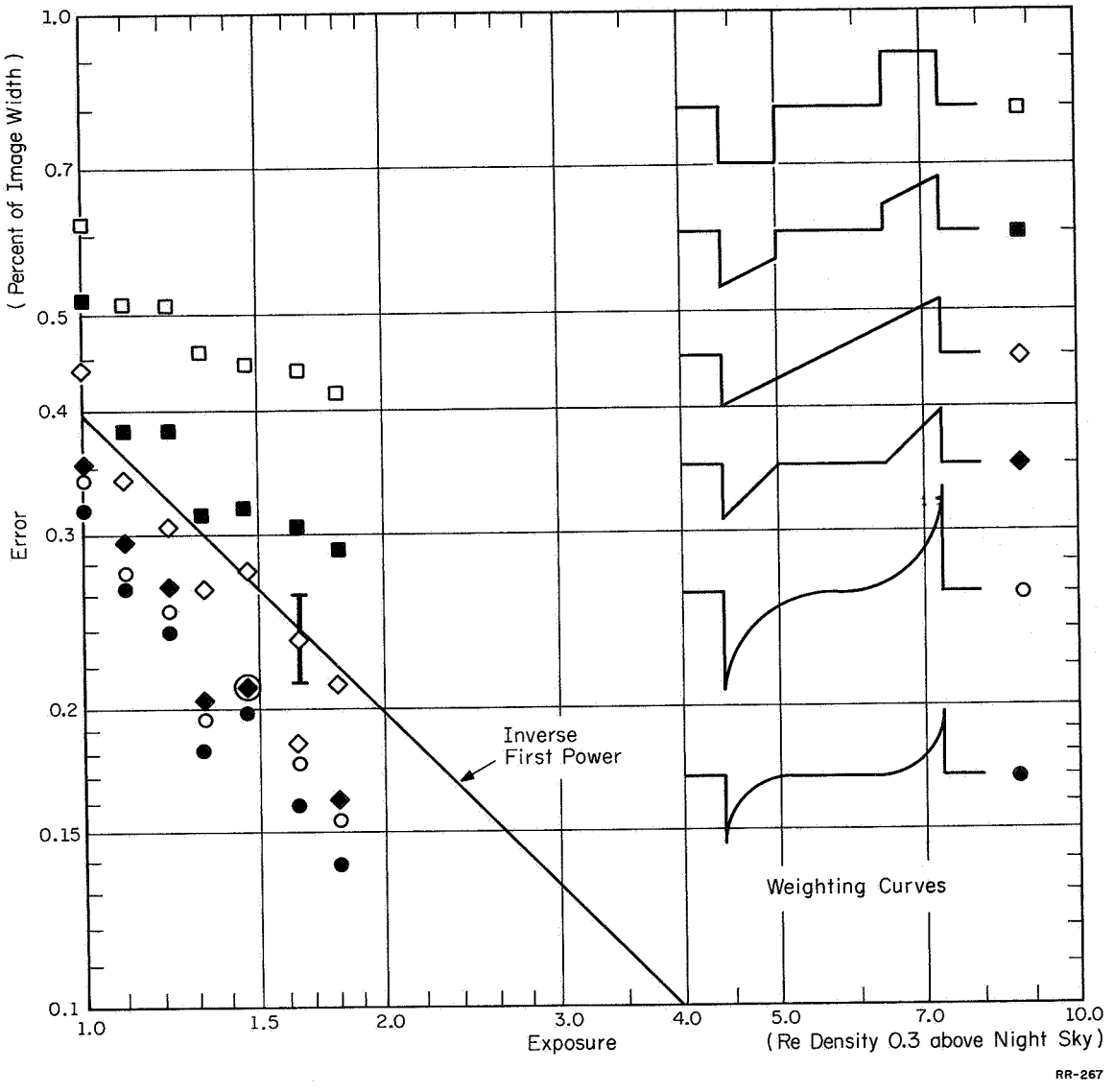

Figure 9.12

Trials of a variety of weighting functions for center-of-gravity types of center-estimation procedures. Root-mean-square-error values are plotted versus central-flash-exposure values. Each point represents 100 statistically independent trials. It is seen that certain weighting functions (solid circles) are much better than the true center-of-gravity weight (open diamonds).

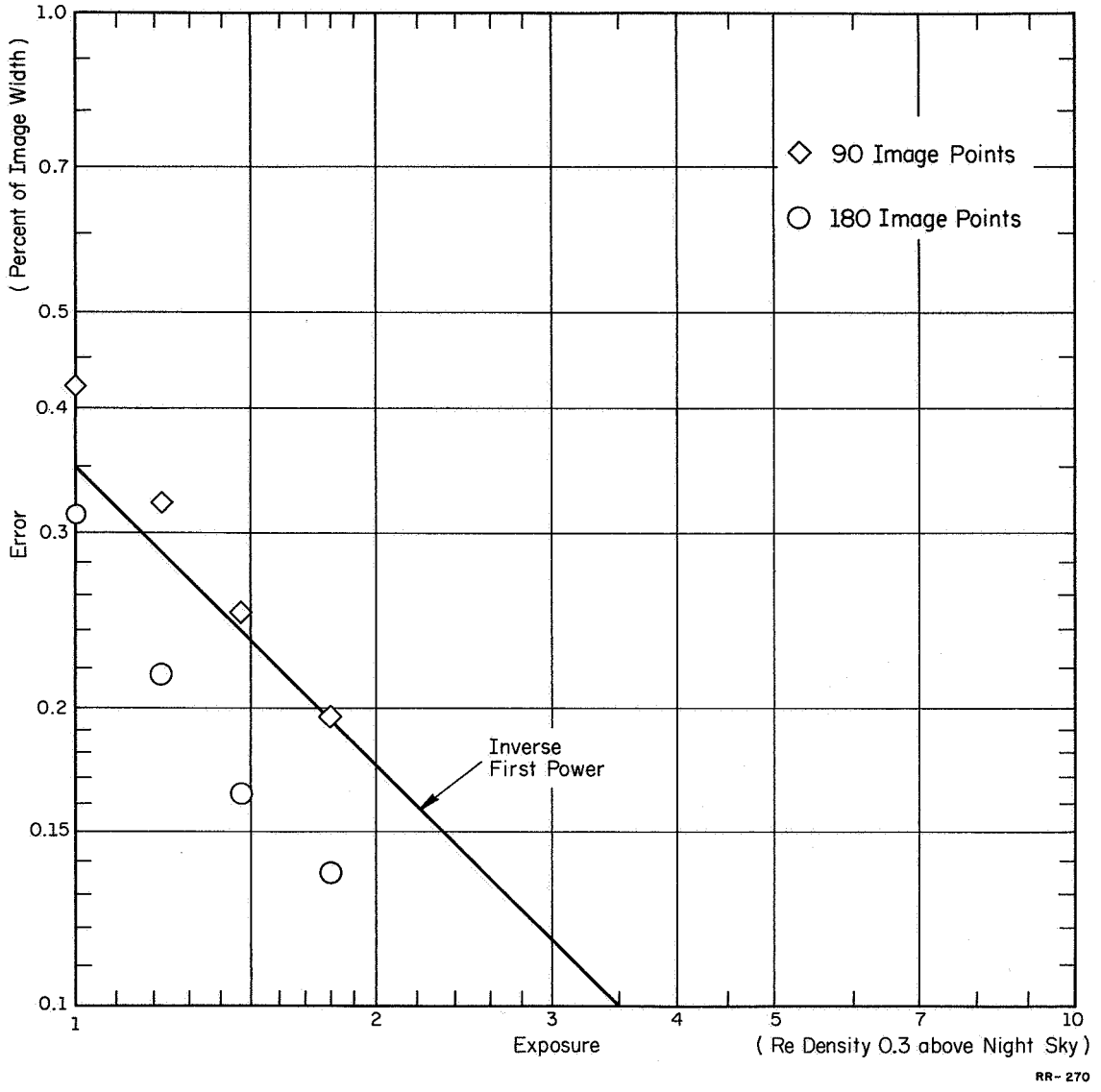

Figure 9.13

Trials of center estimation for resolved flash-pattern images in comparison with unresolved ones. The deletion of alternate image points to leave an image consisting of 90 points, instead of 180 points, results in an increase in rms error by nearly the expected factor, $\sqrt{2}$. Each point represents 1000 statistically independent trials.

methods are to be used. It is seen that deleting half the image points increases the estimation error, for the same exposure values, almost exactly by the expected factor $\sqrt{2}$. One may conclude that a halving of the slant range, which quadruples the exposure value but halves the number of flashes, will lead to a reduction in error by the factor $2\sqrt{2}$, since the dependence upon exposure here is seen to approximate an inverse first-power law.

In order to extend the investigation to larger exposure values than shown in Figs. 9.12 and 9.13, it was necessary to obtain noise-variance data over a greater range of densities. With these data, the 4/3-power law was discovered and used in all later studies. Also in making this extension, it was discovered that the best weighting curve of Fig. 9.12, also used in Fig. 9.13, did not continue to provide for substantial reduction of error with increasing exposure, in that the extrapolations according to an inverse first-power law, as indicated in Figs. 9.12 and 9.13, did not appear to be fulfilled. Accordingly, variations in that weighting were investigated.

The best weighting curve of Fig. 9.12 is one constructed of quadrants of circles, with zero weight assigned to the central third of the image of the solar disc. It was decided to explore variations in the width of this central "shadowed" part by varying the radii of these quadrants, and determine whether there were a best length for the shadowed portion, depending upon the exposure

or central-density values. The results are shown in Fig. 9.14.

In Fig. 9.14, the curves are plots of rms angular error in center estimation given as a percentage of the width of the solar image and plotted versus the percentage of the image that is left unshadowed. The curves terminate at the left in the value 2% for which the angular error is that obtained when the central 98% of the image has been assigned zero weight. Otherwise, the weighting curve is as described in the preceding paragraph. Each curve is labelled with a value of the central density increment above that obtaining for a 1 sec exposure to nignt sky. Each point represents 400 trials. In each of these trials, half the image points had been deleted; if the full complement of image points had been used, the errors plotted would have been smaller by the factor 0.7. The standard accuracy of the B-N camera is marked on the ordinate as 0.06% of the width of the solar disc, the percentage corresponding to 1.1 arcsec.

Some further study would be justified to clarify a few minor points. For example, the night-sky background was maintained at the fixed value produced by a 1 sec exposure. For the farther ranges, exposures nearer 3 sec may be expected, and the actual brightness of the night sky will vary with orientation of the camera, atmospheric conditions, and the distance of the sun below the horizon. The night-sky exposure enters to a slight degree as a background competition primarily for the weaker images, but these would probably

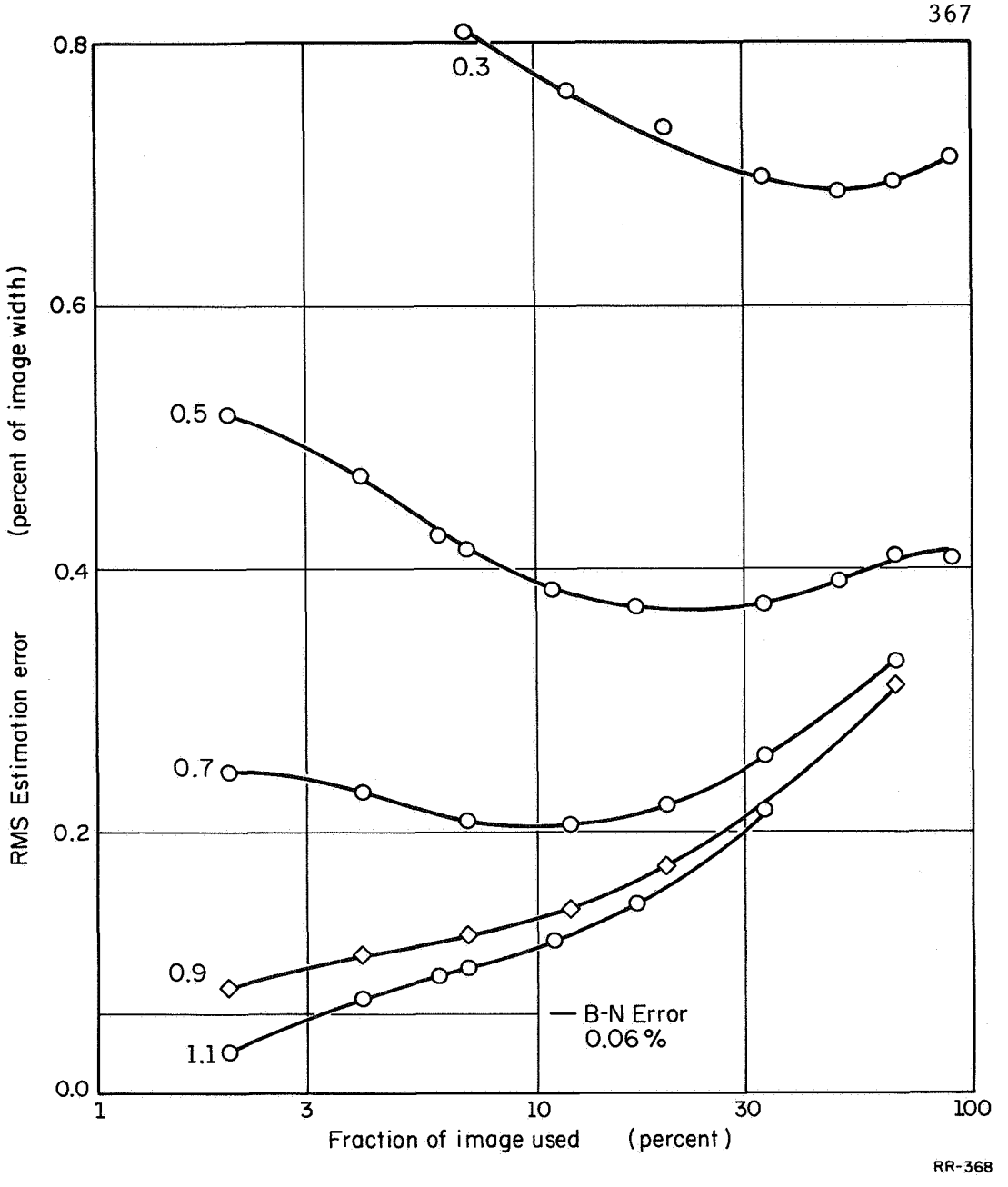

Figure 9.14

Center-estimation trials of high-density images, with a search for the optimal fraction of the image to be used. The weighting function is like that indicated by the solid circles of Fig. 9.12, made up of quadrants of circles with a central "shadowed" portion of zero weight the length of which may be adjusted by adjusting the radius of the quadrants. The plot is of rms error versus the fraction of the image left "unshadowed." The curves are labelled with the central-flash density increment above night sky. Each image consisted of 90 flashes, as with the open diamonds of Fig. 9.13. It is seen that the optimal fraction of the image becomes very small for density increments of 0.8 or larger and that the inherent accuracy of the Baker-Nunn (B-N) camera is attained for density increments of 1.0 for these 90-flash images.

be discarded as introducing too large an error, in any case. For the stronger images, the night sky exposure enters primarily as an augmentation of the exposure because the image is constructed in a flash-by-flash manner each part being treated to pre- and post-exposure to night sky. Though it may be doubted that these variations would significantly alter the conclusions that may be drawn from Fig. 9.14, the point is worth investigation.

Also worthy of further investigation would be the comparisons that may be drawn between the maximum-likelihood estimator and these "practical" estimators, including the computer implementation of the former. Such work is in progress, but the results to date are not yet worthy of presentation here, so that the present interpretations are to be based on the data of Fig. 9.14.

It may be seen that the accuracy of the B-N camera is achieved for density increments of 0.9 to 1.0, depending upon whether the image is essentially continuous, consisting of 180 points, or shows resolvable flashes, some 90 in all. As indicated in Section 9.2, such density increments correspond to an exposure greater than "threshold" by a factor of somewhat less than 5, and it also has been indicated in Section 9.3 that such exposures are obtainable from the mirror flashes at slant ranges of 2500 km.

Studies of the curves of Ω and Δ appearing in the maximum-likelihood estimator in Section 9.8 show the same increasing emphasis of the weight upon the bare fringes of the image as being indicated

for densities near 1.0, with the weight being more broadly distributed for the lower densities. Here, the 2% unshadowed region barely encompasses two datum points at each edge of the image. When the density is such that such a narrowly-based weight should be used, it would appear that the edges could be satisfactorily located by eye and measured with a cross-hair cursor as in a Mann comparator.

Although it would appear that the normal cursor-aided estimation "by eye" will be the most practical, as well as fully accurate, estimator in the end, some slightly more sophisticated techniques will be needed when the image is resolved into individual flashes. The location of these flashes with respect to the center of the image is a happenstance matter of phasing, one for which it might be difficult to make due allowance "by eye." In this resolved-flash circumstance, it would be best to measure the positions of the two outermost flashes, two from eacn edge, and identify these for an independent density (or opacity) measurement. The densitometer operator would also measure the density of a central flash. These data would suffice for a computer implementation of an estimation procedure like those discussed in this report though vastly simplified. Images for which the outermost 4 points (4 from each edge) would be useful might also be of some value. In any case, the practical estimation problem would be very simple, and it would appear that the standard accuracy of the camera would obtain.

9.10. Conclusions.

The principal conclusion that may be drawn is that the photography of the sunlight-illuminated 0.6-m satellite against the night-sky stellar background by means of the Baker-Nunn camera may be expected to provide eminently useful images on the film normally used. Density increments in the neighbornood of 1.0 above the night-sky background may be expected, corresponding to exposures greater by a factor 5 than the threshold defined as producing a density increment of 0.35 ± 0.05, a threshold of 0.8×10^{-10} lm sec/m^2, and this expectation obtains for slant ranges of 2500 km, whether the photography be of the "steady" reflection from the spherical surface of the "glitter" reflection from the optical flats. It has further been snown that the standard accuracy of the B-N camera, 1.1 arcsec, will obtain for the measurement of these images, including the location of tne center of the solar flash pattern, using easily-implemented and practical estimation procedures.

9.11. References.

1. K. B. Henize, "The Baker-Nunn Satellite-Tracking Camera," Sky and Telescope, 107 (Jan. 1957).

2. L. H. Solomon, private communication (Smithsonian Astrophysical Laboratory).

3. Research in Space Science, Special Report No. 74, Smithsonian Astrophysical Observatory (Sept. 18, 1961).

4. C. E. K. Mees and T. H. James, The Theory of the Photographic Process, 3rd Ed., The Macmillan Co., New York (1966).

5. Geodesy, Intelligence, and Mapping Research Agency, Fort Belvoir, Virginia.

6. C. E. K. Mees and T. H. James, op. cit., p. 526.

7. Ibid., p. 421.

8. J. D. Finley and W. W. Marshall, "Image Assessment Research," Final Report, Project JS-412, Data Corporation, Dayton, Ohio (1965).

9. H. Cramer, Mathematical Methods of Statistics, Princeton Univ. Press, Princeton, N. J. (1951).

10. PASSIVE DAMPING OF THE GENERAL RELATIVITY SATELLITE GYRO

10.1. Damping Mechanics of Precessing Body

The demands on a gyro spin axis readout system based on a preferred moment of inertia axis are simplified if the gyro symmetry axis, $\underline{\omega}_3$, angular momentum vector $\underline{h}$ and instantaneous spin axis $\underline{\omega}$ are colinear. In general, when a spinning gyro is suddenly released in free fall, these three axes will not be colinear as shown in Fig. 10.1, resulting in a torque-free motion of the gyro about its angular momentum vector.[1] Even if these axes were colinear, an environmental disturbance such as a micrometeorite collision could cause cratering, thereby shifting the symmetry axis with respect to the angular momentum axis,[2] resulting in a torque-free motion. For an axially symmetric gyro this motion is a steady precession of its instantaneous spin axis $\underline{\omega}$ and symmetry axis $\underline{\omega}_3$ about its angular momentum axis $\underline{h}$, as shown in Fig. 10.2 from the point of view of an observer fixed in inertial space. In this figure the outer cone (body cone), whose axis is $\underline{\omega}_3$, rolls without slipping on the inner cone (space cone), whose axis is $\underline{h}$, and the line of intersection is the instantaneous spin axis $\underline{\omega}$. This precession of the symmetry axis $\underline{\omega}_3$ about $\underline{h}$ complicates the readout problem; consequently, a damping mechanism which aligns the three axes within a reasonable time is required. This report analyzes a passive damping scheme in which energy is dissipated

by virtue of cyclic strains in the gyro body caused by its torque-free precession.[3] The gyro will be considered an axially symmetric solid, spherical in shape except for two diametrically opposite flats, which give a preferred moment-of-inertia C (polar). The moment of inertia about the perpendicular axis is A. The case for a thin, spherical shell has been analyzed.[4,4a]

The analysis of the combined effects of gravity gradient, centrifugal distortion and the statistics of micrometeorite cratering leads to an optimum gyro diameter of about one foot.[5] For a gyro of this diameter the analysis of micrometeorite cratering[6] gives a relationship between the number of hits per year, each of which could cause an angular disturbance of 0.6 arc sec per year, versus (C-A)/C. For one hit per year the ratio $(C-A)/C \approx .01$. Assuming a Poisson distribution for the meteorite flux, this gives a probability of 0.92 for having one month of undisturbed data. It is important, then, that the damping time be quite smaller than one month in order to separate the effects of such cratering from the spin axis orientation data.

The quantities $\underline{\omega}_3$, $\underline{h}$, and $\underline{\omega}$ in Fig. 10.1 are coplaner, and the angles θ and α are related by[1]

$$\tan \theta = \frac{A}{C} \tan \alpha \qquad (1\text{-}1)$$

so that if A = C, then $\underline{h}$ and $\underline{\omega}$ become colinear and $\underline{\omega}_3$ loses its significance. For (C-A)/C = .01 the angle ϵ between $\underline{h}$ and $\underline{\omega}$ will be small

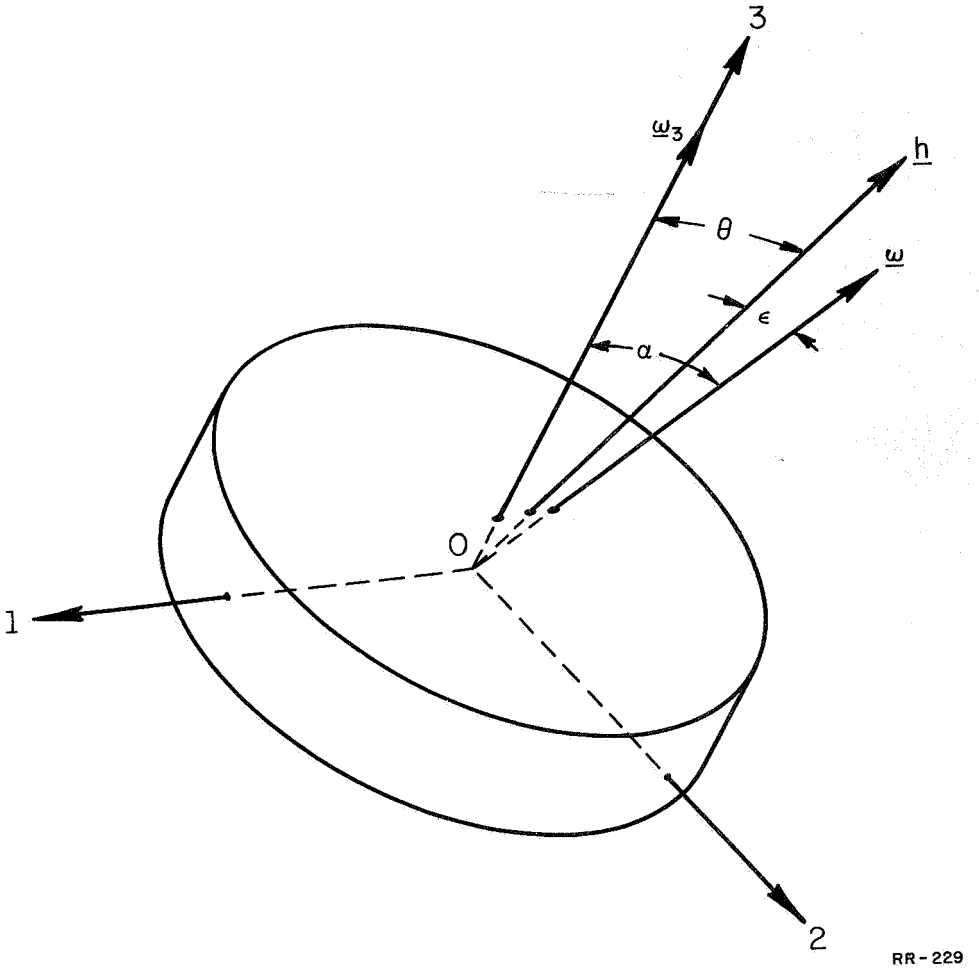

Figure 10.1.

General Relationship of Angular Momentum, Symmetry and Instantaneous Spin Axes of Axially Symmetric Gyro.

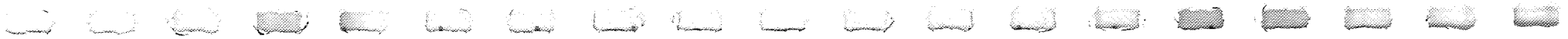

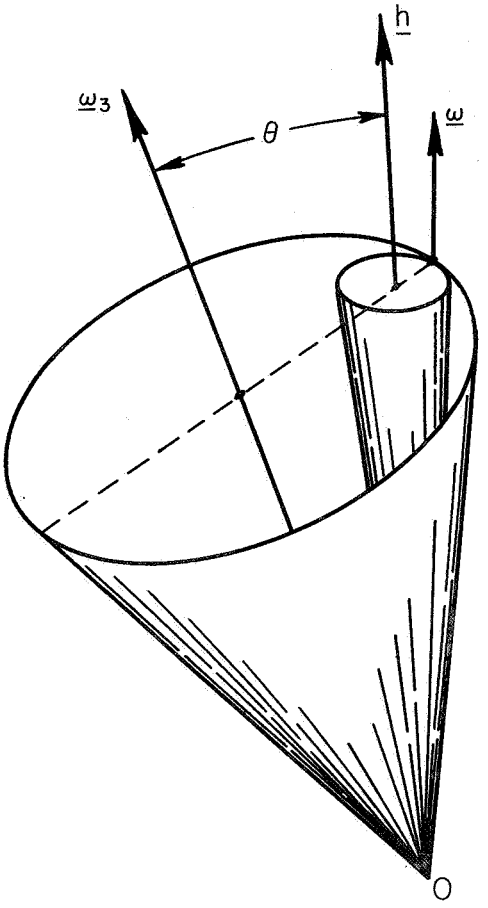

RR-229

Figure 10.2.

Body and Space Cones of Axially Symmetric Gyro in Torque-Free Precession.

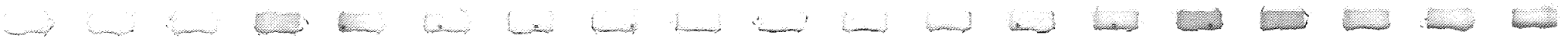

and is given approximately as $\epsilon \approx [(C-A)/C] \tan \alpha$. For example, if $\alpha = 0.4$ degrees, $\epsilon \approx 14$ arc sec. During initial gyro spinup attempts will be made to keep α as small as possible, but there will be some misalignment error. The maximum allowable error is determined by the tolerance within which the satellite spin axis must lie in its orbital plane, which is of the order of 0.4 degrees for the present gyro parameters.[5] This means that $\underline{\omega}_3$ must be known with respect to the gyro body to better than 0.4 degrees.

For axially symmetric bodies the rate $\dot{\Psi}$ at which $\underline{\omega}_3$ and $\underline{\omega}$ precess about $\underline{h}$ for the case of free precession (zero torque) is given by[1]

$$\dot{\Psi} = \frac{C}{A-C} \frac{\phi}{\cos\theta} \tag{1-2}$$

where θ is the angle between $\underline{\omega}_3$ and $\underline{h}$. The quantity $\dot{\phi}$, (later referred to as the elastic vibrating frequency) is the angular rate at which the $\underline{\omega}$ vector moves about the body as viewed by an observer stationed on the body. Therefore, if the spinning body is centrifugally distorted, an observer stationed along $\underline{\omega}_3$ will see the body undergo periodic deformation at a fundamental rate $\dot{\phi}$ corresponding to the rotation rate of the $\underline{\omega}$ vector about the observer. This is shown rigorously in Section 3. Equation (1-2) can be rewritten with the aid of Fig. 10.3, which shows the geometrical relation of the involved

quantities. Since $\omega_o = \dot{\Psi} + \dot{\phi}/\cos\theta$ eliminating $\dot{\Psi}$ gives

$$\dot{\phi} = \frac{A-C}{A}\,\omega_o \cos\theta \tag{1-3}$$

where $\underline{\omega}_o$ is the initial gyro satellite angular velocity.

The periodic deformation of an anelastic body gives rise to a rate of energy dissipation which, among other things, depends upon the fraction of the elastic energy which is dissipated in each deformation or strain cycle.[3] This fraction, γ, is called the hysteretic damping factor, and is a measure of the internal friction of the anelastic body. Metallurgists who measure internal friction usually state results in terms of logarithmic decrement D, quality factor Q, or angle δ by which strain lags stress.[7] The logarithmic decrement is the logarithm to the base e of two successive amplitudes of a freely oscillating body. The various factors which measure internal friction are related as follows, for $Q > 10$:

$$Q = \frac{2\pi}{\gamma} = \frac{\pi}{D} = \tan\delta \ . \tag{1-4}$$

The effect of internal energy dissipation is to decrease the angle θ between the symmetry axis $\underline{\omega}_3$ and $\underline{h}$, which is shown as follows. The kinetic energy T of the axially symmetric body in Fig. 10.1 can be written as

$$T = \frac{1}{2}\,A(\omega_1^{\,2} + \omega_2^{\,2}) + \frac{1}{2}\,C\omega_3^{\,2} \ . \tag{1-5}$$

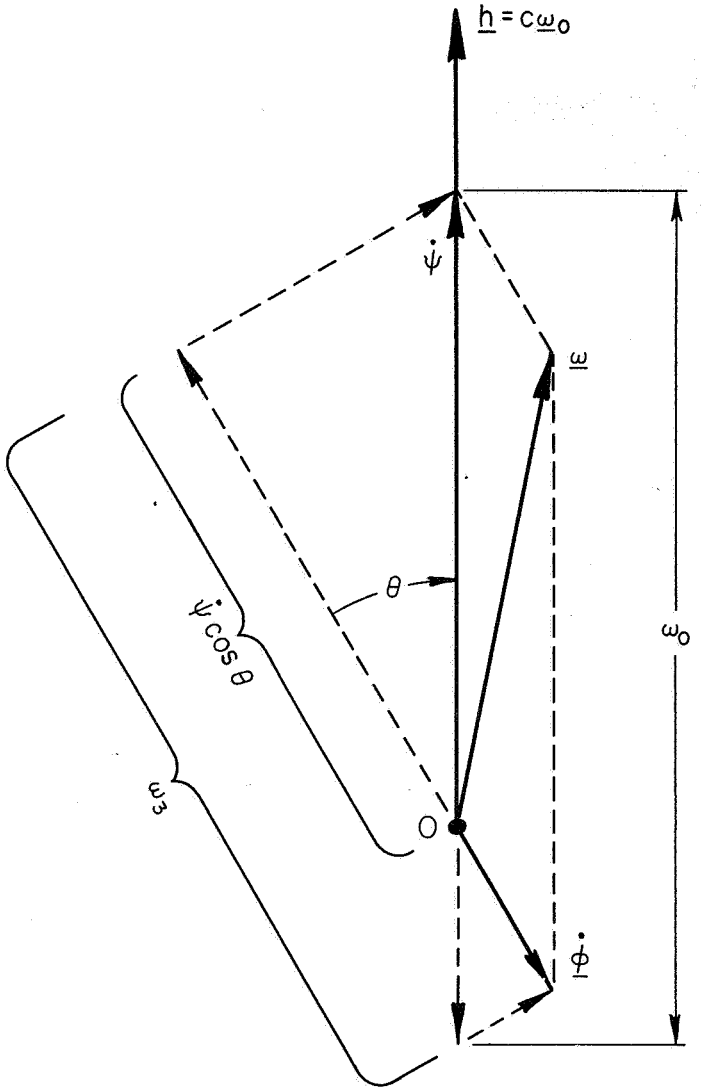

$$\omega_3 = \dot{\Psi} \cos\theta + \dot{\phi}$$

$$\overline{\omega} = \overline{\dot{\phi}} + \overline{\dot{\Psi}}$$

$$\omega_o = \dot{\Psi} + \dot{\phi}/\cos\theta$$

Figure 10.3.

Angular Velocity Relationships of Axially-Symmetric Gyro in Torque-Free Precession.

Also,

$$\underline{h} = \hat{i}A\omega_1 + \hat{j}A\omega_2 + \hat{k}C\omega_3$$

$$\underline{h}\cdot\underline{h} = h^2 = A^2(\omega_1{}^2 + \omega_2{}^2) + C^2\omega_3{}^2 \quad . \tag{1-6}$$

Multiply Eq. (1-5) by 2A and subtract from Eq. (1-6) to get $h^2 - 2AT = C(C-A)\omega_3{}^2$.

Since $C\omega_3 = C\omega_o \cos\theta = h\cos\theta$, solving for T gives

$$T = \frac{h^2}{2A}\left[1 - \left(\frac{C-A}{C}\right)\cos^2\theta\right].$$

For a finite dissipation, with constant $\underline{h}$, the time rate of change of kinetic energy is

$$\dot{T} = \frac{h^2}{A}\left(\frac{C-A}{C}\right)\cos\theta\,\sin\theta\,\dot{\theta}. \tag{1-7}$$

For the case $C > A$, and for a negative value of $\dot{T}$ (energy dissipation), $d\theta/dt$ is negative; therefore, θ decreases.

It is shown later that the total gyro elastic strain energy can be classified into two parts. The first part is independent of $\dot{\phi}$ and is represented as a dc or constant term. Strictly speaking, it is dependent upon θ and $\dot{\theta}$ and hence slowly changing with time, but this change is negligible compared with the second part. The second part of the elastic strain energy varies with time at a rate $\dot{\phi}$, and

all higher harmonics of $\dot{\phi}$ up to the fourth. It is this time varying part which is responsible for the hysteretic damping of precession. If we call W that portion of the gyro elastic strain energy per cycle of stress (whose fundamental frequency is $\dot{\phi}$), then the fraction of this energy which is dissipated per cycle of stress is γW and the rate of dissipation is $\gamma W\dot{\phi}/2\pi$. This must be equal to the rate of decrease in kinetic energy $\dot{T}$ as given by Eq. (1-7). We then have

$$\dot{W} = \frac{\gamma W\dot{\phi}}{2\pi} = -\dot{T} \ .$$

Substituting $\dot{\phi}$ from Eq. (1-3), letting $h = C\omega_o$ and solving for $\dot{\theta}$, one obtains

$$\dot{\theta} = \frac{\gamma W}{2\pi\, C\omega_o \sin\theta} \ . \qquad (1\text{-}8)$$

Sections 2 and 3 describe the method of determining W for a solid, spherical body with preferred moment-of-inertia axis C, such that $C/A \approx 1.01$. There it will be shown that W is a function of gyro radius a, gyro material, spin speed ω_o and angle θ as in the following equation for small values of θ.

$$W = \frac{4\pi^2\rho^2\omega_o{}^4 a^7\theta^2}{E}\,\Gamma \qquad (1\text{-}9)$$

where Γ is a dimensionless quantity which is a function of gyro geometry and material. Substituting this into Eq. (1-8), with $\sin\theta \approx \theta$ and $C \approx (2/5)Ma^2 = (8/15)\pi a^5\rho$ gives

$$\dot{\theta} = \frac{15}{4E}\gamma\rho\omega_o^3 a^2 \Gamma\theta \quad . \tag{1-10}$$

The solution of (1-10) for the damping time t for an initial angle θ_i and a final angle θ_f is

$$t = \frac{4E}{15\,\gamma\rho\omega_o^3 a^2 \Gamma} \mathrm{Ln}\left(\frac{\theta_f}{\theta_i}\right) \quad . \tag{1-11}$$

It remains to determine Γ, which is obtained from the strain energy W for a rotating solid sphere in torque-free precession.

10.2. Inertia Force Field

Consider a solid sphere rotating about an instantaneous axis $\underline{\omega}$ as in Fig. 10.3. The instantaneous axis of rotation $\underline{\omega}$ is misaligned with the angular momentum vector $\underline{h}$ due to some disturbance which has also shifted the symmetry axis $\underline{\omega}_3$ from the momentum axis $\underline{h}$ by a small angle θ according to Eq. (1-1). If $\dot{\theta}$ is assumed to be small in comparison with the spin velocity $\dot{\phi}$ and the precession $\dot{\Psi}$,

then the angular velocity $\underline{\omega}$ can be written as

$$\underline{\omega} = \hat{i}\dot{\Psi}\sin\theta\cos\phi + \hat{j}\dot{\Psi}\sin\theta\sin\phi + \hat{k}(\dot{\phi}+\dot{\Psi}\cos\theta) \qquad (2\text{-}1)$$

where θ, Ψ, ϕ are Euler angles defining the orientation of the body axes x,y,z with respect to the space axes X,Y,Z as shown in Fig. 10.4 and $\hat{i}$, $\hat{j}$, $\hat{k}$ are unit vectors along the axes x,y,z respectively. The angular acceleration $\dot{\underline{\omega}}$ is

$$\dot{\underline{\omega}} = \frac{\partial \underline{\omega}}{\partial t} + \underline{\omega} \times \underline{\omega} \ .$$

Assuming that θ, $\dot{\phi}$, and $\dot{\Psi}$ are constant,

$$\dot{\underline{\omega}} = \dot{\phi}\dot{\Psi}\sin\theta(-\hat{i}\sin\phi + \hat{j}\cos\phi) \ . \qquad (2\text{-}2)$$

Substituting (2-1) and (2-2) into the equation for linear acceleration

$$\underline{a} = \underline{a}_o + \underline{a}' + \underline{\omega} \times (\underline{\omega}\times\underline{r}) + \dot{\underline{\omega}}\times\underline{r} + 2\underline{\omega}\times\underline{v}' \qquad (2\text{-}3)$$

and noting the following approximations[1,3]

$$\underline{a}_o = \underline{a}' = \underline{v}' = 0 \qquad (2\text{-}4)$$

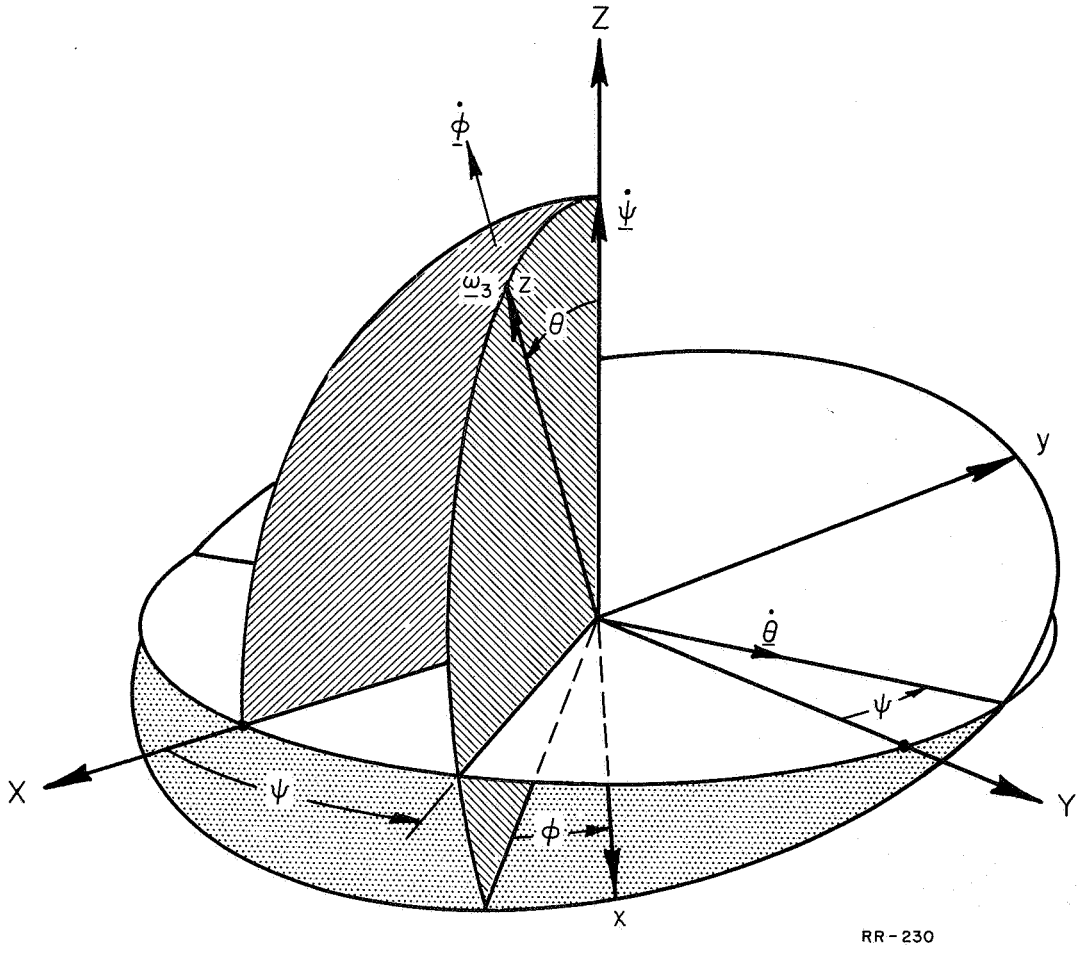

Figure 10.4.

Satellite Gyro Coordinates
with Respect to an Inertial Frame.

$$\begin{aligned}
\underline{a} = \omega_o^2 \hat{i}\Big[& -x\left(\cos^2\theta + \frac{C^2}{A^2}\sin^2\theta\sin^2\phi\right) + y\left(\frac{C}{A}\right)^2 \sin^2\theta\sin\phi\cos\phi \\
& + z\left(\frac{C}{A}\right)\sin\theta\cos\theta\cos\phi + z\left(1 - \frac{C}{A}\right)\frac{C}{A}\sin\theta\cos\theta\cos\phi\Big] \\
& + \omega_o^2 \hat{j}\Big[x\frac{C^2}{A^2}\sin^2\theta\sin\phi\cos\phi - y\left(\cos^2\theta + \frac{C^2}{A^2}\sin^2\theta\cos^2\phi\right) \\
& + z\frac{C}{A}\sin\theta\cos\theta\sin\phi + z\left(1 - \frac{C}{A}\right)\frac{C}{A}\sin\theta\cos\theta\sin\phi\Big] \\
& + \omega_o^2 \hat{k}\Big[x\frac{C}{A}\sin\theta\cos\theta\cos\phi + y\frac{C}{A}\sin\theta\cos\theta\sin\phi - z\frac{C^2}{A^2}\sin^2\theta \\
& - x\left(1 - \frac{C}{A}\right)\frac{C}{A}\sin\theta\cos\theta\cos\phi + y\left(1 - \frac{C}{A}\right)\frac{C}{A}\sin\theta\cos\theta\sin\phi\Big]
\end{aligned} \tag{2-5}$$

Under the assumption that $\dot{\theta}$ is negligible compared with $\dot{\phi}$ and $\dot{\Psi}$, the only time-varying quantity in (2-5) is $\phi = \dot{\phi}t$ and the inertia force varies harmonically at a rate $\dot{\phi}$ and $2\dot{\phi}$ as can be seen from the above equation.

If it is assumed that the body can be approximated by a homogeneous sphere so that the ratio $\frac{C}{A}$ is equal to unity, then the above acceleration becomes

$$\begin{aligned}
\underline{a} = & \hat{i}\omega_o^2\Big[-x(\cos^2\theta + \sin^2\theta\sin^2\phi) + y\sin^2\theta\sin\phi\cos\phi + z\sin\theta\cos\theta\cos\phi\Big] \\
& + \hat{j}\omega_o^2\Big[x\sin^2\theta\sin\phi\cos\phi - y(\cos^2\theta + \sin^2\theta\cos^2\phi) + z\sin\theta\cos\theta\sin\phi\Big] \\
& + \hat{k}\omega_o^2\Big[x\sin\theta\cos\theta\cos\phi + y\sin\theta\cos\theta\sin\phi - z\sin^2\theta\Big] .
\end{aligned} \tag{2-6}$$

The problem is now reduced to finding the displacement field in a sphere subjected to an inertia force $\underline{F} = -\rho\,\underline{a}$.

A general method of solution for a sphere subjected to body force was given by Chree[8] who, as an example, has worked out the displacement field of a sphere rotating about a diametric axis. In that case the problem becomes axisymmetric but such a symmetry is lost when the body force field is that due to acceleration (2-6) which takes into account the influence of precession of the spin axis. In the following, a brief account of Chree's method and its application to the present non-axisymmetric case will be given.

10.3. Displacement Field in a Sphere Subjected to Inertia Force

Chree's method mentioned above is essentially based on the existence of a body force potential which is expanded in spherical harmonics. Consider Navier's equation of equilibrium

$$(\lambda+\mu)\nabla\nabla\cdot\underline{u} + \mu\nabla^2\underline{u} + \rho\underline{F} = 0$$

where λ and μ are Lame's constants, $\underline{u}$ is the displacement and $\underline{F}$ is the inertia force per unit mass due to the acceleration $\underline{a}(= -\underline{F}/\rho)$ expressed by (2-6). This may be written in indicial notation as

$$(\lambda+\mu)\Delta_{,i} + \mu u_{i,kk} + \rho F_i = 0 \qquad (3\text{-}1)$$

$\Delta \equiv \nabla \cdot \underline{u}$ is the dilatation, $P_{,i} \equiv \frac{\partial P}{\partial x_i}$, $i \equiv 1,2,3$ for any function P and the triad x,y,z becomes x_1, x_2, x_3. If F_i and u_i are derivable from potentials V_n (an $n^{\underline{th}}$ order spherical harmonic) and Φ, respectively, such that

$$F_i = F_{n,i}$$
$$u_i = \Phi_{,i} \tag{3-2}$$

then (3-1) becomes

$$(\lambda+\mu)\Phi_{,kk} + \rho V_n = 0 \ . \tag{3-3}$$

Because of the identity

$$(r^m V_n)_{,kk} = m(m + 2n + 1)r^{m-2} V_n \tag{3-4}$$

where m and n are positive integers, Eq. (3-4) is satisfied by

$$\Phi = - \frac{\rho}{2(\lambda+2\mu)\ (2n+3)} r^2 V_n \tag{3-5}$$

The displacement field corresponding to this Φ is, from (3-6) and (3-3),

$$u_i = - \frac{\rho}{2(\lambda+2\mu)\ (2n+3)} (r^2 V_n)_{,i} \tag{3-6}$$

which is accompanied by a surface traction

$$T_i = -\frac{\rho\mu}{r(\lambda+2\mu)}\left[\frac{n+1}{2n+3}\,r^2 V_{n,i} + \left\{\frac{\lambda}{\mu} + \frac{2(n+1)}{2n+3}\right\} x_i V_n\right] \tag{3-7}$$

across any spherical surface r = constant. If a body is bounded by the surface r = a where the surface traction is zero, the displacement u_i is determined by adding to (3-6) the displacements corresponding to ω- and Φ-type solutions.[9] This yields surface tractions

$$\frac{rT_i}{\mu} = (2n+\alpha_n)r^2\omega_{n,i} + \left[2n\left(\frac{\lambda}{\mu} + 1\right) + \alpha\left\{(n+3)\,\frac{\lambda}{\mu} + (n+2)\right\}\right] x_i\omega_n \tag{3-8}$$

$$\alpha_n = -2\,\frac{n\lambda + (3n+1)\mu}{(n+3)\lambda + (n+5)\mu}$$

and

$$\frac{rT_i}{\mu} = 2(n-1)\Phi_{n,i}$$

respectively, where, in this case, ω_n and Φ_n are to be taken as

$$\omega_n = \rho B_1 V_n$$

$$\Phi_n = \rho B_2 V_n \,. \tag{3-10}$$

For the case $T_i = 0$ on $r = a$, these constants B_1 and B_2 are given by

$$B_1 = \frac{\left\{(2n+3)\lambda + (2n+2)\mu\right\}\left\{(n+3)\lambda + (n+5)\mu\right\}}{2(2n+3)(\lambda+2\mu)\mu\left\{(2n^2+4n+3)\lambda + 2(n^2+n+1)\mu\right\}} \tag{3-11}$$

$$B_2 = \frac{n\left\{(n+2)\lambda + (n+1)\mu\right\} a^2}{2(n-1)\mu\left\{(2n^2+4n+3)\lambda + 2(n^2+n+1)\mu\right\}}$$

where n is the order of the spherical harmonic, V_n.

It can be shown easily that the inertia force field due to (2-6) is derivable from the potential

$$V = r^2 V_o + V_2 \tag{3-12}$$

where V_o and V_2 are spherical harmonics of zeroth and second order given by

$$V_o = \frac{\omega_o^2}{3} \quad \text{and} \tag{3-13a}$$

$$\begin{aligned} V_2 = {} & \frac{\omega_o^2}{6}(3\cos^2\theta + 3\sin^2\theta\sin^2\phi - 2)x^2 \\ & + \frac{\omega_o^2}{6}(3\cos^2\theta + 3\sin^2\theta\cos^2\phi - 2)y^2 \\ & + \frac{\omega_o^2}{6}(3\sin^2\theta - 2)z^2 + \\ & - \omega_o^2 \sin^2\theta\sin\phi\cos\phi\, xy \\ & - \omega_o^2 \sin\theta\cos\theta\sin\phi\, yz \\ & - \omega_o^2 \sin\theta\cos\theta\cos\phi\, xz. \end{aligned} \tag{3-13b}$$

It is interesting to note that the potential given by (3-12) and (3-13) reduces, as it should, to that of a spinning sphere given by Chree[8] when the misalignment θ is set to zero.

By substituting (3-12) into (3-6) and superposing the displacements due to ω_n- and Φ_n-type potentials given by (3-10) and (3-11) to ensure the satisfaction of the boundary condition on r = a, after considerable amount of algebra, one obtains the following expressions for the components of the displacement.

$$
\begin{aligned}
u_1 = &\left[\frac{\rho\,\omega_o^2 a^2(5\lambda+6\mu)}{15(\lambda+2\mu)(3\lambda+2\mu)} - \frac{2B_2}{3}\omega_o^2 + B_2\omega_o^2\cos^2\theta + B_2\omega_o^2\sin^2\theta\sin^2\phi\right]x \\
&- \left[B_2\omega_o^2\sin^2\theta\sin\phi\cos\phi\right]y - \left[B_2\omega_o^2\sin\theta\cos\theta\cos\phi\right]z \\
&+ \left[\left\{-\frac{2}{3}B_1 + \frac{1}{35}L + \frac{B_1 M}{3}\right\}\omega_o^2\right. \\
&+ \left\{B_1 - \frac{1}{7}L - \frac{B_1}{2}M\right\}\omega_o^2\cos^2\theta \\
&+ \left.\left\{B_1 - \frac{1}{7}L - \frac{B_1}{2}M\right\}\omega_o^2\sin^2\theta\sin^2\phi\right]x^3 \\
&+ \left[-B_1 + \frac{1}{14}L\right]\omega_o^2\sin^2\theta\sin\phi\cos\phi\,y^3 \\
&+ \left[-B_1 + \frac{1}{14}L\right]\omega_o^2\sin\theta\cos\theta\cos\phi\,z^3 \\
&+ \left[-B_1 + \frac{3}{14}L + B_1 M\right]\omega_o^2\sin^2\theta\sin\phi\cos\phi\,x^2 y \\
&+ \left[-B_1 + \frac{3}{14}L + B_1 M\right]\omega_o^2\sin\theta\cos\theta\cos\phi\,x^2 y \\
&+ \left\{-\frac{2}{3}B_1 + \frac{1}{35}L + \frac{B_1}{3}M\right\}\omega_o^2
\end{aligned}
$$

$$+\left\{B_1 - \frac{1}{7}L - \frac{B_1}{2}M\right\}\omega_o^2\cos^2\theta - \left\{\frac{1}{14}L\right\}\omega_o^2\sin^2\theta$$

$$+\left\{B_1 - \frac{B_1}{2}M\right\}\omega_o^2\sin^2\theta\cos^2\phi\Bigg]y^2x$$

$$+\left[-B_1 + \frac{1}{14}L\right]\omega_o^2\sin^2\theta\cos\theta\cos\phi\, y^2z$$

$$+\Bigg[\left\{-\frac{2}{3}B_1 - \frac{3}{70}L + \frac{B_1}{3}M\right\}\omega_o^2 + B_1\omega_o^2\cos^2\theta - \frac{B_1}{2}M\omega_o^2\sin^2\theta$$

$$+\left\{B_1 - \frac{1}{14}L\right\}\omega_o^2\sin^2\theta\sin^2\phi\Bigg]z^2x$$

$$+\left[-B_1 + \frac{1}{14}L\right]\omega_o^2\sin^2\theta\sin\phi\cos\phi\, z^2y$$

$$+\left[\frac{1}{7}L + B_1M\right]\omega_o^2\sin\theta\cos\theta\sin\phi\, xyz. \qquad (3\text{-}14a)$$

$$u_2 = -B_2\omega_o^2\sin^2\theta\sin\phi\cos\phi\, x$$

$$+\Bigg[\left\{-\frac{2}{3}B_2 + \frac{\rho a^2(5\lambda+6\mu)}{15(\lambda+2\mu)(3\lambda+2\mu)}\right\}\omega_o^2 + B_2\omega_o^2\cos^2\theta$$

$$+B_2\omega_o^2\sin^2\theta\cos^2\phi\Bigg]y - B_2\omega_o^2\sin\theta\cos\theta\sin\phi\, z$$

$$+\left[-B_1 + \frac{1}{14}L\right]\omega_o^2\sin^2\theta\sin\phi\cos\phi\, x^3$$

$$+\Bigg[\left\{-\frac{2}{3}B_1 + \frac{1}{35}L + \frac{B_1}{3}M\right\}\omega_o^2 + \left\{B_1 - \frac{1}{7}L - \frac{B_1}{2}M\right\}\omega_o^2\cos^2\theta$$

$$+\left\{B_1 - \frac{1}{7}L - \frac{B_1}{2}M\right\}\omega_o^2\sin^2\theta\cos^2\phi\Bigg]y^3 + \left[-B_1 + \frac{1}{14}L\right]x$$

$$\omega_o^2\sin\theta\cos\theta\sin\phi\, z^3$$

$$+\left[\left\{-\frac{2}{3}B_1+\frac{1}{35}L+\frac{B_1}{3}M\right\}\omega_o^2+\left\{B_1-\frac{1}{7}L-\frac{B_1}{2}M\right\}\omega_o^2\cos^2\theta\right.$$

$$-\frac{1}{14}L\omega_o^2\sin^2\theta$$

$$\left.+\left\{B_1-\frac{B_1}{2}M\right\}\omega_o^2\sin^2\theta\sin^2\phi\right]x^2y$$

$$+\left[-B_1+\frac{1}{14}L\right]\omega_o^2\sin\theta\cos\theta\sin\phi\,x^2z$$

$$+\left[-B_1+\frac{3}{14}L+B_1M\right]\omega_o^2\sin^2\theta\sin\phi\cos\phi\;y^2x$$

$$+\left[-B_1+\frac{3}{14}L+B_1M\right]\omega_o^2\sin\theta\cos\theta\sin\phi\;y^2z$$

$$+\left[-B_1+\frac{1}{14}L\right]\omega_o^2\sin^2\theta\sin\phi\cos\phi\;z^2x$$

$$+\left[\left\{-\frac{2}{3}B_1-\frac{3}{70}L+\frac{B_1}{3}\right\}\omega_o^2+B_1\omega_o^2\cos^2\theta\right.$$

$$\left.+\left\{B_1-\frac{1}{14}L\right\}\omega_o^2\sin^2\theta\cos^2\phi\right]z^2y$$

$$+\left[\frac{1}{7}L+B_1M\right]\omega_o^2\sin\theta\cos\theta\cos\phi\;xyz. \qquad (3\text{-}14b)$$

$$u_3=-B_2\omega_o^2\sin\theta\cos\theta\cos\phi\;x-B_2\omega_o^2\sin\theta\cos\theta\sin\phi\;y$$

$$+\left[\left\{\frac{B_2}{3}+\frac{\rho a^2(5\lambda+6\mu)}{15(\lambda+2\mu)(3\lambda+2\mu)}\right\}\omega_o^2-B_2\omega_o^2\cos^2\theta\right]z$$

$$+\left[-B_1+\frac{1}{14}L\right]\omega_o^2\sin\theta\cos\theta\cos\phi\ x^3+\left[-B_1+\frac{1}{14}L\right]\times$$

$$\omega_o^2\sin\theta\cos\theta\sin\phi\ y^3$$

$$+\left[\left\{-\frac{12}{15}L+\frac{B_1}{3}M\right\}\omega_o^2+\left\{\frac{1}{7}L-B_1M\right\}\omega_o^2\cos^2\theta\right]z^3$$

$$+\left[-B_1+\frac{1}{14}L\right]\omega_o^2\sin\theta\cos\theta\sin\phi\ x^2y$$

$$+\left[\left\{\frac{B_1}{3}-\frac{3}{70}L+\frac{B_1}{3}M\right\}\omega_o^2-\left\{B_1+\frac{B_1}{2}M\right\}\omega_o^2\cos^2\theta\right.$$

$$\left.-\left\{\frac{1}{14}L+\frac{B_1}{2}M\right\}\omega_o^2\sin^2\theta\sin^2\phi\right]x^2z$$

$$+\left[B_1+\frac{1}{14}L\right]\omega_o^2\sin\theta\cos\theta\cos\phi\ y^2x$$

$$+\left[\left\{\frac{B_1}{3}-\frac{3}{70}L+\frac{B_1}{3}M\right\}\omega_o^2-\left\{B_1+\frac{B_1}{2}M\right\}\omega_o^2\cos^2\theta\right.$$

$$\left.-\left\{\frac{1}{14}L+\frac{B_1}{2}M\right\}\omega_o^2\sin^2\theta\cos^2\phi\right]y^2z$$

$$+\left[-B_1+\frac{3}{14}L+B_1M\right]\omega_o^2\sin\theta\cos\theta\cos\phi\ z^2x$$

$$+\left[-B_1+\frac{3}{14}L+B_1M\right]\omega_o^2\sin\theta\cos\theta\sin\phi\ z^2y$$

$$+\left[\frac{1}{7}L+B_1M\right]\omega_o^2\sin\theta\sin\phi\cos\phi\ xyz. \qquad (3\text{-}14c)$$

where

$$L = \frac{1}{\lambda + 2\mu}$$

$$M = \frac{4\lambda + 14\mu}{5\lambda + 7\mu} \tag{3-15}$$

Terms in these components of displacement can be classified into three categories, the first group being the steady part which does not depend on ϕ at all, the second those which vary with time at a rate $\dot{\phi}$, and lastly those which pulsate at a rate $2\dot{\phi}$. The last two categories which vary with time are responsible for the hysteretic damping of precession.

10.4. Elastic Strain Energy of Solid Sphere

The time varying part of the elastic strain energy can be computed by first taking one half the dot product of the force field $-\rho\underline{a}$, where $\underline{a}$ is given by (2-6), and the displacement field $\underline{u}$, given by (3-15), to give the strain energy density W' such that

$$W' = \frac{1}{2}(-\rho a_i)u_i \tag{4-1}$$

and then dropping all the steady terms which are independent of ϕ. The amount of alternating strain energy W per cycle of precession is

$$W = \int_0^{2\pi} \int_{\Omega} W' \, d\Omega \, d\phi \tag{4-2}$$

where Ω is the volume of the sphere. By substituting (2-6) and (3-14) into (4-1) and (4-2), and dropping terms of the order of $\sin^4\theta$ in comparison with those proportional to $\sin^2\theta$, it is not hard, although tedius, to obtain

$$W = 4\pi^2\rho^2\omega_o{}^4a^7\theta^2\left\{\frac{B_2}{5a^2} + \frac{20}{63}B_1 - \frac{9}{980}L - \frac{19}{630}B_1M\right\} \qquad (4\text{-}3)$$

as the fundamental component of the alternating part of elastic strain energy per unit cycle of precession. Designating the quantity within brackets as Γ', one has

$$\Gamma' = \frac{B_2}{5a^2} + \frac{20B_1}{63} - \frac{9}{980}L - \frac{19}{630}B_1M. \qquad (4\text{-}4)$$

Equation (4-4) may be simplified by first substituting λ and μ into the expressions for L and M of (3-15) and B_1 and B_2 of (3-11), to get

$$L = \frac{(1+\nu)(1-2\nu)}{E(1-\nu)}$$

$$M = \frac{2(7+10\nu)}{7-4\nu},$$

and

$$B_1 = \frac{-(3+\nu)(7-4\nu)(1+\nu)}{7E(1-\nu)(7+5\nu)}$$

$$B_2 = \frac{(3+2\nu)(1+\nu)a^2}{E(7+5\nu)}$$

for n = 2.

These values of L, M, B_1 and B_2 are substituted into (4-4) to get

$$\Gamma' = \frac{1+\nu}{E}\left\{\frac{3+2\nu}{5(7+5\nu)} - \frac{9(1-2\nu)}{980(1-\nu)} + \frac{(3+\nu)(7-4\nu)}{(1-\nu)(7+5\nu)}\left[\frac{19(7-10\nu)}{2205(7-4\nu)} - \frac{20}{441}\right]\right\} \tag{4-5}$$

$$= \frac{\Gamma}{E}$$

which is now only in terms of Poisson's ratio ν and Young's modulus E. Equation (4-3) may be rewritten as

$$W = 4\pi^2\rho^2\omega_o{}^4a^7\theta^2\ \frac{\Gamma}{E}$$

where Γ is a function of ν only. This value of Γ, substituted in (1-11) determines the damping time t for a given gyro.

10.5. Numerical Calculations

The expression for damping time (1-11) may be rewritten in the form

$$t = \frac{4}{15}\frac{E}{\gamma\omega_o\Gamma(\rho\omega_o{}^2a^2)}\ \mathrm{Ln}\left(\frac{\theta_f}{\theta_i}\right) \tag{5-1}$$

From elasticity theory, the maximum stress at the center of a solid, spinning sphere is approximately given by[8]

$$\sigma_{max} + \rho\omega_o^2 a^2 \left(\frac{3 + 2\nu}{7 + 5\nu}\right) \tag{5-2}$$

where ν is Poisson's ratio. Hence, the term $\rho\omega_o^2 a^2$ in the denominator of (5-1) is proportional to the maximum allowable stress for the selected gyro material. Since the optimization study referred to in Section 1 fixes the value of a to be approximately six inches, ω_o for a given material follows from equation (5-2), giving due allowance for a safety factor.

Volume electrical resistivity requirements severely restrict the choice of materials to those between the good conductors ($\rho > 10^3$ ohm cm) and good insulators ($\rho < 10^{10}$ ohm cm). The materials germanium, silicon and titanium dioxide, when properly doped, and certain glasses are among those which appear to satisfy the electrical resistivity requirements. At present, the hysteretic damping factor γ has been obtained only for certain glasses. Among other things, $1/Q$ is a function of the elastic vibrating frequency $\dot{\phi}$ given by equation (1-3). Present gyro parameters indicate a vibration frequency of about 1 to 3 cps. Fortunately, glass has a maximum value for $1/Q(= \gamma/2\pi)$ of about 4×10^{-3} in this range of frequencies[7,11] at room temperature. This makes it a promising high damping factor material.

In order to determine experimentally the approximate value of σ_{max}, thin glass disks were spun to the bursting point in a motor-driven test fixture. For such disks, the maximum stress is also at the center and is, to good approximation

$$\sigma_{max} = \rho\omega^2 a^2 \left(\frac{3 + \nu}{8}\right) . \qquad (5\text{-}3)$$

For glass, $\nu \approx 0.16$ so that the bracketed factors in (5-2) and (5-3) become 0.425 and 0.395 for the sphere and disk, respectively. Hence, the maximum stresses are nearly the same for identical materials, diameters, and spin speed, therefore justifying the use of disks for this test. These tests indicated an upper value of ω_o of about 630 rad/sec for plate glass, with an adequate safety factor. For C/A = 1.01 and θ of the order of half degree, the elastic vibrating frequency $\dot{\phi}$ is about one cps, as seen from equation (1-3).

Using glass as the gyro material, the following parameters have been determined:

$$\gamma = \frac{2\pi}{Q} = .025$$

$$\rho = 2.5 \times 10^3 \text{ kgm/m}^2$$

$$\omega_o = 630 \text{ rad/sec}$$

$a = 7.5$ cm $= .075$ m

$\theta_f = 0.1$ arc sec

$\theta_i = 0.5$ degree

$E = 7 \times 10^{10}$ newtons/m^2

$\nu = 0.16$.

The value of Γ from equation (4-5) becomes $\Gamma = -0.071$. Substituting this and the above values into equation (1-11), the damping time t becomes 8.2 hrs, a reasonable time.

10.6. Conclusion

Using glass as a possible gyro material, the passive damping method for aligning the gyro instantaneous spin axis, angular momentum axis and symmetry axis has been shown to be feasible, requiring about 8¼ hours to damp from $\theta = 0.5$ degree to $\theta = 0.1$ arc sec. The damping time constant $\tau = 0.83$ hours. This value of damping time is probably required only during the initial gyro spin up. The statistics of micrometeorite collisions with this gyro show that there will be a probability of 0.92 for no collisions within the period of one month which could cause an angular disturbance of 0.6 arc sec per year. The effect of such a collision, however, would require only (0.83) (1.8) = 1.5 hours, a reasonable time.

1. Thomson, W. T., "Introduction to Space Dynamics," Wiley, N. Y., 1961, pp. 113-117.

2. Barthel, H. O., "Effects of Micrometeoroid Cratering on the Direction of the Axis of Maximum Moment of Inertia," CSL Report R-274, Coord. Science Lab., Univ. of Illinois, Urbana, Ill., Feb. 1966.

3. Thomson, W. T., and Reither, G. S., "Altitude Drift of Space Vehicles," J. Astronaut. Sci., 7, 29-34 (1960).

4. Palamara, R. D., "Synthesis of a General Relativity Experiment," Ph.D. thesis, Engineering Mechanics Dept., Wayne State Univ., Detroit, Mich., (1964).

5. CSL Progress Report for Dec. 1965, Jan. and Feb. 1966, Coord. Science Lab., Univ. of Illinois, Urbana, Ill.

6. Barthel, H. O., loc. cit., p. 6, Fig. 1.

7. Zener, C., "Elasticity and Anelasticity of Metals," Univ. of Chicago Press, Chicago, 1948, p. 60 ff.

8. Chree, C., Cambridge Phil. Soc. Trans., Vol. 14, Part 3, (1889), p. 292.

9. Love, A. E. H., "A Treatise on Mathematical Theory of Elasticity," Dover Publications, N.Y., 4th ed. pp. 250-252.

10. Bennewitz, K. and Rötger, H., "Uber die Innere Reibung fester Körper; Absorptionsfrequenz von Metallen in akustischen Gebiet," Phys. Zeits chr., 37, 578 (1936).

11. Forry, K. E., "Two Peaks in the Internal Friction as a Function of Temperature in Some Soda Silicate Glasses," Am. Ceram. Soc., 40, [3], 90-94 (1957).

One of the simplest and most reliable types of spacecraft control systems consists of a cold-gas exhaustion through a nozzle from a constant volume supply. This type of system has been used in the past and is being considered for use in bringing the gyro satellite up to the required spin velocity of about 100 revolutions per second. For this application the use of an inert gas in the system will eliminate the possibility of contamination of the satellite gyro optical surfaces. This investigation determines the theoretical performance of the system under quasi-steady flow assumptions and compares the theoretical predictions with experimental results.

In order to derive expressions for the time dependence of the supply parameters, the continuity equation must be used to relate the supply parameters to the rate at which gas is flowing from the supply vessel. For this case,

$$\dot{w} = - \frac{d}{dt}\left(m(t) \right) \tag{1}$$

where m(t) is the mass in the supply at any time t. It is known from one dimensional flow theory, applied at the throat of a choked convergent nozzle, that

$$\dot{w} = \sqrt{\frac{\gamma g}{R}\left(\frac{2}{\gamma+1}\right)^{\frac{\gamma+1}{\gamma-1}}} \frac{P_t A^* C_d}{\sqrt{T_t}} \tag{2}$$

for a perfect gas.

Under the assumption of quasi-steady flow, the value of the weight flow is a function of the instantaneous value of the supply pressure and temperature. Using this assumption, eqs. (1) and (2) can be combined.

$$-\frac{d}{dt}\left(m(t)\right) = \sqrt{\frac{\gamma g}{R}\left(\frac{2}{\gamma+1}\right)^{\frac{\gamma+1}{\gamma-1}}}\ \frac{P_t A^* C_d}{\sqrt{T_t}} \tag{3}$$

In this equation, P_t and T_t are functions of time. The solution of eq.(3) requires that P_t, T_t and m(t) be expressed in terms of a single time dependent variable. The assumption of isentropic conditions in the constant volume supply vessel produces the following equations:

$$\frac{P_t}{P_{to}} = \left(\frac{m}{m_o}\right)^{\gamma} \tag{4}$$

$$\frac{T_t}{T_{to}} = \left(\frac{P_t}{P_{to}}\right)^{\frac{\gamma-1}{\gamma}} \tag{5}$$

Introducing the notation

$$G(t) = \frac{m(t)}{m_o} \tag{6}$$

where G is a dimensionless mass ratio, eqs. (4) and (5) can be re-written as

$$\frac{P_t}{P_{to}} = G^{\gamma}$$

and

$$\frac{T_t}{T_{to}} = G^{\gamma-1}$$

Substituting eqs. (6), (7), and (8) into eq. (3), the following differential equation is obtained

$$\frac{dG}{dt} = - \frac{k}{m_o} G^{\frac{\gamma+1}{2}} \tag{9}$$

where

$$k = \frac{C_d P_{to} A^* \sqrt{\gamma g}}{\left[\left(\frac{\gamma+1}{2}\right)^{\frac{\gamma+1}{\gamma-1}} RT_{to} \right]^{\frac{1}{2}}} \tag{10}$$

This equation can be solved by separating variables and integrating.

$$- \frac{k}{m_o} \int_o^{dt} dt = \int_1^t G^{\frac{-\gamma+1}{2}} \, dG \tag{11}$$

The solution is

$$G = \left[\frac{\gamma-1}{2} \frac{k}{m_o} t + 1\right]^{- \frac{2}{\gamma-1}} \tag{12}$$

Now, since the time dependence of G is established in equation (12), eqs. (7) and (8) can be written as

$$P_t = P_{to} \left[\frac{\gamma-1}{2} \frac{k}{m_o} t + 1\right]^{- \frac{2\gamma}{\gamma-1}} \tag{13}$$

$$T_t = T_{do} \left[\frac{\gamma-1}{2} \frac{k}{m_o} t + 1\right]^{-2} \tag{14}$$

A series of experiments were conducted to check the validity of equations (12), (13) and (14).

The pressure vessel, a 7.8 cubic foot cylindrical steel tank, was filled with nitrogen to an initial pressure of 80 psig, which was read from a precision pneumatic calibrator. Since the filling raises the temperature above that of the surroundings, time was allowed for the gas to come to equilibrium with the surroundings and all runs were conducted from the same initial temperature and pressure of 97^{o}F and 80 psig respectively. The initial temperature of the gas was measured using a copper-constantan thermocouple. The temperature of the reference junction, which was immersed in an ice-bath, was 32^{o}F.

The tank was also instrumented with a 100psi differential pressure transducer. The transducer was fitted into a small valve which was attached to the tank. This allowed the transducer to be detached and atmospheric reference pressure to be recorded before each run. The output from the transducer was fed into a recording oscillograph. The oscillograph recorded the pressure-time history on a 5 inch-wide film strip. The film strip speed was 0.25 inches per second. The valve to the transducer was opened and a second reference reading of 80 psig was recorded. Since the oscillograph output is linear, two reference readings were sufficient.

The gas was then allowed to discharge through an ASME standard long-radius flow nozzle which had a discharge coefficient of 0.99. A two-inch, quick-opening gate valve was attached to the tank. The gas flowed through a two inch diameter, seven inch long

pipe at a Mach number of 0.01 upstream of the nozzle. The oscillograph was turned on several seconds before the valve was opened to take the reference reading and was left on several seconds after the valve was closed to observe the pressure rise due to the heat transfer into the tank.

Seven runs were made, with one of them recording the pressure-time history completely from 80 psig to atmospheric pressure. The other six were stopped after various run times and the pressure and temperature of the remaining gas was measured after equilibrium was again established. From this data, a mass vs. time plot was generated.

The experimental data is compared with the results of the theoretical analysis in figures 11.1, 11.2 and 11.3. Figure 11.1 is a plot of the complete pressure-time history, with the theoretical curve plotted for the choked portion. Discrepancies between the two curves may be due to heat transfer into the supply tank, incorrect value of the ASME standard, long-radius flow nozzle discharge coefficient or incorrect value for volume of the supply tank. A nozzle discharge coefficient of 0.85 gave a better corroboration between theory and experiment. Figure 11.2 is plot of mass ratio versus time and fig. 11.3 shows the variation of the pressure ratio versus the mass ratio.

The above theoretical results were used on spherical and toroidal supply vessels in some preliminary digital computer studies

to investigate whether required gyro spin-up rates could be achieved. Centrifugal effects and increased moment-of-inertia of the system due to the supply tanks were taken into account. These preliminary studies indicated that 100 cps spin velocities can be attained with aluminum spherical containers. It turns out that a large number of smaller containers gives better results than fewer, larger ones.

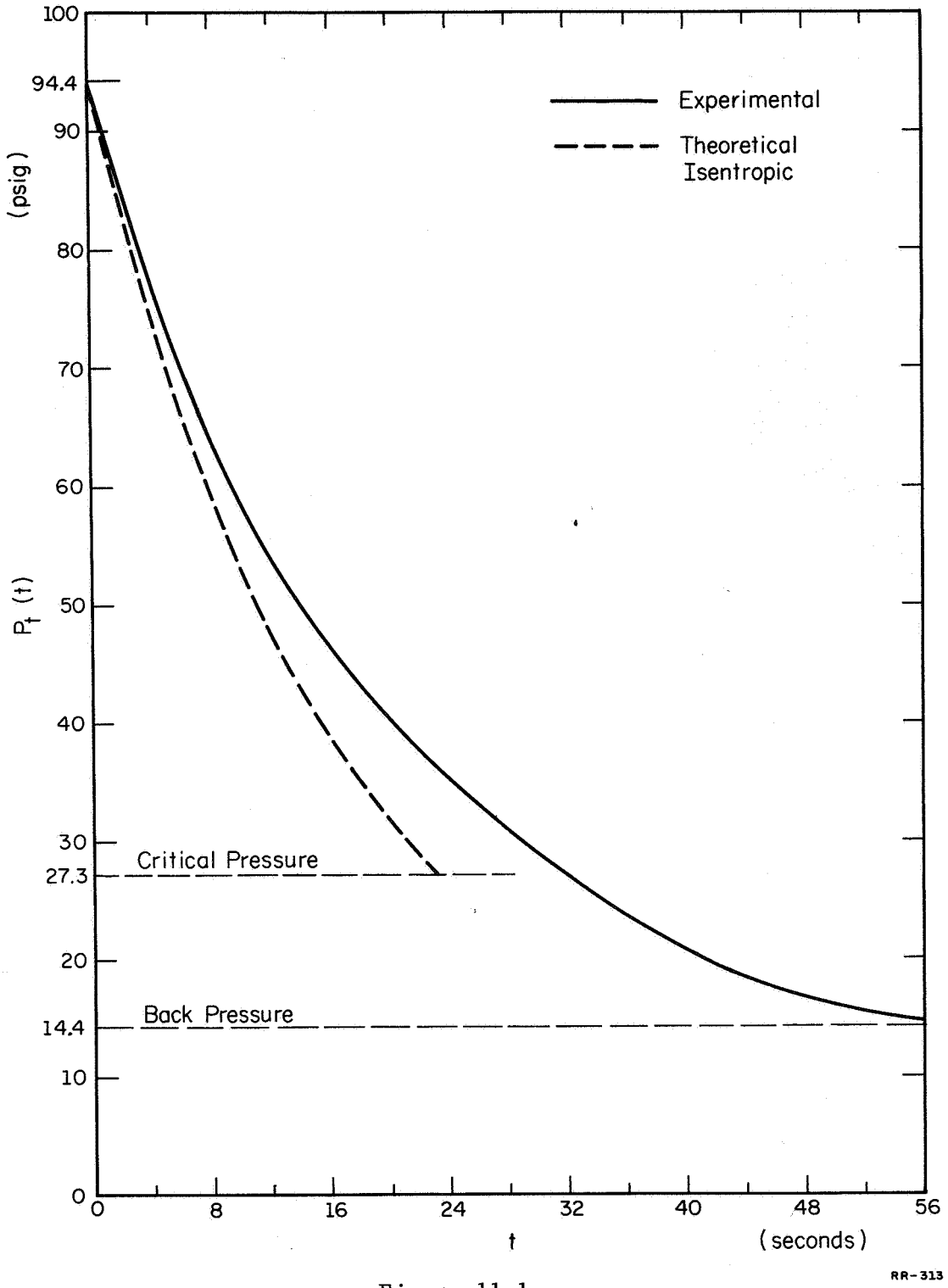

Figure 11.1

Gas pressure vs. time. 7.8 cubic-foot tank filled with nitrogen gas discharging into atmosphere.

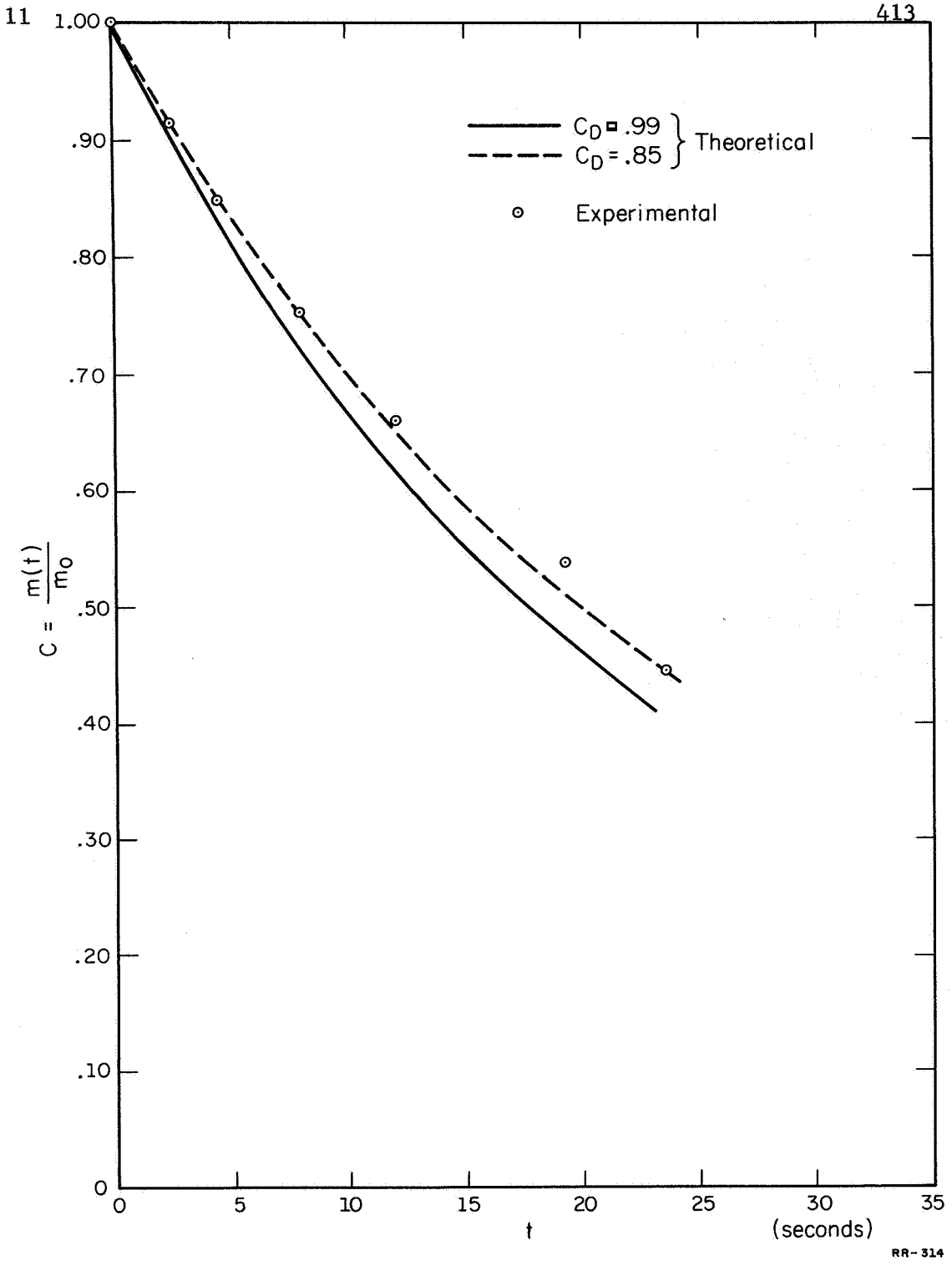

Figure 11.2

Mass ratio vs. time. 7.8 cubic-foot tank filled with nitrogen gas, initially at a pressure of 80 psig, discharging into atmosphere.

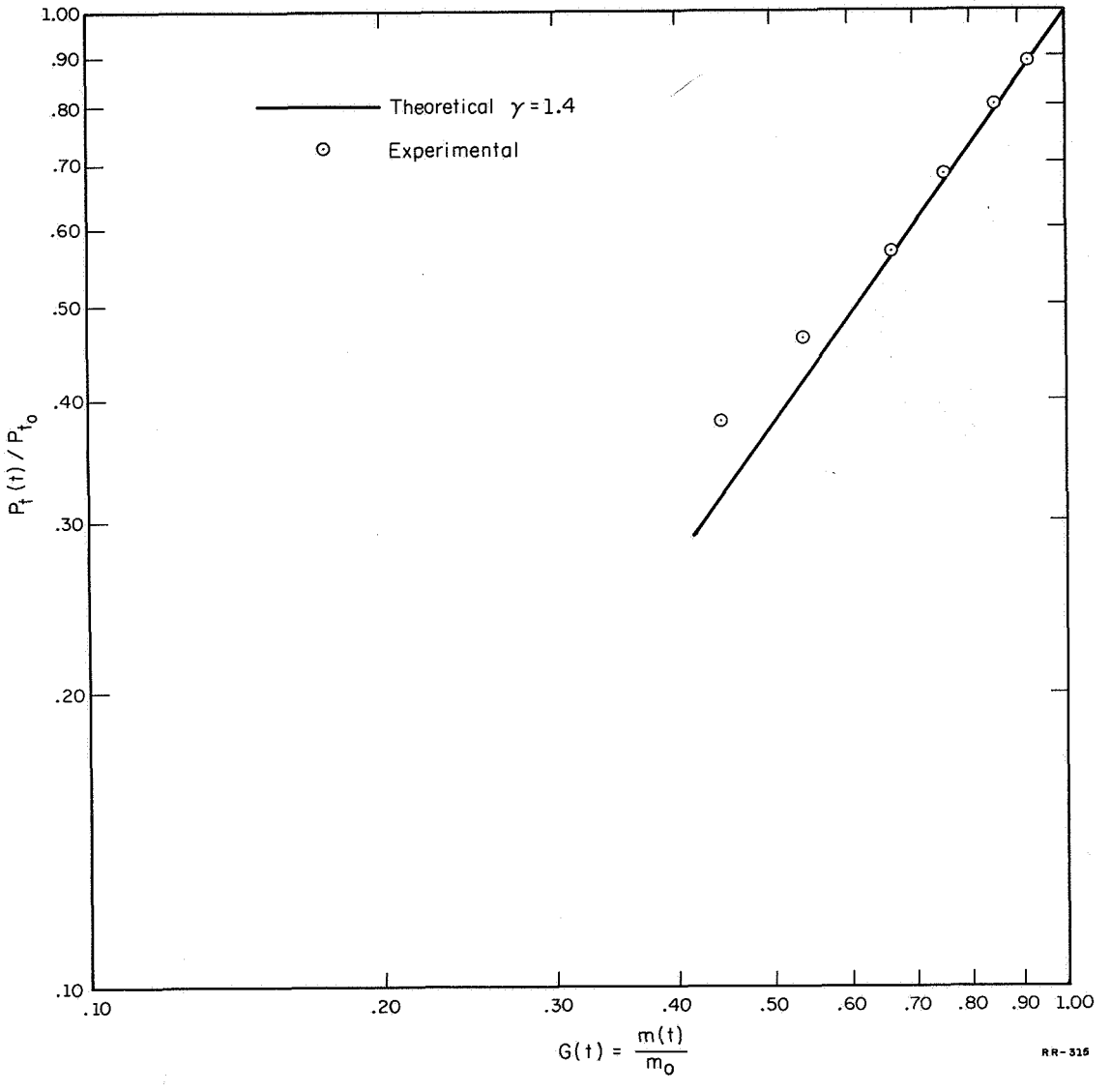

Figure 11.3

Gas pressure ratio vs. mass ratio. 7.8 cubic-foot tank filled with nitrogen gas, initially at a pressure of 80 psig, discharging into the atmosphere.

List of Symbols

Symbol	Definition	Units
A^*	Nozzle throat area	ft^2
C_d	Nozzle discharge coefficient	-
G	Ratio of mass in supply ($\frac{m}{m_o}$)	-
g	Acceleration of gravity	ft/sec^2
m(t)	Mass of gas in supply	lbm
m_o	Mass of gas initially in supply	lbm
$P_t(t)$	Supply pressure	psia
P_{to}	Initial supply pressure	psia
R	Gas constant	$\frac{ft\text{-}lb}{lbm\ {}^oR}$
t	Time	sec
$T_t(t)$	Supply temperature	^oR
T_{to}	Initial supply temperature	^oR
$\dot{w}$	Weight flow	lbm/sec
γ	Specific heat ratio	-

DISTRIBUTION LIST AS OF APRIL 1, 1967

1 Dr. Edward M. Reilley
Asst. Director (Research)
Ofc. of Defense Res. & Engrg.
Department of Defense
Washington, D. C. 20301

1 Office of Deputy Director
(Research and Information Rm. 3D1037)
Department of Defense
The Pentagon
Washington, D. C. 20301

1 Director
Advanced Research Projects Agency
Department of Defense
Washington, D. C. 20301

1 Director for Materials Sciences
Advanced Research Projects Agency
Department of Defense
Washington, D. C. 20301

1 Headquarters
Defense Communications Agency (333)
The Pentagon
Washington, D. C. 20305

50 Defense Documentation Center
Attn: TISIA
Cameron Station, Bldg. 5
Alexandria, Virginia 22314

1 Director
National Security Agency
Attn: TDL
Fort George G. Meade, Maryland 20755

1 Weapons Systems Evaluation Group
Attn: Col. Daniel W. McElwee
Department of Defense
Washington, D. C. 20305

1 National Security Agency
Attn: R4-James Tippet
Office of Research
Fort George G. Meade, Maryland 20755

1 Central Intelligence Agency
Attn: OCR/DD Publications
Washington, D. C. 20505

1 Colonel Kee
AFRSTE
Hqs. USAF
Room 1D-429, The Pentagon
Washington, D. C. 20330

1 Colonel A. Swan
Aerospace Medical Division
Brooks Air Force Base, Texas 78235

1 AUL3T-9663
Maxwell AFB, Alabama 36112

1 AFFTC (FTBPP-2)
Technical Library
Edwards AFB, California 93523

1 Space Systems Division
Air Force Systems Command
Los Angeles Air Force Station
Los Angeles, California 90045
Attn: SSSD

1 Major Charles Waespy
Technical Division
Deputy for Technology
Space Systems Division, AFSC
Los Angeles, California 90045

1 SSD(SSTRT/Lt. Starbuck)
AFUPO
Los Angeles, California 90045

1 Det. #6, OAR (LOOAR)
Air Force Unit Post Office
Los Angeles, California 90045

1 Systems Engineering Group (RTD)
Technical Information Reference Branch
Attn: SEPIR
Directorate of Engineering Standards
& Technical Information
Wright-Patterson AFB, Ohio 45433

1 ARL (ARIY)
Wright-Patterson AFB, Ohio 45433

1 Dr. H. V. Noble
Air Force Avionics Laboratory
Wright-Patterson AFB, Ohio 45433

1 Mr. Peter Murray
Air Force Avionics Laboratory
Wright-Patterson AFB, Ohio 45433

1 AFAL (AVTE/R.D. Larson)
Wright-Patterson AFB, Ohio 45433

2 Commanding General
Attn: STEWS-WS-VT
White Sands Missile Range,
New Mexico 88002

1 RADC (EMLAL-I)
Griffiss AFB, New York 13442
Attn: Documents Library

1 Academy Library (DFSLB)
U. S. Air Force Academy
Colorado Springs, Colorado 80912

1 Lt. Col. Bernard S. Morgan
Frank J. Seiler Research Laboratory
U. S. Air Force Academy
Colorado Springs, Colorado 80912

1 APGC (PGBPS-12)
Elgin AFB, Florida 32542

1 Commanding Officer
Human Engineering Laboratories
Aberdeen Proving Ground, Maryland 21005

1 Director
U. S. Army Engineer Geodesy, Intelligence
and Mapping
Research and Development Agency
Fort Belvior, Virginia 22060

1 Commandant
U. S. Army Command and General Staff College
Attn: Secretary
Fort Leavenworth, Kansas 66270

1 Dr. H. Robl
Deputy Chief Scientist
U. S. Army Research Office (Durham)
Box CM, Duke Station
Durham, North Carolina 27706

1 Commanding Officer
U. S. Army Research Office (Durham)
Attn: CRD-AA-IP (Richard O. Ulsh)
Box CM, Duke Station
Durham, North Carolina 27706

1 Librarian
U. S. Army Military Academy
West Point, New York 10996

1 The Walter Reed Institute of Research
Walter Reed Medical Center
Washington, D. C. 20012

1 Commanding Officer
U. S. Army Electronics R&D Activity
Fort Huachuca, Arizona 85163

1 Commanding Officer
U. S. Army Engineer R&D Laboratory
Attn: STINFO Branch
Fort Belvoir, Virginia 22060

1 Commanding Officer
U. S. Army Electronics R&D Activity
White Sands Missile Range, New Mexico 88002

1 Dr. S. Benedict Levin, Director
Institute for Exploratory Research
U. S. Army Electronics Command
Fort Monmouth, New Jersey 07703

1 Director
Institute for Exploratory Research
U. S. Army Electronics Command
Attn: Mr. Robert O. Parker, Executive
Secretary, JSTAC (AMSEL-XL-D)
Fort Monmouth, New Jersey 07703

1 Commanding General
U. S. Army Electronics Command
Fort Monmouth, New Jersey 07703

Attn: AMSEL-SC
RD-D
RD-G
RD-GF
RD-MAT
XL-D
XL-E
XL-C
XL-S
HL-D
HL-CT-R
HL-CT-P
HL-CT-L
HL-CT-O
HL-CT-I
HL-CT-A
NL-D
NL-A
NL-P
NL-R
NL-S
KL-D
KL-E
KL-S
KL-T
VL-D
WL-D

1 Chief of Naval Research
Department of the Navy
Washington, D. C. 20360
Attn: Code 427

3 Chief of Naval Research
Department of the Navy
Washington, D. C. 20360
Attn: Code 437

2 Naval Electronics Systems Command
ELEX 03
Falls Church, Virginia 22046

1 Naval Ship Systems Command
SHIP 031
Washington, D. C. 20360

1 Naval Ship Systems Command
SHIP 035
Washington, D. C. 20360

2 Naval Ordnance Systems Command
ORD 32
Washington, D. C. 20360

2 Naval Air Systems Command
AIR 03
Washington, D. C. 20360

2 Commanding Officer
Office of Naval Research Branch Office
Box 39, Navy No. 100 F.P.O.
New York, New York 09510

1 AFETR Technical Library
(ETV, MU-135)
Patrick AFB, Florida 32925

1 AFETR (ETLLG-I)
STINFO Officer (For Library)
Patrick AFB, Florida 32925

1 Dr. L. M. Hollingsworth
AFCRL (CRN)
L. G. Hanscom Field
Bedford, Massachusetts 01731

1 AFCRL (CRMXLR)
AFCRL Research Library, Stop 29
L. G. Hanscom Field
Bedford, Massachusetts 01731

1 Colonel Robert E. Fontana
Department of Electrical Engineering
Air Force Institute of Technology
Wright-Patterson AFB, Ohio 45433

1 Colonel A. D. Blue
RTD (RTTL)
Bolling Air Force Base, D. C. 20332

1 Dr. I. R. Mirman
AFSC (SCT)
Andrews AFB, Maryland 20331

1 Colonel J. D. Warthman
AFSC (SCTR)
Andrews AFB, Maryland 20331

1 Lt. Col. J. L. Reeves
AFSC (SCBB)
Andrews AFB, Maryland 20331

2 ESD (ESTI)
L. G. Hanscom Field
Bedford, Massachusetts 01731

1 AEDC (ARO, INC)
Attn: Library/Documents
Arnold AFS, Tennessee 37389

2 European Office of Aerospace Research
Shell Building
47 Rue Cantersteen
Brussels, Belgium

5 Lt. Col. Robert B. Kalisch
Chief, Electronics Division
Directorate of Engineering Sciences
Air Force Office of Scientific Research
Arlington, Virginia 22209

1 U. S. Army Research Office
Attn: Physical Sciences Division
3045 Columbia Pike
Arlington, Virginia 22204

1 Research Plans Office
U. S. Army Research Office
3045 Columbia Pike
Arlington, Virginia 22204

1 Commanding General
U. S. Army Materiel Command
Attn: AMCRD-RS-DE-E
Washington, D. C. 20315

1 Commanding General
U. S. Army Strategic Communications Command
Washington, D. C. 20315

1 Commanding Officer
U. S. Army Materials Research Agency
Watertown Arsenal
Watertown, Massachusetts 02172

1 Commanding Officer
U. S. Army Ballistics Research Laboratory
Attn: V. W. Richards
Aberdeen Proving Ground
Aberdeen, Maryland 21005

1 Commandant
U. S. Army Air Defense School
Attn: Missile Sciences Division, C&S Dept.
P.O. Box 9390
Fort Bliss, Texas 79916

1 Redstone Scientific Information Center
Attn: Chief, Document Section
Redstone Arsenal, Alabama 35809

1 Commanding General
Frankford Arsenal
Attn: SMUFA-1310 (Dr. Sidney Ross)
Philadelphia, Pennsylvania 19137

1 U. S. Army Munitions Command
Attn: Technical Information Branch
Picatinney Arsenal
Dover, New Jersey 07801

1 Commanding Officer
Harry Diamond Laboratories
Attn: Dr. Berthold Altman (AMXDO-TI)
Connecticut Avenue and Van Ness Street, N.W.
Washington, D. C. 20438

1 Commanding Officer
U. S. Army Security Agency
Arlington Hall
Arlington, Virginia 22212

1 Commanding Officer
U. S. Army Limited War Laboratory
Attn: Technical Director
Aberdeen Proving Ground
Aberdeen, Maryland 21005

1 Commanding Officer
Office of Naval Research Branch Office
219 South Dearborn Street
Chicago, Illinois 60604

1 Commanding Officer
Office of Naval Research Branch Office
1030 East Green Street
Pasadena, California 91101

1 Commanding Officer
Office of Naval Research Branch Office
207 West 24th Street
New York, New York 10011

1 Commanding Officer
Office of Naval Research Branch Office
495 Summer Street
Boston, Massachusetts 02210

8 Director, Naval Research Laboratory
Technical Information Officer
Washington, D. C. 20390
Attn: Code 2000

1 Commander
Naval Air Development and Material Center
Johnsville, Pennsylvania 18974

2 Librarian
U. S. Naval Electronics Laboratory
San Diego, California 95152

1 Commanding Officer and Director
U. S. Naval Underwater Sound Laboratory
Fort Trumbull
New London, Connecticut 06840

1 Librarian
U. S. Navy Post Graduate School
Monterey, California 93940

1 Commander
U. S. Naval Air Missile Test Center
Point Mugu, California 95468

1 Director
U. S. Naval Observatory
Washington, D. C. 20390

2 Chief of Naval Operations
OP-07
Washington, D. C. 20350

1 Director, U. S. Naval Security Group
Attn: G43
3801 Nebraska Avenue
Washington, D. C. 20016

2 Commanding Officer
Naval Ordnance Laboratory
White Oak, Maryland 21162

1 Commanding Officer
Naval Ordnance Laboratory
Corona, California 91720

1 Commanding Officer
Naval Ordnance Test Station
China Lake, California 93555

1 Commanding Officer
Naval Avionics Facility
Indianapolis, Indiana 46218

1 Commanding Officer
Naval Training Device Center
Orlando, Florida 32813

1 U. S. Naval Weapons Laboratory
Dahlgren, Virginia 22448

1 Weapons Systems Test Division
Naval Air Test Center
Patuxtent River, Maryland 20670
Attn: Library

1 Head, Technical Division
U. S. Naval Counter Intelligence Support Center
Fairmont Building
4420 North Fairfax Drive
Arlington, Virginia 22203

1 Mr. Charles F. Yost
Special Asst. to the Director of Research
National Aeronautics and Space Administration
Washington, D. C. 20546

1 Dr. H. Harrison, Code RRE
Chief, Electrophysics Branch
National Aeronautics and Space Administration
Washington, D. C. 20546

1 Goddard Space Flight Center
National Aeronautics and Space Administration
Attn: Library C3/TDL
Green Belt, Maryland 20771

1 NASA Lewis Research Center
Attn: Library
21000 Brookpark Road
Cleveland, Ohio 44135

1 National Science Foundation
Attn: Dr. John R. Lehmann
Division of Engineering
1800 G Street, N.W.
Washington, D. C. 20550

1 U. S. Atomic Energy Commission
Division of Technical Information Extension
P. O. Box 62
Oak Ridge, Tennessee 37831

1 Los Alamos Scientific Laboratory
Attn: Reports Library
P. O. Box 1663
Los Alamos, New Mexico 87544

2 NASA Scientific & Technical Information
Facility
Attn: Acquisitions Branch (S/AK/DL)
P. O. Box 33
College Park, Maryland 20740

1 Director
Research Laboratory of Electronics
Massachusetts Institute of Technology
Cambridge, Massachusetts 02139

1 Polytechnic Institute of Brooklyn
55 Johnson Street
Brooklyn, New York 11201
Attn: Mr. Jerome Fox
Research Coordinator

1 Director
Columbia Radiation Laboratory
Columbia University
538 West 120th Street
New York, New York 10027

1 Director
Coordinated Science Laboratory
University of Illinois
Urbana, Illinois 61801

1 Director
Stanford Electronics Laboratories
Stanford University
Stanford, California 94305

1 Director
Electronics Research Laboratory
University of California
Berkeley, California 94720

1 Director
Electronic Sciences Laboratory
University of Southern California
Los Angeles, California 90007

1 Professor A. A. Dougal, Director
Laboratories for Electronics and Related
Sciences Research
University of Texas
Austin, Texas 78712

1 Division of Engineering and Applied Physics
210 Pierce Hall
Harvard University
Cambridge, Massachusetts 02138

1 Aerospace Corporation
P. O. Box 95085
Los Angeles, California 90045
Attn: Library Acquisitions Group

1 Professor Nicholas George
California Institute of Technology
Pasadena, California 91109

1 Aeronautics Library
Graduate Aeronautical Laboratories
California Institute of Technology
1201 East California Boulevard
Pasadena, California 91109

1 Director, USAF Project RAND
Via: Air Force Liaison Office
The RAND Corporation
1700 Main Street
Santa Monica, California 90406
Attn: Library

1 The Johns Hopkins University
Applied Physics Laboratory
8621 Georgia Avenue
Silver Spring, Maryland 20910
Attn: Boris W. Kuvshinoff
Document Librarian

1 Hunt Library
Carnegie Institute of Technology
Schenley Park
Pittsburgh, Pennsylvania 15213

1 Dr. Leo Young
Stanford Research Institute
Menlo Park, California 94025

1 Mr. Henry L. Bachmann
Assistant Chief Engineer
Wheeler Laboratories
122 Cuttermill Road
Great Neck, New York 11021

1 School of Engineering Sciences
Arizona State University
Tempe, Arizona 85281

1 University of California at Los Angeles
Department of Engineering
Los Angeles, California 90024

1 California Institute of Technology
Pasadena, California 91109
Attn: Documents Library

1 University of California
Santa Barbara, California 93106
Attn: Library

1 Carnegie Institute of Technology
Electrical Engineering Department
Pittsburgh, Pennsylvania 15213

1 University of Michigan
Electrical Engineering Department
Ann Arbor, Michigan 48104

1 New York University
College of Engineering
New York, New York 10019

1 Syracuse University
Department of Electrical Engineering
Syracuse, New York 13210

1 Yale University
Engineering Department
New Haven, Connecticut 06520

1 Airborne Instruments Laboratory
Deerpark, New York 11729

1 Bendix Pacific Division
11600 Sherman Way
North Hollywood, California 91605

1 General Electric Company
Research Laboratories
Schenectady, New York 12301

1 Lockheed Aircraft Corporation
P. O. Box 504
Sunnyvale, California 94088

1 Raytheon Company
Bedford, Massachusetts 01730
Attn: Librarian

1 Dr. G. J. Murphy
The Technological Institute
Northwestern University
Evanston, Illinois 60201

1 Dr. John C. Hancock, Director
Electronic Systems Research Laboratory
Purdue University
Lafayette, Indiana 47907

1 Director
Microwave Laboratory
Stanford University
Stanford, California 94305

1 Emil Schafer, Head
Electronics Properties Info Center
Hughes Aircraft Company
Culver City, California 90230